7-1-2016

First amplitude analysis of $B^+ \to J/...$

Thomas Britton
Syracuse University

Abstract

The first amplitude analysis of $B^+ \to J/\psi\phi K^+$, $J/\psi \to \mu^+\mu^-$, $\phi \to K^+K^-$ events is performed in Isobar approximation using all six degrees of freedom of their decay kinematics and 3 fb^{-1} of pp collision data collected at $\sqrt{s} = 7-8$ TeV with the LHCb detector. A number of $K^{*+} \to \phi K^+$ states are observed, including $K^*(1680)$, which is observed in this decay mode for the first time (8σ significant). A number of $J/\psi\phi$ mass structures are also observed which cannot be described with K^{*+} contributions alone. A broad and significant (7.6σ) enhancement just above the kinematic threshold is best described as a $D_s^+ D_s^{*-}$ cusp, but a resonant interpretation is also possible with the mass consistent with the $X(4140)$ state, but with a much larger width than previously claimed. The J^{PC} is determined to be 1^{++} at 5.7σ. Previously inconclusive evidence for the second peak is confirmed with a mass consistent with the 0^{-+} $D_s^+ D_{s0}^{*-}$ cusp, however, much better described in our model as a $X(4274)$ 1^{++} resonance (6.0σ significant). The high $J/\psi\phi$ mass region shows evidence for more structures of high significance, possibly two 0^{++} resonances. More data and going beyond the Isobar model may be required to clarify the nature of all $J/\psi\phi$ mass structures observed in this decay mode.

First amplitude analysis of $B^+ \to J/\psi\, \phi K^+$

Thomas Britton

DISSERTATION

Submitted in partial fulfillment of the requirements for the degree of Doctor of Philosophy in Physics

Syracuse University July 2016

"The brick walls are there for a reason. The brick walls are not there to keep us out. The brick walls are there to give us a chance to show how badly we want something. Because the brick walls are there to stop the people who don't want it badly enough" –Randy Pausch, *The Last Lecture*

This work is dedicated to all who supported the endeavor:

To my adviser, Tomasz Skwarnicki, whose expertise and support I relied on at every point during this project. I don't think there was ever a time that went smoothly on this very complicated project and while it was easy to become discouraged your guidance and support allowed me to push forward every day.

To Steve Blusk, Marina Artuso, Sheldon Stone, Ray Mountain, and JC Wang who were always willing to take the time to lend their expertise on all manner of topics from hardware to electronics and more. I learned a great deal over the years and each one of you had an impact on me both personally and as a student of physics.

To Bin Gui, Bilas Pal, and Nathan Jurik whose own work and advice I greatly appreciated throughout the years we shared an office.

I also wanted to thank all of the of the staff of the Syracuse University physics department who were always supportive and who always made sure I was on track.

To my wife, Meghan Britton, who stood by me through all of the trials and tribulations of graduate school. I know it was not easy but your constant support kept me grounded and healthy and your strength, especially during the last few months of consistently shifting goal lines, was necessary.

And finally to Declan, while you aren't quite out into the world you provided the catalyst for completing this chapter of life and are the motivating factor as I look towards the future.

Contents

List of Figures

List of Tables

1 Introduction

The Standard Model is the framework supporting all of the current understandings of the fundamental forces in the universe. It concerns itself with the electromagnetic, weak, and strong interactions, with much work devoted to bringing gravity under its purview. Additionally the Standard Model allows for the classification of all subatomic particles. There are three main categories for fundamental particles to fall into: quarks, leptons, and bosons. Leptons and quarks have half-integer spin, while bosons have integer spin and mediate the fundamental forces. Quarks participate in all interactions. Leptons do not feel the strong force. Quarks and leptons come in three generations.

Hadrons are particles made up of quarks (and/or anti-quarks) and held together by the strong force. These strong interactions are governed by Quantum Chromo-Dynamics (QCD) in the Standard Model. In QCD quarks have color-charge and are often considered to be red, blue, or green or an anti color *e.g.* anti-red. QCD then describes the binding of these colored quarks together in colorless groups via exchange of gluons (the carrier of the strong force). The simplest colorless groups are $q\overline{q}$ pairs, in which the anti-quark carries the anti-color of the quark, or qqq triplets in which each quark carries one of the three colors (or anti-colors). The former doublets are referred to as mesons while the triplets are referred to as baryons.

Mesons ($q\overline{q}$), baryons (qqq) and baryonic molecules (*i.e.* atomic nuclei) are all very well established bound states of quarks. However, the theory governing the strong interaction (QCD) does allow for the existence of other "exotic" states. These states could be mesonic molecules $(q\overline{q})(q\overline{q})$, tightly bound tetraquarks ($qq\overline{q}\overline{q}$), penataquarks $qqqq\overline{q}$ in the form of loosely bound meson-baryon molecules or tightly bound systems, tightly bound di-baryons ($qqqqqq$) etc. Bound states involving gluons as constituents are also possible, hybrids ($q\overline{q}g$) that involve both quarks and glouns, or even gluonia (gg) are thought to exist. However, no clear evidence for exotic hadronic states has been found in light quark

spectroscopy. It was not until 2003 and the discovery of the $X(3872)$ state by Belle in the $B \to X(3872)K \to (J/\psi\,\pi^+\pi^-)K$ channel that charmonium spectroscopy began to offer many neutral states with properties inconsistent with pure $c\bar{c}$ states.

In 2007 the Belle collaboration discovered the first charged state decaying to a charmonium state and a charged pion, $Z(4430)^+$. The minimal quark content of such a structure necessarily involves two quarks and two anti-quarks (a tetraquark candidate). Since BaBar could not confirm this state, it took until 2014 for LHCb to confirm its existence. The amplitude analysis presented here follows in the footsteps of the $Z(4430)^+$ analysis. This year charged states decaying to J/ψ and a proton have been discovered by LHCb, their minimal quark content is four quarks and an anti-quark, the long sought pentaquarks. The amplitude fitter code used in this analysis has been developed based on the experience gained in the $Z(4430)^+$ analysis and generalized to handle a broader scope of analysis. The code developed for this analysis became the starting point for the Syracuse pentaquark fitter. We benefited from some improvements implemented during the pentaquark analysis, particularly speed-ups, for which we thank Nathan Jurik and Liming Zhang.

The work presented in this note is concerned with the investigation of a resonant structure in $B^+ \to J/\psi\,\phi K^+$ decays. In 2008 the CDF Collaboration presented evidence for a narrow 12 MeV near-threshold structure in the mass spectrum of $J/\psi\,\phi$ coming from this decay [1]. The PDG refers to it as $X(4140)$, though some papers (including CDF) refer to it as $Y(4140)$. A narrow resonance decaying to such a final state is necessarily exotic, as any $c\bar{c}$ resonance at this mass would have OZI allowed decays to pairs of $D^{(*)}$ mesons and be very wide with a very small decay fraction to the phase-space suppressed $J/\psi\,\phi$ and thus remain unobserved unless exotic. In the unpublished update to their analysis [2], the CDF collaboration claimed 5σ significance for the still narrow $X(4140)$ ($\Gamma = 15.3^{+10.4}_{-6.1} \pm 2.5$ MeV) and presented 3.1σ evidence for a second state at $4274.4^{+8.4}_{-6.7} \pm 1.9$ MeV also with a relatively narrow width - see the compilation of all relevant previous results in Tables 1

and 2.

The LHCb collaboration looked for and did not see any evidence for the narrow 15.3 MeV $X(4140)$ state in the early 2011 data (0.37 fb^{-1} was used) and was reported in a conference note [3]. An upper limit on its production in $B^+ \to J/\psi\,\phi K^+$ decays was set, which was at a 2.4σ disagreement with the unpublished CDF results. This upper limit on the narrow $X(4140)$ analysis was later published by LHCb in 2012 [4]. It has been known since September 2011 that our data did indicate a broad threshold enhancement in the region where $X(4140)$ was originally observed.[1] However, a proper analysis of a broad structure required an amplitude analysis with larger statistics, which was later accumulated. The early LHCb data were inconsistent with the state at 4274 MeV suggested by CDF; both analyses were based on naive $J/\psi\,\phi$ mass fits, and an upper limit on its production was also published [4].

Meanwhile, the CMS collaboration confirmed the $X(4140)$ state in 2011 data with 5σ significance, albeit with a larger $28^{+15}_{-11} \pm 19$ MeV width [5]. Their data also showed rather strong peaking at $4313.8.0 \pm 5.3 \pm 7.3$ MeV with $38^{+30}_{-15} \pm 16$ MeV width. However, CMS chose not to claim an observation of the 2nd state since they could not estimate the significance of this structure reliably. We note that the mass measured by CMS is inconsistent with the mass of the 2nd peak in the CDF data at 3.16σ. Since CMS has a much larger data set from Run I than published, an update of their results is likely in the near future.

The D0 collaboration observed the narrow $X(4140)$, though with marginal significance and large errors [6]. There is also some peaking at 4328 MeV in their data, but they could not fit this structure when floating its width.

Adding to the mystery, the D0 collaboration very recently claimed a significant signal for prompt $p\bar{p} \to X(4140)$+anything, $X(4140) \to J/\psi\,\phi$ signal with narrow width. The

[1] See the presentation by T. Skwarnicki on Sept. 6, 2011 at the LHCb Software & Analysis week.

prompt signal is observed on a very large background parameterized by D0 with an ad hoc function. We find it surprising that they did not evaluate systematic uncertainty related to the choice of functional form, thus their systematic errors in this measurements are likely underestimated.

The e^+e^- experiments did not have enough statistics to provide significant input on these states, possibly because of sharply falling reconstruction efficiency near the $J/\psi\,\phi$ mass threshold in $B \to J/\psi\,\phi K$ decays. There is an unpublished 2009 conference report by Belle [7] and the recently published analysis by BaBar [8]. No significant evidence for any $J/\psi\,\phi$ states were observed, but the upper limits did not contradict the claims from the hadronic colliders.

The Belle collaboration saw 3.2σ evidence for a state at $4350.6^{+4.6}_{-5.1} \pm 0.7$ MeV with $13^{+18}_{-9} \pm 4$ MeV width in $\gamma\gamma$ production, which implies $J^P = 0^+$ or 2^+, and found no evidence for $X(4140)$ in this reaction [9].

Table 1: Previous results concerned with $X(4140) \to J/\psi\,\phi$ resonance in $B^+ \to J/\psi\,\phi K^+$ decays. The first significance for the 2nd D0 paper is for the prompt production component, whereas the second for the non-prompt production. The average excludes the CDF 2008 result.

Year	Experiment	$B \to J/\psi\,\phi K$	$X(4140)$			
	luminosity	statistics	M_0 MeV	Γ_0 MeV	sign.	fraction %
2008	CDF 2.7 fb^{-1} [1]	58 ± 10	$4143.0 \pm 2.9 \pm 1.2$	$11.7^{+8.3}_{-5.0} \pm 3.7$	3.8σ	
2011	CDF 6.0 fb^{-1} [2]	115 ± 12	$4143.4^{+2.9}_{-3.0} \pm 0.6$	$15.3^{+10.4}_{-6.1} \pm 2.5$	5.0σ	$14.9 \pm 3.9 \pm 2.4$
2011	LHCb 0.37 fb^{-1} [4]	346 ± 20	4143.4 fixed	15.3 fixed		< 7 @90%CL
2013	CMS 5.2 fb^{-1} [5]	2480 ± 160	$4148.0 \pm 2.4 \pm 6.3$	$28^{+15}_{-11} \pm 19$	5.0σ	10 ± 3
2013	D0 10.4 fb^{-1} [6]	215 ± 37	$4159.0 \pm 4.3 \pm 6.6$	$19.9 \pm 12.6^{+1.0}_{-8.0}$	3.1σ	$21 \pm 8 \pm 4$
2014	BaBar 422 fb^{-1} [8]	189 ± 14	4143.4 fixed	15.3 fixed	1.6σ	< 13.3 @90%CL
2015	D0 10.4 fb^{-1} [10]	$p\bar{p} \to J/\psi\,\phi$...	$4152.5 \pm 1.7^{+6.2}_{-5.4}$	$16.3 \pm 5.6 \pm 11.4$	4.7σ (5.7σ)	
Average			4146.9 ± 2.3	17.8 ± 6.8		

All of the previous analyses that were performed used naive one-dimensional (1D) fits to the invariant $J/\psi\,\phi$ mass ($m_{J/\psi\,\phi}$) with X states added incoherently to non-resonant background which was in turn modeled based on ad-hoc assumptions, which often assumed a 3-body phase-space distribution. Even though no narrow peaks are observed in the

Table 2: Previous results concerned with possible heavier $X \to J/\psi\,\phi$ resonances. The average excludes the CDF 2008, D0 and Belle results. Since the masses are inconsistent between the CDF and CMS, we increased the error on the average to account for it.

Year	Experiment luminosity	$B \to J/\psi\,\phi K$ statistics	$X(4274-4351)$ state(s) M_0 MeV	Γ_0 MeV	sign.	fraction %
2008	CDF 2.7 fb^{-1} [1]	58 ± 10	not observed			
2011	CDF 6.0 fb^{-1} [2]	115 ± 12	$4274.4^{+8.4}_{-6.7} \pm 1.9$	$32.3^{+21.9}_{-15.3} \pm 7.6$	3.1σ	
2011	LHCb 0.37 fb^{-1} [4]	346 ± 20	4274.4 fixed	32.3 fixed		< 8 @90%CL
2013	CMS 5.2 fb^{-1} [5]	2480 ± 160	$4313.8 \pm 5.3 \pm 7.3$	$38^{+30}_{-15} \pm 16$		
2013	D0 10.4 fb^{-1} [6]	215 ± 37	4328.5 ± 12.0	30 fixed		
2014	BaBar 422 fb^{-1} [8]	189 ± 14	4274.4 fixed	32.3 fixed	1.2σ	< 18.1 @90%CL
2010	Belle 825 fb^{-1} [9]	$\gamma\gamma \to J/\psi\,\phi$	$4350.6^{+4.6}_{-5.1} \pm 0.7$	$13^{+18}_{-9} \pm 4$	3.2σ	
Average			4293 ± 20	35 ± 16		

ϕK^+ mass distribution, it is clear that a number of known K^{*+} resonances can contribute. Their interference with potential X resonances can have profound effects on the numerical results for these exotic states, as exemplified by the dramatic changes in the reported $Z(4430)^-$ mass and width in $B^0 \to \psi(2S)\pi^- K^+$ decays. In this case the naive mass fits by Belle gave it a mass of $4433 \pm 4 \pm 2$ MeV and a width of 45^{+18+30}_{-13-13} MeV [11] The proper 4D amplitude analysis of the Belle data changed these parameters to 4485^{+22+28}_{-22-11} MeV and 200^{+41+26}_{-46-35} MeV [12], with a 2D amplitude analysis on the Dalitz plane producing numbers in between the 1D and the 4D fits [13]. The 4D amplitude fit results were confirmed by the LHCb 4D amplitude analysis [14]. Not only did the central values change under the proper analysis, taking into account the interference of the $Z(4430)^- \to \psi(2S)\pi^-$ with $K^{*0} \to K^+\pi^-$ contributions, but also the reported statistical and systematic errors ballooned. Performing an amplitude analysis in all dimensions of the decay kinematics is also the best way to gain sensitivity to the quantum numbers of the observed resonances, which is of crucial importance for their theoretical interpretation.

The amplitude analysis presented here uses all $3\,\text{fb}^{-1}$ collected by the LHCb collaboration from 2011 through 2012, which gives us 4289 ± 151 of reconstructed $B^+ \to J/\psi\,\phi K^+$ events, which is a factor of 2 larger data sample than analyzed by the CMS collaboration

and has a much more favorable signal-to-background ratio.

Full decay kinematics of $B^+ \to J/\psi\,\phi K^+$, $J/\psi \to \mu^+\mu^-$, $\phi \to K^+K^-$ decays involves six dimensions. All of them are utilized to eliminate any biases and to gain the best sensitivity to the decay dynamics. After selection of $B \to J/\psi\,\phi K$ events we will study not only the $J/\psi\,\phi$ spectrum but also the spectrum of the two other combinations: ϕK and $J/\psi\,K$. We will first describe the data used and the preparations made before performing the amplitude fits. Next, we will explain the formalism by which the data is analyzed. We will then construct the matrix elements necessary for this analysis. Finally, the results of the amplitude analysis will be presented together with their implications.

2 The LHC

2.1 The Large Hadron Collider

The Large Hadron Collider (LHC) is a particle collider in a tunnel located under the border between France and Switzerland. With a circumference of 27 km and energies exceeding 7 TeV, it is currently the largest and most powerful particle accelerator in the world. Along the ring there are four places where the beams of protons, which circulate in opposite directions, are forced to cross. At each crossing sits one of four LHC experiments: A Large Ion Collider Experiment (ALICE), A Toroidal LHC ApparatuS (ATLAS), Compact Muon Solenoid (CMS), and LHC beauty quark experiment (LHCb). When crossed the beams of protons, with very high energies, collide. At such high energies these collisions result in the creation of new particles, both known and potentially unknown. Figure 1 shows schematically the entirety the path of the protons as they circulate throughout the LHC.

The beams of protons used in the LHC begin their journey as hydrogen atoms. Once the electrons are stripped off only protons are left. These protons start at the Linac2, a linear accelerator commissioned in the 1980s. The Linac2 requires that the beam have a current of 180mA by the time it reaches the Proton Synchrotron Booster (PSB). It is at this point the energy of the protons is 1.4GeV with a pulse length of 100μs. The beams are then moved via kicker magnets from the rings of the PSB and combined to form one long stream comprised of proton bunches. The beams are then sent to the Proton Synchrotron (PS). The PS accelerate the protons to an energy of 25 GeV with bunch spacing of 25 ns and 72 bunches per stream. Several streams are injected into the Super Proton Synchrotron (SPS) every 3.6 seconds. The SPS once again increases the beam energy to 450GeV. Before injection into the LHC for collisions the current in the magnets, as well as other systems is increases. Additionally the timing phase of the SPS must be in

sync with the LHC to insure proper injection timing. The bunches are compressed and cleaned such that there are no errant tails and the proton bunches are fairly uniform. The beams are then injected at a rate of 40MHz into the LHC. For a more detailed look at the LHC the reader is invited to look at Ref. [15].

The injected beams are sent to the LHC by two transfer lines; TI-2, which injects beams towards ALICE, and TI-8, which injects beams towards LHCb. The beams then circulate around the LHC in opposite directions and are crossed at four points along the ring (the four main experiments previously enumerated). Collisions occur at these four points and relevant data can be collected by each individual experiment.

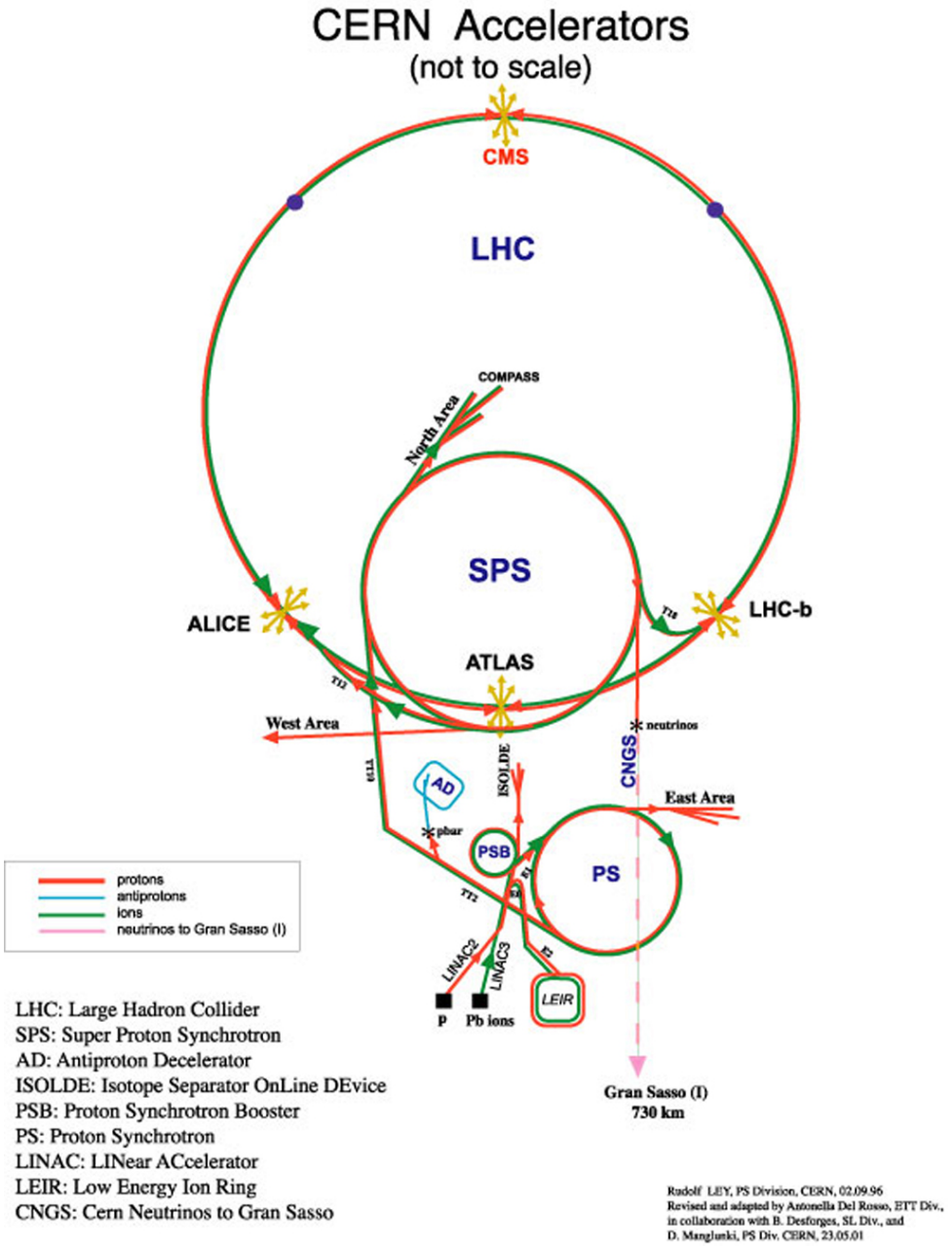

Figure 1: A top down view of the LHC with LINAC2 on the bottom.

2.2 The LHCb Detector

The LHCb detector [16], [17] is a single-arm forward spectrometer covering the psuedo-rapidity range $2 < \eta < 5$, designed for the study of particles containing b or c quarks. The detector includes a high-precision tracking system surrounding the pp interaction region (VELO), which consists of a silicon strip vertex detector. Further downstream is a large-area silicon-strip detector (RICH1), which sits upstream of a dipole magnet with a bending power of approximately 4 Tm. Beyond that there are three stations of silicon-strip detectors and straw drift tubes (T1,T2,T3). The tracking system provides a measurement of momentum, p, of charged particles with a relative uncertainty that varies from 0.5% at low momentum to 1.0% at high momentum (200 GeV/c). The impact parameter, which is defined as the minimum distance of a track to a primary vertex, is measured with a resolution of $(15 + 29/p_{\mathrm{T}})\,\mu$m, where p_{T} is the component of the momentum transverse to the beam, in GeV/c. Photons, electrons, and hadrons are identified by a calorimeter system consisting of scintillating-pad and preshower detectors, an electromagnetic calorimeter and a hadronic calorimeter. Charged hadrons are distinguished by using information gathered by two ring-imaging Cherenkov detectors. Muons are identified by a system made of alternating layers of iron and multiwire proportional chambers. Online event selection is performed by a trigger, which consists of a hardware stage that triggers based on data from the calorimeter and muon systems, followed by a software stage which performs a full event reconstruction. An overview of the the LHCb detector is shown in Figure 2.

2.3 VELO

The VErtex LOcator (VELO) [18] is a silicon microstrip detector that surrounds the pp interaction region. Its primary purpose is to provide spatial measurements of tracks in order to identify primary and secondary interaction verticies, a distinctive feature of hadrons containing b or c quarks. The VELO was designed to cover the forward region in

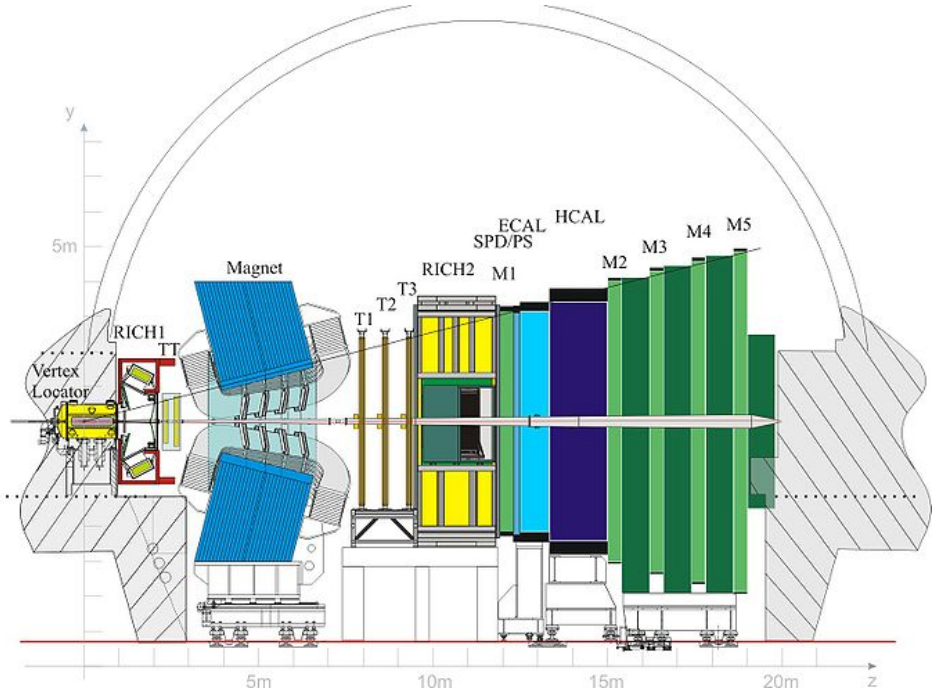

Figure 2: A cross section of the LHCb detector with the interaction region on the far left.

such a way that tracks inside the normal LHCb acceptance (15-300 mrad) would cross at least three of the VELO stations. In doing so, the detector can fully reconstruct 27% of b and $\overline{b}$ production at 7 TeV center of mass energy. The VELO, and specifically its ability to reconstruct primary and secondary vertecies, is a key component in high level triggering which reduces the 1MHz event rate to a few kHz.

The VELO is constructed from a series of silicon modules, arranged along the beam line (z-axis). It is comprised of two retractable halves of 21 modules each that, when closed, lie only 7mm from the beam. These halves are designed to overlap each other to ensure full angular coverage and to aid in alignment. The layout of the silicon modules along the beam pipe as well as the open and closed positions of the VELO are illustrated in Figure 3. When viewed in cylindrical polar coordinates (r,θ,ϕ) each module contains one r and one ϕ coordinate measuring sensor; these are known as R and Φ sensors and are shown in Figure 4. The inter-strip pitch varies across each sensor, from about 40

to 100 µm. Each strip is read out by Beetle analogue front-end ASICs around the circumference of the sensor via routing lines on the sensors. The Beetles are operated at a 40MHz sampling rate and have their signals digitized and processed into clusters by an FPGA-based readout board known as TELL1. Because of the close positioning of the VELO to the beam, it is exposed to very high levels of radiation fluence and $n^+ - on - n$ sensors are used. The only exception is one of the most upstream sensors which utilizes $n^+ - on - p$ sensors.

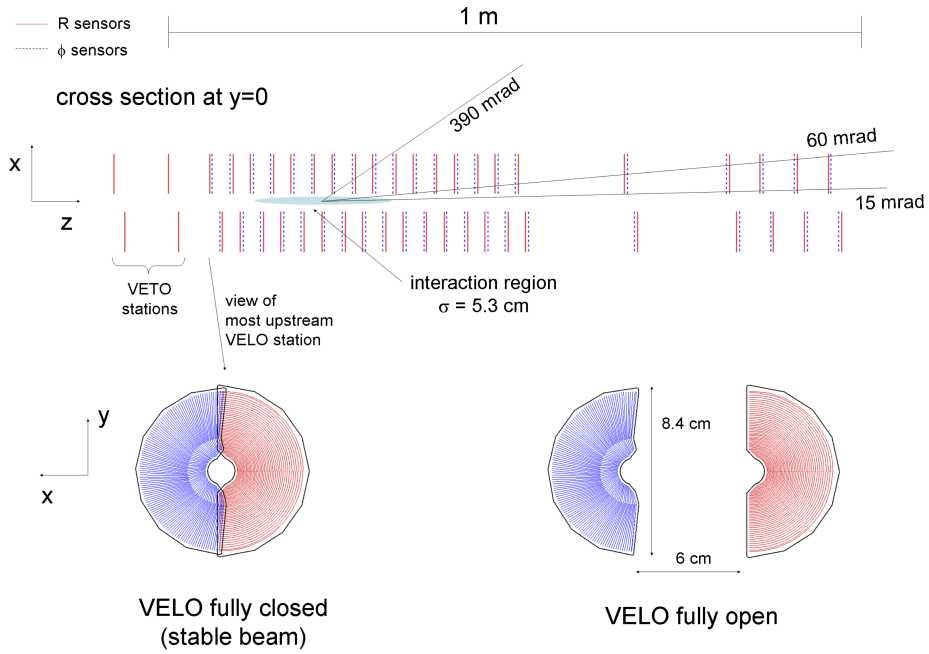

Figure 3: The top of this figure illustrates the arrangement of the silicon sensors along the beam pipe. The bottom illustrates the open and closed positions of the VELO including the overlap present in the closed system

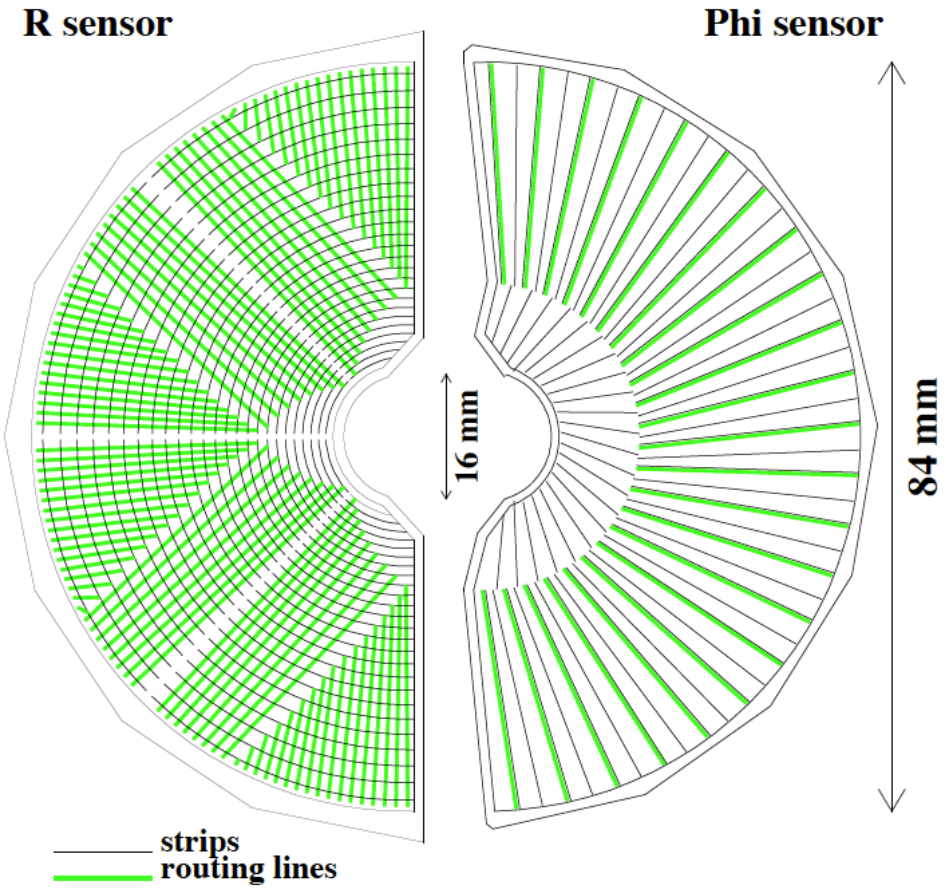

Figure 4: An illustration of the r and ϕ sensors that make up the VELO detector.

2.4 RICH

Located immediately downstream of the VELO is one of the two Ring Imaging CHerenkov detectors (RICH), with the second located downstream of the three tracking stations located behind the magnet. The RICH detectors are tasked with particle identification. This is accomplished by looking at Cherenkov radiation that is emitted by a particle that travels through a medium, a dense gas (C_4F_{10}) in this case, faster than light travels through the medium [19]. This is analogus to an aircraft's sonic boom, in which a conal shockwave is produced when a plane exceeds the speed of sound in air. The RICH system measures the shape of the cone of light that is produced by fast moving particles and since the shape of the cone is related to the velocity of the particle, the particle's velocity can be measured. This information, measured by both RICH1 and RICH2, can be coupled with the trajectory and momentum information from the magnet and tracking stations to calculate the mass and charge of a particle. With this, the identity of a particle can be determined. Particle identification (PID) is key to surpress backgrounds generated from "uninteresting decays" which can be plentiful due to both pions and kaons being common products of B meson decays. It is very important to obtain good discrimination between particle identifications; the RICH gives the necessary information to help get the job done.

The upstream detector, RICH1 [20], is suited to detecting low momentum charged particles with momentum between about 1 and 60 GeV. In contrast, RICH2 [21] is designed to cover higher momentum particles with momentum up to 100 GeV or more. The acceptance of each detector is also markedly different. RICH1 covers the entirety of the LHCb acceptance where as RICH2 has a much more narrow scope of coverage; this is by design as RICH2 focuses on a region of acceptance where high momentum particles are more likely to be found. Both detectors, RICH1 and RICH2, are designed to focus Cherenkov light using both spherical and flat mirrors to direct the light away from the detector acceptance. Hybrid Photo Dectrors (HPD)

are then employed to detect the Cherenkov radiation and form a cone originating from a charged track. A diagram of RICH1 and RICH2 can be found in Figures 5 and 6, respectively. The images the rings observe from the phototube planes are compared with patterns expected from different particle hypothesis. A likelihood, $L^{RICH}(h)$, is then calculated [22], [23] and thusly the particle can be identified. Most of the hadron discrimination of the LHCb detector can be ascribed to the two RICH detectors.

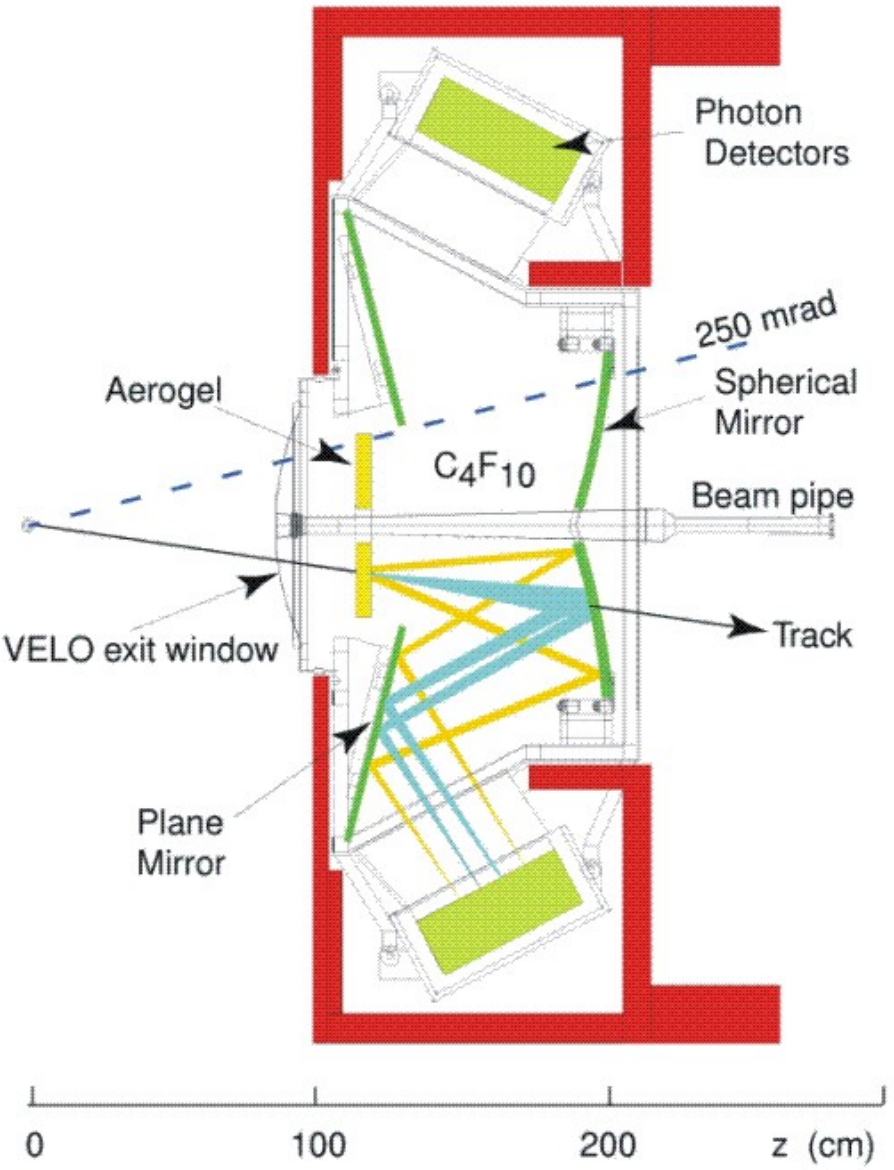

Figure 5: A schematic of the the RICH1 detector located just down stream of the VELO detector.

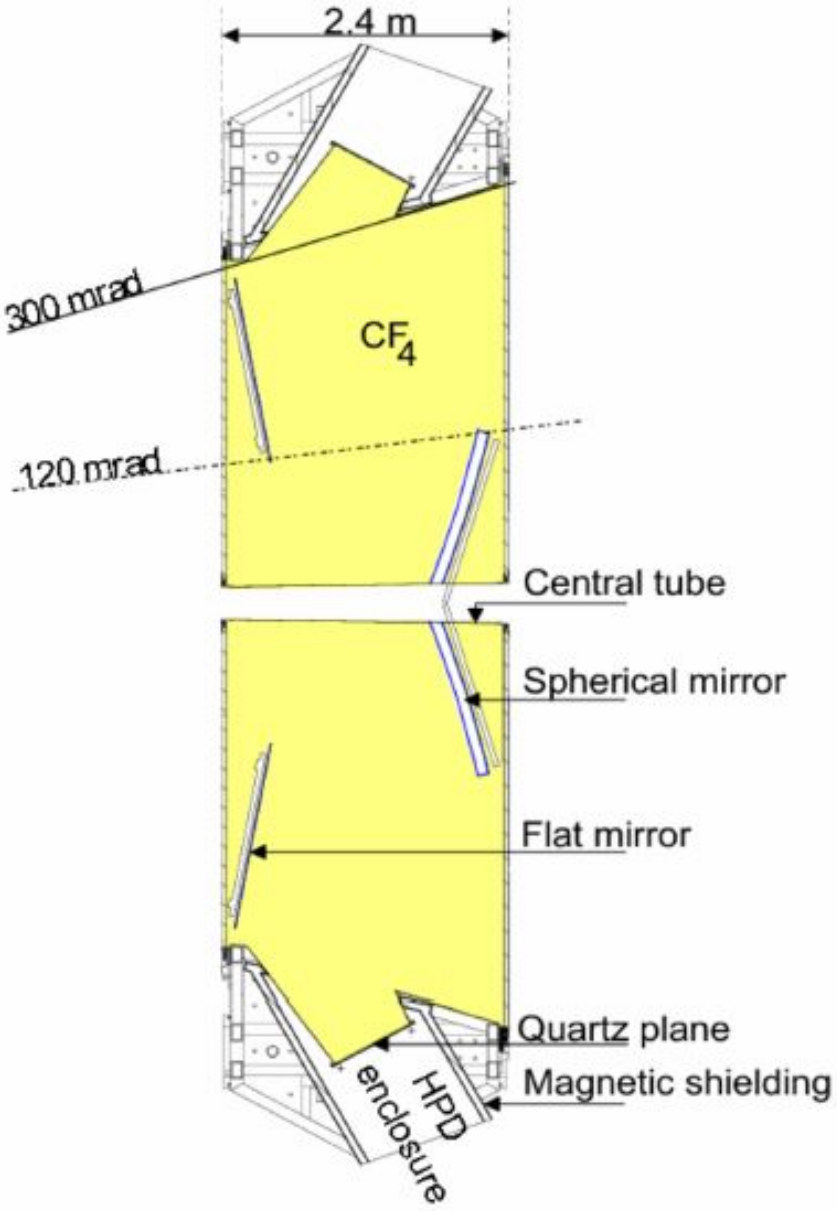

Figure 6: A schematic of the the RICH2 detector located just down stream of the third T station.

2.5 Dipole Magnet

Immediately downstream of the VELO sits a large dipole bending magnet [24]. Through the magnet, particles, which normally travel in a relatively straight line, bend. The direction of bending and curvature of the path are dependent upon both the particle's charge and momentum. The magnet is designed to have 4Tm of integrated field for tracks measuring 10m in length. This provides better track separation for the tracking stations downstream. Even with such a high field the magnet is not superconducting, as such a solution would be uncessary and cost ineffective. The dipole magnet is contructed from two seperate coils shaped like a saddle mounted in a frame and illustrated in Figure 7. Each coil weighs 27 tons and is constructed from 10 layers wound from about 3 km of aluminum cable. When in operation the current in the coils reaches about 5.8 kA. The specific ohmic resistance of the coils is below 28Ωm at 20 °C. With such a large current, heat is generated and provides the greatest stress on the magnet. To combat this a 25mm diameter cooling channel lies within each coil.

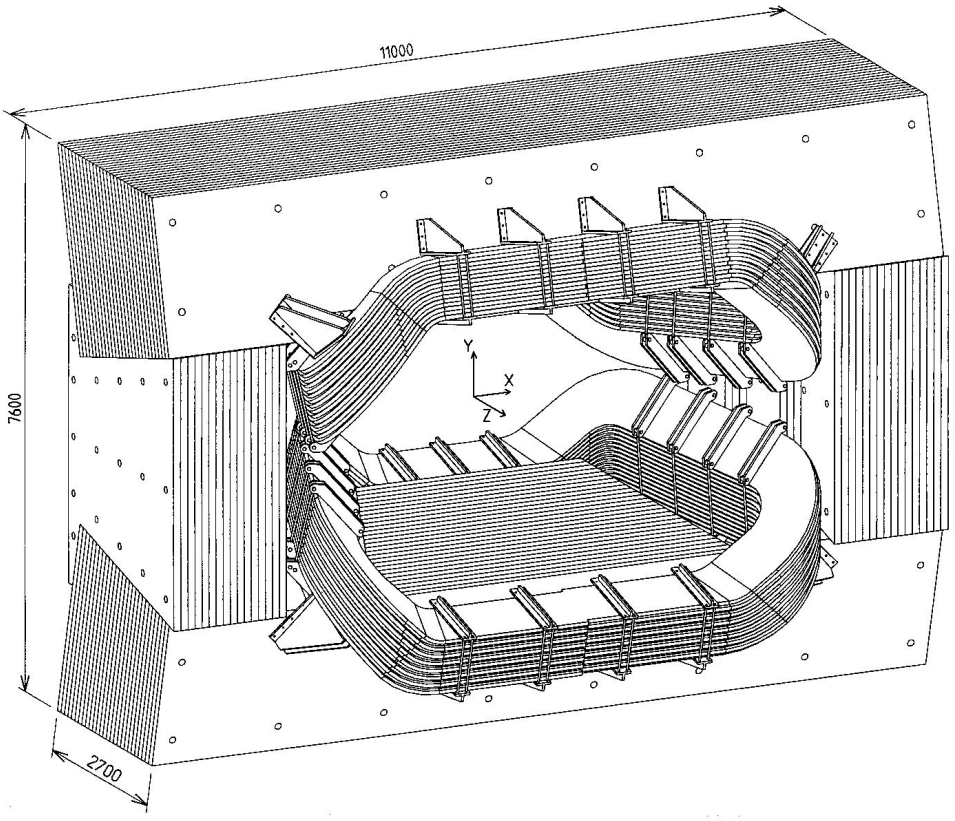

Figure 7: An illustration of the dipole bending magnet in the LHCb expirement.

2.6 Trackers (TT,IT, OT)

Downstream of the Dipole Magnet and before RICH 2 sits three tracking stations aptly labeled T1, T2, and T3. The inner tracker (IT) is one of two detectors making up a tracking station (T-station) with the other being the Tracking Turincensis (TT). The TT is 150cm wide and 130cm high and covers the typical acceptance of the LHCb detector. The size and scope of the TT makes it able to detect particles entering it with over 99% efficiency [25]. The TT is constructed from four layers of rows of silicon sensors. Each row consists of seven silicon sensors that are grouped into two or three sectors to be read out. The readout hybrid which contains all of the necessary electronics for readout of a sector is mounted on the end of the row. The first and last of the four layers have silicon strips read out vertically while the second and third layers have strips rotated +5° and -5° with respect to the x-axis respectively (Fig. 8. This configuration better provides a precise measurement of the individual track positions used in momentum determination in the bending plane of the dipole magnet [26]. Each detector has 400 μm thick silicon strips each with a pitch of 183 μm and give about 50 μm resolution spatially.

The inner tracker (IT) sits closest to the beam pipe and consists of three stations. Each station consists of four boxes located in a cross shape on the x and y axis (Fig. 9. Each box houses four layers with silicon strips with a pitch of approximately 200 μm and, similar to the TT, the IT has its first and last layers measuring the x-direction while the second and third layers are angled at +5° and -5° with respect to the x-axis respectively. Each layer is comprised of seven staggered silicon ladders. Layers are assembled as long ladders connected to readout at one end (Fig. 10). Each layer is either one or two sensors wide. The ladders used in the top and bottom of the IT are one sensor wide whereas the left and right boxes use two sensor wide ladders. These two types of sensors are completely identical in all ways except their thickness; the one-sensor modules have a thickness of 320 μm and the two-sensor modules have a thickness of 410 μm. This choice was made to

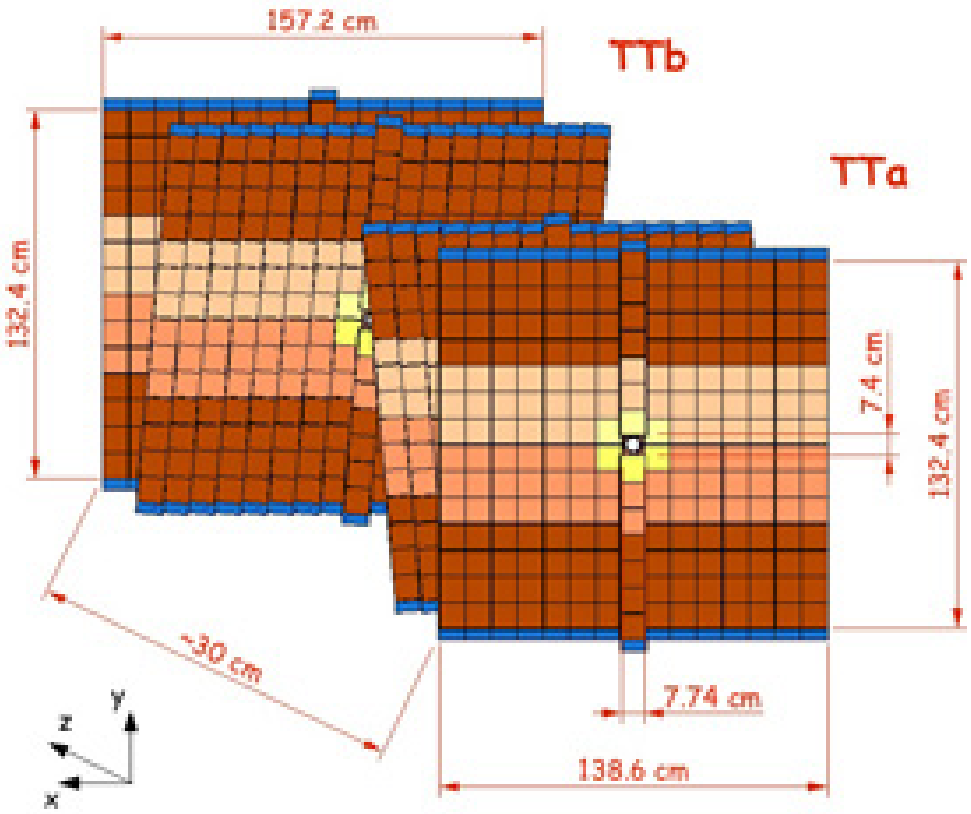

Figure 8: The layout of the 4 TT layers with readout electronics in blue and different readout sectors shaded. Note the angles of the second and third layer.

preserve high signal to noise ratios while at the same time reducing cost. In total the IT covers a 120cm wide and 40cm high cross region centered on the beam.

Taken together the TT covers regions of lower particle density and the IT covers the region around the beam, where the particle density is the highest. While employing the same silicon technology as the VELO, the precision is not as good due to the increased pitch and sensor thickness.

The outer tracker [27] (OT) again consists of three tracking stations, each with four layers arranged in the same angular pattern of both the TT and IT. The OT stations sit around the IT stations and are made up of a gas-tight strawtube module array. Each

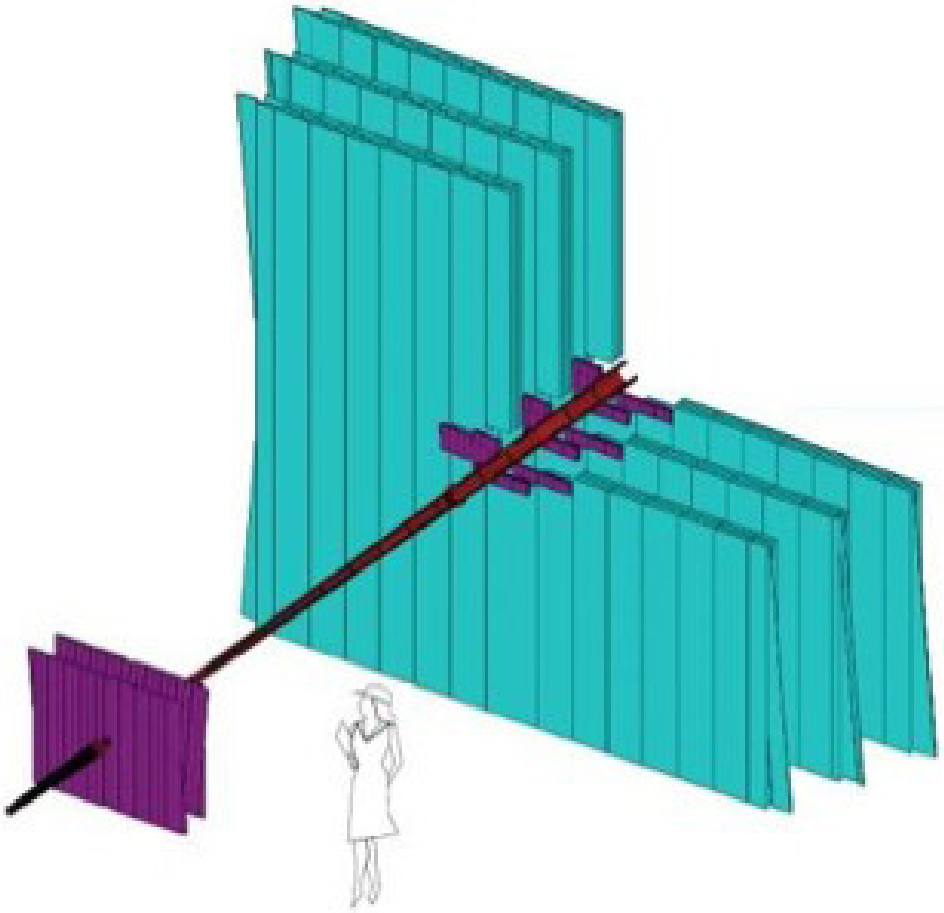

Figure 9: The layout of the IT (in purple) with respect to the TT (light blue).

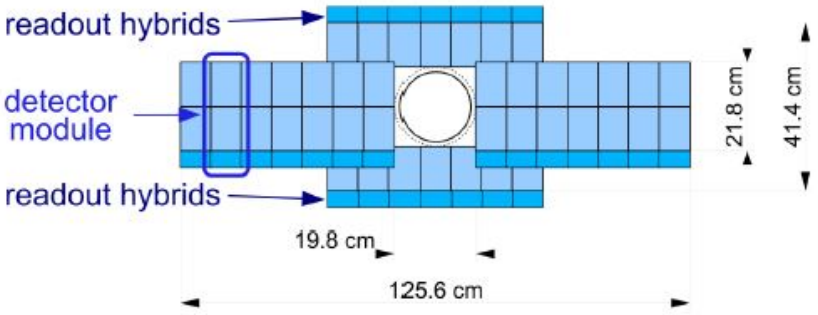

Figure 10: The layout of the IT with beam pipe running into the page in the center.

module is made up of 64 tubes in two offset layers which provide maximal coverage; a cross-sectional view is given in Figure 11. The OT is a drift-time detector and tracks charged particles over a large acceptance areas. Drift-time detectors work on simple principles. Each cylindrical tube coaxially contains a wire held at a positive voltage and filled with gas. The cylinder's wall is held at either ground or an equal negative voltage. When particles enter the tube the gas is ionized and begin releasing electrons. The electrons are attracted to the the coaxial wire held at +V and produce a signal in the wire which can be carried to electronics outside the detector by the wire. The time it takes for the electrons to reach the wire is related to both the radial distance from the wire to the ionized electron as well as the velocity of the electron. Time measurements from each tube can be combined to indicate the direction of travel through the OT. Each tube of the OT is constructed from a strip of 40 µm carbon-doped polyamide foil which is wound simultaneously with 37.5 µm thick laminante of kapton and aluminum. This is done for gas-tightness, good noise shielding, and for fast signal transmission in the tube. The gas is a 70% Argon 30% CO_2 mixture, which gives a drift time of around 50ns. The coaxial wire is made of gold-plated tungsten and has a diameter of 25.4 µm. In total, there are 128 tubes in each short module and 256 tubes in each long module. With 96 short modules and 198 long modules in the OT there are almost 63,000 channels accross the entirety of the OT.

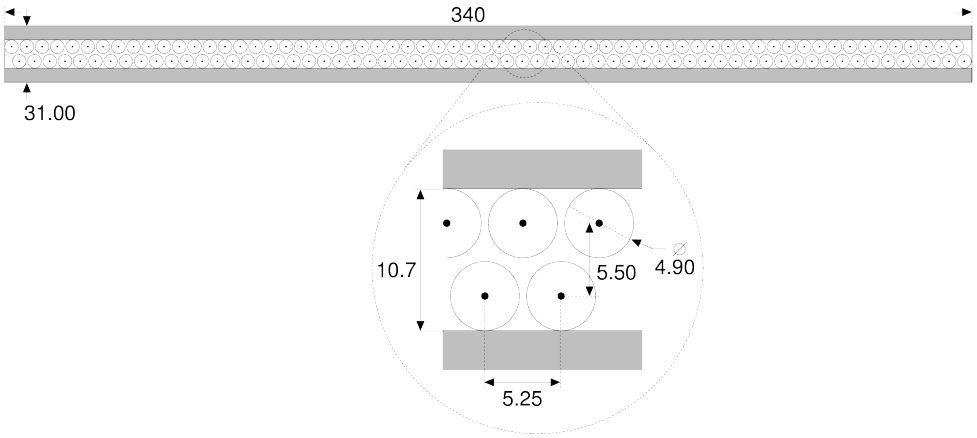

Figure 11: Cross-sectional view of the outer tracker in the LHCb. Note all units are in millimeters.

2.7 Calorimeters (ECAL,HCAL)

Downstream from the three tracking station are LHCb's two main calorimeters, the Electron Calorimeter (ECAL) and the Hadron Calorimeter (HCAL) [16]. In addition to these two calorimeters there exists, upstream, two detectors. The first is the Scintillator Pad Detector (SPD) and the second is the PreShower detector (PS). Each calorimeter utilizes the same principles in operation. Namely, when charged particles move through material, they lose energy via the electromagnetic interaction with the Coulomb fields. This ionizes the material through which the particle passes. The excited atoms then attempt to reach their ground state. This is accomplished when the atom releases energy obtained from the interaction with the charged particles. The energy is released in the form of photons, which, when in the visible spectrum, is called scintillation. This scintillation is then transmitted to a Photo-Multiplier Tube (PMT) via wavelength-shifting (WLS) fibers. The WLS fibers absorb the light and re-emit photons with a larger wavelength (lower energy). This shift is important as the PMTs have a higher efficiency for blue light as opposed to green light. The PMTs focuses particles onto stacked multipliers so that the photo-electrons, electrons released when struck by photons, are multiplied many times. This has the effect of creating a large electrical signal from a photon.The SPD and PS that exist immediately upstream from the calorimeters are designed to signal the presence of charged particles prior to their entrance to the ECAL. This helps reduce high backgrounds, specifically backgrounds associated with π^0 with high transverse energy.

The HCAL (Fig. 12) is a large rectangular structure measuring 8.4m in height, 6.8m width, and 1.65m in depth. It is made of layers of 16mm thick iron and 4mm thick scintillating tiles. Each tile is wrapped in 120 to 150 μm of $TYVEK^{\textcircled{R}}$ which protects the surface of the tiles, enhancea the collection of the WLS fibers, and reduces cross-talk between fibers. The WLS fibers have a diameter equal to 1.2mm and a length of 1.6m and read out the light from the scintillators via total internal reflection. They run parallel

along the edges of the tiles of the HCAL and are connected to PMTs which in turn are connected to electronics for readout. Each fiber services three tiles along the direction of the hadron shower development. Each PMT reads one fiber, or a cell of three tiles. As in other parts of the detector, the higher particle density near the beam necessitates the division of HCAL into two sections; the outer section, with 608 channels, and the inner section with 860 channels (Fig. 13). This also helps preserve the outer section, as the inner section becomes increasingly damaged due to the higher level of radiation. With such sectioning, the position and angle of incident for particles can be measured, thus allowing for more accurate particle identification.

What is actually measured by HCAL are hadronic cascades. Hadronic cascades are caused when fast traveling hadrons penetrate and interact with the material in the calorimeter. These interactions produce many secondary particles (mainly pions and nucleons). These secondary particles repeat the process creating tertiary particles which create further particles. This cycle repeats until all the energy is lost. These hadronic showers have been extensively studied and it is known that the maximum length of the shower is dependent on the energy of the primary particle as well as the absorption length of the material [28]. As such it is known to be approximated by,

$$L_{max}(\lambda) \approx 0.2ln(E) + 2.5\lambda E^(0.13) + 0.7, \quad (1)$$

where the energy (E) is measured in GeV and λ is the material's absorption length. Figure 14 illustrates how the two calorimeters combined with the SPD and PS detector can be used to identify particles.

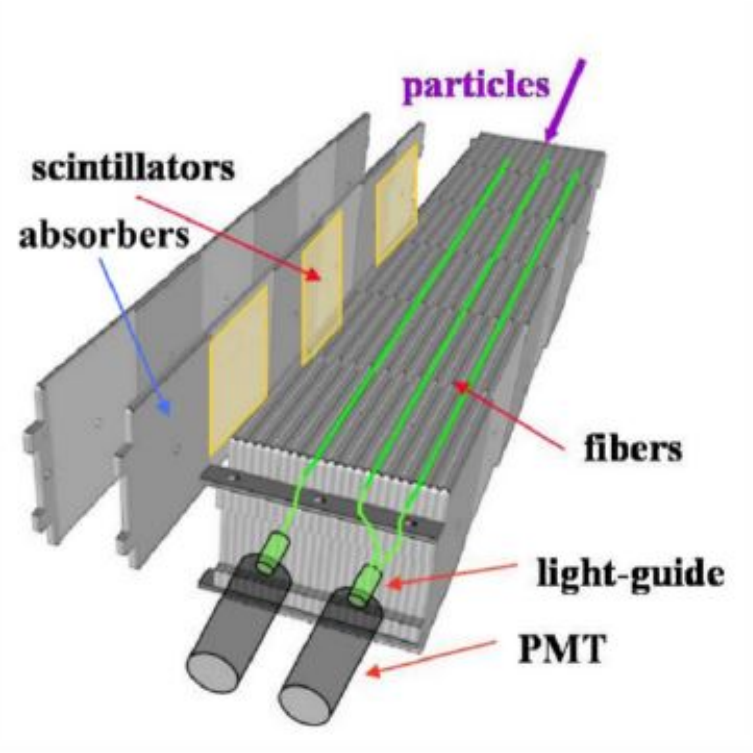

Figure 12: The layout of one quarter of the HCAL. The layers of absorbers and scintillating tiles are placed parallel to the beam as opposed to the ECAL which has them perpendicular.

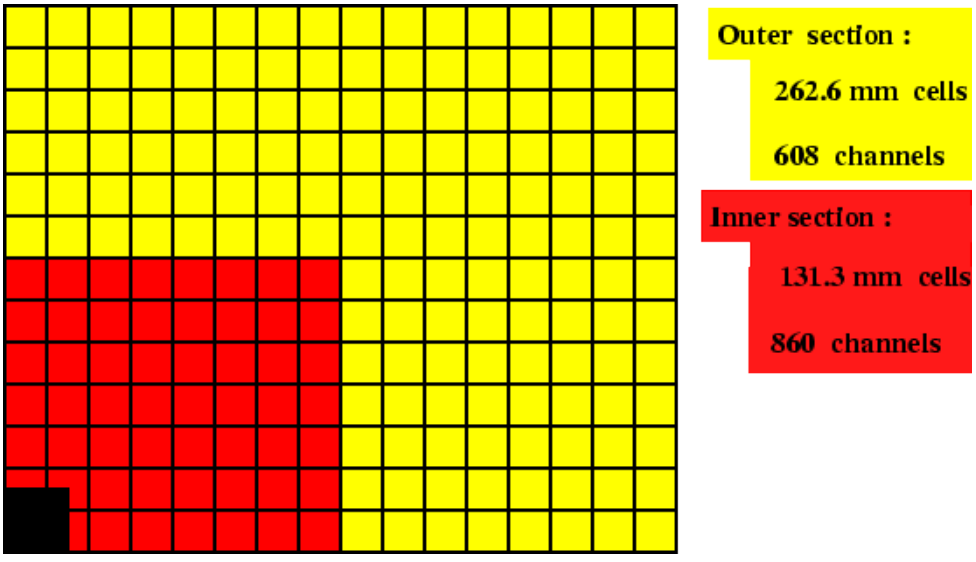

Figure 13: The layout of one quarter of the HCAL showing the sectioning used. With the beampipe in black.

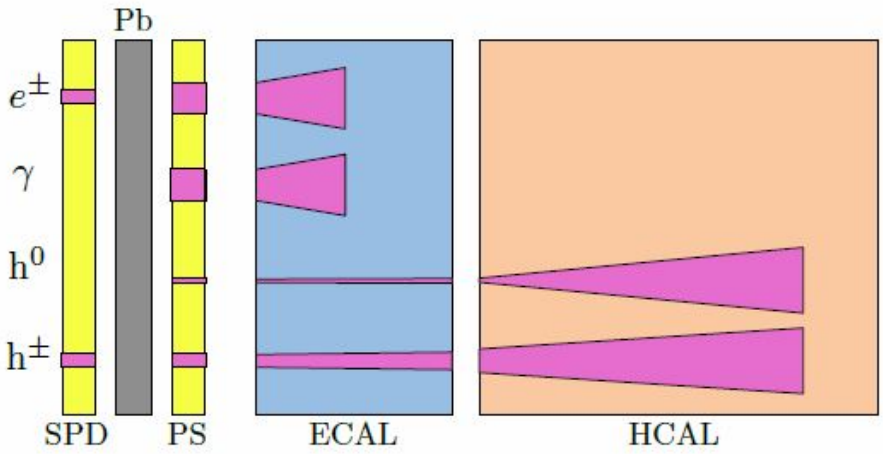

Figure 14: Example of how the calorimeter sub-detectors in the LHCb can be used to classify different types of particles.

2.8 MUON system

The last stop downstream from the interaction region is the muon system [29]. The muon system is made up of 5 stations (M1-M5) with 80cm thick iron absorber walls between each station, as shown in figure 15. All but M1 are located downstream of the calorimeters, with M1 coming just upstream from the calorimeters. Similarly, each station is split into four regions, labeled R1 to R4 16. Each region represents a distinct range of distances from the beam, with R1 being the closest and thus subjected to the highest levels of radiation. All regions use Multi-Wire Proportional Chambers (MWPC) except for R1 of M1, which uses triple Gas Electron Multiplier detectors (GEM). GEMs were chosen specifically for this region because of their ability to tolerate the high radiation environment present in R1 of station one.

The MWPCs that are used in virtually all of the muon system regions are very similar to drift tubes. Instead of a cathode cylinder with a single coaxial wire (as in the the OT), there are two cathode planes with a plane of wires in between. The gas in between the wires is not the 70/30 mixture of Ar to CO_2. Instead, a mixture of Ar/CO_2/CF_4 is used in the proportion 40/55/5, respectively. This mixture was chosen to optimize the detector [30]. A negative voltage is applied to the planes which creates an electric field that is very uniform except where distorted near the wires due to their finite cylindrical nature. When radiation passes through the gas in the chamber, the electrons are ionized and drift towards the wires. Due to the distortions near the wire, the ionized electrons are accelerated. This acceleration causes a cascade of electron-ion pairs. These electrons cause a negative signal in the wire they pass but also cause surrounding wires to pick up a positive signal. In this way in can be unambiguously determined which wire has been passed by the particle.

The GEM used in R1 of M1 is a different type of detector. It is comprised of 50 μm copper clad kapton foil densely covered in hourglass shaped holes. Each hole has an

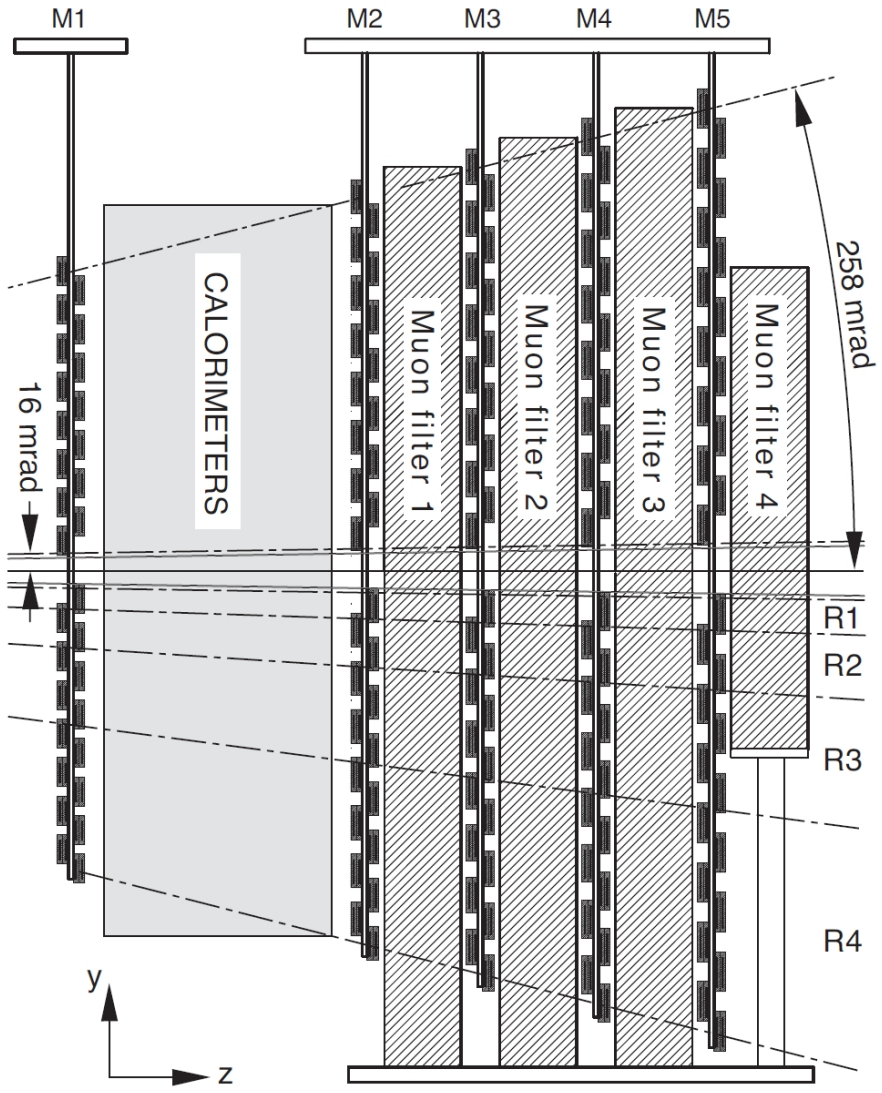

Figure 15: A cross section of the muon system with the regions R1 to R5 marked. Each filter is 80cm thick iron.

external diameter of 70 μm and an internal diameter of 50 μm; the pitch of the hole is 140 μm. The detector is a triple GEM detector which means it is made up of three gas electron multiplier foils between anode and cathode planes. The gas mixture is, once again, $Ar/CO_2/CF_4$ only with a different ratio (45/15/40). When a voltage is applied to one side of the planes, an electric field is produced between the planes and holes. The holes act as

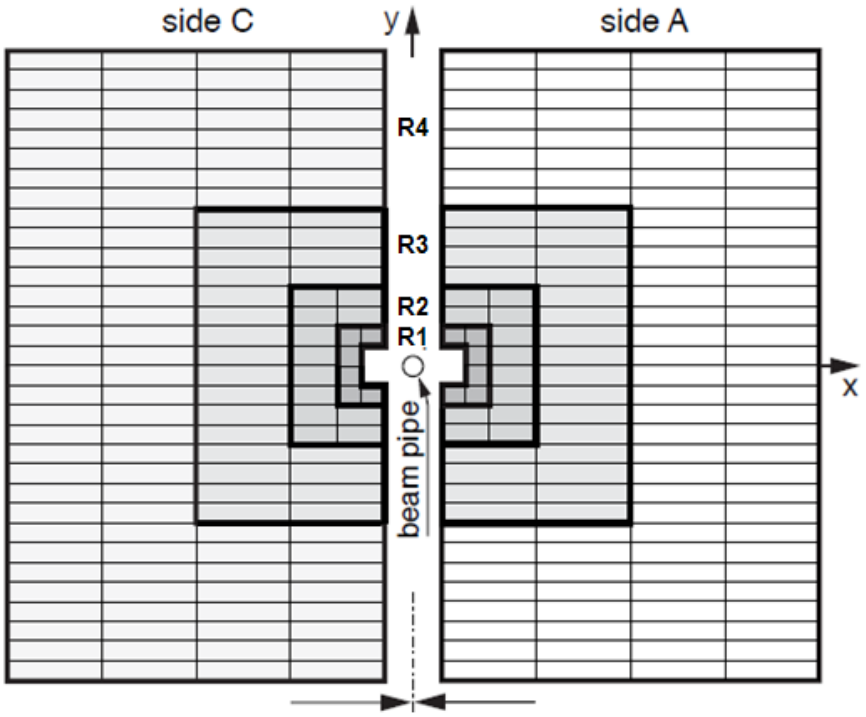

Figure 16: A front view of the muon system with the beam running perpendicular to the page and regions R1 to R5 clearly marked.

electron multiplication channels for electrons released by the ionizing radiation of the gas. This is effectively used as a tracking detector [31]. This is important, as station M1 is placed upstream of the calorimeters in order to improve p_{T} measurements for the trigger.

2.9 The Trigger System

The trigger system (Fig. 17) is designed to filter out uninteresting decays [32] from the initial 40 MHz (bunch crossing rate), leaving about 2-4kHz [33] of interesting decays (with a focus on B mesons), which can reasonably be written to disk. The final rate is chosen as it represents the current bandwidth limit for writing events to offline storage. There are two trigger levels in the LHCb, called Level0 (L0) and the High Level Trigger (HLT). The HLT is broken up into two stages, HLT1 and HLT2, which can be seen in Figure 17.

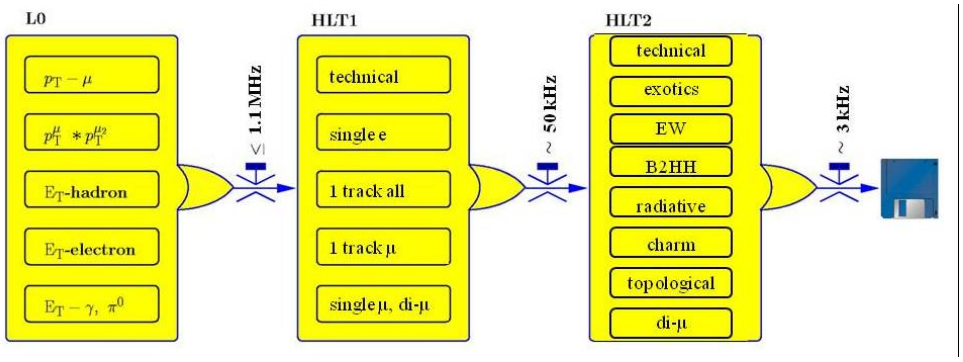

Figure 17: A chart of the various triggers and their output rates.

L0 is a hardware trigger built from custom electronics, with a fixed latency of 4μs, that accepts events at a rate of 40MHz and reduces that rate to 1MHz for the HLT. The HLT1 stage takes events that pass L0 and performs a partial reconstruction of the event and reduces the rate by another factor of 20 to about 50kHz. It is at this point that HLT2 performs an almost-full online event reconstruction, selecting out the events destined for storage. Whereas the L0 is a hardware based trigger the HLT is a software filter that runs on a CPU farm. The Event Filter Farm (EFF) processes events in parallel and is comprised of over 20000 CPU Cores.

2.9.1 The L0 Trigger

The L0 trigger utilizes objects with high transverse momentum (p_{T}) in the event by reconstructing the highest transverse energy hadron, electron, and photon clusters in the calorimeters as well as reconstructing the two highest p_{T} muon tracks from the muon stations. Both of these conditions are a good indication that heavy particles, such as B-mesons, have decayed. The L0 receives input from the VELO pile-up system as well as the calorimeters and muon systems. All data is read in parallel and it is up to the L0 Decision Unit (L0DU) to make the final decision. The final decision is derived from the logical *or* of the output from each branch. Specifically:

- **L0 Calorimeter**: finds and selects clusters with high E_{T} (L0Hadron, L0Electron, and L0Photon lines). The line used depends on the deposited energy in the SPD/PS, ECAL. and HCAL. the HCAL can also be used to reject events that are triggered by halo muons. The total number of hits in the SPD gives a quick hardware driven estimation of charged track multiplicity of an event.

- **L0 muon** [34]: selects high p_{T} muons via the L0Muon and L0DiMuon lines. An independent procedure searches for hits in the Muon stations that are consistent with a straight line pointing towards the point of interaction. The highest p_{T} muon segments are used for this decision.

- **VELO pile-up**: utilizes the two pile-up modules just upstream from the VELO. Initially it was designed to reject events with multiple bunch-crossings and is currently used only to trigger beam-gas interactions.

2.9.2 The HLT: Stage 1

The first stage of the HLT (HLT1) is responsible for reconstructing particles in the VELO to give a first approximation of primary vertices (PVs) in an event. It is also responsible

for reducing the event rate sufficiently to allow HLT2 to fully reconstruct selected events. Several lines of decision making are run in parallel such that the total decision time per event is on the order of 10ms. Specifically:

- **Single Track Trigger** [35]: searches for a single high momentum track in the event which is displaced from the PV. The three dimensional VELO tracks are a seed for reconstruction and no input from L0 is required. All that is required is a good quality track with large impact parameter (IP) to be found. This aids in selecting the decays of long lived hadrons comprised of b or c.

- **Muon Triggers** [36]: This line is only run if the event had been triggered by either the L0Muon or L0DiMuon lines. This line gets all VELO tracks that are extrapolated and matched with the muon segments used in the L0 decision, providing lifetime unbiased muon track samples. Single and dimuon lines are run, depending on the requirements that have been applied to the momentum of the particles and the invariant mass of composed objects.

- e **and** γ **Triggers**: uses the information gathered by the ECAL

2.9.3 The HLT: Stage 2

With an input rate of about 50kHz the HLT2 is able to access the full body of information for an event and look for secondary vertices and composed particles. Global Event Cuts (GEC), which includes the total number of reconstructed tracks, are used to reject events which would require too much time to process, such as events with high multiplicity of tracks. Many selections are made, both inclusive and exclusive, to maximize the number of possible final states. Events selected by the HLT2 are permanently stored as well as all of the signal trigger candidates. This allows offline comparisons of the objects that fired a given trigger line and the reconstructed signal candidates. The total bandwidth of HLT2

is shared among the topological muon and charm triggers, several exclusive lines and some inclusive lines such as the prompt J/ψ and ϕ triggers.

3 Data selection

The data selection used in this analysis is very similar to that used in the previous analysis of $B \to J/\psi\,\phi K$ performed by LHCb [4]. Muons detected by the muon system, which is composed of alternate layers of iron and multiwire proportional systems, are required to have transverse momentum ($p_{\rm T}$) $> 550\,$MeV. Opposite signed muons are combined to form $J/\psi \to \mu^+\mu^-$ candidates[2] so long as they are in the mass window of $3040 < m_{\mu^+\mu^-} < 3140$ MeV, the χ^2 per degree of freedom of the two muons forming a common vertex, $\chi^2_{vtx}(\mu^+\mu^-)/ndf < 9$, and the resulting J/ψ candidate has a transverse momentum ($p_{\rm T}$)$> 1500\,$MeV. Any charged track with transverse momentum greater than 250 MeV, which misses all primary vertices by at least 3 standard deviations ($IP\chi^2_{\rm PV} > 9$), and is classified by the particle identification system (PID) as more likely a kaon than a pion is considered a kaon candidate. [3] The J/ψ candidates are then combined with $K^+K^-K^+$ ($K^-K^+K^-$) candidates to form five track $B^+(B^-)$ candidates which then must originate from a common vertex ($\chi^2_{vtx}(J/\psi\,K^+K^-K^+)/ndf < 9$), have a decay time with respect to the primary vertex of at least $0.25\,$ps , a mass (m_B)$> 4200\,$MeV , and a transverse momentum ($p_{\rm T}$)$> 2000\,$MeV. Trigger signals are required to be associated with reconstructed B^+ candidates.[4]

We require that there is at least one ϕ candidate in the $J/\psi\,K^+K^-K^+$ combination defined as $|m_{K^+K^-} - M_\phi| < 15$ MeV.

Background suppression is also provided by selecting events based on a likelihood ratio. The total likelihood is a product of the probability density functions ($\mathcal{P}$s) of four sensitive

[2] Inclusive $J/\psi \to \mu^+\mu^-$ candidates from the `FullDSTDiMuonJpsi2MuMuDetached` stripping line are used (Stripping20).

[3] Kaons from the `StdAllLooseKaons` selection are used as starting point.

[4] The trigger requirements for this analysis are:
($\rm L0Muon_{TOS}$|$\rm L0DiMuon_{TOS}$)&
($\rm Hlt1TrackAllL0_{TOS}$|$\rm Hlt1TrackMuon_{TOS}$|$\rm Hlt1DiMuonHighMass_{TOS}$)&
(Hlt2TopoMu(2,3,4)$\rm BBDT_{TOS}$|
$\rm Hlt2DiMuonDetachedJPsi_{TOS}$|$\rm Hlt2DiMuonDetachedHeavy_{TOS}$).

variables (x_i):

- the minimum impact parameter (IP) χ^2 of K with respect to the closest primary vertex (PV),
- $\chi^2_{\rm vtx}$/ndf of the B candidate,
- the B candidate IP significance ($\chi^2_{\rm IP}$),
- and cosine of the largest opening angle between the J/ψ candidate and K candidates in the plane transverse to the beam.

The signal $\mathcal{P}$s ($\mathcal{P}_{sig}(x_i)$) are obtained from Monte Carlo simulation of $B \to J/\psi\,\phi K$. Phase-space Monte Carlo events were used as the variables x_i are insensitive to the the kinematic details of the decay. The background $\mathcal{P}$s ($\mathcal{P}_{bkg}(x_i)$) come from the B signal's far-side-band region in data ($5600 - 6400$ MeV).

With $\mathcal{P}_{sig}(x_i)$ and $\mathcal{P}_{bkg}(x_i)$ in hand we form the logarithm of their ratio, $DLL_{\rm sig/bkg} = -2\sum_{i=1}^{4} \ln(\mathcal{P}_{\rm sig}(x_i)/\mathcal{P}_{\rm bkg}(x_i))$. Figure 18 shows the good agreement between data and simulation on the DLL distribution as well as the discrimination between signal and background of $B \to J/\psi\,\phi K$. An additional requirement of $DLL_{sig/bkg} < 5$ was imposed, the value was chosen to maximize $N_{\rm sig}/\sqrt{N_{\rm sig} + N_{\rm bkg}}$, where N_{sig} is the expected signal yield and N_{bkg} is the background yield in the region of the B peak. The normalization of N_{sig} and N_{bkg} is obtained from a fit to the B mass distribution.

The mass of the J/ψ candidate is constrained to the nominal J/ψ mass, and the $J/\psi\,K^+K^-K^+$ candidate is constrained to point to the nearest primary vertex when calculating masses of the ϕ and B^+ candidates. The $J/\psi\,K^+K^-K^+$ candidate is also constrained to the nominal B^+ mass, before any quantities used in the amplitude fit are calculated.

The data contains events in which reconstruction of ϕ is ambiguous, that is to say that both pairs of oppositely charged kaons have $m_{K^+K^-}$ within ± 15 MeV of the nominal ϕ

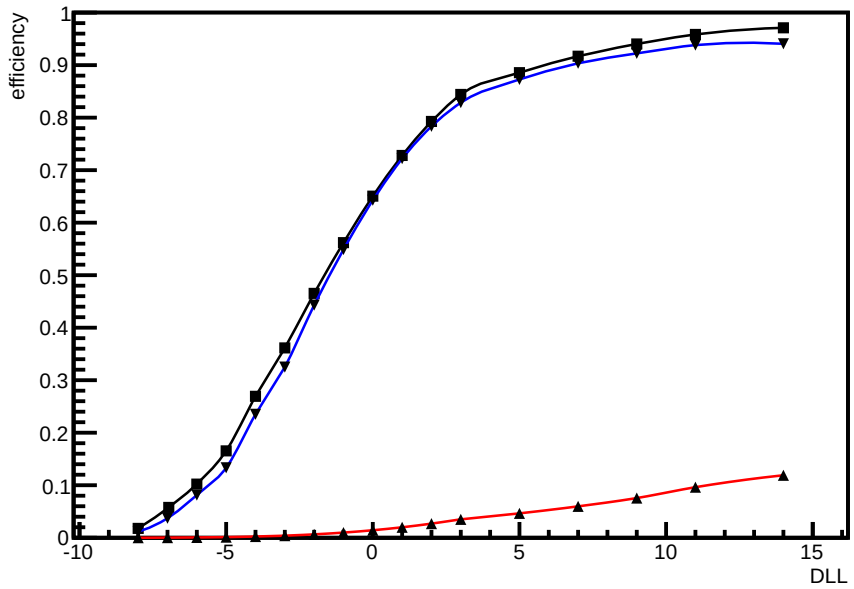

Figure 18: Fraction of the $B^+ \to J/\psi\,\phi K^+$ signal events passing a cut $DLL < x$ for the data (blue), the signal MC (black), and fraction of the background events (B^+ sideband) passing this cut(red).

mass. These events are subsequently vetoed. It should be noted that such events only account for 3.2% of $B \to J/\psi\,\phi K$ candidates. Non-ϕ background under the ϕ peak is very small, as illustrated in Fig. 19, where we plot $m_{K^+K^-}$ for $B^+ \to J/\psi\,K^+K^-K^+$ events (two entries per event) before any ϕ selection criteria have been applied (but after all other cuts). The $m_{K^+K^-}$ distribution has been fit with a P–wave relativistic Breit-Wigner on top of 2-body phase-space distribution representing non-ϕ background, both smeared with a Gaussian mass resolution. The ϕ width is fixed to the PDG value (4.266 MeV). The fitted parameters are ϕ and background amplitudes, ϕ mass (1019.6 ± 0.1 MeV), and the mass resolution (1.24 ± 0.11 MeV). The p–value of the fit is 85%. Integrating the total and the background PDFs within the $\pm$15 MeV range around the peak, we determine non-ϕ fraction to be (5.3 ± 0.5)% within the nominal ϕ selection window.[5] After the double-ϕ

[5] For the narrower selection windows of 10 and 7 MeV, the non-ϕ fractions are (3.8 ± 0.4)% and (2.9 ± 0.3)%, respectively.

veto, non-ϕ component of $B^+ \to J/\psi K^+K^-K^+$ decays is at the level of $5.3 - 3.2 = 2.1\%$.

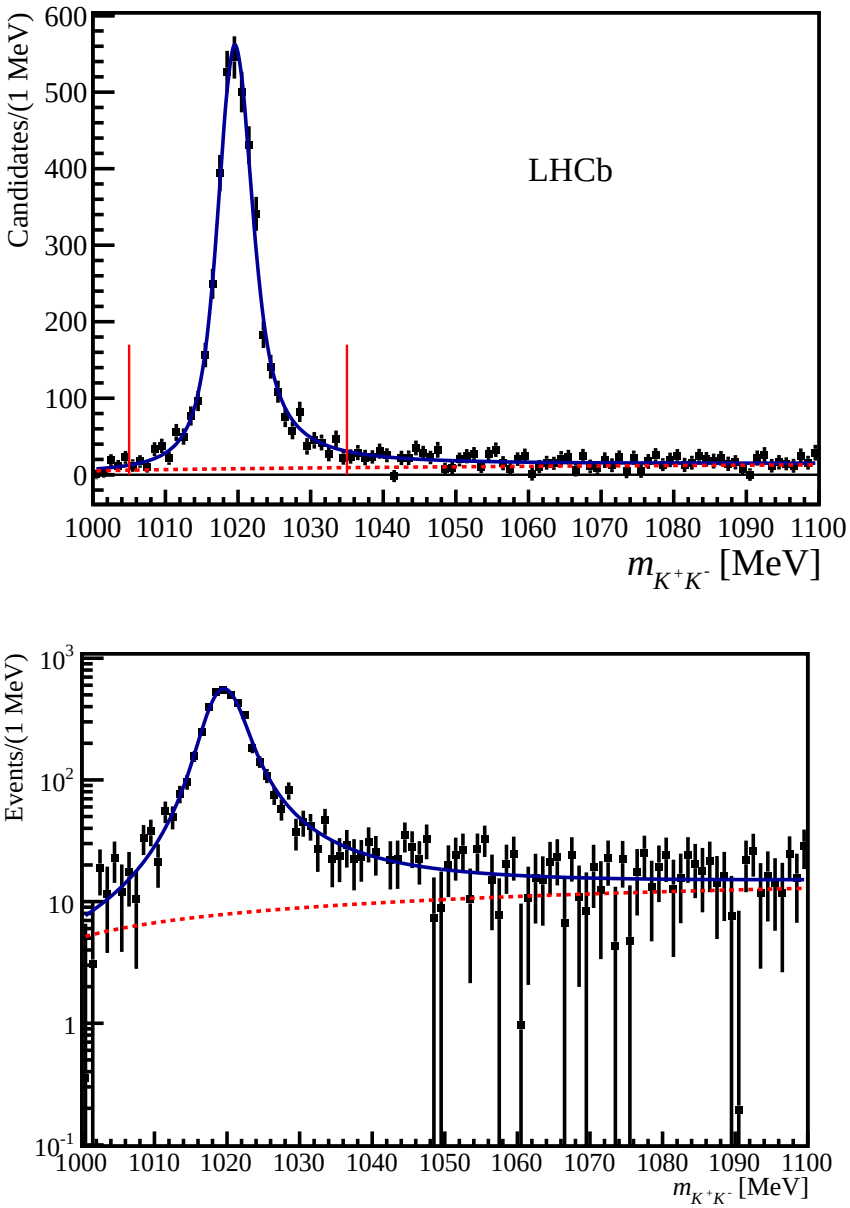

Figure 19: The distribution of $m_{K^+K^-}$ near the ϕ peak region before the ϕ candidate selection in the linear (top) and log (bottom) scales. The default selection cut in ± 15 MeV around the ϕ peak. The backgrounds have been subtracted using sWeights set by the fit to the $m_{J/\psi K^+K^-K^+}$ distribution. The fit of ϕ Breit-Wigner shape plus 2-body phase-space function, smeared with the Gaussian mass resolution, is superimposed. The total fit PDF is shown as a blue solid line, while the 2-body phase-space function representing non-ϕ contribution is shown as a dashed red line.

The distribution of $B \to J/\psi\,\phi K$ candidates in invariant $J/\psi\,\phi K^+$ mass is shown in Fig. 20. We fit this distribution using a symmetric double-sided Crystal Ball shape for the signal and a quadratic function for the background. The fit yields 4289 ± 151 $B \to J/\psi\,\phi K$ events with a B mass resolution of $\sigma_m = 4.88 \pm 0.17$ MeV.[6] The selected $B \to J/\psi\,\phi K$ signal yield constitutes about 69% of all $B^+ \to J/\psi\,K^+K^-K^+$ signal events selected with no $\phi \to K^+K^-$ requirement (see Appendix E).

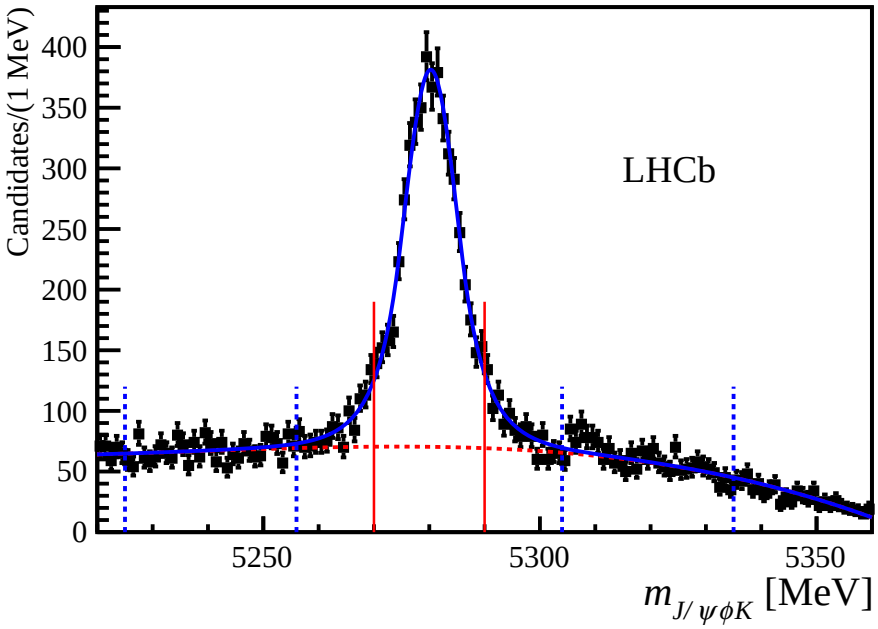

Figure 20: Mass of $B \to J/\psi\,\phi K$ candidates in the data (black points with the error bars) together with the fit (blue line) of the double-sided Crystal Ball shape for the signal on top of quadratic function for the background (green line). The fit is used to determine the background fraction under the peak in the mass range used in the amplitude analysis (see the text).

We then define the $B \to J/\psi\,\phi K$ signal region as $5270.2 < m_{J/\psi\,\phi K} < 5289.8$ ($\pm 2\sigma_m$) and the two B-mass side-bands as [5225.3,5256.1] MeV and [5303.9,5334.7] MeV ($4.9 - 11.2\sigma_m$). The amplitude fits are performed to the events in the signal region. The sidebands are

[6]Power parameter in the parameterization of tails was fixed to $n = 10$ based on fits to the simulated data. The shape is insensitive to a detail value of n chosen. The parameter α describing where the Gaussian part turns into the tails (in units of the Gaussian σ_m value) was fitted to the data and yielded $\alpha = 1.2 \pm 0.1$.

used to derive the background PDF used in these amplitude fits as described later in Sec. 5.4. In the default amplitude fit we use both sidebands merged together. The lower side-band and upper side-band are compared to each other for the variables used in the amplitude fit in Fig. 21 (see Sec. 5 for their definition). No dramatic changes are observed, though since there are some differences, we also perform fits using events from only one sideband when evaluating systematics (see Sec. 9).

For a relative normalization of the background and signal PDFs, the background fraction in the signal region (β) must be determined. After integration of the functions describing the signal and background in the fit to B^+ candidate mass distribution (Fig. 20), we find $\beta = (22.8 \pm 0.4)\%$ (statistical error). To evaluate systematic uncertainty, we varied the fit to $m_{J/\psi\,\phi K}$ by increasing the order of the background polynomial function (results in $\beta = 22.3\%$) or replacing the Crystal Ball line shape with a simple Gaussian ($\beta = 27.0\%$). The largest deviation ($\beta = 28.6\%$) is obtained when changing both (see Fig. 22). We use this value when evaluating systematic uncertainties on amplitude fit results (Sec. 9).

All cuts are summarized in Table 3. The number of multiple-entries per event in the signal region used in the fit is 0.4%. The rate increases to 3.4% when the $J/\psi\,\phi K^+$ mass range is extended to cover the B^+ sidebands used for the background parameterization in the fit.

The background subtracted and efficiency corrected Dalitz plots (one for each pair of ϕK, $J/\psi\,\phi$, $J/\psi\,K$) after the selection are shown in Fig. 23. The efficiency does vary over the Dalitz plane, it is plotted in Fig. 29, and is discussed in the next section. The three mass projections of data without background subtraction or efficiency corrections are shown in Fig. 24. And the three mass projections after background subtraction (and efficiency correction) are shown in Figure 25

Table 3: Data selection requirements.

Particle	Quantity	Requirement
All tracks	Track quality: χ^2/ndf	< 4
All tracks(2012)	GhostProb.	< 0.47
All tracks	Clone	Default
μ	p_{T}	$> 550\,\mathrm{MeV}$
μ	IsMuon	True
μ	PID_μ (DLL(μ-π))	> 0
Di-μ	Vertex quality: χ^2/ndf	< 9
Di-μ	p_{T}	> 1.5 GeV
J/ψ	$m_{\mu^+\,\mu\mathrm{m}}$ window	[3.040,3.140] GeV
K	PID_K (DLL(K-π))	> 0
K	p_{T}	$> 250\,\mathrm{MeV}$
K	χ^2_{IP}	> 9
ϕ	$\lvert m_{K^+K^-} - M_\phi \rvert$	< 15 MeV
ϕ	# of ϕ candidates	$= 1$
B	$m_{J/\psi\,\phi K^+}$ window	[5.10, 5.5] GeV
B	Vertex quality: χ^2/ndf	< 9
B	p_{T}	> 2.0 GeV
B	Lifetime: τ	> 0.25 ps
B	Trigger	L0, Hlt1, Hlt2 TOS (see text)
B	DLL	< 5

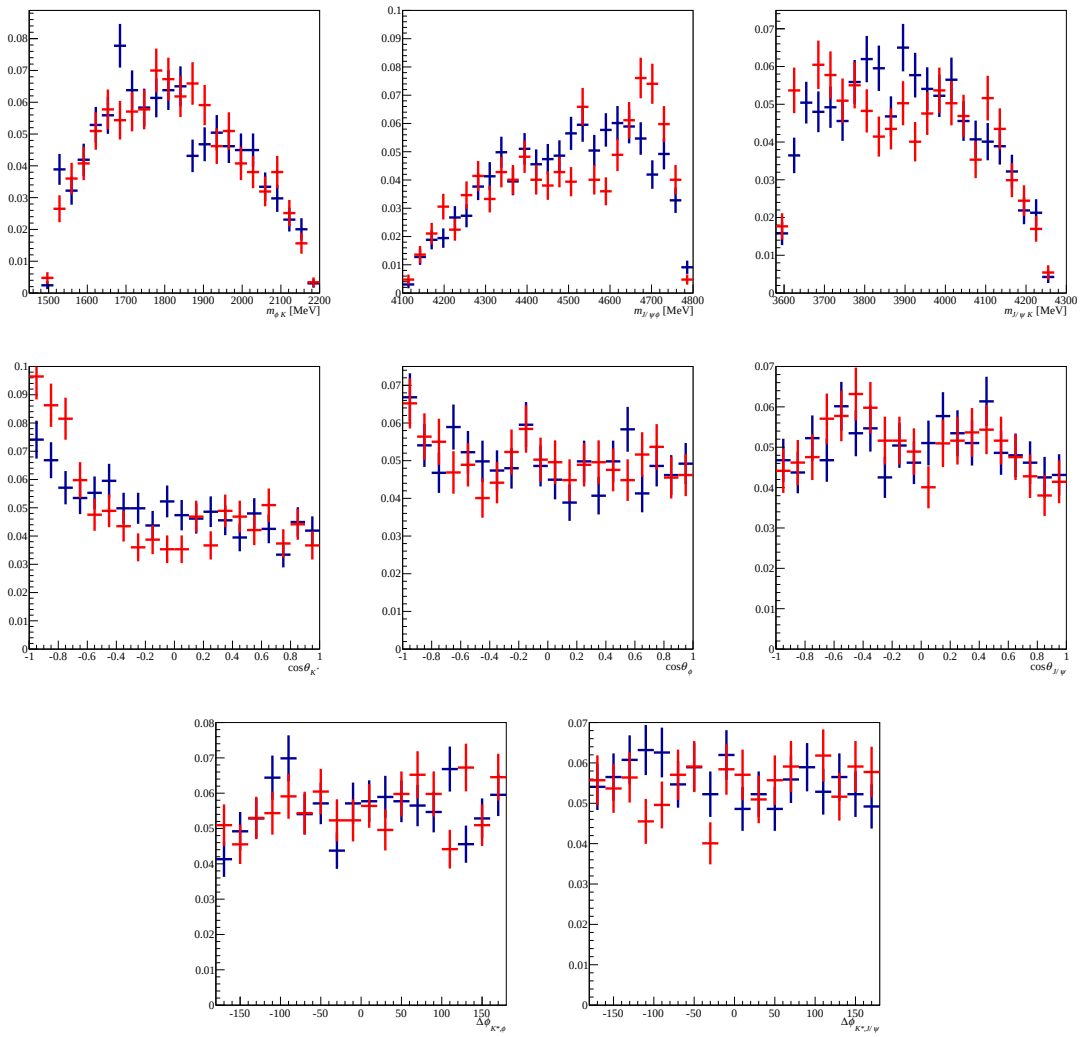

Figure 21: Comparison of the lower side-band (dark blue) and upper side-band (red) for $m_{\phi K}$, $m_{J/\psi\,\phi}$, $m_{J/\psi\,K}$ (left to right in the top row), $\cos\theta_{K^*}$, $\cos\theta_{\phi}$, $\cos\theta_{J/\psi}$ (left to right in the middle row), and $\Delta\phi_{K^*,\phi}$ and $\Delta\phi_{K^*,J/\psi}$ (left to right in the bottom row). Definition of all these variables appears in Sec. 5.

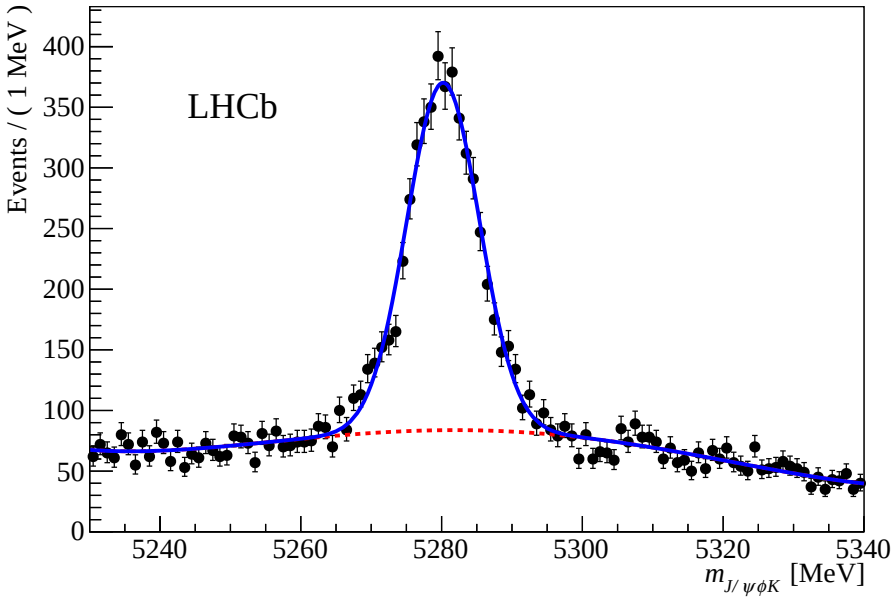

Figure 22: Mass of $B \to J/\psi\,\phi K$ candidates in the data (black points with the error bars) together with the fit (blue line) of the Gaussian shape for the signal on top of cubic function for the background (red dashed line). The fit is used to evaluate systematic uncertainty in the background fraction under the peak in the mass range used in the amplitude analysis (see the text). Compare to the default fit in Fig. 20.

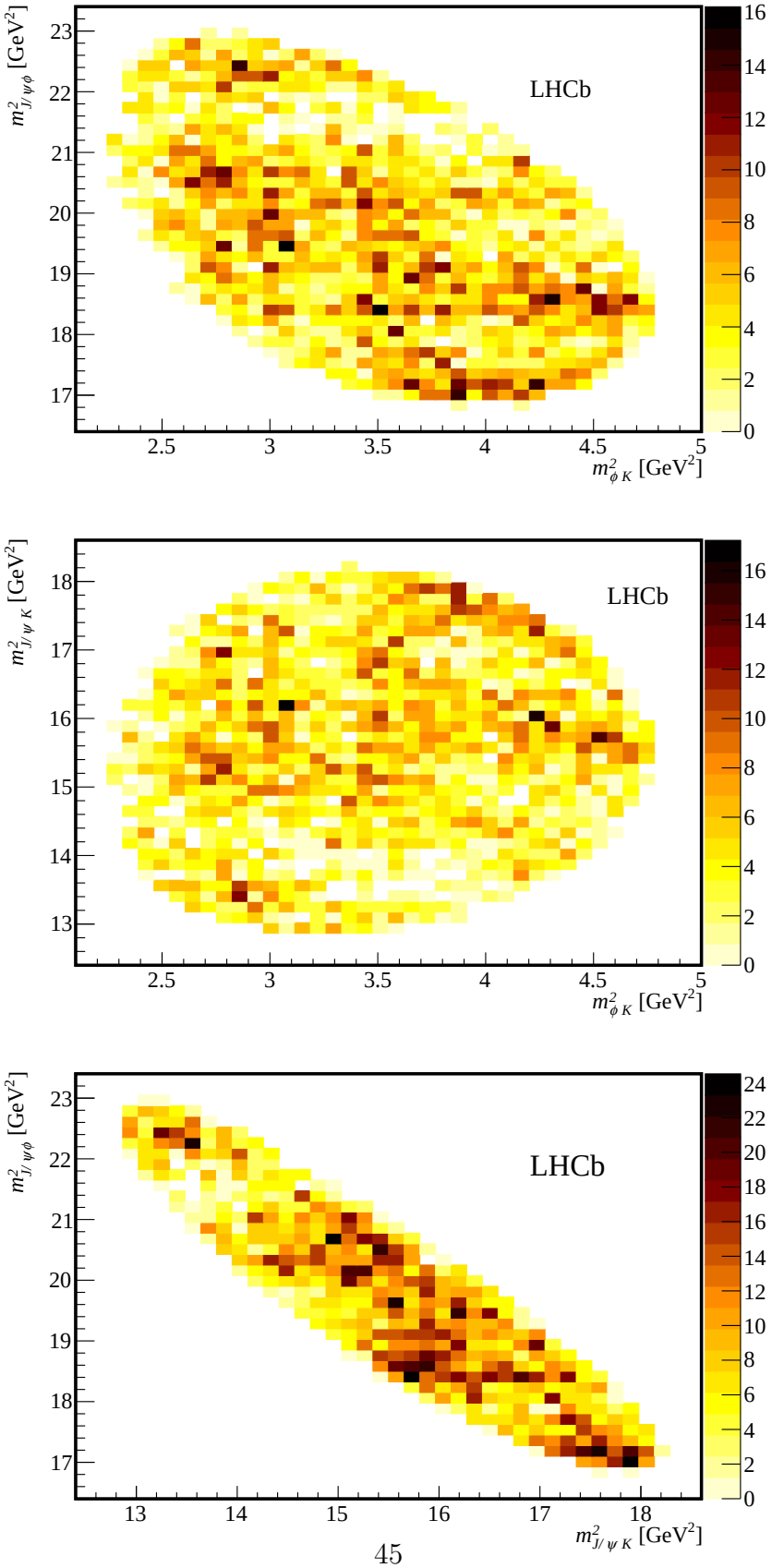

Figure 23: Background subtracted and efficiency corrected Dalitz plots of $B \to J/\psi\phi K$ events. The backgrounds have been subtracted using the scaled sidebands. The density of points is proportional to the number of entries in each bin.

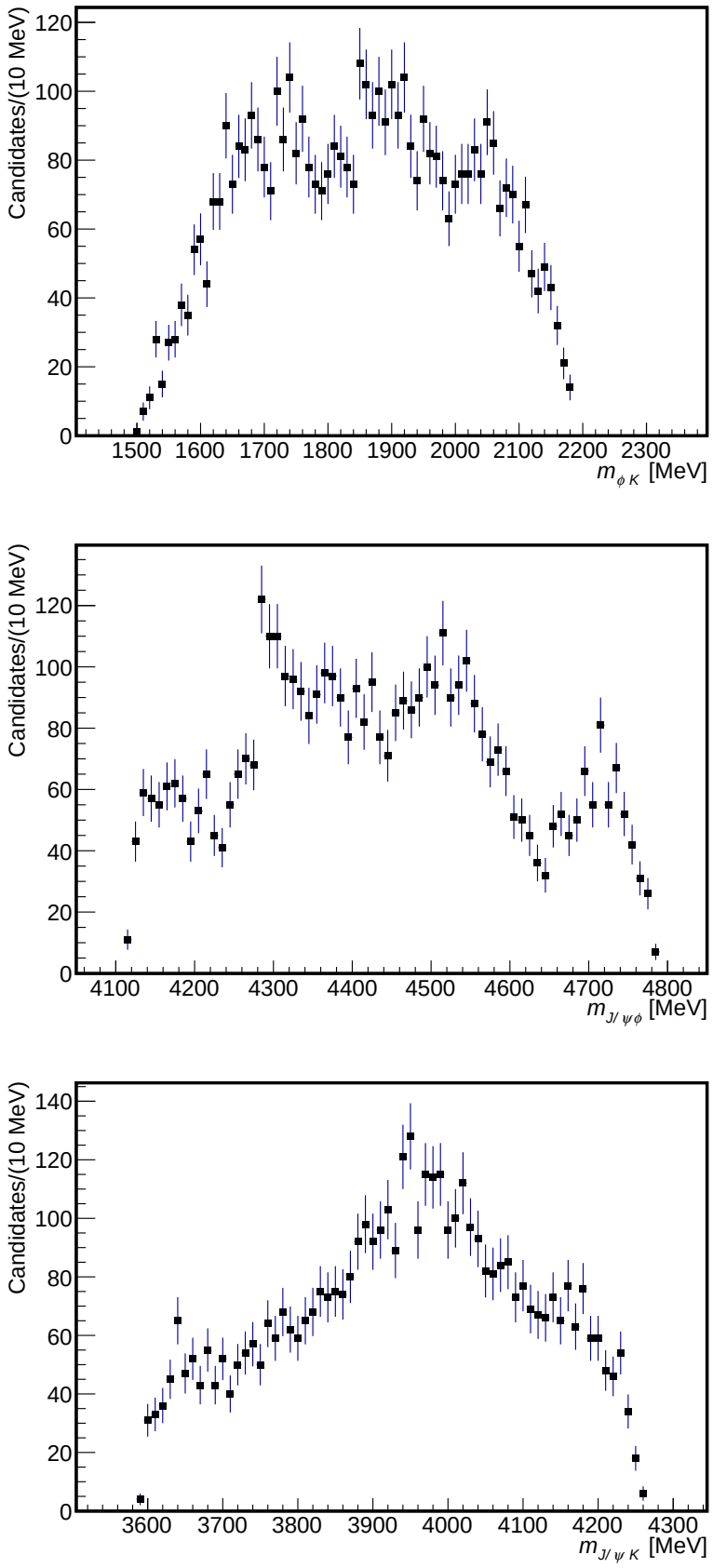

Figure 24: Distributions of $m_{\phi K}$ (top), $m_{J/\psi\phi}$ (middle), and $m_{J/\psi K}$ (bottom) in the data sample used in the amplitude fits. No background subtraction nor any efficiency corrections have been applied.

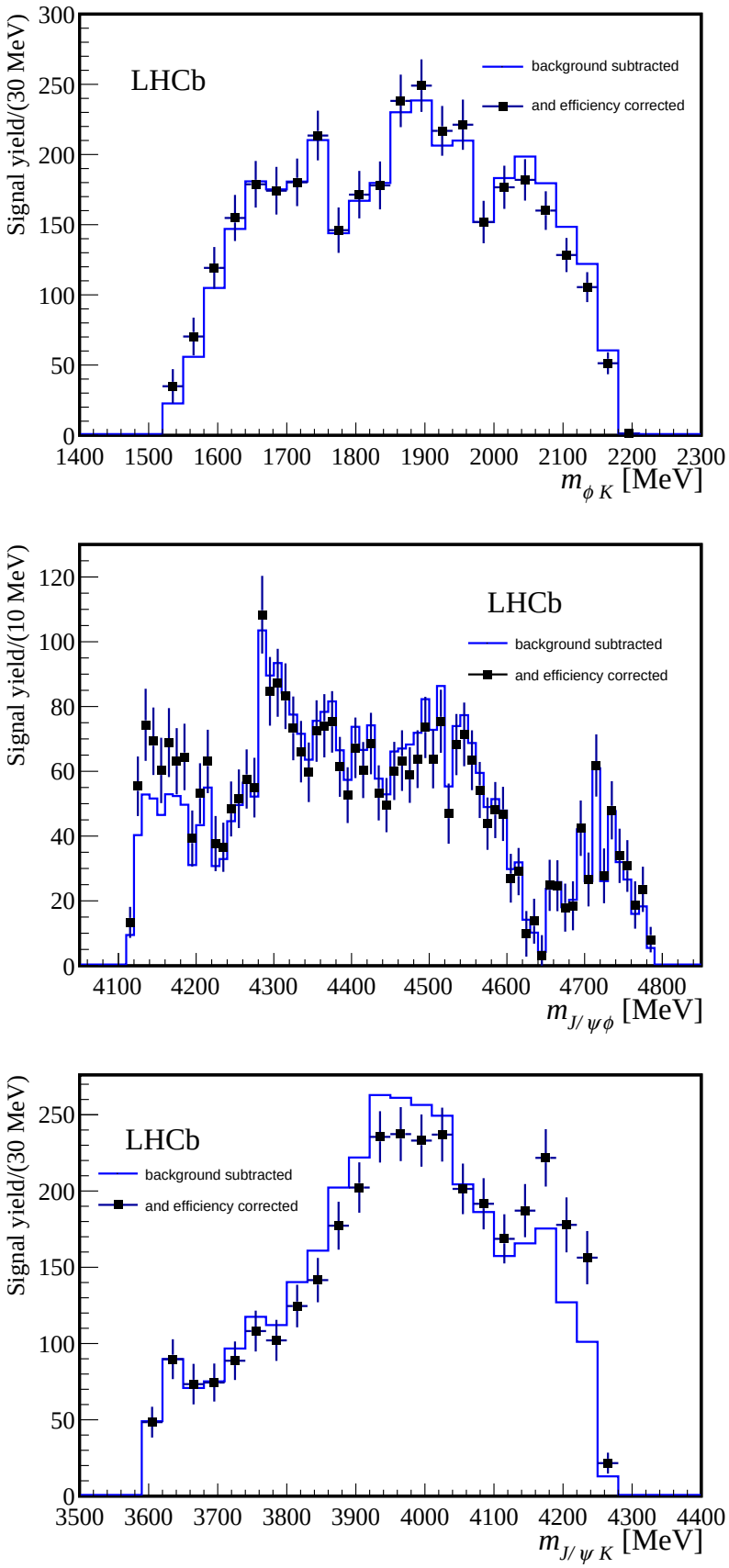

Figure 25: Distributions of $m_{\phi K}$ (top), $m_{J/\psi\phi}$ (middle), and $m_{J/\psi K}$ (bottom) in the data sample used in the amplitude fits. Background subtraction alone has been performed on the data (blue histogram). Both background subtraction and efficiency correction has been performed (black points).

4 Kinematic re-weighting of Monte Carlo events

To correct for possible inaccuracies in the modeling of the B^+ production within the LHCb acceptance and in the modeling of the detector efficiency, we give Monte Carlo events weights ($w^{\rm MC}$) based on the relative yields of the data and MC in certain kinematic or event variables. The phase-space MC events are used, re-weighted by the preliminary amplitude fits to the data, and any corrections which have been applied previously in the iterative procedure. The variables corrected for in this study are: the transverse momentum of the B^+ ($p_{\rm T}(B)$), the number of tracks in the event (n_{trk}), and the momenta of each kaon ordered according to their decreasing momenta ($p(K_0), p(K_1), p(K_2)$). The overall weight applied to a Monte Carlo event is the product of the individual weights for each variable:

$$w^{\rm MC} = w_{p_{\rm T}(B)} \cdot w_{n_{trk}} \cdot w_{p(K_0)} \cdot w_{p(K_1)} \cdot w_{p(K_2)}. \quad (2)$$

To calculate a given weight, a normalized plot of both data and Monte Carlo was produced. A binning was chosen based on trends in discrepancy as well as statistical errors. This leads to a finer binning at lower variable values (*e.g.* low momentum) and a coarser binning at higher values (*e.g.* high momentum). Once an appropriate binning has been established, a ratio of data to Monte Carlo is found for each bin. Then each Monte Carlo event is weighted by the ratio of the bin it belongs to. After weighting, all kinematic variables of both data and MC are once again plotted and compared to ensure proper agreement. After recursion through the kinematic variables listed above the Monte Carlo set was found to be in good agreement with the data set. The individual weights used in this analysis are obtained from the plots in Fig. 26, while the final comparison between the data and MC is shown in Fig. 27.

Fitting the data while using unweighted Monte Carlo events in the fitter produces surprisingly little change in the fit results and is included among systematic uncertainties

(see Sec. 9).

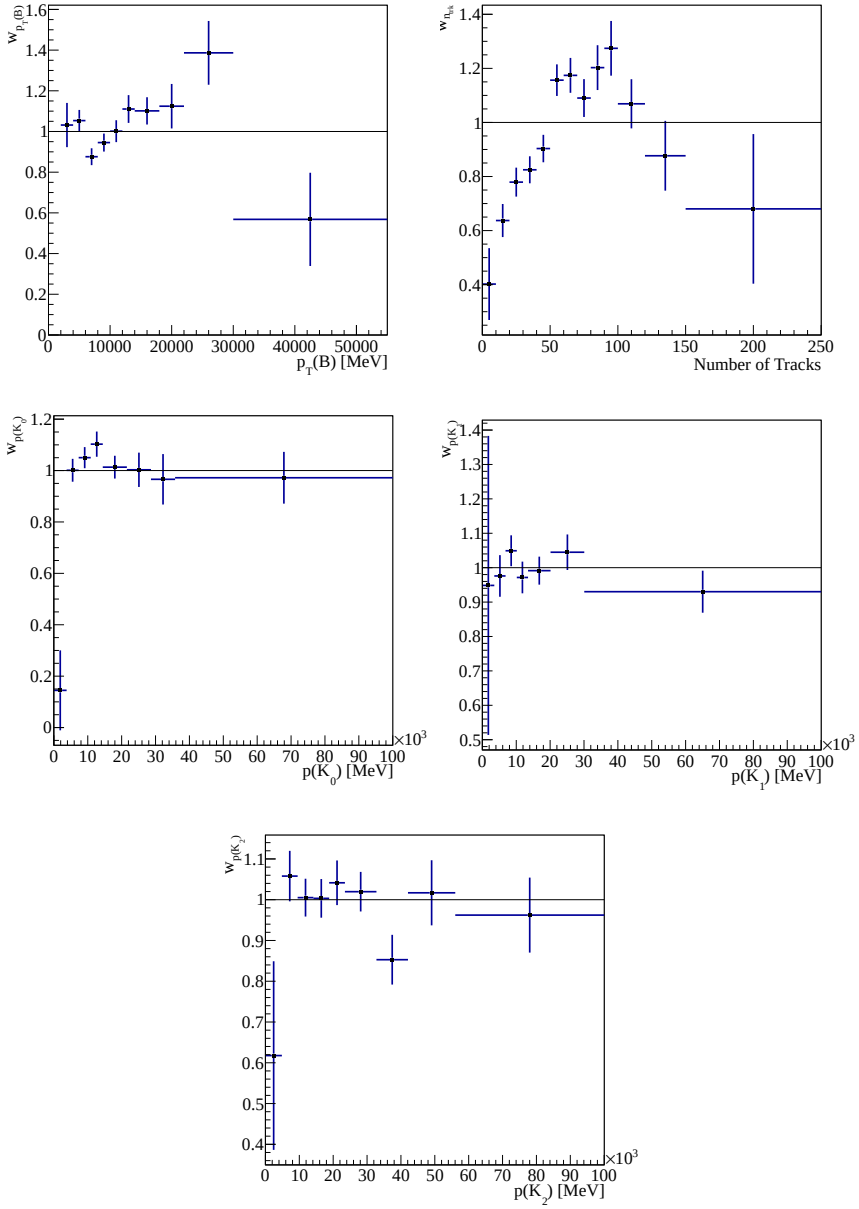

Figure 26: Plots of the weights used to re-weight MC. Weights are applied in order (left to right, top to bottom); the transverse momentum of B, the number of tracks, the momentum of the fastest kaon, the momentum of the second fastest kaon, and the momentum of the slowest kaon.

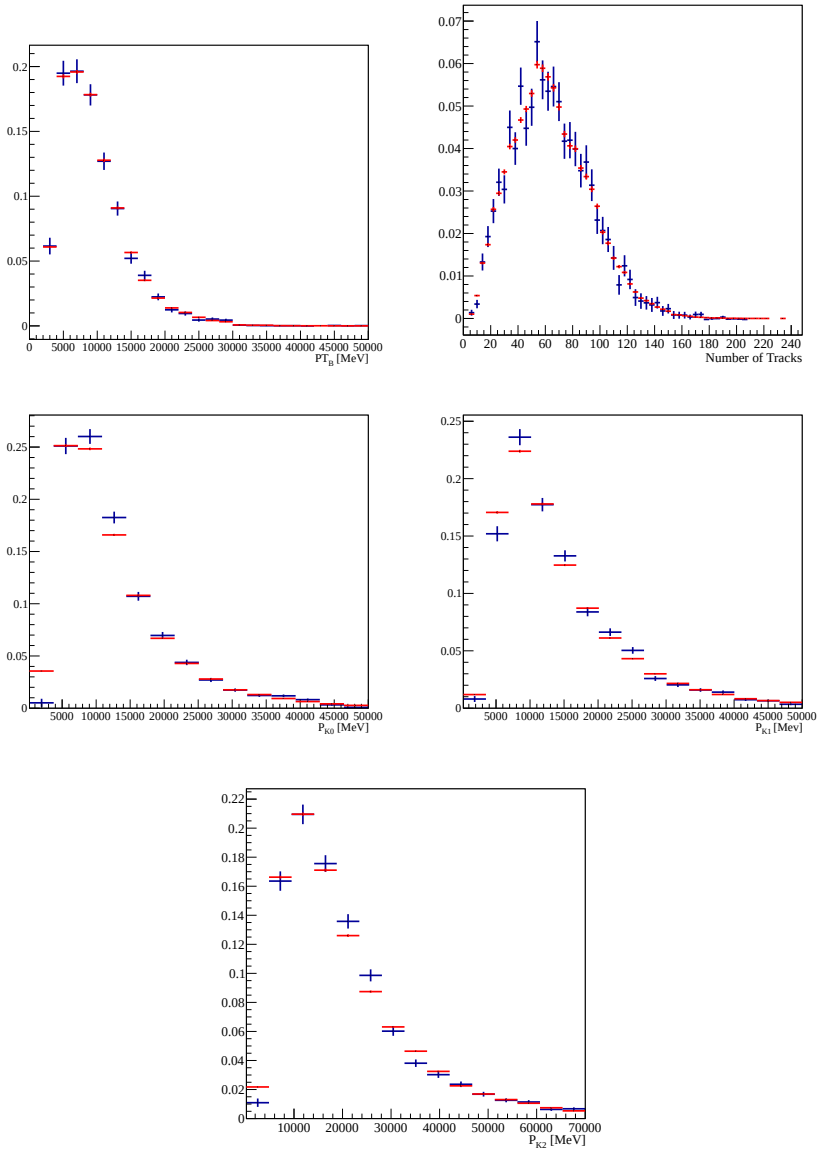

Figure 27: Comparison of MC (red) and data (black) for the 5 kinematic variables used to re-weight MC after complete re-weighting.

5 Amplitude analysis

The primary objective of this study is to look for evidence of exotic states in the $J/\psi\,\phi$ system, and to attempt to completely model the $B \to J/\psi\,\phi K$ system. In doing so we seek to learn more about the properties of any exotic states (*e.g.* mass, width, spin, parity and fit fraction), should they exist, as well as seek a description of any structures present in $\mathrm{m}_{J/\psi\,\phi}$ as reflections of non-exotic K^* contributions. To accomplish this we will use an unbinned maximum likelihood fit with explicit parametrization of the background (often called "cFit" in LHCb). We will first survey non-exotic K^* models involving both previously observed K^*s and those predicted by the relativistic quark model in the kinematically allowed range. Only after these models have been studied thoroughly will we move to models involving one or more exotic contributions (*i.e.* X, Z). In the section below we will describe the formalism of the fit.

5.1 Fitted Kinematic Variables

The decay of $B \to J/\psi\,\phi K^+$, $J/\psi \to \mu^+\mu^-$, $\phi \to K^+K^-$ has exactly three quasi-two-body decay chains, each with their own helicity structure and their own set of six independent variables that fully describe the kinematics of the decay. First, we consider the $B^+ \to J/\psi\,K^{*+}$, $K^{*+} \to \phi K^+$, $J/\psi \to \mu^+\mu^-$, $\phi \to K^+K^-$ decay chain which shall be known as the K^* decay chain and has the following independent variables (diagrammed in Figure 28):

$m_{\phi K}$ **-** the invariant mass of ϕK^+,

$\cos\theta_{K^*}$ **-** the cosine of the helicity angle of K^*, which is the angle of the resonance's daughter (K^+ for the K^* chain) and of the B^+ in the rest frame of K^*,

$\cos\theta_{J/\psi}$ **-** the cosine of the helicity angle of J/ψ, which is the angle of the μ^+ and B^+ in the rest frame of J/ψ,

$\cos\theta_\phi$ - the cosine of the helicity angle of ϕ, which is the angle of its daughter K^+ and K^* in the rest frame of ϕ,

$\Delta\phi_{K^*,\phi}$ - the angle between the decay planes of the K^* and ϕ,

$\Delta\phi_{K^*,J/\psi}$ - the angle between the decay planes of the K^* and J/ψ.

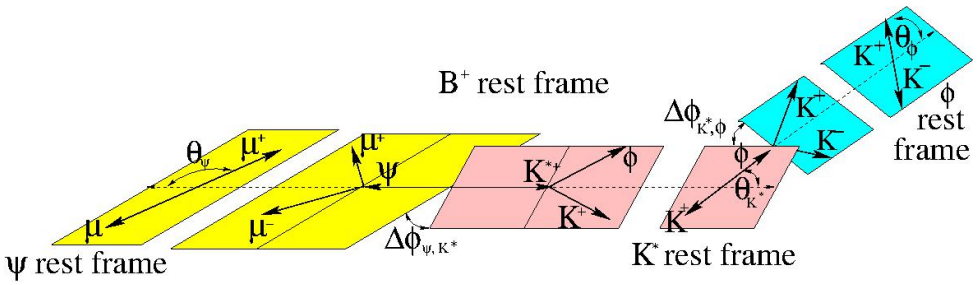

Figure 28: A pictographic representation of the angles involved in the K^* decay chain.

Next we consider the $B^+ \to X K^+$, $X \to J/\psi\,\phi$, $J/\psi \to \mu^+\mu^-$, $\phi \to K^+K^-$ decay chain which will be referred to as the X decay chain. It has the following variables describing the decay:

$m_{J/\psi\,\phi}$ - the invariant mass of $J/\psi\,\phi$,

$\cos\theta_X$ - the cosine of the helicity angle of X, which is the angle of the resonance's daughter (J/ψ for the X chain) and the B^+ in the rest frame of X,

$\cos\theta^X_{J/\psi}$ - the cosine of the helicity angle of J/ψ, which is the angle of μ^+ and X in the rest frame of J/ψ,

$\cos\theta^X_{\phi}$ - the cosine of the helicity angle of ϕ, which is the angle of its daughter K^+ and X in the rest frame ϕ,

$\Delta\phi_{X,\phi}$ - the angle between the decay planes of the X and ϕ,

$\Delta\phi_{X,J/\psi}$ - the angle between the decay planes of the X and J/ψ.

The helicity angles of J/ψ and of ϕ in this decay chain are different from those in the K^{*+} decay chain, due to the difference in parent particles between the two decay chains. Therefore, we have given them a superscript X. Nevertheless, we often neglect to obey this explicit notation, thus which helicity angle is meant depends on the decay chain it refers to. All variables describing the X decay chain, while independent of each other, can be derived from the six variables used to describe the K^{*+} decay chain. Therefore, they do not increase dimensionality of the analysis. Finally, we consider the $B^+ \to \phi Z^+$, $Z^+ \to J/\psi\,K^+$, $\phi \to K^+K^-$, $J/\psi \to \mu^+\mu^-$ decay chain which shall be referred to as the Z decay chain, with the following variables describing the decay:

$m_{J/\psi\,K}$ - the invariant mass of $J/\psi\,K^+$,

$\cos\theta_Z$ - the cosine of the helicity angle of Z, which is the angle of the resonance's daughter (J/ψ for the Z chain) and the B in the rest frame of Z,

$\cos\theta^Z_{J/\psi}$ - the cosine of the helicity angle of J/ψ, which is the angle of μ^+ and Z in the rest frame of J/ψ,

$\cos\theta^Z_\phi$ - the cosine of the helicity angle of ϕ, which is the angle of its daughter K^+ and B^+ in the rest frame ϕ,

$\Delta\phi_{Z,\phi}$ - the angle between the decay planes of the Z and ϕ,

$\Delta\phi_{Z,J/\psi}$ - the angle between the decay planes of the Z and J/ψ.

Similar comments to those made above for the X decay chain also apply to the Z decay chain variables. In fact, the Z decay chain is directly analogous to that of K^* with J/ψ and ϕ transposed.

It is important to note that the helicity states for the final state muons are not the same between different decay chains and a correction must be considered to properly describe the interference between the various decay chains. To align the muon helicity frames of two decay chains with the third one, additional azimuthal rotations are needed. The choice of decay chain to use as reference is arbitrary and for this study the K^* decay chain was used. The azimuthal rotation angle α^X (or α^Z) about the μ^+ momentum in the J/ψ rest frame is derivable again from the six variables in any of the decay chains.

The calculations for all above angles as well as how the charge conjugated B^- decays were dealt with is the same as in the $Z(4430)^+$ analysis [12]. These calculations were checked with two other independent methods to avoid mistakes.

To maximize the sensitivity of our analysis we performed six-dimensional unbinned maximum likelihood fits to the data.

5.2 Calculation of the angles used in this analysis

The fifteen angles, five for each of the three decay chains, are calculated in an analogous way to that done in the Belle 4D amplitude analysis of the $Z(4430)^+$ signal [12] and programmed along the same lines as LHCb's $Z(4430)^+$ amplitude analysis [37]. In total, the five angles for each decay chain are the cosine of the three helicity angles of J/ψ, ϕ and the resonance in question (*e.g.* K^*) and two angles between the decay plane of the resonance and the decay plane of either J/ψ or ϕ. In addition, a rotation is needed to align the muon frames of the X and Z^+ decay chains to that of the K^* decay chain in order to properly describe the interferences between the various possible states. The choice of K^* as decay chain of reference is arbitrary.

Cosine of a helicity angle of particle P, produced in two-body decay $A \to P\,B$, and decaying to two particles $P \to C\,D$ is calculated from (Eq. 16 in Ref. [12]):

$$\cos\theta_P = -\frac{\vec{p}_B \cdot \vec{p}_C}{|\vec{p}_B|\,|\vec{p}_C|}, \tag{3}$$

where the momentum vectors are in the rest frame of the particle P.

For $B^+ \to J/\psi\,K^{*+}$ decay, the angle between the $J/\psi \to \mu^+\mu^-$ and $K^{*+} \to \phi K^+$ decay planes is calculated from (Eq.14-15 in Ref. [12]):

$$\Delta\phi_{K^*,J/\psi} = \text{atan2}(\sin\Delta\phi_{K^*,J/\psi}\ ,\ \cos\Delta\phi_{K^*,J/\psi}) \tag{4}$$

$$\cos\Delta\phi_{K^*,J/\psi} = \frac{\vec{a}_{K^+} \cdot \vec{a}_{\mu^+}}{|\vec{a}_{K^+}|\,|\vec{a}_{\mu^+}|} \tag{5}$$

$$\sin\Delta\phi_{K^*,J/\psi} = \frac{[\vec{p}_{J/\psi} \times \vec{a}_{K^+}] \cdot \vec{a}_{\mu^+}}{|\vec{p}_{J/\psi}|\,|\vec{a}_{K^+}|\,|\vec{a}_{\mu^+}|} \tag{6}$$

$$\vec{a}_{K^+} = \vec{p}_{K^+} - \frac{\vec{p}_{K^+} \cdot \vec{p}_{K^{*+}}}{|\vec{p}_{K^{*+}}|^2}\,\vec{p}_{K^{*+}} \tag{7}$$

$$\vec{a}_{\mu^+} = \vec{p}_{\mu^+} - \frac{\vec{p}_{\mu^+} \cdot \vec{p}_{J/\psi}}{|\vec{p}_{J/\psi}|^2}\,\vec{p}_{J/\psi}\,, \tag{8}$$

with all vectors being in the B^+ rest frame. For $B^+ \to Z^+\phi$ decay, the angle between the $Z^+ \to J/\psi\, K^+$ and $\phi \to K^+K^-$ decay planes, $\Delta\phi_{Z,\phi}$, can be calculated in the same way with $J/\psi \to \phi$, $\mu^+ \to K^+$ (the K^+ from the ϕ decay) and the bachelor K^+ staying the same.

The angle between the decay planes of two sequential decays, e.g. between the $Z^+ \to J/\psi\, K^+$ and $J/\psi \to \mu^+\mu^-$ decay planes after the $B^+ \to Z^+\phi$ decay, is calculated from (Eq.18-19 in Ref. [12]):

$$\Delta\phi_{Z,J/\psi} = \text{atan2}(\sin\Delta\phi_{Z,J/\psi}\ ,\ \cos\Delta\phi_{Z,J/\psi}) \tag{9}$$

$$\cos\Delta\phi_{Z,J/\psi} = \frac{\vec{a}_\phi \cdot \vec{a}_{\mu^+}}{|\vec{a}_\phi|\,|\vec{a}_{\mu^+}|} \tag{10}$$

$$\sin\Delta\phi_{Z,J/\psi} = \frac{-[\vec{p}_{K^+} \times \vec{a}_\phi] \cdot \vec{a}_{\mu^+}}{|\vec{p}_{K^+}|\,|\vec{a}_\phi|\,|\vec{a}_{\mu^+}|} \tag{11}$$

$$\vec{a}_\phi = \vec{p}_\phi - \frac{\vec{p}_\phi \cdot \vec{p}_{K^+}}{|\vec{p}_{K^+}|^2}\,\vec{p}_{K^+} \tag{12}$$

$$\vec{a}_{\mu^+} = \vec{p}_{\mu^+} - \frac{\vec{p}_{\mu^+} \cdot \vec{p}_{K^+}}{|\vec{p}_{K^+}|^2}\,\vec{p}_{K^+}, \tag{13}$$

with all vectors being in the J/ψ rest frame. The other angles of this type are calculated the same way, with appropriate substitutions. For example, $\Delta\phi_{K^*,\phi}$ between the $K^{*+} \to \phi K^+$ and $\phi \to K^+K^-$ decay planes after $B^+ \to K^{*+}J/\psi$ decay, with $\phi \to J/\psi$, $\mu^+ \to K^+$ (K^+ from the ϕ decay), and the bachelor K^+ staying the same (with all vectors now in the ϕ rest frame).

The angle aligning the muon helicity frames between the K^{*+} and and Z^+ decay chains

is calculated from (Eq.20-21 in Ref. [12]):

$$\alpha^Z = \text{atan2}(\sin\alpha^Z\,,\,\cos\alpha^Z) \tag{14}$$

$$\cos\alpha^Z = \frac{\vec{a}_{K^+}\cdot\vec{a}_{K^{*+}}}{|\vec{a}_{K^+}|\,|\vec{a}_{K^{*+}}|} \tag{15}$$

$$\sin\alpha^Z = \frac{-[\vec{p}_{\mu^+}\times\vec{a}_{K^+}]\cdot\vec{a}_{K^{*+}}}{|\vec{p}_{\mu^+}|\,|\vec{a}_{K^+}|\,|\vec{a}_{K^{*+}}|} \tag{16}$$

$$\vec{a}_{K^{*+}} = \vec{p}_{K^{*+}} - \frac{\vec{p}_{K^{*+}}\cdot\vec{p}_{\mu^+}}{|\vec{p}_{\mu^+}|^2}\,\vec{p}_{\mu^+} \tag{17}$$

$$\vec{a}_{K^+} = \vec{p}_{K^+} - \frac{\vec{p}_{K^+}\cdot\vec{p}_{\mu^+}}{|\vec{p}_{\mu^+}|^2}\,\vec{p}_{\mu^+}, \tag{18}$$

where the K^+ is the bachelor kaon and all vectors are in the J/ψ rest frame. Similarly, α^X is obtained from the above equations with the $K^+ \to \phi$ substitution.

For the $B^- \to J/\psi\,\phi K^-$ decays, the same formulae apply with the bachelor kaon being K^-, μ^+ replaced by μ^- and K^+ from the ϕ decay replaced by the K^- from the ϕ decay. All azimuthal angles ($\Delta\phi$ and α) have their signs flipped after applying the formulae above (see the bottom of Appendix IX in Ref. [12]).

5.3 The signal PDF

The signal probability density function (PDF), $\mathcal{P}_{\text{sig}}$, is a function of 6 independent dimensions, $m_{\phi K}$, and the independent angular variables in the K^* decay chain collectively called Ω. The PDF also depends on the fit parameters, $\overrightarrow{\omega}$ (the helicity couplings, possibly masses and widths of resonances, etc.) Note that the invariant mass of $J/\psi\,\phi$ and the various angular variables in the X decay chain depend on $m_{\phi K}$ and Ω, therefore they don't represent independent dimensions. The signal PDF is given by

$$\frac{d\mathcal{P}}{dm_{\phi K}\,d\Omega} \equiv \mathcal{P}_{\text{sig}}(m_{\phi K},\Omega|\overrightarrow{\omega}) = \frac{1}{I(\overrightarrow{w})}\,|\mathcal{M}(m_{\phi K},\Omega|\overrightarrow{\omega})|^2\,\Phi(m_{\phi K})\epsilon(m_{\phi K},\Omega), \tag{19}$$

where $\mathcal{M}(m_{\phi K}, \Omega|\overrightarrow{\omega})$ is the matrix element. $\Phi(m_{\phi K}) = p\,q$ is the phase space function, where p is the momentum of the ϕK^+ system (i.e. K^*) in the B^+ rest frame, and q is the momentum of K^+ in the K^* rest frame. $\epsilon(m_{\phi K}, \Omega)$ is the signal efficiency. $I(\overrightarrow{\omega})$ is the normalization integral:

$$I(\overrightarrow{\omega}) \equiv \int \mathcal{P}_{\rm sig}(m_{\phi K}, \Omega)\, dm_{\phi K}\, d\Omega \propto \frac{\Sigma_j w_j^{\rm MC}\, |\mathcal{M}(m_{Kp\ j}, \Omega_j|\overrightarrow{\omega})|^2}{\Sigma_j w_j^{\rm MC}}. \tag{20}$$

where the sum is over simulated events, which are generated uniformly in phase-space and passed through the detector simulation and the data selection. The weights $w_j^{\rm MC}$ contain corrections of the production kinematics of the B^+ and of the detector simulation. They are specified in Sec. 4. The simulation sample contains 132232 events, approximately 30 times the signal size. This procedure folds in the efficiency corrections without a need to parameterize them, since in the log-likelihood sum over the data events,

$$\begin{aligned} & \ln L(\overrightarrow{\omega}) = \sum_i \ln \mathcal{P}_{\rm sig}(m_{Kp\ i}, \Omega_i|\overrightarrow{\omega}) \\ = \quad & \sum_i \ln |\mathcal{M}(m_{Kp\ i}, \Omega_i|\overrightarrow{\omega})|^2 - N \ln I(\overrightarrow{\omega}) + \sum_i \ln[\Phi(m_{Kp\ i})\epsilon(m_{Kp\ i}, \Omega_i)], \end{aligned} \tag{21}$$

the last term does not depend on $\overrightarrow{\omega}$ and can be dropped (N is the total number of the events in the fit).

5.4 Description of cFit procedure

In addition to the signal PDF, $\mathcal{P}_{\rm sig}(m_{\phi K},\Omega|\overrightarrow{\omega})$, a background PDF, $\mathcal{P}_{\rm bkg}(m_{\phi K},\Omega)$, is built from the side-bands. We minimize the log-likelihood defined as,

$$
\begin{aligned}
&-\ln L(\overrightarrow{\omega}) = -\Sigma_i \ln\left[(1-\beta)\,\mathcal{P}_{\rm sig}(m_{\phi K\ i},\Omega_i|\overrightarrow{\omega}) + \beta\,\mathcal{P}_{\rm bkg}(m_{\phi K\ i},\Omega_i)\right] \\
&= -\Sigma_i \ln\left[(1-\beta)\,\frac{\left|\mathcal{M}(m_{\phi K\ i},\Omega_i|\overrightarrow{\omega})\right|^2\,\Phi(m_{\phi K\ i})\epsilon(m_{\phi K\ i},\Omega_i)}{I(\overrightarrow{\omega})} + \beta\,\frac{\mathcal{P}^u_{\rm bkg}(m_{\phi K\ i},\Omega_i)}{I_{\rm bkg}}\right] \\
&= -\Sigma_i \ln\left\{\frac{(1-\beta)\,\Phi(m_{\phi K\ i})\epsilon(m_{\phi K\ i},\Omega_i)}{I(\overrightarrow{\omega})}\ \left[\left|\mathcal{M}(m_{\phi K\ i},\Omega_i|\overrightarrow{\omega})\right|^2\right.\right. \\
&\qquad\qquad\left.\left. + \frac{\beta\,I(\overrightarrow{\omega})}{(1-\beta)\,I_{\rm bkg}}\,\frac{\mathcal{P}^u_{\rm bkg}(m_{\phi K\ i},\Omega_i)}{\Phi(m_{\phi K\ i})\epsilon(m_{\phi K\ i},\Omega_i)}\right]\right\} \\
&= -\Sigma_i \ln\left[\left|\mathcal{M}(m_{\phi K\ i},\Omega_i|\overrightarrow{\omega})\right|^2 + \frac{\beta\,I(\overrightarrow{\omega})}{(1-\beta)I_{\rm bkg}}\,\frac{\mathcal{P}^u_{\rm bkg}(m_{\phi K\ i},\Omega_i)}{\Phi(m_{\phi K\ i})\epsilon(m_{\phi K\ i},\Omega_i)}\right] + N\ln I(\overrightarrow{\omega}) + \text{constant},
\end{aligned}
\tag{22}
$$

where N is the number of events, $\beta = 0.228$ is the background fraction in the peak region determined from the fit to the $m_{J/\psi\phi K}$ distribution (Fig. 20), $I(\overrightarrow{\omega})$ is the normalization of the signal PDF (Eq. (20)), $\mathcal{P}^u_{\rm bkg}(m_{\phi K},\Omega)$ is the unnormalized background density proportional to the density of side-band events, with its normalization determined by[7]

$$
I_{\rm bkg} \equiv \int \mathcal{P}^u_{\rm bkg}(m_{\phi K})\,dm_{\phi K}\,d\Omega \;\propto\; \frac{\Sigma_j w_j^{\rm MC}\frac{\mathcal{P}^u_{\rm bkg}(m_{\phi K\ j},\Omega_j)}{\Phi(m_{\phi K\ i})\epsilon(m_{\phi K\ j},\Omega_j)}}{\Sigma_j w_j^{\rm MC}}. \tag{23}
$$

The background term is then efficiency corrected so it can be added to the efficiency-independent signal probability expressed by $|\mathcal{M}|^2$. This way the signal efficiency parametrization, $\epsilon(m_{\phi K},\Omega)$, becomes a part of the background parametrization which ultimately affects only a small part of the total PDF (22.8%). The efficiency corrections to the signal part are discussed in Sec. 5.3 and don't rely on any parametrization.

[7]Notice that the distribution of MC events includes both the $\Phi(m_{\phi K})$ and $\epsilon(m_{\phi K},\Omega)$ factors, which cancel their product in the numerator.

The efficiency in the background term is assumed to factorize as

$$\epsilon(m_{\phi K},\Omega) = \epsilon_1(m_{\phi K},\cos\theta_{K^*})\cdot\epsilon_2(\cos\theta_\phi|m_{\phi K})\cdot\epsilon_3(\cos\theta_{J/\psi}|m_{\phi K})\cdot\epsilon_4(\Delta\phi_{K^*,\phi}|m_{\phi K})\cdot\epsilon_5(\Delta\phi_{K^*,J/\psi}|m_{\phi K}). \tag{24}$$

The $\epsilon_1(m_{\phi K},\cos\theta_{K^*})$ term is obtained by binning a 2D histogram of the simulated events. Each event is given a $1/(p\cdot q)$ weight, since at the generator level the phase space is flat in $\cos\theta_{K^*}$ but has a $p\cdot q$ dependence on $m_{\phi K}$. A bi-cubic interpolation is used to interpolate between bin centers. The $\epsilon_1(m_{\phi K},\cos\theta_{K^*})$ efficiency and its visualization across the normal Dalitz plane are shown in Fig. 29. The other terms are again built from 2D histograms, but with each bin divided by the number of simulated events in the corresponding $m_{\phi K}$ slice to remove the dependence on this mass. They are shown in Fig. 30.

The background PDF, $\mathcal{P}^u_{\rm bkg}(m_{\phi K},\Omega)/\Phi(m_{\phi K})$, is built using the same approach,

$$\frac{\mathcal{P}^u_{\rm bkg}(m_{\phi K},\Omega)}{\Phi(m_{\phi K})} = P_{{\rm bkg}_1}(m_{\phi K},\cos\theta_{K^*})\cdot P_{{\rm bkg}_2}(\cos\theta_\phi|m_{\phi K})$$
$$\cdot P_{{\rm bkg}_3}(\cos\theta_{J/\psi}|m_{\phi K})\cdot P_{{\rm bkg}_4}(\Delta\phi_{K^*,\phi}|m_{\phi K})\cdot P_{{\rm bkg}_5}(\Delta\phi_{K^*,J/\psi}|m_{\phi K}). \tag{25}$$

The background function $P_{{\rm bkg}_1}(m_{\phi K},\cos\theta_{K^*})$ is shown in Fig. 31 and the other terms are shown in Fig. 32.

After background parametrization, the data side-bands can be compared to the background PDF which can be used to ensure proper parametrization in the fit. The results of the comparisons are shown in Figure 33 and show good agreement between the parametrization and the background sample from the data.

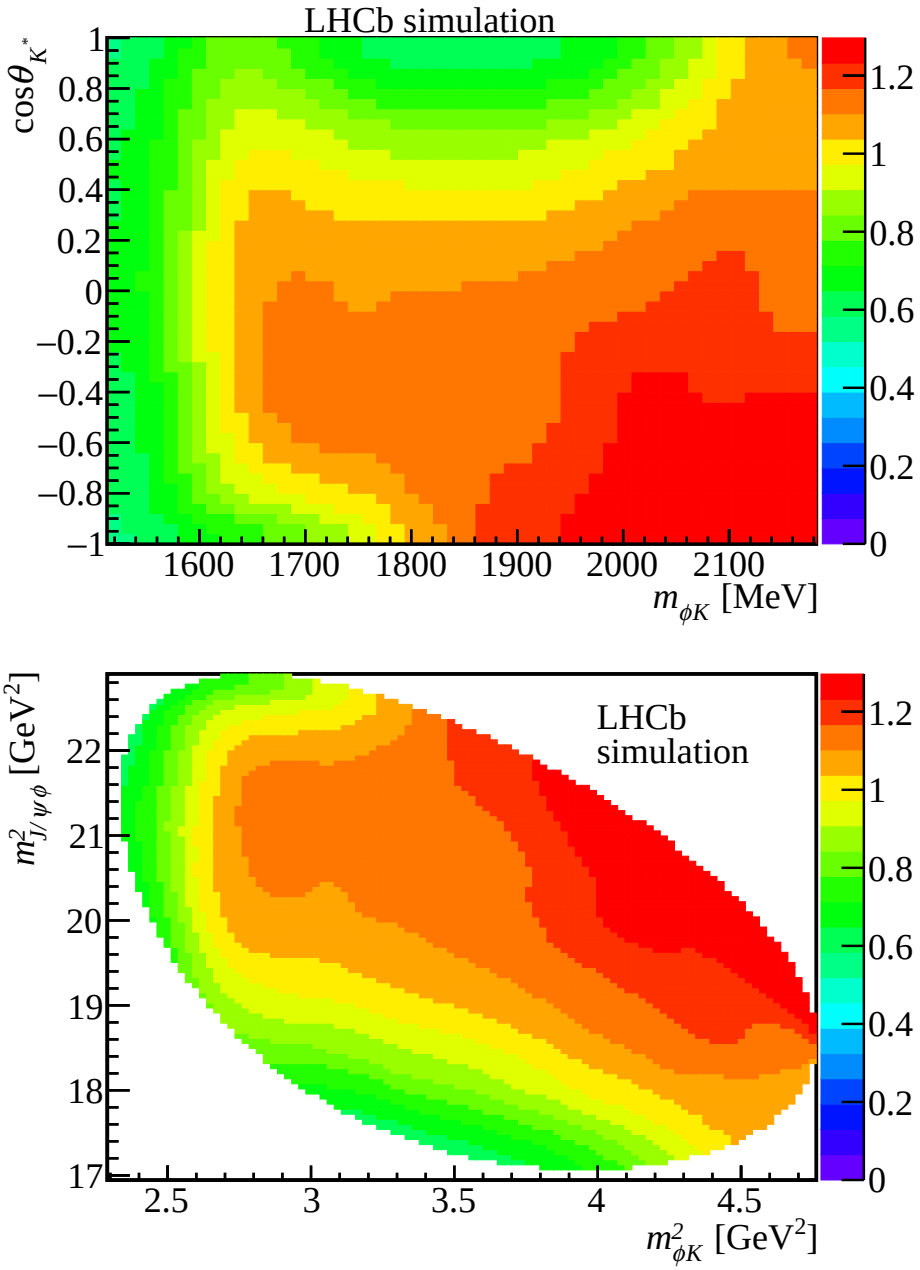

Figure 29: Parameterized efficiency $\epsilon_1(m_{\phi K}, \cos\theta_{K^*})$ function (top) and its representation in the Dalitz plane $({m_{\phi K}}^2, {m_{J/\psi\,\phi}}^2)$ (bottom). The normalization arbitrarily corresponds to an average efficiency of 1 over the phase-space.

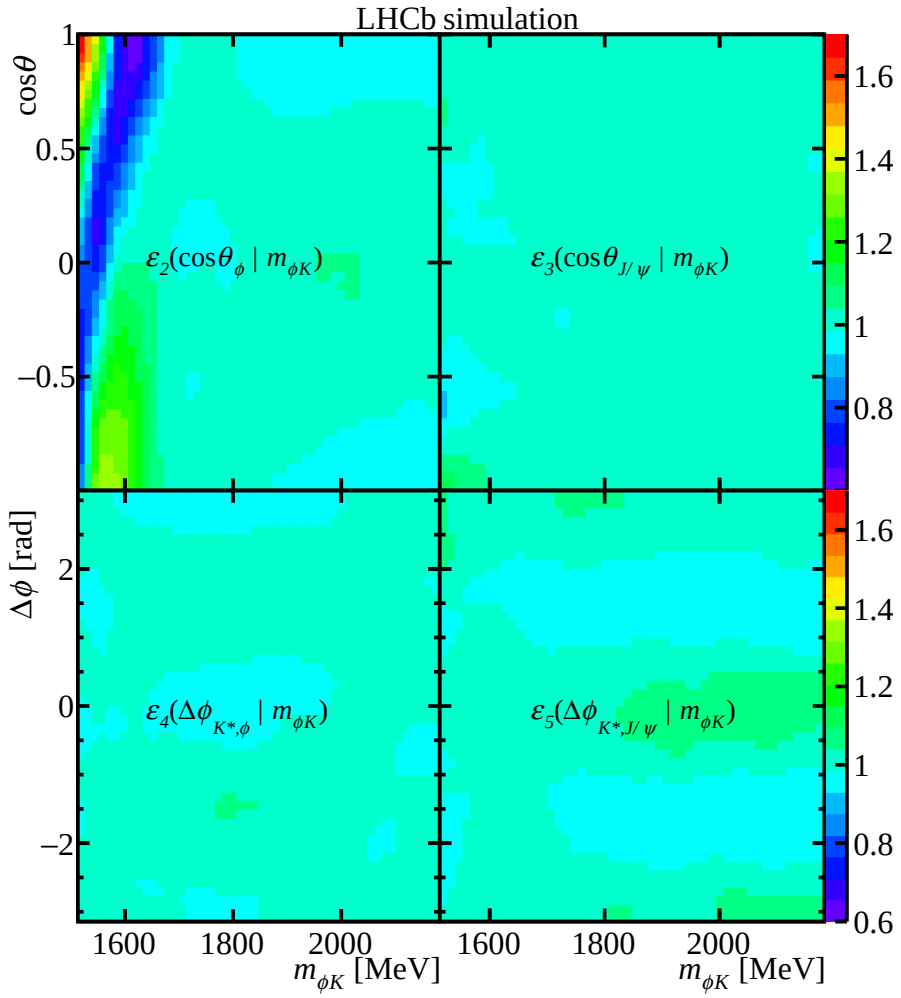

Figure 30: Parameterized efficiency $\epsilon_2(\cos\theta_\phi|m_{\phi K})$, $\epsilon_3(\cos\theta_{J/\psi}|m_{\phi K})$, $\epsilon_4(\Delta\phi_{K^*,\phi}|m_{\phi K})$, $\epsilon_5(\Delta\phi_{K^*,J/\psi}|m_{\phi K})$ functions. By construction they integrate to 1.0 at each $m_{\phi K}$ value. The structure in $\epsilon_2(\cos\theta_\phi|m_{\phi K})$ present between 1500 and 1600 MeV is an artifact of removing $B \to J/\psi KKK$ events in which both K^+K^- combinations pass the ϕ mass selection window.

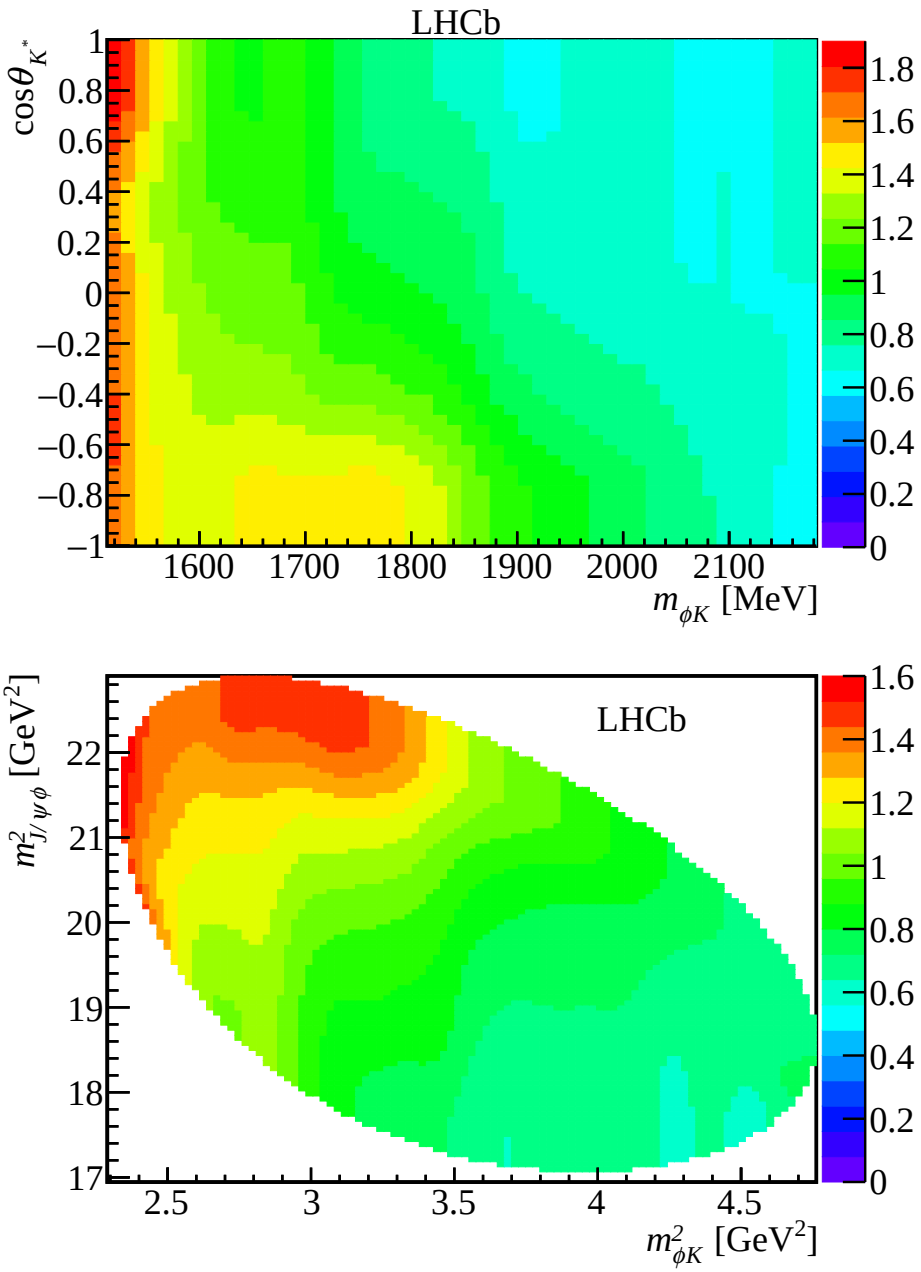

Figure 31: Parameterized background $P_{\text{bkg}_1}(m_{\phi K}, \cos\theta_{K^*})$ function (top) and its representation in the Dalitz plane $({m_{\phi K}}^2, {m_{J/\psi\phi}}^2)$ (bottom). The normalization arbitrarily corresponds to an average efficiency of 1 over the phase-space.

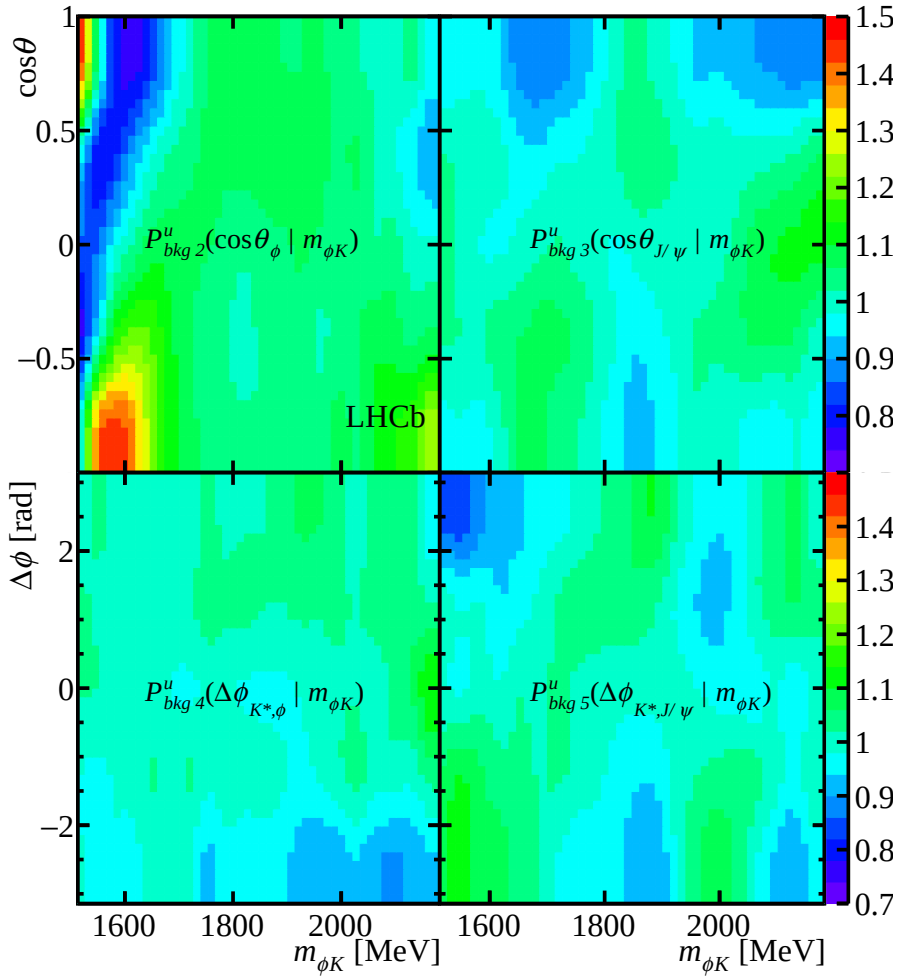

Figure 32: Parameterized efficiency functions: $P^u_{\mathrm{bkg}\,2}(\cos\theta_\phi|m_{\phi K})$, $P^u_{\mathrm{bkg}\,3}(\cos\theta_{J/\psi}|m_{\phi K})$, $P^u_{\mathrm{bkg}\,4}(\Delta\phi_{K^*,\phi}|m_{\phi K})$, $P^u_{\mathrm{bkg}\,5}(\Delta\phi_{K^*,J/\psi}|m_{\phi K})$ By construction they integrate to 1.0 at each $m_{\phi K}$ value.

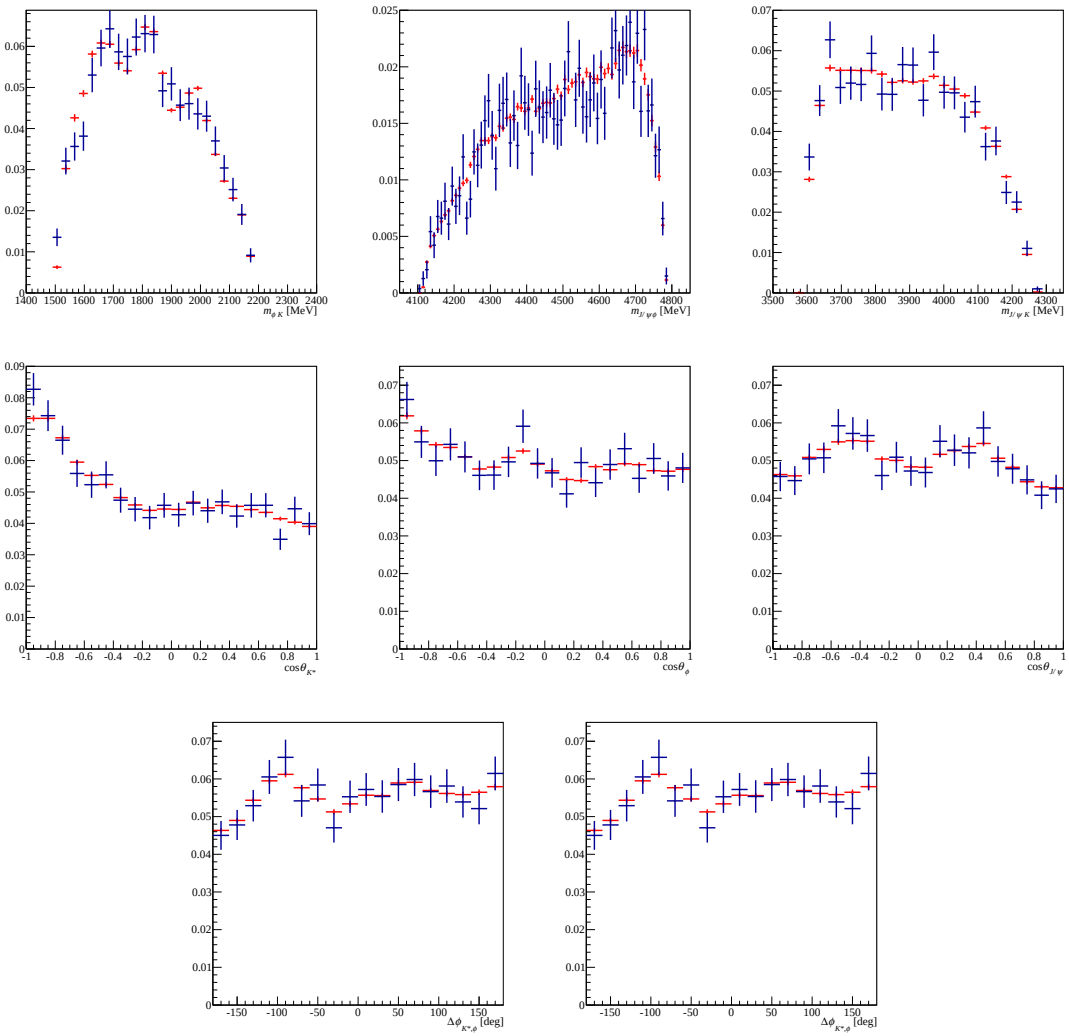

Figure 33: Comparison of the background from the data (black) and the parameterized background (red) for $m_{\phi K}$, $m_{J/\psi\,\phi}$, $m_{J/\psi\,K}$ (left to right in the top row), $\cos\theta_{K^*}$, $\cos\theta_{\phi}$, $\cos\theta_{J/\psi}$ (left to right in the middle row) , and $\Delta\phi_{K^*,\phi}$ and $\Delta\phi_{K^*,J/\psi}$ (left to right in the bottom row).

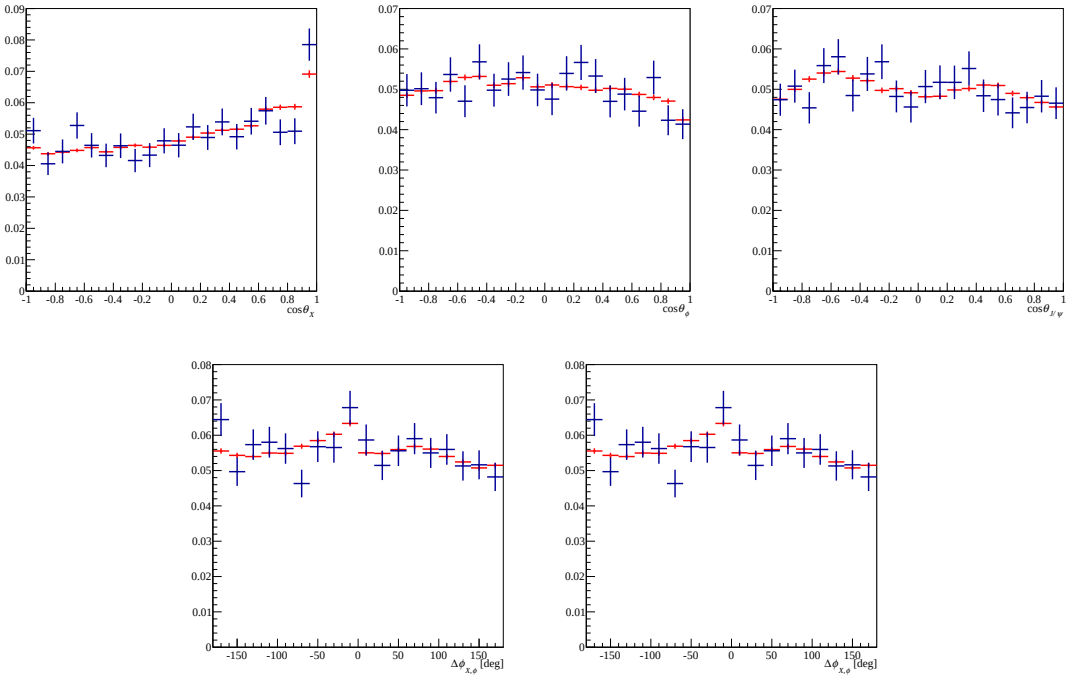

Figure 34: Comparison of the background from the data (black) and the parameterized background (red) for $\cos\theta_X$, $\cos\theta_\phi$, $\cos\theta_{J/\psi}$ (left to right in the top row) , and $\Delta\phi_{X,\phi}$ and $\Delta\phi_{X,J/\psi}$ (left to right in the bottom row).

6 Helicity formalism and matrix element

We use the Isobar model in the default fit to parameterize the decay amplitude, *i.e.* we construct the overall amplitude by summing over the individual Breit-Wigner terms representing individual K^*, X, and Z resonances (quasi-2-body model). We also allow non-resonant terms.

Here we describe the application of the helicity formalism to each decay chain as well as the construction of the complete matrix element in which the different decay chains can interfere. The matrix formulation is similar to that used in the $Z(4430)^+$ analysis [12]. The complexity of matrix element is increased here, since there are two spin 1 particles involved in each decay chain and there is an additional $\phi \to K^+K^-$ decay to describe. Each decay chain comes with its own unique structure for helicity couplings and individual set of six kinematic variables. Like in the $Z(4430)^+$ analysis, there are also additional azimuthal angles which realign the muon helicity states between the different decay chains.

6.1 Helicity formalism for the K^* decay chain

In the K^* decay chain B decays proceed via $B \to J/\psi\, K^*$, $K^* \to \phi K$, with ϕ and J/ψ decaying via $\phi \to KK$ and $J/\psi \to \mu\mu$ respectively. This is the only "non-exotic" of the three decay chains. As discussed later there are several known K^{*+} resonances which are expected to contribute to the decay.

The full 6D matrix element for the K^* decay chain is given by:

$$\mathcal{M}^{K^*}_{\Delta\lambda_\mu} \equiv \sum_j \sum_{\lambda_{J/\psi}=-1,0,1} \sum_{\lambda_\phi=-1,0,1} A^{B\to J/\psi\, K^*\, j}_{\lambda_{J/\psi}}\, A^{K^*\to\phi K\, j}_{\lambda_\phi}$$

$$d^{J_{K^*}\, j}_{\lambda_{J/\psi},\lambda_\phi}(\theta_{K^*})\, d^1_{\lambda_\phi,0}(\theta_\phi)\, e^{i\lambda_\phi \Delta\phi_{K^*,\phi}}\, d^1_{\lambda_{J/\psi},\Delta\lambda_\mu}(\theta_{J/\psi})\, e^{i\lambda_{J/\psi}\Delta\phi_{K^*,J/\psi}}\, R(m_{\phi K}|M_{0\,K^*\,j}, \Gamma_{0\,K^*\,j}),$$

$$|\mathcal{M}|^2 = \sum_{\Delta\lambda_\mu=\pm1} \left|\mathcal{M}^{K^*}_{\Delta\lambda_\mu}\right|^2, \tag{26}$$

where j sums over different K^{*+} resonances. The resonance dependent terms are given this index. J_{K^*} is the spin of the K^* resonance. λ is helicity of the particle (projection of the particle spin onto its momentum in the rest frame of its parent) and $\Delta\lambda_\mu \equiv \lambda_{\mu^+} - \lambda_{\mu^-}$. $d^J_{\lambda_1,\lambda_2}(\theta)$ are the Wigner d-functions. $R(m_{\phi K})$ is the mass dependence of the contribution (usually a complex Breit-Wigner amplitude including Blatt-Weisskopf factors), which will be discussed in more detail later. $A^{B\to J/\psi\, K^*}_{\lambda_{J/\psi}}$ and $A^{K^*\to\phi K}_{\lambda_\phi}$ are complex helicity couplings describing the decay dynamics of the subsequent weak and strong decays of B^+ and K^{*+}, respectively. They are j dependent. There are three independent complex $A^{B\to J/\psi\, K^*}_{\lambda_{J/\psi}}$ couplings to fit ($\lambda_{J/\psi} = -1, 0, 1$) per K^* resonance, unless $J_{K^*} = 0$ in which case there is only one since $\lambda_{J/\psi} = \lambda_{K^*}$ due to $J_B = 0$. The parity conservation in the strong K^* decay limits the number of independent helicity couplings $A^{K^*\to\phi K}_{\lambda_\phi}$. More generally, parity conservation requires

$$A^{A\to B\,C}_{-\lambda_B,-\lambda_C} = P_A\, P_B\, P_C\, (-1)^{J_B+J_C-J_A}\, A^{A\to B\,C}_{\lambda_B,\,\lambda_C}, \tag{27}$$

which, for the decay $K^{*+} \to \phi K^+$, leads to:

$$A_{\lambda_\phi} = P_{K^*}(-1)^{J_{K^*}+1}\, A_{-\lambda_\phi} \tag{28}$$

This reduces the number of independent couplings in the K^* decay to one or two. Since the overall magnitude and phase of these couplings can be absorbed in the $A^{B\to J/\psi\, K^*}_{\lambda_{J/\psi}}$, in practice the K^* decay contributes no or one complex parameter to fit per K^* resonances.

6.2 Helicity formalism for the X decay chain

In the X decay chain B decays proceed via $B{\to}XK$, $X \to J/\psi\,\phi$, with ϕ and J/ψ decaying via $\phi \to KK$ and $J/\psi \to \mu\mu$, respectively. The full 6D matrix for the X decay chain is formulated in a similar manner as in the K^* decay chain, except it involves the six

kinematic variables associated with the X decay chain enumerated earlier. The matrix element for the X decay chain also has unique helicity couplings and is given by:

$$\mathcal{M}^{X}_{\Delta\lambda_\mu} \equiv \sum_{j} \sum_{\lambda_{J/\psi}=-1,0,1} \sum_{\lambda_\phi=-1,0,1} A^{X\to J/\psi\,\phi\,j}_{\lambda_{J/\psi},\lambda_\phi}$$
$$d^{J_X\,j}_{0,\lambda_{J/\psi}-\lambda_\phi}(\theta_X)\, d^{1}_{\lambda_\phi,0}(\theta^X_\phi)\, e^{i\lambda_\phi\Delta\phi_{X,\phi}}\, d^{1}_{\lambda_{J/\psi},\Delta\lambda_\mu}(\theta^X_{J/\psi})\, e^{i\lambda_{J/\psi}\,\Delta\phi_{X,J/\psi}}\, R(m_{J/\psi\,\phi}|M_{0\,X\,j},\Gamma_{0\,X\,j})$$
$$|\mathcal{M}^{K^*+X}|^2 = \sum_{\Delta\lambda_\mu=\pm1} \left|\mathcal{M}^{K^*}_{\Delta\lambda_\mu} + e^{i\alpha^X\Delta\lambda_\mu}\mathcal{M}^{X}_{\Delta\lambda_\mu}\right|^2, \tag{29}$$

where j sums over all X resonances. To add $\mathcal{M}^{K^*}_{\Delta\lambda_\mu}$ and $\mathcal{M}^{X}_{\Delta\lambda_\mu}$ coherently it is necessary to introduce the $e^{i\alpha^X\Delta\lambda_\mu}$ term, which corresponds to the rotation about μ^+ momentum axis by the angle α^X in the rest frame of J/ψ after arriving to it by the boost from the X rest frame. This realigns the coordinate axes for the muon helicity frame to be the same in the X and K^* decay chains. This problem is discussed in Ref. [12].

The helicity couplings are very different in the X decay chain than in the K^* decay chain. The decay $B^+ \to XK^+$ does not contribute any helicity couplings to the fit since X is produced fully polarized $\lambda_X = 0$.[8] The X decay contributes a resonance dependent matrix of the helicity couplings $A^{X\to J/\psi\,\phi}_{\lambda_{J/\psi},\lambda_\phi}$. Fortunately, the parity conservation discussed previously reduces the number of independent couplings to 1 for $J^P_X = 0^-$, 2 for 0^+, 3 for 1^+, 4 for 1^- and 2^-, and at most 5 independent couplings for 2^+.

6.3 Helicity formalism for the Z decay chain

In the Z decay chain B decays proceed via $B \to \phi Z$, $Z \to J/\psi\,K$, with ϕ and J/ψ decaying via $\phi \to KK$ and $J/\psi \to \mu\mu$, respectively. As before we may construct its matrix element using the same formalism. The Z decay chain also picks up a rotation to align the muon

[8] To be more precise, there is only one coupling which can be absorbed into redefinition of the other couplings which are free parameters.

frames to the ones used in the K^* decay chain and allows for the proper description of interference between the three decay chains. The full 6D matrix element is given by:

$$\mathcal{M}^{Z}_{\Delta\lambda_\mu} \equiv \sum_j \sum_{\lambda_{J/\psi}=-1,0,1} \sum_{\lambda_\phi=-1,0,1} A^{B\to Z\phi\, j}_{\lambda_\phi}\, A^{Z\to J/\psi\, K\, j}_{\lambda_{J/\psi}}$$

$$d^{J_Z\, j}_{\lambda_{J/\psi},\lambda_{J/\psi}}(\theta_Z)\, d^{1}_{\lambda_\phi,0}(\theta^Z_\phi)\, e^{i\lambda_\phi \Delta\phi_{Z,\phi}}\, d^{1}_{\lambda_{J/\psi},\Delta\lambda_\mu}(\theta^Z_{J/\psi})\, e^{i\lambda_{J/\psi}\Delta\phi_{K^*,J/\psi}}\; R(m_{J/\psi\, K}|m_{0\, Z\, j},\Gamma_{0\, Z\, jz})$$

$$|\mathcal{M}^{K^*+X+Z}|^2 = \sum_{\Delta\lambda_\mu=\pm 1} \left|\mathcal{M}^{K^*}_{\Delta\lambda_\mu} + e^{i\alpha^X\Delta\lambda_\mu}\mathcal{M}^{X}_{\Delta\lambda_\mu} + e^{i\alpha^Z\Delta\lambda_\mu}\mathcal{M}^{Z}_{\Delta\lambda_\mu}\right|^2,$$

The parity conservation in the Z decay requires

$$A^{B\to Z\phi}_{\lambda_{J/\psi}} = P_Z(-1)^{J_Z+1}\, A_{-\lambda^{B\to Z\phi}_{J/\psi}} \tag{31}$$

and provides similar reduction of the couplings as discussed for the K^* decay chain.

By fitting the data we discovered that we don't need any Z contributions to obtain an accurate description of the data. A possible extension of the present analysis would be to set upper limits on Z fit fractions, thus we have documented the full matrix element allowing for three interfering decay chains.

6.4 LS couplings

Instead of fitting the helicity couplings $A^{A\to B\,C}_{\lambda_B\,\lambda_C}$ as free parameters, after imposing the parity conservation for the strong decays, it is convenient to express them by equivalent number of independent LS couplings (B_{LS}), where L is the orbital angular momentum in the decay and S is the total spin of B and C, $\vec{S} = \vec{J}_B + \vec{J}_C$ ($min(0, |J_B - J_C|) \leq S \leq J_B + J_C$). Possible combinations of L and S values are constrained via $\vec{J}_A = \vec{L} + \vec{S}$. The relation

involves the Clebsch-Gordan coefficients:

$$A^{A\to BC}_{\lambda_B,\lambda_C} = \sum_L \sum_S \sqrt{\frac{2L+1}{2J_A+1}}\, B_{L,S} \left(\begin{array}{cc|c} J_B & J_C & S \\ \lambda_B & -\lambda_C & \lambda_B - \lambda_C \end{array} \right) \left(\begin{array}{cc|c} L & S & J_A \\ 0 & \lambda_B - \lambda_C & \lambda_B - \lambda_C \end{array} \right). \tag{32}$$

The parity conservation in the strong decays is imposed by satisfying the following relation

$$P_A = P_B\, P_C\, (-1)^L. \tag{33}$$

Use of the B_{LS} couplings has an advantage over the direct use of the helicity couplings, since the fitted couplings are less correlated; but since an additional equation is involved, care has to be taken to cache the helicity couplings in each fit iteration as to not compromise the CPU performance of the fitter. Also, since one coupling in the fit has to be fixed to $(1, 0)$ to define overall magnitude and phase convention of all couplings in the fit[9], it is safer to fix the lowest L and the lowest S coupling as the major contribution to the matrix element[10], instead of choosing ad hoc helicity combination.

Since the helicity or LS couplings not only shapes the angular distributions but also describes the overall strength and phase of the given contribution relative to all other contributions in the matrix element, we factor these roles out by always setting the lowest L, the lowest S $B_{L_{min}S_{min}}$ coupling for given contribution to $(1, 0)$ and multiplying the sum in Eq. 32 by the complex fit parameter $\mathcal{A}$ (this is equivalent to factoring out $B_{L_{min}S_{min}}$). This has an advantage when interpreting numerical values of these parameters. The $\mathcal{A}_j$ describes relative magnitude and phase of the $B_{L_{min}S_{min}\,j}$ to the other contributions, and fitted $B_{LS\,j}$ values have a meaning of the ratio, $B_{LS\,j}/B_{L_{min}S_{min}\,j}$, and determine the

[9]The overall magnitude has no physical meaning in the fits in which the PDF is automatically scaled to the number of fitted events. An overall phase of the total matrix element is always unobservable.

[10]In the default fit we use non-resonant $J/\psi\,\phi$ component to set the magnitude and phase conventions, since it has the largest fit fraction. Normalizing to the most significant K^* component, $K^*(1680)$, led to identical log-likelihood value and the same mass, width and fit fraction results for all the components.

angular distributions.

6.5 Amplitude dependence on the invariant masses

Each contribution to the matrix element comes with its own $R(m_A)$ function, which gives its dependence on the invariant mass of the intermediate resonance in the decay chain A ($A = K^*$, X or Z). Usually it is given by the Breit-Wigner amplitude, but there are special cases which we discuss below.

In principle, also the ϕ resonance has a variable mass. However, since the ϕ resonance is very narrow ($\Gamma_0 = 4.3$ MeV, mass resolution 1.2 ± 0.1 MeV) we omit the amplitude dependence on the invariant $m_{K^+K^-}$ mass from the ϕ decay. This speeds up the already CPU consuming fits tremendously and avoids complications which would have been introduced by unavoidable convolution of the ϕ Breit-Wigner amplitude with the mass resolution function which is not completely negligible for such a narrow state.

6.5.1 Single resonant contribution

A single resonant contribution in the decay chain $B^+ \to A...$, $A \to ...$ is parameterized by the relativistic Breit-Wigner amplitude together with Blatt-Weisskopf functions:

$$R(m|M_0,\Gamma_0) = B'_{L_B}(p,p_0,d)\left(\frac{p}{p_0}\right)^{L_B} BW(m|M_0,\Gamma_0)\, B'_{L_A}(q,q_0,d)\left(\frac{q}{q_0}\right)^{L_A}, \qquad (34)$$

where

$$BW(m|M_0,\Gamma_0) = \frac{\sqrt{k}}{M_0^2 - m^2 - iM_0\Gamma(m)}\,, \qquad (35)$$

is the Breit-Wigner amplitude including the mass dependent width,

$$\Gamma(m) = \Gamma_0\left(\frac{q}{q_0}\right)^{2L_A+1}\frac{M_0}{m}B'_{L_A}(q,q_0,d)^2\,. \qquad (36)$$

Here, p is the momentum of the resonance A (K^*, X or Z) in the rest frame of B^+. q is the momentum of the A resonance's daughter in the rest frame of the A resonance. The symbols p_0 and q_0 are used to indicate values of these quantities at the resonance peak mass ($m = M_0$). The orbital angular momentum in B decay is denoted as L_B, while in the decay of the resonance A as L_A. The orbital angular momentum barrier factors, $p^L\, B'_L(p, p_0, d)$, involve the Blatt-Weisskopf functions:

$$B'_0(p, p_0, d) = 1\,, \quad (37)$$

$$B'_1(p, p_0, d) = \sqrt{\frac{1 + (p_0\, d)^2}{1 + (p\ \ d)^2}}\,, \quad (38)$$

$$B'_2(p, p_0, d) = \sqrt{\frac{9 + 3(p_0\, d)^2 + (p_0\, d)^4}{9 + 3(p\ \ d)^2 + (p\ \ d)^4}}\,, \quad (39)$$

$$B'_3(p, p_0, d) = \sqrt{\frac{225 + 45(p_0\, d)^2 + 6(p_0\, d)^4 + (p_0\, d)^6}{225 + 45(p\ \ d)^2 + 6(p\ \ d)^4 + (p\ \ d)^6}}\,, \quad (40)$$

$$B'_4(p, p_0, d) = \sqrt{\frac{11025 + 1575(p_0\, d)^2 + 135(p_0\, d)^4 + 10(p_0\, d)^6 + (p_0\, d)^8}{11025 + 1575(p\ \ d)^2 + 135(p\ \ d)^4 + 10(p\ \ d)^6 + (p\ \ d)^8}}\,, \quad (41)$$

$$B'_5(p, p_0, d) = \sqrt{\frac{893025 + 99225(p_0\, d)^2 + 6300(p_0\, d)^4 + 315(p_0\, d)^6 + 15(p_0\, d)^8 + (p_0\, d)^{10}}{893025 + 99225(p\ \ d)^2 + 6300(p\ \ d)^4 + 315(p\ \ d)^6 + 15(p\ \ d)^8 + (p\ \ d)^{10}}}\,, \quad (42)$$

which account for the difficulty in creating the orbital angular momentum (L) and depends on the momentum of the decay products in the rest frame of the decaying particle (p) as well as the size of the decaying particle given by the constant d. In this analysis we set this parameter to a nominal value of $d = 3.0$ GeV^{-1}, but we vary its values between 1.5 and 5.0 GeV^{-1} in the evaluation of the systematic errors (see Sec. 9).

In the helicity approach, each helicity state is a mixture of many different L values. We follow the usual approach of using in the functions above the minimal L value allowed by the quantum numbers of the given resonance A. Higher values are set in estimating the systematic errors.

The k constant appearing in the Breit-Wigner amplitude (Eq. (35)) is conventional and is introduced here in an attempt to decouple the numerical values of the helicity couplings

to be fit from M_0 and Γ_0 parameters of the resonance:

$$k \equiv \frac{M_0 \Gamma_0 \gamma}{\sqrt{{M_0}^2 + \gamma}} \tag{43}$$

with $\gamma \equiv \sqrt{{M_0}^2 \left({M_0}^2 + {\Gamma_0}^2\right)}$ (see Wikipedia for the Relativistic Breit-Wigner). This factor makes an integral of $|BW(m)|^2$ M_0 and Γ_0 independent when integrated in the infinite mass range. When integrated in the finite phase-space there is a residual M_0 and Γ_0 dependence, but this approach is the best one can do short of the numerical integration of each contribution squared at each iteration of M_0 and Γ_0 values. Introduction of this factor does not change the fit results, but it makes relative numerical values of the resonant couplings better reflect the relative strengths of various resonances and reduces correlation coefficients between the couplings, M_0 and Γ_0 if the latter are left free in the fit, which in principle can reduce CPU consumption.

6.5.2 Non-resonant contribution

We set $BW(m|M_0, \Gamma_0) = 1.0$ for the non-resonant (NR) contributions, which means we assume that both magnitude and phase have negligible m dependence. As the available phase-space in the $B^+ \to J/\psi\, \phi K^+$ decays is small (the energy release is only 12% of the B mass) this is a well justified assumption. The non-resonant contributions are allowed to be shaped by the Blatt-Weisskopf functions in Eq. 34 if the quantum numbers assigned to the NR term dictate $L \neq 0$. The M_0 values used in the calculations of p_0 and q_0 are set to the mid-range for the given decay chain. Since $p_{0\,NR}$ and $q_{0\,NR}$ only play a role in the scaling factor, this choice does not affect the fit results, but affects only numerical values of the complex coupling describing relative strength and phase of the NR contribution relative to the other terms in the amplitude.

7 States decaying to ϕK^+

The only conventional hadrons which can contribute to $B^+ \to J/\psi\,\phi K^+$ decays are excitations of the strange charged meson, $(u\bar{s})$, hereafter denoted as K^{*+}, decaying to ϕK^+ via $s\bar{s}$ popping. Kinematically allowed K^{*+} masses, $1513 - 2182$ MeV, cover higher excitations of this system. There are many known K^{*+} resonances in this mass range. A few additional K^{*+} states are expected in the quark model but have no experimentally identified candidates yet.

There is also a possibility of contributions from exotic tetraquarks, e.g. in di-quark model $((us)(\bar{s}\bar{s}))$, decaying to ϕK^+ via disintegration. This is rather remote possibility since no undisputed tetraquark candidates made out of the light quarks have been observed. Even when heavy quarks are involved, there are several experimental candidates for 4-quark states decaying to $\psi\pi^+$ (which could be $((uc)(\bar{d}\bar{c}))$ or $((u\bar{c})(\bar{d}c))$ molecules), but none have been found in ψK^+ decay mode (which would be $((uc)(\bar{s}\bar{c}))$ or $((u\bar{c})(\bar{s}c))$). If exotic hadrons decaying to ϕK^+ exist, they would have quantum numbers already expected among the $(u\bar{s})$ excitations, thus could mix with them or show up as extra bound states. From an experimental point of view, for this and previous measurements, both conventional and exotic hadrons decaying to ϕK^+ manifest themselves the same way.

We first review theoretical expectations for the $(u\bar{s})$ states and discuss to which extent the observed K^{*+} states match these expectations. We then review what is known from the previous experiments sensitive to $K^* \to \phi K$ decays. We then present results from the attempts to describe our data with the amplitude models containing only ϕK^+ contributions.

7.1 Kaon excitations

Different radial ($n = 1, 2, 3, \dots$) and orbital angular momentum ($L = S, P, D, F, \dots$) excitations of the $u\bar{s}$ system, together with the total spin of the two quarks ($S = 0, 1$), result in an expectantly rich mass spectrum. Each excitation is traditionally labeled with these intrinsic quantum numbers and with total angular momentum $J = 0, 1, 2, \dots$ *i.e.* with the K^{*+} spin ($\vec{J} = \vec{L} + \vec{S}$): $n^{2S+1}L_J$. The parity of each state is also well defined, $P = +, -$, with $P = (-1)^{L+1}$. The higher the quantum numbers, the higher the mass. Widths tend to increase with n, as the binding is weaker for the higher excitations and there are more decay channels open to it. A spin-singlet state of $L \neq S$ levels is likely to mix with the spin-triplet of the same nL multiplet, since they have identical J^P numbers (n^1P_1 with n^3P_1, n^1D_2 with n^3D_2 etc.). There are still two states expected, not too different in mass, as the hyperfine splitting (spin-spin interactions) cannot be very large except for the $L = S$ states. Approximate masses of the kaon excitations were predicted in a relativistic potential model by Godfrey-Isgur [38] and are listed in Table 4. They are compared to the K^{*+} states listed in PDG [39] according to the most likely interpretation of each observed state. Excluding a few outliers (1^3P_0, 2^3S_1, 2^1P_1, 3^1S_0, 3^3S_1), 16 remaining states have mass correctly predicted within ± 30 MeV.[11] Therefore, it is reasonable to use this theoretical model as a guide for which masses yet unobserved kaon excitations may be contributing to our data. We will refer to these predictions, and to the K^{*+} PDG states, listed in Table 4 when constructing models of the K^{*+} contributions to our data.

All confirmed K^{*+} states find their natural explanation in the predicted $u\bar{s}$ excitations.

[11] As discussed later in the text, in the case of the biggest outlier (2^1P_1), the fault is likely on the PDG side which made the controversial choice for the mass of 1^+ enhancements observed in this mass region in various experiments. The second biggest outlier (3^1S_0) is also not an established resonance from the paper in which no experimental errors were given. The third largest outlier (1^3P_0) has 0^+ quantum numbers which are not allowed in ϕK^+ decays. Its mass may be affected by the same type of long distance strong interactions as proposed for $K(800)$ (*i.e.* κ), not included in Godfrey-Isgur model and relevant only for low mass 0^+ states. We do not have any explanations why the observed mass of the 2^3S_1 candidate is 166 ± 16 MeV lower than the predictions. A hint of the 3^3S_1 state has been possibly seen (see the next subsection) also at significantly lower mass than predicted.

Two unconfirmed K^{*+} states in the mass range relevant for this analysis included in the long PDG listing but do not find explanation among the expected $u\bar{s}$ states (thus they are not listed in Table 4) are $K_2(1580)$ $J^P = 2^-$ state with mass ~ 1580 MeV (width ~ 110 MeV), and $K(1630)$ with undetermined quantum numbers and 1629 ± 7 MeV and 16^{+19}_{-16} MeV width. Both are very questionable from the experimental point of view. There is also an unconfirmed $K_3(2320)$ $J^P = 3^+$ state well above the kinematic limit imposed by $B^+ \to J/\psi\, K^{*+}$ decays, with mass 2324 ± 24 MeV and width 150 ± 30 MeV, which does not match $u\bar{s}$ levels (~ 300 MeV below the expectations for the $2F_3$ states).

The last column in Table 4 summarizes our own assessment of the previous experimental results on possible states decaying to ϕK, which are reviewed in the next subsection.

Table 4: Excitations of $u\bar{s}$ predicted by Godfrey-Isgur [38], together with the best experimental candidate, named if listed in PDG [39]. Bold font names indicate the well established states. All masses and widths are in units of MeV. The last column is our own assessment of the previous results for $K^* \to \phi K$ decays summarized in the next subsection: "seen" if peaking of such partial wave at nearby mass range was observed in at least one experiment (in some cases also backed up by the phase information); "possibly seen" if non-zero intensity of the partial wave at relevant mass was detected by at least one experiment without evidence for peaking; "no data" if no sufficient statistics were available to probe for such wave. In all cases of "seen" or "possibly seen" entries, there was at least one experiment which did not support such classification, possibly because of the lack of statistical sensitivity or because of systematic uncertainties.

$n^{2S+1}L_J$	J^P	M_{th}	Candidate PDG state			$\Delta M =$	ϕK
			Name	M_{exp}	Γ	$M_{exp} - M_{th}$	decay?
States below the ϕK^+ decay threshold							
1^1S_0	0^-	470	$\mathbf{K}^+$	494		$+24 \pm 5$	below threshold
1^3S_1	1^-	900	$\mathbf{K}^*(892)^+$	892 ± 0.3	51 ± 1	-8 ± 5	below threshold
1^3P_0	0^+	1240	$\mathbf{K_0^*(1430)}^+$	1425 ± 50	270 ± 80	$+185 \pm 50$	forbidden
1^1P_1	1^+	1340	$\mathbf{K_1(1270)}^+$	1272 ± 7	90 ± 20	-68 ± 9	below threshold
1^3P_1	1^+	1380	$\mathbf{K_1(1400)}^+$	1403 ± 7	174 ± 13	$+23 \pm 9$	below threshold
1^3P_2	2^+	1430	$\mathbf{K_2^*(1430)}^+$	1426 ± 1	98 ± 3	-4 ± 5	below threshold
2^1S_0	0^-	1450	$K(1460)^+$	$\sim 1400 - 60$	~ 250	-20 ± 30	below threshold
2^3S_1	1^-	1580	$\mathbf{K}^*(1410)^+$	1414 ± 15	232 ± 21	-166 ± 16	below threshold
States above the ϕK^+ decay threshold (1513 MeV)							
1^3D_1	1^-	1780	$\mathbf{K}^*(1680)^+$	1717 ± 27	322 ± 110	-63 ± 27	possibly seen
1^1D_2	2^-	1780	$\mathbf{K_2(1770)}^+$	1773 ± 8	188 ± 14	-7 ± 9	seen
1^3D_2	2^-	1810	$\mathbf{K_2(1820)}^+$	1816 ± 13	276 ± 35	$+6 \pm 14$	part of $K_2(1770)$?
1^3D_3	3^-	1790	$\mathbf{K_3^*(1780)}^+$	1776 ± 7	159 ± 21	-14 ± 9	no data
2^3P_0	0^+	1890	$K_0^*(1950)^+$	1945 ± 22	201 ± 78	$+55 \pm 22$	**forbidden**
2^1P_1	1^+	1900	$K_1(1650)^+$	1650 ± 50	150 ± 50	-250 ± 50	seen, 1840?
2^3P_1	1^+	1930					see entry above
2^3P_2	2^+	1940	$K_2^*(1980)^+$	1973 ± 26	373 ± 69	$+33 \pm 26$	seen
3^1S_0	0^-	2020	$K(1830)^+$	~ 1830	~ 250	-190	seen
3^3S_1	1^-	2110		1910 ± 40	500 ± 200	-200 ± 40	seen
1^3F_2	2^+	2150					part of $K_2^*(1980)$?
1^1F_3	3^+	2120					possibly seen
1^3F_3	3^+	2150					possibly seen
1^3F_4	4^+	2110	$\mathbf{K_4^*(2045)}^+$	2045 ± 9	198 ± 30	-65 ± 10	no data
States right above the maximum allowed in $B^+ \to J/\psi K^{*+}$ (2182 MeV)							
2^3D_1	1^-	2250					no data
2^1D_2	2^-	2230	$K_2(2250)^+$	2247 ± 17	180 ± 30	$+17 \pm 18$	no data
2^3D_2	2^-	2260					no data
2^3D_3	3^-	2240					no data
1^3G_5	5^-	2390	$K_5^*(2380)^+$	2382 ± 24	178 ± 49	-8 ± 24	no data
1^1G_4	4^-	2410					no data
1^3G_4	4^-	2440	$K_4(2500)^+$	2490 ± 20	~ 250	$+50 \pm 21$	no data
1^3G_3	3^-	2460					no data

7.2 Previous experimental results for states decaying to ϕK^+

Only $K_1(1650)$, $K_2(1770)$ and $K(1830)$ are listed in PDG as seen in ϕK decays (among these only $K_2(1770)$ is a well established state). However, it would be wrong to conclude from this that the other known K^* states don't decay to ϕK. In fact, there are no upper limits on branching fraction to ϕK for the other known K^* states for a good reason; activity at other ϕK masses for a variety of J^P values have been observed by the past experiments; the data was just inconclusive about its resonant composition.

Theoretically, only 0^+ states are forbidden by angular momentum and parity conservation to decay to ϕK. In fact, the decay diagram with $s\bar{s}$ popping is the same as the decay diagrams with $u\bar{u}$ and $d\bar{d}$, which lead to other common K^* decay modes, $K\pi$, $K^*(892)\pi$, $K\rho$, $K\omega$ etc. Except for the region very near the kinematic threshold for the ϕK decay, the phase-space suppression of this decay mode relative to $K\pi$ decay is modest: $< 50\%$ for masses > 1720 MeV). Thus, there are no good theoretical reasons to exclude from our K^{*+} matrix element model any kaon excitation which is within the mass range allowed in $B^+ \to J/\psi K^{*+}$, $K^{*+} \to K^+\phi$ decays, except for the 2^3P_0 (0^+) state which is forbidden by parity and angular momentum conservation. The actual decay width is driven by angular momentum factors and exact decay dynamics via its interplay with the internal structure of the K^{*+}, ϕ and K^+ mesons. Broken $SU(3)_f$ symmetry comes into play in these considerations. We know of only one theoretical model which attempted to quantitatively predict decay rates of various kaon excitations to various final states - the flux-tube breaking model by Kokoski-Isgur [40]. Inspection of their predictions confirms the naive arguments given above; essentially all kinematically allowed kaon excitations are expected to have reasonably large decay widths to the ϕK^+ final state.

We will now review in more details what has been observed in the past experiments which were sensitive to ϕK states. All previous experiments involved scattering charged kaon beams off of a fixed proton target, as opposed to pp collisions investigated at LHCb.

However, they all differed from one another, often by multiple factors: the type of the beam (K^- or K^+) and its energy, the reconstructed final state (charged or neutral kaons were used, with p or n as the final state baryon), the detector acceptance and model dependent choices in unfolding the partial waves. While the ϕK decay rates of potential K^* states contributing to these samples must be the same for all experiments, their production rates may be very different between them. This should be kept in mind when comparing one experiment to another, since, in fact, the differences are sometimes large. The strong production mechanisms present at these scattering experiments are also very different from the weak production mechanism present in our data. Therefore, intensity of potential K^* contributions observed in various scattering experiments may not be representative of the intensities of the same K^* states expected in our data. While some experiments were, in principle, at the position to quantify relative ϕK decay rates to the other decay rates of the same K^* states, none of them attempted to do so. Thus, the best we can hope for from inspection of these results are hints rather than firm expectations.

All experiments used similar technique: extraction of double-moments of decay angles in $K^* \to K\phi$ and in $\phi \to K^+K^-$ decays in a function of ϕK mass, followed by unfolding of these moments for various partial waves in each ϕK mass bin. Many model dependent assumptions are made in this process (*e.g.* which moments to consider, the amplitude model used in unfolding, which partial waves to allow in unfolding etc.). Efficiency corrections are highly non-trivial and performed iteratively, thus they are somewhat model dependent. Some backgrounds are present but are often neglected. The partial waves are labeled with the J^P of the ϕK system (*i.e.* of K^*). Sometimes the orbital angular momentum between ϕ and K in its decay, L_{K^*}, is also given. The partial wave label may also include $\lambda^{\eta}_{K^*}$, where λ_{K^*} is the helicity of the K^* state (commonly denoted as Λ in the scattering papers) and η is "the naturality" of spin-parity, *i.e.* $P(-1)^J$, of the particle exchanged between the beam and the target in the process assumed (and biased by the selection

cuts) to be diffractive - see Fig. 35a. For $\lambda_{K^*} = 0$, "natural" parity exchanges ($\eta = +$) lead to "unnatural" K^* quantum numbers: 0^-, 1^+, 2^-, ..., while $\eta = -$ lead to 1^+, 1^-, 2^+, ... A possible additional analysis step involves fitting a Breit-Wigner amplitude to the partial wave, often assumed to be the only important contribution in a given mass range. Such fits are usually done to the magnitudes of the partial waves only. In some situations, running of the phase of the partial wave with the mass is also inspected, if the reference partial wave is known not to change its phase significantly over the mass range of the interest. Only statistical errors are reported from such fits (and propagated to the PDG listing). Some publications don't even present statistical errors, but make qualitative observations with "eye balled" numbers for masses and widths of possible resonant contributions. There are no quantitative measures of significance of the claimed resonances. The number of events subject to such analyses was on the order of a few thousand, thus not much different than what is available in our own data.

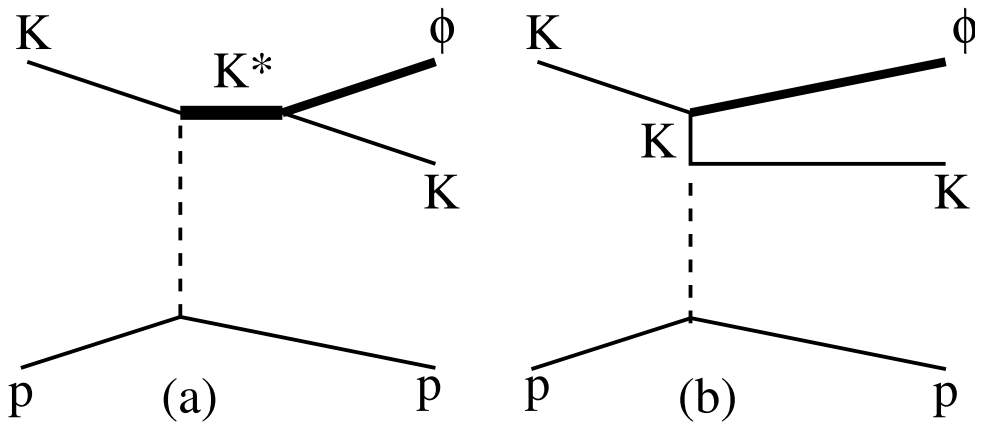

Figure 35: Diagrams in diffractive Kp scattering for: (a) production of K^* resonance decaying to ϕK; (b) non-resonant production of ϕK via a Deck mechanism.

7.2.1 The results from $K^-p \to \phi K^-p$ scattering data

The 1982 paper by Armstrong *et al.* [41] contains the analysis of 7.7k $K^-p \to \phi K^-p$ events (18.5 GeV K^- beam) reconstructed with the CERN Ω spectrometer. Contributions from dominant $\Lambda^* \to K^-p$ states (e.g. $\Lambda(1520)$) were suppressed by requiring $m_{K^-p} > 1950$ MeV, which reduces sensitivity of this experiment to high ϕK mass ($m_{\phi K} < 2200\,\text{MeV}$ was analyzed). The remaining Λ^* contributions were neglected. Non-ϕ background was about 15% and neglected (all K^+K^- pairs selected as ϕ candidates were assumed to have $J^P = 1^-$). The partial waves allowed in the fit to the selected double-moments are shown in Fig. 36. The production mechanism in this experiments favors $\eta = +$, and thus unnatural J^P combinations for ϕK^- states.[12]

The largest intensities are observed in the 1^+ waves, with a broad peak at $\sim$ 1.7 GeV. However, interpretation of this partial wave is complicated by the expected contribution from non-resonant Deck scattering (Fig. 35b). Satisfactory description of this wave was obtained by combining the model of the Deck amplitude with a K^* 1^+ resonance with mass $\sim$ 1840 MeV (width $\sim$ 250 MeV), which is close to where the $2P_1$ states are expected (Table 4).

Both 2^- and 0^- waves have large and peaking intensities, with the relative phase to the 1^+S0^+ wave undergoing significant resonant-like change in these regions. Thus, these data are indicative of 2^- and 0^- resonances with masses (widths) $\sim$ 1730 MeV and $\sim$ 1830 MeV ($\sim$ 220 MeV and $\sim$ 250 MeV), respectively. The 2^- peak is in the region of well established $K_2(1770)$ and $K_2(1820)$ states (a two Breit-Wigner interpretation was not tried here) observed also in other decay modes [42], in particular decays to ωK [43], matching the predictions for the two $1D_2$ states. The 0^- peak observed here gave rise to the $K(1830)$ listing in PDG and has not been confirmed until now. This could be a 3^1S_0

[12]The notation used in Ref. [41] uses different symbols than used in this note; λ_{K^*} is denoted as μ and our η is denoted as ϵ, while η is used as $P(-1)^J$ of K^*.

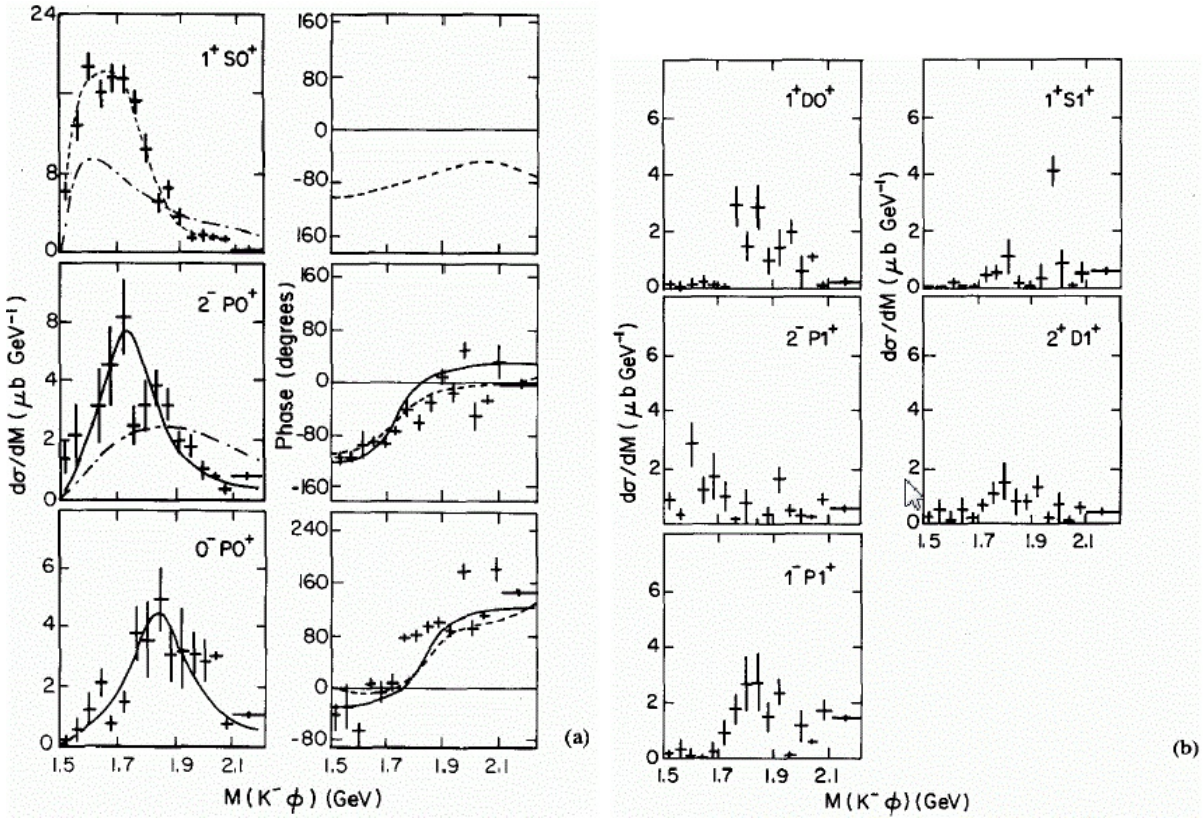

Figure 36: Intensities of various partial waves extracted from the $K^- p \to \phi K^- p$, $\phi \to K^+ K^-$ scattering data at 18.5 GeV using the CERN Ω spectrometer from Ref. [41]. The partial wave labels, $J^P\, L_{K^*}\, \lambda^{\eta}_{K^*}$ are explained in the text of this note. The right column of figure (a) contains a phase of the corresponding waves relative to the 1^+S0^+ wave.

state, though the mass is significantly below the predicted value.

Two waves with natural $J^P = 1^-$ and 2^+ were allowed with $\lambda_{K^*} = 1$ and $\eta = +$ in the fit to the moments, and were found to have small intensities. It is useful to stress that this is due to the production mechanism in this experiments being unfavorable for production of natural spin-parity combinations and should not be interpreted as an observation that K^* states with such quantum numbers do not have decays to ϕK final state.

7.2.2 The results from $K^+p \to \phi K^+p$ scattering data

The 1985 paper by Frame *et al.* [44] contains the analysis of 10.5k $K^+p \to \phi K^+p$ events (13 GeV K^+ beam) also reconstructed with the CERN Ω spectrometer (with an additional Cherenkov counter added), but by a completely new collaboration.[13] With the K^+ beam, there is no background from strange baryon excitations since pK^+ states would have been exotic. Non-ϕ background was $< 5\%$ and neglected. Like in the K^-p scattering experiment discussed above, the production mechanism favors $\eta = +$, and thus unnatural J^P K^* quantum numbers. The choices made about which double-moments to fit, the formalism and assumption used in the fit are somewhat different than in the K^-p work. In particular, $\lambda_{K^*} \neq 0$ were not allowed and $J^P = 3^+$ was added when unfolding the moments for the partial waves, even though like in the K^-p work, only K^* moments with rank up to 4 were used in the unfolding of the partial wave. The intensities of production partial waves allowed in the fit to the double-moments are shown in Fig. 37.

The 1^+ wave dominates as in the K^-p analysis, but falls off with mass a bit faster in the K^+p data (since the beam energy and the acceptance after the cuts are not the same, this does not necessarily constitute a disagreement). The fit of Deck scattering formula plus a Breit-Wigner gave 1650 ± 50 MeV and 150 ± 50 MeV for the mass and width of the resonance. The mass is lower than in the similar fit to the 1^+ wave in the K^-p data, perhaps because different models for the Deck scattering were used. This result prompted the PDG to represent the 1^+ effects in Kp scattering via $K_1(1650)$ entry (omitted from the summary PDG tables). We find this to be a questionable choice, since the higher ~ 1840 mass extracted in the analysis of the K^-p data (see above) agreed better with ~ 1800 MeV extracted from the 1^+ wave of $K^-p \to K^-\pi^+\pi^-p$ scattering data [45].

The second most intense wave is again 2^-, with the parameters of the fitted resonance, 1810 ± 20 MeV mass (140 ± 40 MeV width) in good agreement with the K^-p analysis.

[13] None of the authors of 1985 paper appeared on 1982 paper discussed previously.

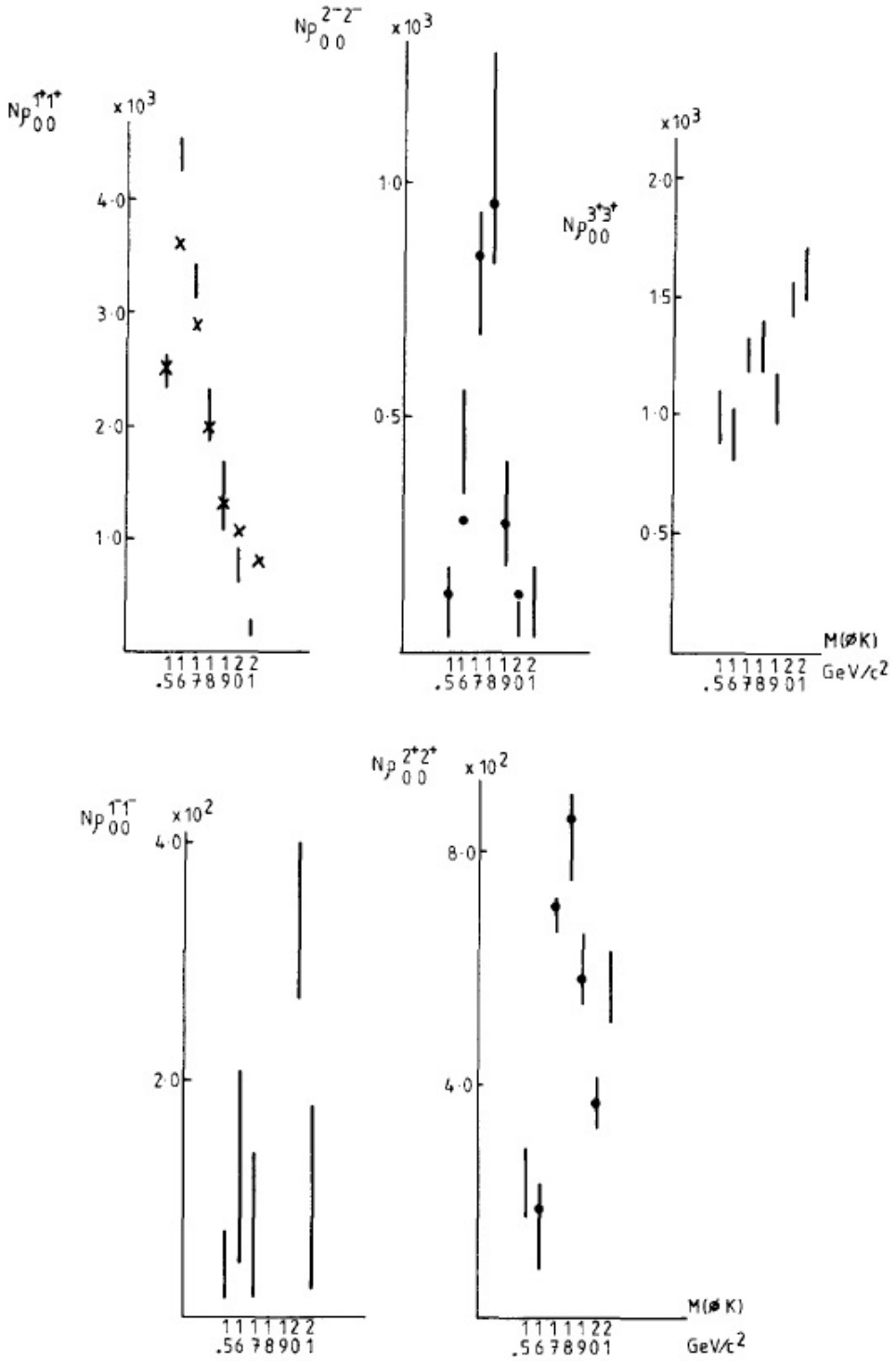

Figure 37: Intensities of the fitted production spin density matrix extracted from the $K^+p \to \phi K^+p$, $\phi \to K^+K^-$ scattering data at 13 GeV using the modified CERN Ω spectrometer from Ref. [44]. The partial wave labels give J^P of ϕK^+ states (repeated twice in the superscripts; zeros in the subscripts denote $\lambda_{K^*} = 0$). The superimposed points are Breit-Wigner fits. The superimposed crosses show the fit of the Deck model.

The 3^+ intensity is found to be almost equally large, rising with mass, but with no clear indication of a resonant structure. We are puzzled why the higher moments of K^* decay angles were not analyzed to clarify the nature of this evidence. This wave was not included when unfolding the K^-p double-moments of the partial waves.

The 0^- wave was found to be consistent with zero and is not shown in the paper. This observation clashes with the K^-p results in which the 0^- was very significant with a good evidence for a resonant behavior (peaking intensity associated with rapid change of phase). Perhaps the origin of this disagreement reflects systematic uncertainties in unfolding moments of the partial waves, which involves constructing a fit model.

The natural spin-parity combinations have low intensities as expected. The 1^- wave intensities have large statistical errors and "could not be determined" in the 1750-1950 MeV range (no explanation was offered).

The 2^+ wave intensity is small, but significant, peaking at 1800 ± 50 MeV with a width of 150 ± 50 MeV. The 2^+D1^+ wave in K^-p analysis shows also a small peak at this mass (Fig. 36b), which is not far from the 2^3P_2 state predicted at 1940 MeV by Godfrey-Isgur and the $K_2^*(1980)$ state observed by LASS in $K^-p \to \bar{K}^0\pi^+\pi^-n$ [46] and in $K^-p \to \bar{K}^0\pi^-p$ [47] (omitted from the PDG summary tables).

7.2.3 The results from $K^-p \to \phi\bar{K}^0n$ scattering data

The analysis of $K^-p \to \phi\bar{K}^0n$, $\phi \to K^+K^-$, $\bar{K}^0 \to \pi^+\pi^-$ data (11 GeV kaon beam) collected with the LASS spectrometer was not published but it is presented in the 1993 Ph.D. thesis of Y. Kwon [48]. Unlike the $Kp \to \phi Kp$ scattering data, which are dominated by the exchange of effective 0^+ quantum numbers between the beam and the target, $Kp \to \phi Kn$ scattering involves single pion exchange, thus 0^- dominates ($\eta = -$), making intensities of K^* states with natural J^P combinations (1^-, 2^+, 3^-, ...) more pronounced. To suppress $\bar{K}^0n$ baryonic contributions which become significant above 2 GeV in $m_{\phi\bar{K}^0}$,

events with $m_{\bar{K}^0 n} > 1.9$ GeV were removed, leaving about 1.3k signal events to analyze after the substantial non-ϕ background subtraction ($\sim 50\%$). Thus, unfortunately, this unique sample suffered from large statistical errors (equivalent background-free sample would have been only ~ 640 events). Moments of K^* decay angles with rank up to 4 were analyzed, thus allowing extraction of partial waves with J up to 2. Their intensities are shown in Fig 38.

Intensities of the unnatural spin-parity combinations are smaller than of the natural combination, as expected (see above). The 1^+ wave has huge statistical errors, but perhaps shows some peaking at ~ 1800 MeV. Unlike in the $Kp \to \phi Kp$ samples, no peaking is observed in the 2^- wave, but the statistics are poor and the production mechanism is different. The 0^- wave is consistent with zero.

The natural 1^- and 2^+ waves dominate the data. Peaking is observed in the 2^+ wave at a mass of 2010 ± 30 MeV, with a width[14] of ~ 400 MeV, in much better agreement than in the $K^+p \to \phi K^+p$ analysis (see above) with the mass of the $K_2^*(1980)$ state observed in the other decay modes. The 1^- wave also peaks at the higher mass, 1910 ± 40 MeV, and is very broad, $\Gamma = 500 \pm 200$ MeV, possibly signaling presence of 3^3S_1 state predicted by Godfrey-Isgur at 2110 MeV. Non-zero intensity extends to the region of the 1^3D_1 candidate, the $K^*(1680)$ resonance ($M = 1717 \pm 27$, $\Gamma = 322 \pm 110$) well established in the other decays modes.

7.2.4 Summary of the previous studies of $K^* \to \phi K$ decays

The three previous experiments sensitive to ϕK states do not paint a very clear picture. Their statistical power was rather limited. The two $Kp \to \phi Kp$ experiments had good sensitivity only to unnatural spin-parity combinations. The 1^+ ϕK wave intensity was dominant, but its resonant interpretation was obscured by non-resonant Deck scattering.

[14] Read out from the curve superimposed in 38.

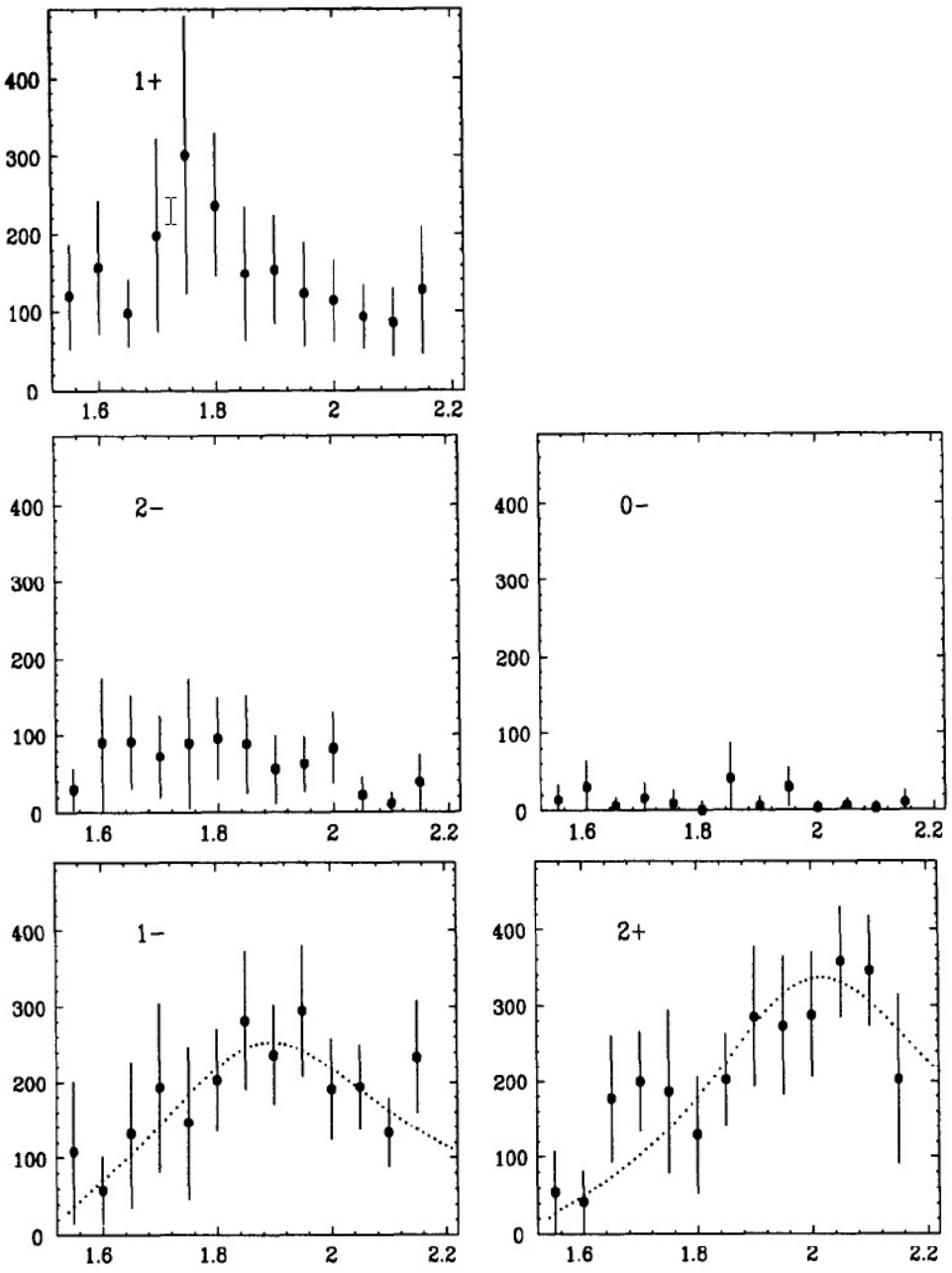

Figure 38: Intensities of the fitted partial waves extracted from the $K^- p \to \phi \bar{K}^0 n$, $\phi \to K^+ K^-$ scattering data at 11 GeV using the LASS spectrometer from Ref. [48]. The superimposed curves are Breit-Wigner fits.

These results definitely leave room for two $1P_1$ states predicted above the ϕK threshold.

Both experiments had good evidence for a resonance in the 2^- wave, consistent with the

well established $K_2(1770)$. Two-resonance interpretation of this structure was not tried. The third unpublished measurement using $Kp \to \phi Kn$ did not support such peaking, but its sensitivity was mostly to natural spin-parities. The third unnatural spin-parity wave, 0^-, came out inconsistent from the two experiments sensitive to it, with one experiment presenting solid evidence for a resonance at 1830 MeV but the other not showing any significant intensity in this wave. This inconsistency is likely due to systematic effects, which are poorly addressed in all three analyses, most likely model dependent choices in unfolding of the angular moments to the partial waves. Moving to natural spin-parity combinations, all experiments saw evidence for peaking structure in the 2^+ wave, but with somewhat inconsistent masses and widths. The $Kp \to \phi Kn$ data, with the best sensitivity to this mode, gave the mass closest to $K_2^*(1980)$ state observed also in other decay modes, a likely 2^3P_2 state. This measurement had also the best sensitivity to the 1^- wave, and saw a very broad structure peaking at high mass, perhaps a 3^3S_1 state, or an overlap of it with the lower mass 1^3D_1 state (likely $K^*(1680)$ which was well identified in other decay modes). The two $Kp \to \phi Kp$ measurements showed a different 1^- wave structure, but this could be due to either the different production mechanism or systematic errors in the extraction of this wave for which they lacked primary sensitivity. One experiment claimed a broad 3^+ wave rising with mass in the questionable analysis in which the moments most sensitive to such contribution were not included. The other experiments did not allow spin 3 contributions.

Since peaking structures were observed in all $J \leq 2$ waves in at least one experiment, and there was little sensitivity to the higher spins, these measurements suggest that all allowed J^P numbers should be tried. Theoretical expectations lead to the same suggestion.

7.3 Amplitude models of the ϕK^+ states

We investigate all allowed quantum numbers of ϕK^+ contributions in our amplitude models with J^P up to 4^+. We represent them as a sum of Breit-Wigner amplitudes with free mass and width and free B_{LS} amplitudes.

In addition to the resonant contributions, we also include a non-resonant ϕK^+ term ($\mathrm{NR}_{\phi K}$) which does not dependent on $m_{\phi K}$. There is no significant improvement in fit qualities when allowing the non-resonant ϕK^+ to fall off exponentially with mass. We do include, however, such a possibility among systematic variations. We associate $\mathrm{NR}_{\phi K}$ with $J^P = 1^+$ quantum numbers, since in this case, the minimal orbital angular momenta between the J/ψ and the ϕK^+ systems, as well as between the ϕ and K^+ systems are both zero. Nevertheless, we do not constrain this term to ${B_{0,0}}^{B^+ \to J/\psi\, K^{*+}\, \mathrm{NR}_{\phi K}}$ coupling only (*i.e.* $\mathcal{A}_{\mathrm{NR}_{\phi K}}$), but also fit to the data non-resonant ${B_{1,1}}^{B^+ \to J/\psi\, K^{*+}\, \mathrm{NR}_{\phi K}}$, ${B_{2,1}}^{B^+ \to J/\psi\, K^{*+}\, \mathrm{NR}_{\phi K}}$ and ${B_{2,2}}^{B^+ \to J/\psi\, K^{*+}\, \mathrm{NR}_{\phi K}}$, as well as the ratio ${B_{2,1}}^{K^{*+} \to \phi K^+\, \mathrm{NR}_{\phi K}} / {B_{0,1}}^{K^{*+} \to \phi K^+\, \mathrm{NR}_{\phi K}}$.

We first try to fit the data with the K^* states listed in PDG, plus additional states at higher masses predicted by Godfrey-Isgur: 3^3S_1, 1^3F_2, 1^1F_3, 1^3F_3 (see Table 4). In this initial fit, we fix masses and widths of the PDG states to the PDG values. For the predicted states we fix the masses to the predicted values and the widths are left as free parameters. While the $m_{\phi K}$ (Fig. 39) and $m_{J/\psi K}$ (Fig. 40) distributions are reasonably well reproduced by the fit, the $m_{J/\psi\phi}$ distribution (Fig. 41) is not. Calculating a χ^2 between the data and the fit for these one dimensional projections and converting them to p–values ($p_{1\mathrm{D}}$) by assuming the number of degrees of freedom is equal the number of bins minus one[15], we obtain 3.6%, 43% and $6 \cdot 10^{-10}$%, respectively.

To rule out that this disagreement is due to faulty values of the fixed masses or widths, we also perform fits in which they are allowed to float. Even though the number of

[15]This gives the upper limit on $p_{1\mathrm{D}}$, since effective ndf may be reduced by free parameters in the fit as discussed in Appendix 8.13.

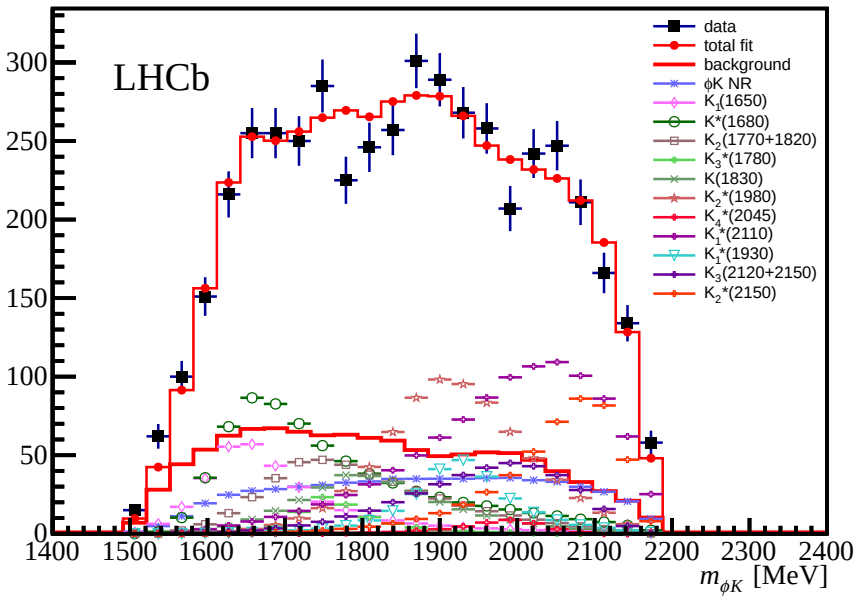

Figure 39: The distribution of $m_{\phi K}$ for the data and the fit with the K^{*+}s listed in PDG, plus additional states predicted at the higher mass. Masses of the states are fixed to either the PDG or predicted values. The widths are fixed to the PDG values or left free for the predicted states.

states, and their initial masses are guided by the Godfrey-Isgur predictions, when fit unconstrained these fit components can adjust to any ϕK^+ states present in the data. To avoid fit components converging to unphysically narrow or wide states we limit them to 100-1000 MeV range. The narrowest known K^{*+} state above the kinematic limit for the ϕK^+ decay has a width of 159 ± 21 MeV (see Table 4). Any ϕK^+ state narrower than 100 MeV in this mass range would have to be exotic. While we investigate such a possibility later on, in this section we are testing if the data can be described with conventional hadrons alone. We also limit the resonance poles to be within available phase-space. The fit yields the following results for fit fractions and masses (widths) of the resonances:

1^+ total 36% containing $\mathrm{NR}_{\phi K}$ 79% interfering destructively with two resonances: 1904 ± 27 (507 ± 77) MeV 78% and 1909 ± 10 (139 ± 30) MeV 20%. Two states were allowed since 2^1P_1 and 2^3P_1 states are expected in the analyzed mass range (see Table 4 for

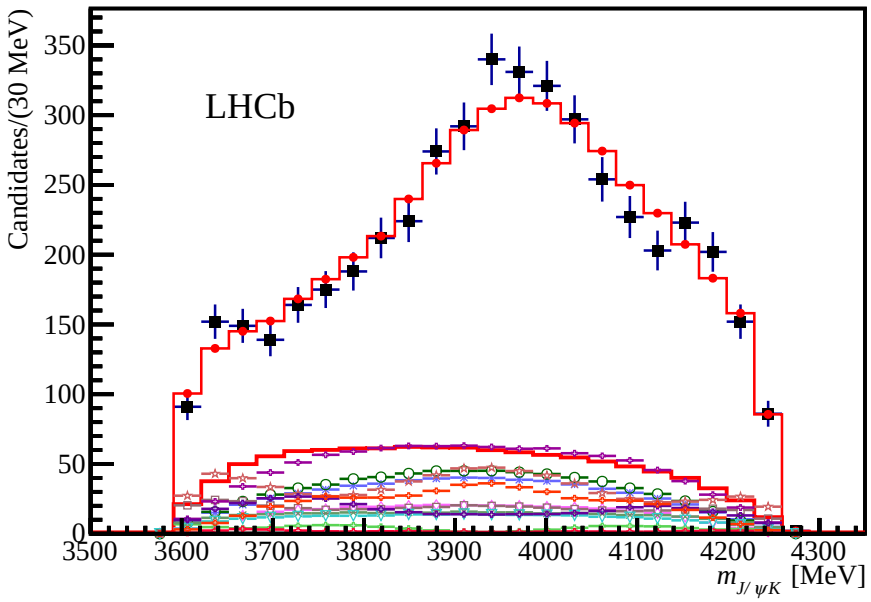

Figure 40: The distribution of $m_{J/\psi K}$ for the data and the fit with the K^{*+} listed in PDG, plus additional states predicted at the higher mass. Masses of the states are fixed to either the PDG or predicted values. The widths are fixed to the PDG values or left free for the predicted states.

the mass predictions).

2^- total 20% with two resonances: 1742 ± 13 (123 ± 32) MeV 4.2% 2182 ± 7 (652 ± 114) MeV 16%. Two states were allowed because of the two well established $K_2(1770)^+$ and $K_2(1820)^+$ states and 1^1D_2, 1^3D_2 expectations. The narrower state returned by the fit is consistent with $K_2(1770)^+$, while the second one is not, but in principle, could be due to 2^1D_2, 2^3D_2 states.

3^+ total 15% with a very broad 2151 ± 45 (1000 ± 1593) MeV resonance (the width reaches the upper limit and is poorly defined). Such large fit fraction is implausible for the state which requires $L = 3$ to be produced in B^+ decay, especially in the part of phase-space with no Q available. The mass is in the expected 1^1F_3, 1^3F_3 range. Allowing two states produces also an implausible result, in which each state has a $\sim$4000% F.F., but the states nearly cancel each other to contribute 17% in total.

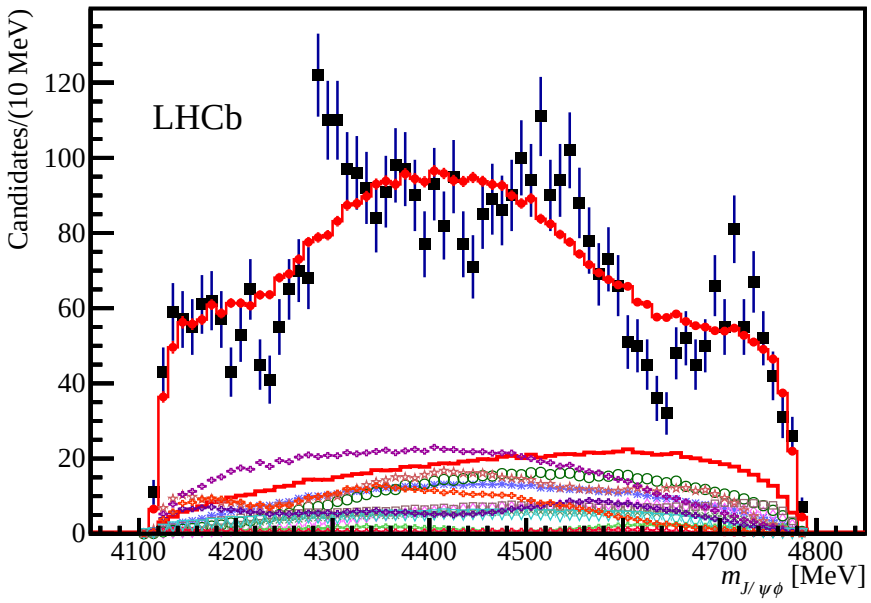

Figure 41: The distribution of $m_{J/\psi\phi}$ for the data and the fit with the K^{*+} listed in PDG, plus additional states predicted at the higher mass. Masses of the states are fixed to either the PDG or predicted values. The widths are fixed to the PDG values or left free for the predicted states.

1^- total 15% with two resonances: 1816 ± 45 (693.7 ± 179) MeV 24% (close to the well established $K^*(1680)^+$ state and 1^3D_1 expectations) and 1999 ± 17 (166 ± 37) MeV 10% (consistent with 3^3S_1 expectations).

0^- total 9.1% with only one resonance 1791 ± 23 (364 ± 78) MeV, which is consistent with not well established $K(1830)^+$ and 3^1S_0 expectations;

2^+ total 1.7% with two resonances: 1822 ± 28 (217 ± 85) MeV 1.7% (possibly 2^3P_2 state and not well established $K_2^*(1980)^+$) and 2095 ± 16 (100 ± 18) MeV 0.5% (possibly 1^3F_2);

3^- total 2.4% with only one resonance 1916 ± 23 (1000 ± 150.6) MeV, which disagrees with the well established $K_3^*(1780)^+$ state;

4^+ total 0.5% with only one resonance 2182 ± 19 (259 ± 105) MeV, close to the well

established $K_4^*(2045)$ state.

This model describes the $m_{\phi K}$ (Fig. 42 $p_{1\mathrm{D}} = 42\%$) and $m_{J/\psi K}$ (Fig. 43 $p_{1\mathrm{D}} = 71\%$) distributions very well, but still fails miserably to describe $m_{J/\psi\phi}$ (Fig. 44 $p_{1\mathrm{D}} = 1 \cdot 10^{-5}\%$). Since the model does not describe the data, we do not expect fit components to behave in a defensible way. In fact, several components don't. Excluding them makes the fit qualities even worse. Adding more components fails to produce a defensible K^* resonant composition and does not cure the very poor fit qualities in the $m_{J/\psi\phi}$ distribution.

We therefore conclude that the data cannot be described by amplitude models containing only K^{*+} states.

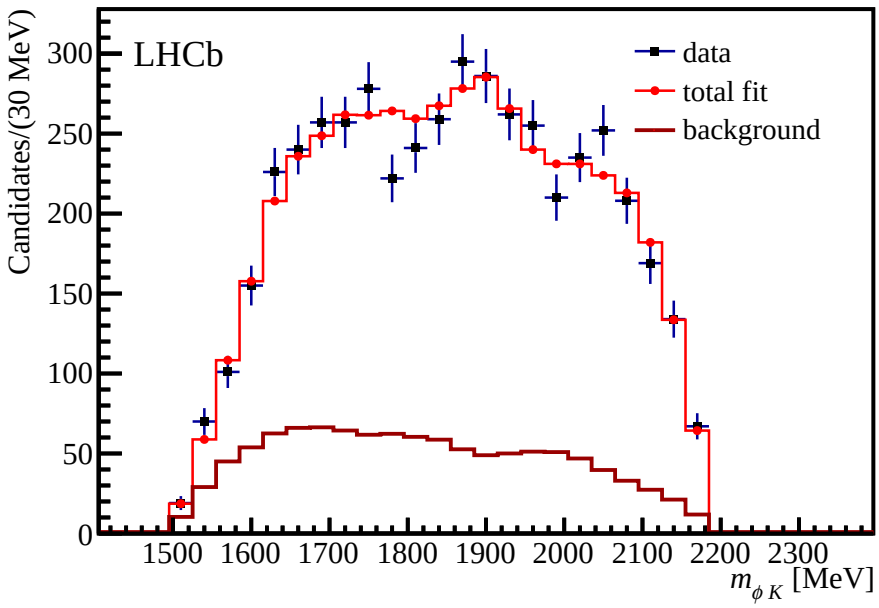

Figure 42: The distribution of $m_{\phi K}$ for the data and the fit with K^* model in which masses and widths were free parameters.

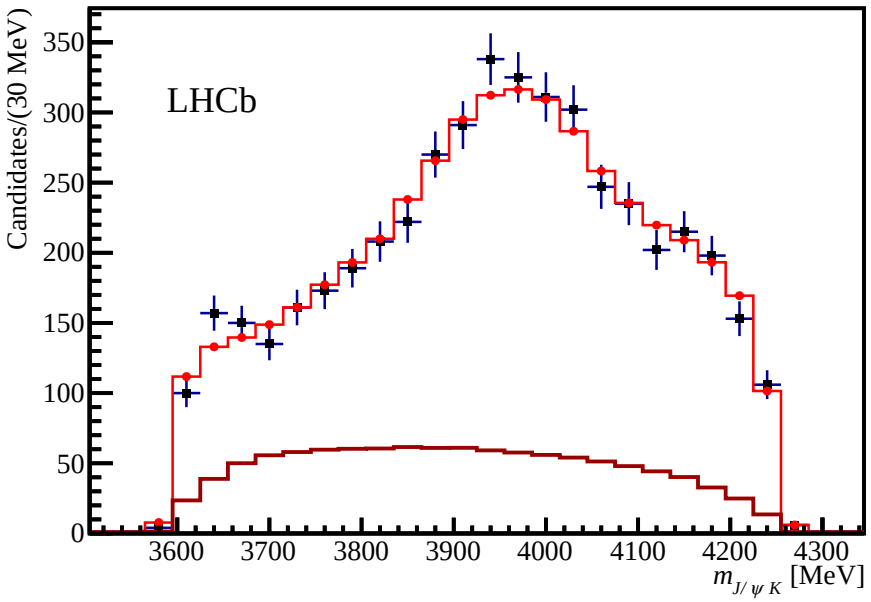

Figure 43: The distribution of $m_{J/\psi K}$ for the data and the fit with K^* model in which masses and widths were free parameters.

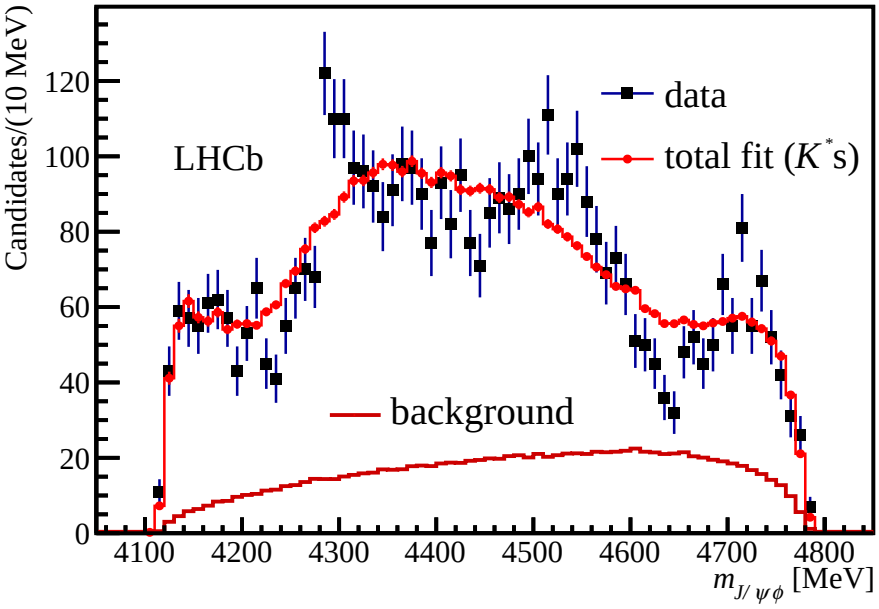

Figure 44: The distribution of $m_{J/\psi\phi}$ for the data and the fit with K^* model in which masses and widths were free parameters.

8 Default amplitude model

To obtain good quality fits to the data we found it necessary to include exotic $X \to J/\psi\,\phi$ contributions in the amplitude model. We have been guided by the $J/\psi\,\phi$ mass structures seen in the data but missed by the K^* model fits discussed in the previous section. Different number of X states with various quantum number combinations have been tried. The best description of the data is obtained with two $J^P = 1^+$ resonances, which we label $X(4140)$ and $X(4274)$, followed by two 0^+ states, labeled $X(4500)$ and $X(4700)$. The minimal angular momenta in the production and decay of X 0^+ contributions are zero. A non-resonant $J/\psi\,\phi$ 0^+ contribution is also needed and included with free helicity couplings, ${B_{0,0}}^{X\to J/\psi\,\phi\,\mathrm{NR}_{J/\psi\,\phi}}$ (*i.e.* $\mathcal{A}_{\mathrm{NR}_{J/\psi\,\phi}}$) and ${B_{2,2}}^{X\to J/\psi\,\phi\,\mathrm{NR}_{J/\psi\,\phi}}$. We retain only significant K^{*+} contributions in the default amplitude model. Fit results for the default model are of interest not only for the parameters of the X states, but also for the parameters of the ϕK^+ contributions.

The significance of a contribution in the amplitude model which has a fixed mass shape can be calculated using Wilks theorem, according to which a change in the log-likelihood value, $\Delta(-2\ln\mathcal{L})$, when a spurious contribution is added to the model follows the $\chi^2(\mathrm{ndf})$ distribution, with the number of degrees of freedom ndf equal to the number of free parameters added to the fit (Δn_{par}). From the actual $\Delta(-2\ln\mathcal{L})$ value on the data, a p–value of the hypothesis that the contribution is spurious can be calculated. We turn the p–value into equivalent number of standard deviations in the Gaussian distribution[16] n_σ. In our default model, only the non-resonant contributions have a fixed mass shape. Wilks theorem is not satisfied when mass and width of resonant contribution are free parameters of the fit. When naively used, it sets an upper limit on the significance. Statistical simulations are needed, and were performed on some selected states, to obtain probability density of $\Delta(-2\ln\mathcal{L})$. Such simulations performed for the similar amplitude

[16] Using the ROOT program, $n_\sigma = \sqrt{2}\,$`TMath :: ErfcInverse ( TMath :: Prob(`$\Delta(-2\ln\mathcal{L})$`, ndf) )`.

analysis concerned with $Z(4430)^+$ yielded $\Delta(-2\ln\mathcal{L})$ distribution which was well described with χ^2(ndf) distribution with ndf approximately equal twice $\Delta n_{\rm par}$ [49]. For important contributions, like the X resonances, explicit statistical simulations have been performed and are discussed in Appendix 8.14. These simulations show that effective ndf to be used varies from $1.2\Delta n_{\rm par}$ to $1.7\Delta n_{\rm par}$. Nevertheless, we use a conservative approach and use $2.0\Delta n_{\rm par}$ whenever mass and width of a resonance are free fit parameters.

The significance of contributions included in the default model are shown in Table 5, together with their fit fractions, masses, and widths if appropriate. The significances of additional contributions which have been investigated but excluded from the default amplitude model are in Table 6. As previously discussed, the narrowest known K^{*+} state above the kinematic limit for the ϕK^+ decay has a width of 159 ± 21 MeV (see Table 4). Therefore, we set a lower limit of 100 MeV on all the widths of K^{*+} resonances. This makes it less likely that fit will tune a small contribution to a local statistical fluctuation. A number of fits have reached these limits. On the other hand, if exotic tetraquark or molecular states decaying to ϕK^+ existed, their decay dynamics could be different than of excited kaons. Therefore, we also investigate fits in which the width is allowed to vary down to 10 MeV. We also cap the width to be smaller than 1000 MeV. To prevent resonances running away from the fitted range, we limit their pole masses to be in the visible phase-space range ($1513 - 2182$ MeV). Different resonant K^{*+} components are initially labeled as $K^{(*)}(J^P)$ for the first state in the given J^P wave, $K^{(*)'}(J^P)$ for the second etc., to stress that since their masses and widths are completely unconstrained they do not necessarily represent any previously observed or predicted states. However, if the mass comes close to the predicted value of a kaon excitation, we list the mass predicted by Godfrey-Isgur below the fit result. If there is a K^* state matching our observation listed in the PDG we also include its mass and width below the fitted values for a comparison.

All invariant mass distributions are reasonably well described by the default fit as

shown in Fig. 46 for $m_{J/\psi\phi}$ ($\chi^2_{\rm 1D}/({\rm N_{bin}}-1) = 71.5/67$, $p_{\rm 1D} = 33\%$), Fig. 45 for $m_{\phi K}$ ($\chi^2_{\rm 1D}/({\rm N_{bin}}-1) = 37.9/22$, $p_{\rm 1D} = 2\%$) and Fig. 47 for $m_{J/\psi K}$ ($\chi^2_{\rm 1D}/({\rm N_{bin}}-1) = 21.1/23$, $p_{\rm 1D} = 58\%$). The $p_{\rm 1D}$ probabilities neglect the effect of free parameters in the fit on the χ^2 values. When properly calibrated with the statistical simulations, these probabilities (P_{χ^2}) are 22%, 0.6% and 39% - see a more detailed discussion in Appendix 8.13.

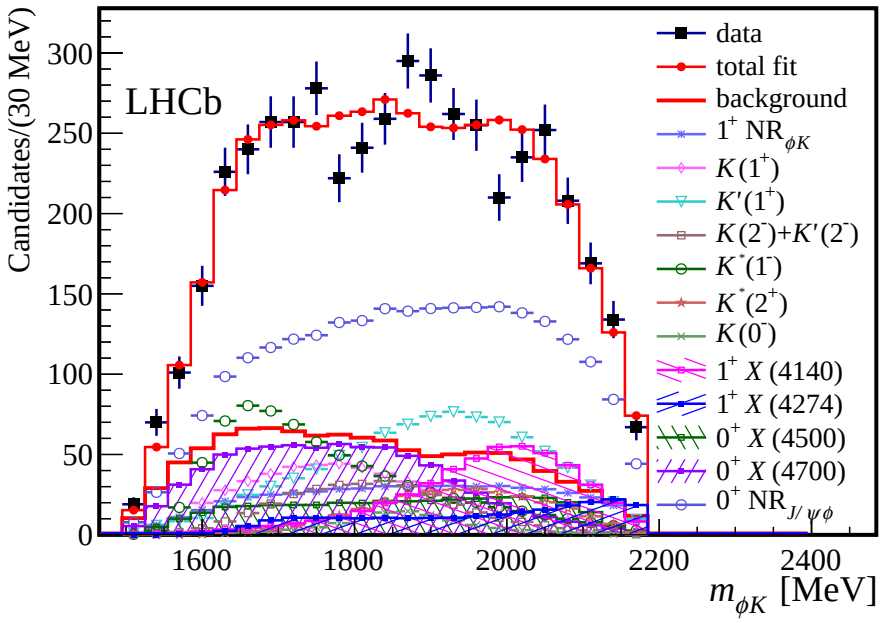

Figure 45: The invariant mass of ϕK with the data in black and the total fit in red.

In following subsections we discuss each partial wave (defined in this note by a J^P value) included in the default amplitude model along with a plot of the contribution(s) made by that specific partial wave to the overall default model. We also discuss partial waves not included in the default fit.

Since for partial waves with many interfering components, a total contribution is better determined than individual ones, we show fit displays with only total partial waves outlined in Figs. 48, 49 and 50.

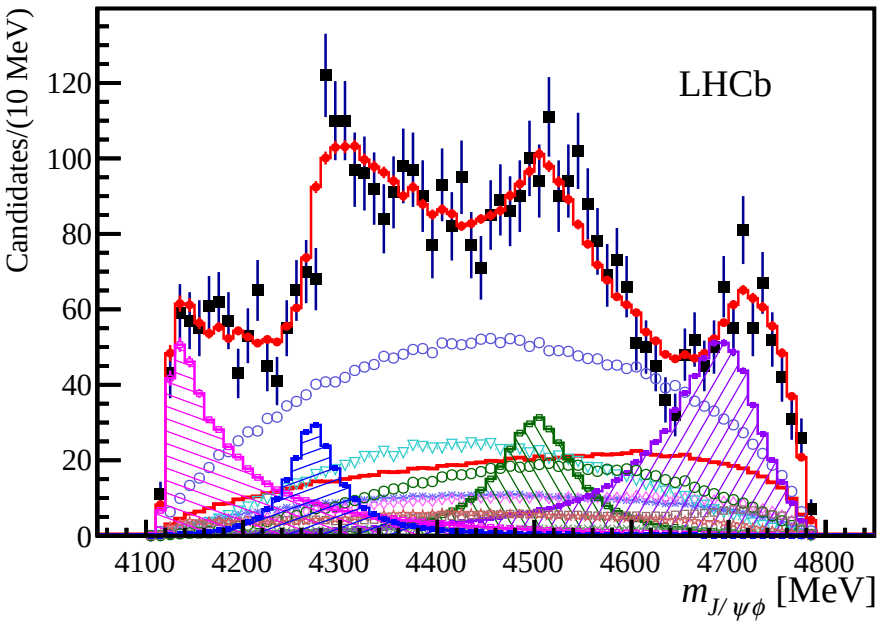

Figure 46: The invariant mass of $J/\psi\,\phi$ with the data in black and the total fit in red. See the legend in Fig. 45 for a description of all shown components.

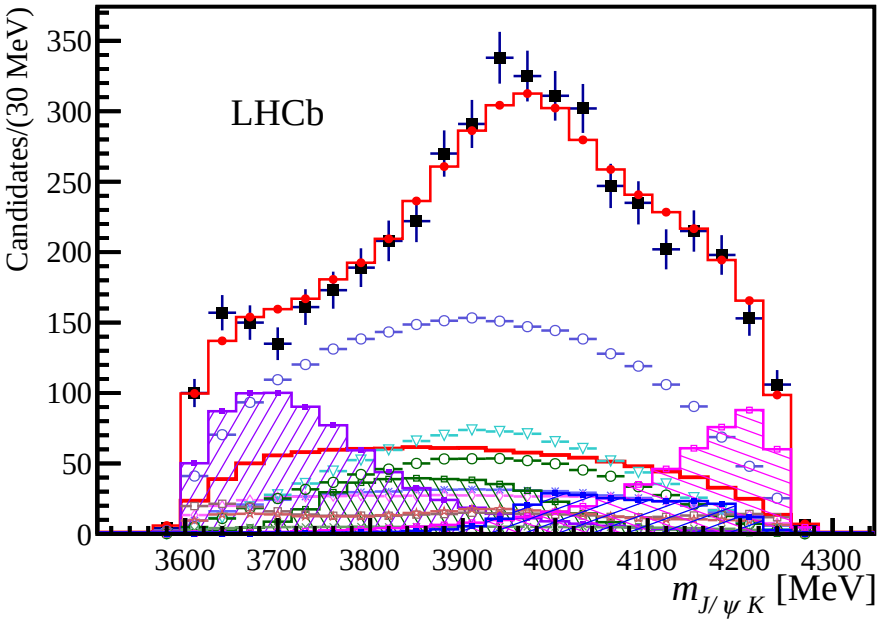

Figure 47: The invariant mass of $J/\psi\,K$ with the data in black and the total fit in red. See the legend in Fig. 45 for a description of all shown components.

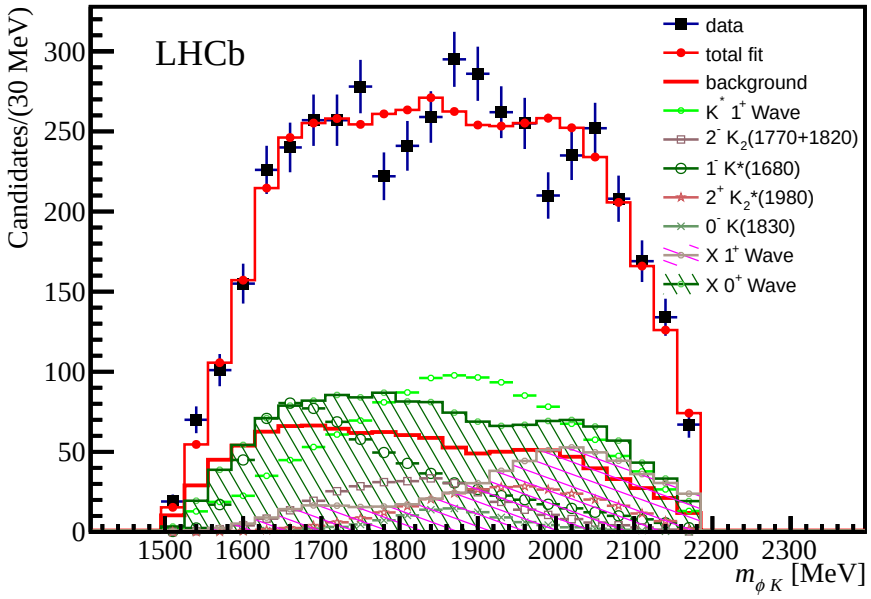

Figure 48: The invariant mass of ϕK with the data in black and the total fit in red. Combined effect of all contributions of the same J^P value are also shown. The individual contributions are shown in Fig. 45.

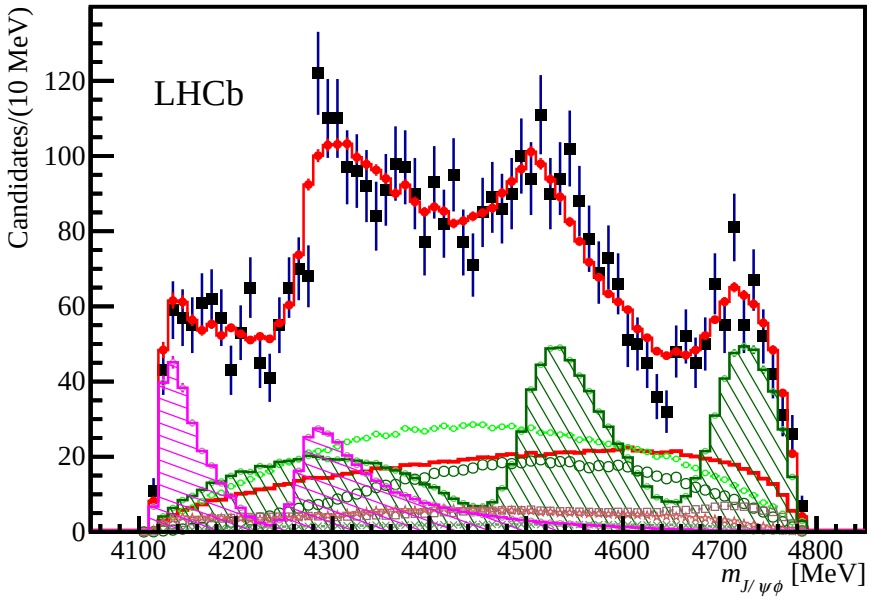

Figure 49: The invariant mass of $J/\psi\,\phi$ with the data in black and the total fit in red. Combined effect of all contributions of the same J^P value are also shown. See the legend in Fig. 48 for a description of all shown components. The individual contributions are shown in Fig. 46.

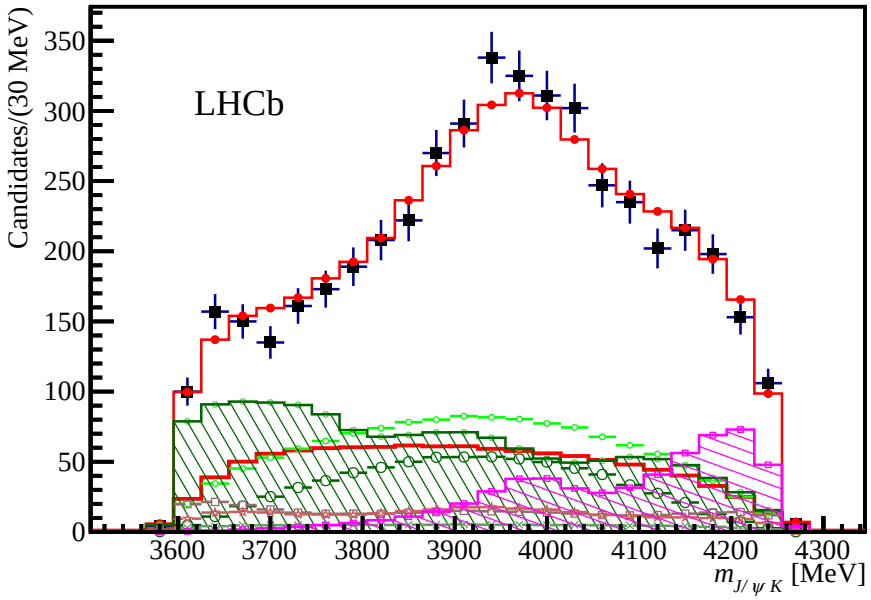

Figure 50: The invariant mass of $J/\psi K$ with the data in black and the total fit in red. Combined effect of all contributions of the same J^P value are also shown. See the legend in Fig. 48 for a description of all shown components. The individual contributions are shown in Fig. 47.

Table 5: The results for significances, fit fractions, masses, and widths (statistical errors only) of the components included in the default amplitude model. Possible interpretations in terms of kaon excitation levels are given, together with the masses predicted by Godfrey-Isgur model [38] (italic font). Possible interpretations in terms of the previously experimentally observed K^* state listed in PDF are also given (italic font). For the $X(4140)$ and $X(4274)$ states we compare our results to the averages over the other experimental determinations compiled in Tables 1-2. Well established states have the particle label in bold font.

Contribution	J^P	n_σ with ndf =		Fit results		
		$\Delta n_{\rm par}$	$2\Delta n_{\rm par}$	M_0 MeV	Γ_0 MeV	F.F. %
Included in the default amplitude model						
all $K(1^+)$	1^+	12.0σ	8.0σ			**41.7 ± 8.1**
$\mathrm{NR}_{\phi K}$						15.9 ± 13.1
$K(1^+)$		8.9σ	7.6σ	1793 ± 59	365 ± 157	11.7 ± 10.3
2^1P_1				*1900*		
$K^{'}(1^+)$		3.4σ	1.9σ	1968 ± 65	396 ± 170	23.4 ± 20.4
2^3P_1				*1930*		
all $K(2^-)$	2^-	7.6σ	5.6σ			**10.8 ± 2.8**
$K(2^-)$		6.4σ	5.0σ	1777 ± 35	217 ± 116	14.2 ± 10.9
1^1D_2				*1780*		
PDG $\mathbf{K_2(1770)}$				*1773 ± 8*	*188 ± 14*	
$K^{'}(2^-)$		4.5σ	3.0σ	1853 ± 27	167 ± 58	11.8 ± 11.2
1^3D_2				*1810*		
PDG $\mathbf{K_2(1820)}$				*1816 ± 13*	*276 ± 35*	
$K^*(1^-)$	1^-	9.5σ	8.5σ	1722 ± 20	354 ± 75	**6.7 ± 1.9**
1^3D_1				*1780*		
PDG $\mathbf{K^*(1680)}$				*1717 ± 27*	*322 ± 110*	
$K^*(2^+)$	2^+	6.6σ	5.4σ	2073 ± 94	678 ± 311	**2.9 ± 0.9**
2^3P_2				*1940*		
PDG $K_2^*(1980)$				*1973 ± 26*	*373 ± 69*	
$K(0^-)$	0^-	4.3σ	3.5σ	1874 ± 43	168 ± 90	**2.6 ± 1.2**
3^1S_0				*2020*		
PDG $K(1830)$				$\sim$ *1830*	$\sim$ *250*	
All $X(1^+)$	1^+					**16.0 ± 2.8**
$\mathbf{X(4140)}$		10.6σ	9.5σ	4146.5 ± 4.5	82.8 ± 20.7	13.0 ± 3.2
Other exp. Tab. 1				*4146.9 ± 2.3*	*17.8 ± 6.8*	
$X(4274)$		7.9σ	6.8σ	4273.3 ± 8.3	56.2 ± 10.9	7.1 ± 2.5
Other exp. Tab. 2				*4293.0 ± 20.0*	*35.0 ± 16.0*	
All $X(0^+)$	0^+					**27.6 ± 5.1**
$X(4500)$		7.7σ	6.8σ	4506.1 ± 11.1	91.9 ± 21.1	6.6 ± 2.4
$X(4700)$		7.1σ	6.1σ	4704.2 ± 10.1	119.7 ± 30.7	12.4 ± 4.9
$\mathrm{NR}_{J/\psi\phi}$		6.4σ				46.2 ± 10.7

Table 6: The results for significances, fit fractions, masses and widths (statistical errors only) of the components tried as additions to the default amplitude model. The widths were limits in the fits to be between 100 and 1000 MeV. When the lower limit was reached, we also show a fit without this limit. Possible interpretations in terms of kaon excitation levels are given, together with the masses predicted by Godfrey-Isgur model [38] (italic font). Possible interpretations in terms of the previously experimentally observed K^* state listed in PDF are also given (italic font). Well established states have the particle label in bold font.

Contribution	J^P	n_σ with ndf =		Fit results		
		$\Delta n_{\rm par}$	$2\Delta n_{\rm par}$	M_0 MeV	Γ_0 MeV	F.F. %
Not included in the default amplitude model						
$K''(2^-)$	2^-	0.8σ	0.1σ	2143 ± 22	100 ± 74	1.5
		1.3σ	0.2σ	2013 ± 17	94 ± 42	1.5
2^1D_2				*2230*		
$K'''(2^-)$	2^-	1.2σ	0.2σ			
2^3D_2				*2260*		
$K^{*'}(1^-)$	1^-	2.8σ	1.4σ	1872 ± 15	100 ± 7	1.0
		3.9σ	2.6σ	1853 ± 5	33 ± 11	1.0
3^3S_1				*2110*		
$K^{*''}(1^-)$	1^-	0.1σ	0.0σ			
2^3D_1				*2250*		
$\mathbf{K^*(1410)}$	1^-	1.2σ	0.3σ	*1414* fixed	*232* fixed	1.6
2^3S_1				*1580*		
$K^{*'}(2^+)$	2^+	2.1σ	0.7σ	1967 ± 14	100 ± 62	4.2
		2.2σ	0.9σ	1969 ± 4	20 ± 15	1.0
1^3F_2				*2150*		
$K'(0^-)$	0^-	0.9σ	0.2σ	1960 ± 41	424 ± 138	
4^1S_0						
$K(3^+)$	3^+	3.3σ	1.7σ	1931 ± 15	100 ± 38	2.0
		3.3σ	1.8σ	1929 ± 17	91 ± 37	2.0
1^1F_3				*2120*		
$K'(3^+)$	3^+	1.5σ	0.3σ			
1^3F_3				*2150*		
$\mathbf{K_3^*(1780)}$	3^-	2.0σ		*1776* fixed	*159* fixed	0.5
$K^*(3^-)$	3^-	4.8σ	3.5σ	1804 ± 20	1000 ± 705	0.7
1^3D_3				*1790*		
$\mathbf{K_4^*(2045)}$	4^+	0.6σ		*2045* fixed	*198* fixed	0.1
$K^*(4^+)$	4^+	3.3σ	1.9σ	1888 ± 8	100 ± 48	0.9
		3.3σ	2.0σ	1869 ± 6	56 ± 20	0.8
1^3F_4				*2110*		

8.1 ϕK^+ 1^+ partial wave

Table 7: Mass projection of the ϕK^+ 1^+ partial wave and contributions

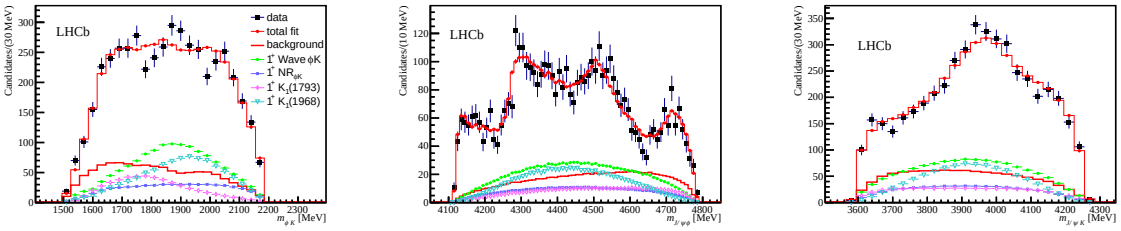

The most intense K^{*+} wave is $J^P = 1^+$ 7, (42% total fit fraction), which is perhaps not surprising since no angular momentum is needed to produce such states in $B^+ \to J/\psi\, K^{*+}$ decay or to decay them to ϕK^+. We represent them by a non-resonant contribution (16%), interfering with two wide resonances (12% and 23%). The incoherent sum of their fit fractions is 21% larger relative to the coherent fit fraction, implying only a modest amount of negative interference between them. The significance of the total 1^+ K^{*+} contribution is $8 - 12\sigma$. We do not quote significance of the $\mathrm{NR}_{\phi K}$ contribution alone, since when it is removed from the model, the higher mass 1^+ resonance becomes unphysically broad (958 ± 507 MeV), becoming effectively non-resonant in nature. The significance of the first 1^+ state added to the amplitude, $7.6 - 8.9\sigma$, is determined from the $\Delta(-2\ln\mathcal{L})$ value between the fits with the $\mathrm{NR}_{\phi K}$ contribution only and with just one 1^+ resonance added (its fitted mass and width in this case are 1898 ± 14 MeV and 349 ± 34 MeV, respectively). The significance of the second 1^+ state added, $1.9 - 3.4\sigma$, comes from the $\Delta(-2\ln\mathcal{L})$ value between the fits with one and two 1^+ resonances. Even though the second state has borderline significance, we retain it in the default model since both resonances have large fit fractions and because the quark model predicts two closely spaced 1^+ states, 2^1P_1 and 2^3P_1. The observed masses, 1793 ± 59 MeV and 1968 ± 65 MeV, are in the right region for this interpretation. Their splitting, 175 ± 92 MeV is 1.5σ larger than the predicted one by Godfrey-Isgur, 30 MeV. However, this model also predicted a small hyperfine splitting

of the $1P_1$ states, 40 MeV, whereas the observed splitting is 131 ± 10 MeV (see Table 4).

The 1^+ states claimed in this analysis appear in the mass range where the $K^-p \to \phi K^-p$ scattering experiment found evidence for a 1^+ state with $M_0 \sim 1840$ MeV, $\Gamma_0 \sim 250$ MeV [41] (Fig. 36), also seen in the $K^-p \to K^-\pi^+\pi^-p$ scattering data [45]. They are inconsistent with the unconfirmed $K_1(1650)$ state listed in PDG, based on the single evidence from the $K^-p \to \phi K^-p$ scattering experiment [44]. See Sec. 7.2 for a review of these measurements.

Since already the second 1^+ state added to the amplitude has a border-line significance, we have not tried to add a third one. In the systematic studies we performed, we removed the second state to study the effect on the other fit components.

8.2 ϕK^+ 2^- partial wave

Table 8: Mass projection of the ϕK^+ 2^- partial wave

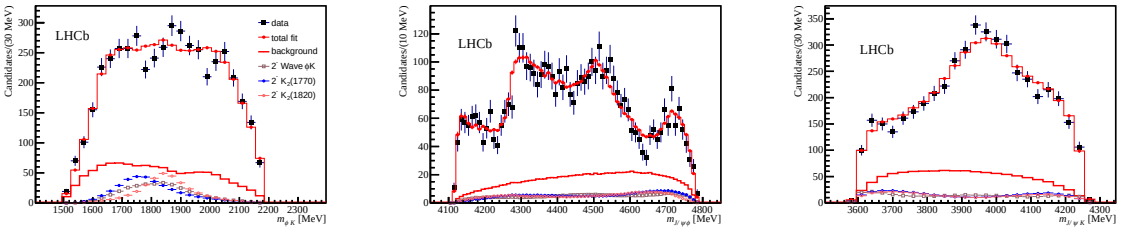

The second most intense wave among ϕK^+ contributions is 2^- 8. It requires at least one unit of orbital angular momentum in the production from B^+ decay and one in its own decay.

The significance of the first resonance deployed in this wave (from the $\Delta(-2\ln\mathcal{L})$ value for the fits with one and no 2^- state) is $5.0 - 6.4\sigma$. With only one state in this wave, its mass is 1889 ± 27 MeV, width 376 ± 94 MeV, and fit fraction 6.8%. This is close to the mass of 1^3D_2 state predicted by Godfrey-Isgur, 1810 MeV, and $K_2^*(1820)$ state considered established by PDG with mass 1816 ± 13 and width 276 ± 35 MeV, in the other

decay modes. The analysis of $K^- p \to \phi K^- p$ scattering data provided a strong evidence for a 2^- resonant state at ~ 1840 MeV and width ~ 250 MeV [41] (Fig. 36). Also the $K^+ p \to \phi K^+ p$ scattering data supported such state with mass 1810 ± 20 MeV, but much narrower width, 140 ± 40 MeV [44] (Fig. 37).

Since experimentally, there is a second well established 2^- state, $K_2(1770)$ (mass 1776 ± 7 MeV, width 186 ± 14 MeV) matching theoretical expectations that there should also be 2^1D_2 state at 1780 MeV, we also try a fit with two resonances in this wave. The significance of the second resonance is $3.0 - 4.5\sigma$. Both resonances acquire similar fit fractions, 14.2% and 11.8%, but with rather strong negative interference pattern, thus together they contribute 10.8%. The statistical simulations discussed in Appendix 8.13 show that the fit results for the individual fit fractions of these states are expected to be very unstable and therefore cannot be trusted. Only the combined fit fraction should be considered to be determined. The mass and width of the lower mass state, 1777 ± 35 MeV and 217 ± 116 MeV are in excellent agreement with the PDG values. The heavier state with mass, 1853 ± 27 MeV, and width, 167 ± 58 MeV, remains very consistent with the $K_2(1820)$ parameters.

The observed mass splitting, 76 ± 51 MeV is consistent within the large error with the value predicted by Godfrey-Isgur, 30 MeV.

Even though the significance of the 2nd state is not overwhelming, we retain it in the default model since two states are very well motivated both theoretically and from the known K^* states.

Additional 2^- states can be present in our data, since the $2D_2$ doublet has masses predicted slightly above the upper mass limit in our data. We have tried adding one or two extra 2^- states to our fits, but their significances were $< 1.2\sigma$ (Table 6).

Table 9: Mass projection of the ϕK^+ 1^- partial wave

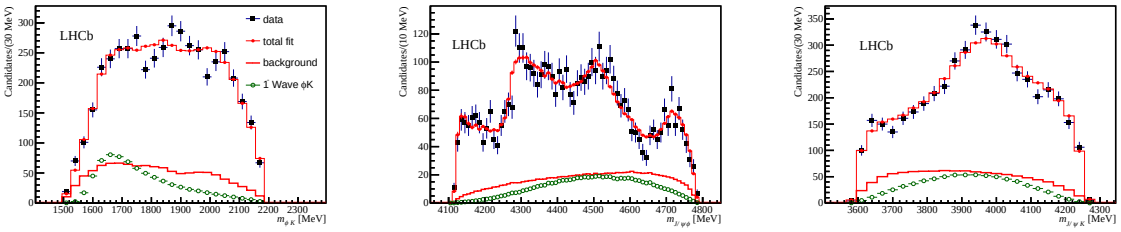

8.3 ϕK^+ 1^- partial wave

The third most intense ϕK^+ wave in our data is 1^- 9, which does not require orbital angular momentum in B^+ decay, but at least one in its own decay.

The significance of the first state in this wave is overwhelming ($8.5 - 9.5\sigma$). Its fit fraction is 6.7%. The dominant two partial waves have unnatural spin-parity, while this combination is natural. Production of both with large intensity is not surprising given that B^+ decays weakly. This is unlike in the scattering experiment which have strong production mechanisms giving preference to one of the $P(-1)^J$ combinations.

The fitted mass and width, 1722 ± 20 MeV and 354 ± 75 MeV, are in excellent agreement with the mass and width of the $K^*(1680)$ state, 1717 ± 27 MeV and 322 ± 110 MeV, which is well established in the other decay modes. The mass is close to Godfrey-Isgur prediction for the 1^3D_1 state, 1780 MeV.

The only scattering experiment $K^-p \to \phi\bar{K}^0n$, which had good primary sensitivity to the 1^- ϕK wave, had rather poor statistics (see Sec. 7.2). Even though these unpublished results show some intensity in the $K^*(1680)$ mass range, the intensity peaks at higher mass (~ 1910 MeV), suggestive of production of 3^3S_1 or 2^3D_1 states [48]. The significance of an additional 1^- state added to our model is $1.4 - 2.8\sigma$ at the mass of 1872 ± 15 MeV and the width reaching the lower limit of 100 MeV. When allowing narrower widths, the state gets more significant, $2.6 - 3.9\sigma$. With the width of 33 ± 9 MeV it would necessarily have to be exotic. We do not find any candidates that could make a molecular $(u\bar{s})(s\bar{s})$ state

with such quantum numbers, thus it would have to be a tightly bound tetraquark. When states are allowed to be narrower in the fit, they are more susceptible to overestimation of their significance via the naive use of Wilks's theorem (3.9σ), due to larger impact of the "look elsewhere effect" (more places to find a statistical fluctuation). Even doubling the effective $\Delta n_{\rm par}$, which leads to 2.6σ, may not be enough to correct for this effect. Thus, evidence for this state falls far short for what would be required to claim an exotic meson. We do not include a 2nd 1^- ϕK^+ state in our default model, but we do consider it in the systematic errors.

The preliminary amplitude analysis of 1 fb^{-1} of LHCb data on $B^0 \to J/\psi\, K^+\pi^-$ decays[17] indicated $K^*(1680)$ fit fraction of 0.36%, in agreement with $0.3^{+0.2}_{-0.1}$% from similar analysis by Belle [50]. Using $\mathcal{B}(B^0 \to J/\psi\, K^+\pi^-) = (1.2 \pm 0.6)\, 10^{-3}$ and $\mathcal{B}(B^+ \to J/\psi\, \phi K^+) = (5.2 \pm 1.7)\, 10^{-5}$ [39] and combining this with the 6.7% $K^*(1680)$ fit fraction determined in this analysis, we obtain $\mathcal{B}(K^*(1680) \to K\phi)/\mathcal{B}(K^*(1680) \to K\pi) = 0.53 \pm 0.32$, where the error does not include errors on the fit fractions and is very large because of the large errors on the B branching fractions. This estimate compares very well with the predictions of Kokoski-Isgur, in which this ratio is ranging between 0.36 and 0.67 for the 1^3D_1 state [40].

In the default fit we do not include any states with masses below the kinematic limit for ϕK^+ decay. However, $K^*(1410)^+$ 1^- state has a mass which is $-0.43\Gamma_0$ ($= -1.0\Gamma_0/2.35$) below the threshold and could be contributing via its tail. When added to the fit[18], its contribution is insignificant ($0.3 - 1.2\sigma$), therefore, it is considered only among systematic errors. The other below threshold K^* resonances (see Table 4) are even more units of Γ_0 below the threshold and have not been considered.

[17] Presented by Tomasz Skwarnicki at LHCb Workshop on Multi-body decays of B and D mesons at CBPF, Rio de Janeiro, July 2015, https://indico.cern.ch/event/359085/.

[18] The mass and width were fixed to the world average values [39]. The mass dependence of the width was assumed to be dominated by its dominant decay ($K^*(892)\pi$).

8.4 ϕK^+ 2^+ partial wave

Table 10: Mass projection of the ϕK^+ 2^+ partial wave

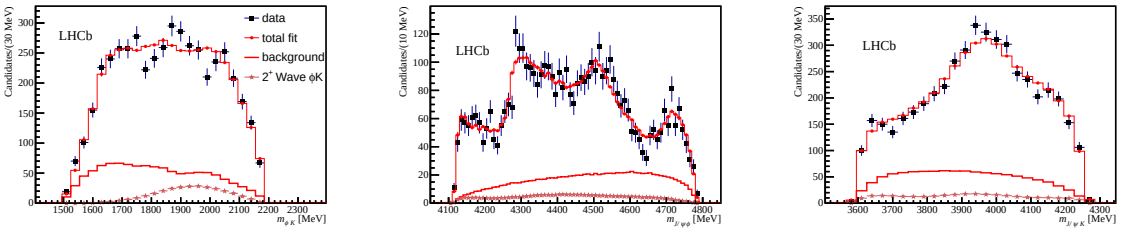

It takes at least one unit of orbital angular momentum in B decays to produce a 2^+ ϕK^+ state, and at least two units to decay it. There is a small, 2.9%, but significant, $5.4-6.6\sigma$ contribution in the 2^+ ϕK^+ wave 10. It peaks at 2073 ± 94 MeV and is very broad, with poorly determined width, 678 ± 311 MeV. Its mass fits Godfrey-Isgur prediction for the mass of the 2^3P_2 state, 1940 MeV, and agrees with the $K_2^*(1980)$ entry in PDG (omitted from the summary tables) based on observations in the other decay modes, listed with a mass of 1973 ± 26 MeV and a width of 373 ± 69 MeV. Our result also agrees well with the $K^-p \to \phi\bar{K}^0 n$ scattering data which showed peaking at 2010 ± 30 MeV with a width of about 400 MeV [48] (Fig. 38).

Allowing a second 2^+ mass, to account for a possibility of 1^3F_2 state, predicted by Godfrey-Isgur at 2150 MeV, results in an insignificant $0.7-2.1\sigma$ peak at 1967 ± 14 MeV. Given its lack of significance, we do not include it in the default model.

8.5 ϕK^+ 0^- partial wave

It takes at least one unit of orbital angular momentum in production of 0^- ϕK^+ state and exactly one to decay it. We find a significant $3.5-4.3\sigma$ state at 1874 ± 43 MeV with a width of 168 ± 90 MeV with a small 2.6% fit fraction 11. This mass is significantly below the mass predicted by Godfrey-Isgur for 3^1S_0 state, 2020 MeV. However, our results agree

Table 11: Mass projection of the ϕK^+ 0^- partial wave

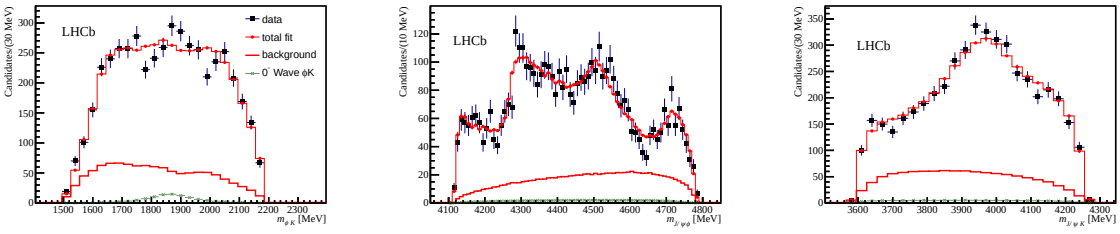

well with the unconfirmed state $K(1830)$ state listed in PDG on the basis of the evidence from $K^-p \to \phi K^-p$ scattering, $M_0 \sim 1830$ MeV and $\Gamma_0 \sim 250$ MeV [41] (Fig. 36).

Even though the mass of a 4^1S_0 kaon excitation has not been predicted, it could come into the mass range covered by our data if its mass would also be shifted down relative to naive expectations. Allowing a second 0^- state in our model gives an insignificant $0.2 - 0.9\sigma$ state at 1960 ± 41 MeV and is not included in our default model.

8.6 ϕK^+ 3^+ partial wave

It takes at least two units of orbital angular momentum in production of 3^+ ϕK^+ state and at least two to decay it, thus suppression of such states is expected. There are two $1F_3$ states predicted by Godfrey-Isgur at 2120 and 2150 MeV. The $K^+p \to \phi K^+p$ scattering data found evidence for significant 3^+ intensity rising with the mass [44] (Fig. 37) in the somewhat questionable analysis (see Sec. 7.2). When allowing one 3^+ resonance in our model, its significance is $1.7 - 3.3\sigma$ at 1931 ± 15 MeV, and the state tries to be narrow reaching the lower limit of 100 MeV we have imposed. The second 3^+ state in the fit is even less significant, $0.3 - 1.5\sigma$.

We do not include 3^+ contributions in our default model but do include the addition of such a state in systematic variation.

8.7 ϕK^+ 3^- partial wave

It takes at least two units of orbital angular momentum to produce a 3^- ϕK^+ state and at least three to decay it, thus, such a contribution is not likely. There is a well established $K_3^*(1780)$ state with mass and width which is likely to be 1^3D_3 state expected at 1790 MeV. This wave has not been probed by the scattering experiments sensitive to ϕK decays. When probing for this state, with the mass and width fixed to the PDG values, its significance in our fits is 2.0σ. When floating mass and width in the fit, it becomes significant $3.5 - 4.8\sigma$ but becomes unphysically broad reaching the upper limit of 1000 MeV we have set. Such essentially non-resonant contribution in the partial wave suppressed by orbital angular momentum barrier is not plausible, thus we do not include it in the default model.

8.8 ϕK^+ 4^+ partial wave

It takes at least three units of orbital angular momentum to produce a 4^+ ϕK^+ state and at least three to decay it. Even though not likely to be produced, we investigate this wave since there is a well established state in other decay modes; the $K_4^*(2045)$ state (likely 1^3F_4 state) with the mass 2045 ± 9 MeV ($\Gamma_0 = 198 \pm 30$ MeV, which is within the range of our data. When allowing it with the mass and width fixed to the PDG values it is only 0.6σ significant. When floating with variable mass and width it is $1.9 - 3.3\sigma$ significant, with the mass significantly below the $K_4^*(2045)$ mass and with the width reaching the lower limit of 100 MeV (56 ± 20 MeV if unlimited). Because of poor motivation for such a contribution, we do not include it in the default model.

This is the highest spin we have investigated in our ϕK^+ model.

Table 12: Mass projection of the $J/\psi\,\phi$ 1^+ partial wave

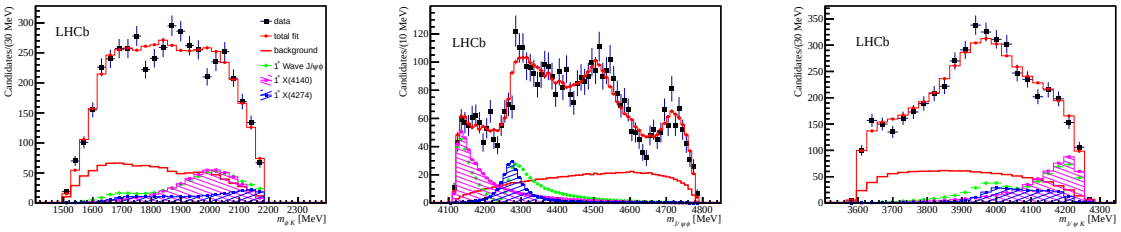

8.9 $J/\psi\,\phi$ 1^+ partial wave

As discussed in Sec. 1 and summarized in Table 1, the $X(4140)$ state first seen by CDF as the narrow $\Gamma_0 = 11.7^{+8.3}_{-5.0} \pm 3.7$ MeV near-threshold resonance [1], with the width later updated to $15.3^{+10.4}_{-6.1} \pm 2.5$ MeV (5σ significant), was confirmed by CMS (5σ), albeit with somewhat larger width of $28^{+15}_{-11} \pm 19$ MeV. Also D0 claimed an observation though with marginal significance. Recently, the D0 collaboration has claimed the observation of $X(4140)$ in prompt production at the Tevatron, both with narrow widths. The average of CDF, CMS, and two D0 measurements gives 4146.9 ± 2.3 MeV mass and 17.8 ± 6.8 MeV width.

The LHCb analysis of 0.37 fb^{-1} of data revealed no narrow resonance at the threshold and an upper limit on the production of $M_0 = 4143.2$ MeV $\Gamma_0 = 15.3$ MeV resonance was set which was at a mild 2.4σ disagreement with the CDF claim.

Our present 3 fb^{-1} data are consistent with the claim that there is no narrow, 15.3 MeV wide, resonance near the threshold. A wide near threshold structure is present with $9.5 - 10.6\sigma$ significance (before the systematics) and 13% fit fraction. It can be described as a Breit-Wigner with the mass 4146.5 ± 4.5 MeV, in astonishing agreement with the average over the previous measurements, but significantly larger width 82.8 ± 20.7 MeV (3σ disagreement without LHCb systematic uncertainties). The most likely J^P alternative is 2^+, which can be rejected at 7.6σ as discussed in Sec. 10. This is the first determination of quantum numbers of this state, which is of crucial importance for its

theoretical interpretation.

CDF observed 3.1σ evidence for the second $X(4274)$ state with a mass of $4274.4^{+8.4}_{-6.7}\pm1.9$ MeV and width of $32.3^{+21.9}_{-15.3}\pm7.6$ MeV. The early LHCb data showed peaking around 4300 MeV, but this structure was not analyzed. CMS observed a second peak at a mass $4313.8\pm5.3\pm7.3$ MeV ($\Gamma_0 = 38^{+30}_{-15}\pm16$ MeV) which was at 3.2σ disagreement in mass with the CDF. The CMS did not evaluate significance of this peak. These results are compiled in Table 2.

Our data requires a second 1^+ resonance at $6.8-7.9\sigma$ significance and 7.1% fit fraction, with a mass of 4273.3 ± 8.3 MeV, which is in a very good agreement with the CDF value. That agreement may be misleading since the data and the total fit intensities peak at higher mass, which is caused by the interference with the other contributions. Had we done a simple-minded 1D mass fits again, the result would have been higher and fallen in between the CDF and CMS values. It is entirely possible that the disagreement between the CDF and CMS, and between CDF and 2011 LHCb analysis, is due to different acceptance regions picking a different interference pattern of this state with the other contributions. This underscores the importance of performing a full amplitude analysis. The determined width is 56.2 ± 10.9 MeV in statistical agreement with the average between CDF and CMS values, 35 ± 16 MeV. The most likely J^P alternative is 1^-, which can be rejected at 6.4σ as discussed in Sec. 10. This is the first determination of quantum numbers of this state.

The combined fit fraction of the two 1^+ resonances is 16.0%, thus a negative interference between them decreases the total fit fraction by a modest 26% of its value.

8.10 $J/\psi\phi$ 0^+ partial wave

The 0^+ $J/\psi\phi$ partial wave is the easiest to produce in $B^+\to XK^+$, $X\to J/\psi\phi$ decays since no orbital angular momentum is needed in either the first or the second decay (one unit of angular momentum is needed to produce the 1^+ partial wave). For that reason, we

Table 13: Mass projection of the $J/\psi\,\phi$ 0^+ partial wave

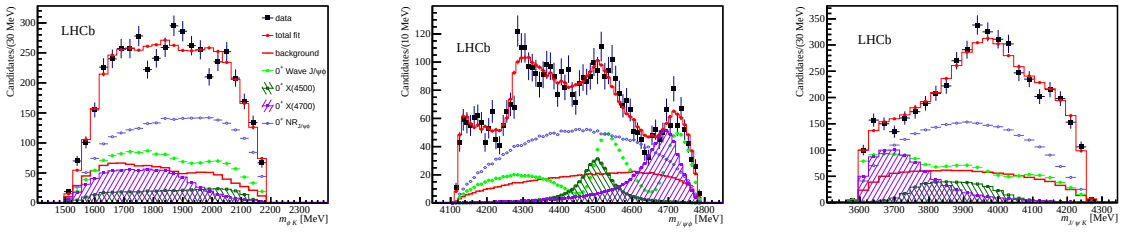

allowed a non-resonant contribution in this wave.

The high $J/\psi\,\phi$ mass region contains perhaps the strongest visible mass structure in our data, with a deep minimum around 4650 MeV surrounded by peaking structures on both sides. The high intensity on the high mass side is remarkable, since this region is kinematically suppressed by the decreasing phase-space function when approaching the upper limit on this mass. This is similar to the surprisingly large intensity near the lower limit on the $J/\psi\,\phi$ mass, where $X(4140)$ resides. The best description of the high mass region is obtained by two 0^+ resonances interfering with each other and the non-resonant contribution. We label them by their approximate masses, $X(4500)$ and $X(4700)$. Their masses and widths are given in Table 5. CDF, CMS and D0 did not inspect this mass range. Belle and BaBar did not have meaningful statistics. Thus, there are presently no other measurements to compare to.

All three 0^+ contributions are significant on their own: $X(4500)$ $6.8-7.7\sigma$ (6.6% fit fraction), $X(4700)$ $6.1-7.1\sigma$ (12.4% fit fraction) and $\mathrm{NR}_{J/\psi\,\phi}$ 6.4σ (46.2% fit fraction). The large $\mathrm{NR}_{J/\psi\,\phi}$ intensity is misleading since there are strong negative interferences of this contribution with the 0^+ resonances, bringing the total 0^+ fit fraction down to 27.6%. The most likely J^P alternative for both of these states is 1^+ which can be rejected at 5.2σ and 4.9σ level (Sec. 10), respectively.

We have also considered a contribution from virtual B^{*0}_{s0} in this partial wave, $B^+ \to K^+ B^{*0}_{s0}$, $B^{*0}_{s0} \to J/\psi\,\phi$. Since the B^{*0}_{s0} state has not been experimentally observed and could

be broad we allowed it in the fit with free mass and width. The mass was limited to $5415 - 5830$ MeV range. The lower limit corresponds to the B_s^* mass. Its initial value was set to 5620 MeV. The fitted mass reached the lower limit, 5415 ± 91 MeV with a width of 256 ± 78 MeV. The $\Delta(-2\ln\mathcal{L})$ improved by only 3.0, which is completely insignificant for 6 free parameters added to the fit ($0.1 - 0.2\sigma$). Such above the kinematic limit resonance contributes a smooth tail to the $m_{J/\psi\,\phi}$ distribution modifying mostly the $\mathrm{NR}_{J/\psi\,\phi}$ contribution. The overall 0^+ fit fraction changes by a modest amount, +3.9%. The fit fraction (masses) of $X(4500)$ and $X(4700)$ change by -0.9% and -1.8% (+0.1 and +3.2 MeV), respectively. The other two states in the $1P$ triplet, $B_{s1}(5830)$ and $B_{s2}(5840)$, have been observed at much higher masses and with small mass splitting. Thus, the fitted B_{s0}^{*0} mass value is unrealistically low. Being only 48 MeV above the B_s^0 mass, such state would also have to be narrow. Therefore, we do not include this fit among the fits used to evaluate systematic errors.

8.11 Multidimensional fit qualities

In addition to the fit quality evaluated for the 1D mass projections discussed previous, we also quantify the fit quality on the Dalitz plane of $m^2_{J/\psi\,\phi}$ vs. $m^2_{\phi K}$ by using adaptive binning procedure. A data bin is split at the median value of a variable, alternating the variables used in the division until bin content is less than 20 entries. Summing up the pulls squared over all bins yields $\chi^2_{\mathrm{2D}}/(\mathrm{N_{bin}} - 1) = 438.7/495$. The pull calculation includes an estimate of the statistical error from the background subtraction.[19] The χ^2 values for unbinned likelihood fit follow $\chi^2(\mathrm{ndf})$ PDF with $\mathrm{N_{bin}} - 1 - n_{\mathrm{par}} \leq \mathrm{ndf} \leq \mathrm{N_{bin}} - 1$, where $n_{\mathrm{par}} = 98$ is the number of free parameters in the fit. This bounds p–value of the hypothesis that the fit describes the data well obtained from the χ^2_{2D} to $7.3\% < p_{\mathrm{2D}} < 97\%$. The statistical

[19] A pull in given bin is calculates as $(N_{\mathrm{data}} - N_{\mathrm{fit}})/\sqrt{N_{\mathrm{data}} + \sigma(N_{\mathrm{fit}})^2 + s_b^2\, N_{sideband}}$, where $\sigma(N_{\mathrm{fit}})$ is the error on re-weighted MC events according to the fit PDF and s_b is the scaling factor from the B^+ mass side-bands to the fit region. The error on the data bin content dominates.

simulations discussed later 8.13 can be used to determine effective ndf value, which leads to $P_{\chi^2_{2D}} \equiv p_{\rm 2D}^{\rm calibrated} = 17\%$. For a comparison, the fit with all known plus predicted K^{*+} resonances discussed in the previous section gives a $\chi^2_{\rm 2D}$ value worse by 7.9^2 in spite of more free parameters in the fit ($n_{\rm par} = 104$).

The $\Delta(-2\ln\mathcal{L})$ values between the default fit and the fit with all known plus predicted K^{*+} resonances and no exotic contributions is 13.9^2.

We also apply the adaptive binning procedure in 6 dimensions using $m^2_{J/\psi\,\phi}$,$m^2_{\phi K}$,$\cos\theta_\Phi{}^X$,$\cos\theta_{J/\psi}{}^X$, $\Delta\phi_{X,J/\psi}$ and $\Delta\phi_{X,\Phi}$. The $\Delta\phi$ variables are folded into $0^0 - 90^0$ range since the data statistics is too small to get meaningful subdivision of these angles.[20] We divide the mass variables twice, divide all angular variables once and attempt to divide the masses squared again, at which point the bin content reaches about 10 entries in each bin and subdivision terminates. The default fit gives $\chi^2_{\rm 6D}/({\rm N_{bin}} - 1) = 462.9/500$ and $2\% < p_{\rm 6D} < 88\%$. The simulations discussed below 8.13 give $P_{\chi^2_{6D}} \equiv p_{\rm 6D}^{\rm calibrated} = 2.3\%$. The fit with the K^* components only gives $\chi^2_{\rm 6D}$ value worse by 5.7^2.

Projections of all pulls obtained with the 2D and 6D binning for the default fit are shown in Figs. 52. When fitting the Gaussian distribution to the pull distributions we obtain mean (rms) values of 0.02 ± 0.04 (0.94 ± 0.03) and 0.02 ± 0.04 (0.96 ± 0.03) for the 2D and 6D pulls, respectively.

Yet another way to illustrate fit quality on the Dalitz plane is to look at the $m_{J/\psi\,\phi}$ and $m_{J/\psi\,K}$ distributions in slices of $m_{\phi K}$ and vice versa. Such distributions are shown in

[20] The folding algorithm is:

$$
\begin{aligned}
&\texttt{if}(\Delta\phi > 0)\{ \\
&\qquad\qquad \texttt{if}(\Delta\phi < 90)\{\texttt{return}\,\Delta\phi;\}\,\texttt{else}\,\{\texttt{return}\,180 - \Delta\phi;\} \\
&\quad \}\,\texttt{else}\,\{ \\
&\qquad\qquad \texttt{if}(\Delta\phi > -90)\{\texttt{return}\,-\Delta\phi;\}\,\texttt{else}\,\{\texttt{return}\,180 + \Delta\phi;\} \\
&\qquad \}
\end{aligned}
\tag{44}
$$

Figs. 56 and 57.

8.12 Searches for Additional X states

Even though the $m_{J/\psi\phi}$ distribution is already well described by the default model, which contains two 1^+ X resonances, two 0^+ X resonances and 0^+ non-resonant contribution, we have considered adding more X states. We have tried all J^P combinations (for $J \leq 2$) seeded in different $m_{J/\psi\phi}$ regions. The highest significance (using ndf $= 2n_{\rm par}$) for each J^P value is listed in Table 14. The 1^+ combination is omitted, since the fitted masses in such fits collapse into the mass of one of the 1^+ states already included in the default model. Since the highest significance is only 2σ, we do not include any additional $J/\psi\phi$ contributions in our default model.

Table 14: Best candidates for a fifth $X \to J/\psi\phi$ state for each J^P combination. Note: $J^P = 1^+$ is omitted due to it collapsing into the other 1^+ X states.

J^P	Largest Significance
0^-	1.3σ
0^+	2.0σ
1^-	1.1σ
2^-	1.0σ
2^+	1.0σ

8.13 Fitter Validation

To validate the fitter code and to calibrate various goodness-of-fit measures we generate pseudo-experiments ("toy" experiments) according to the default amplitude model extracted from the fit to the real data. This includes the background generation in the amplitude fit sample and in the sidebands. Each pseudo-experiment has the same statistics as the real data sample. The detector efficiency is generated according to the parameterization described in Sec. 5.4. The Monte Carlo sample used in the matrix element integration

is also generated according to this parameterization with the same statistics as used in the fit to the real data. Every pseudo-experiment is subject to the same fit procedure as the real data, including forming the background parameterization, thus all statistical effects are included in the simulation. Fit fractions and resonance masses and widths averaged over all pseudo-experiments are shown in Table 15. While the total fit fractions are reasonably well reproduced, individual fit fractions for the strongly overlapping 2^- $K_2(1770)$ and $K_2(1820)$ states have a huge spread beyond the reported fit errors (the latter rely on Gaussian approximation of the likelihood). It is clear that the strong destructive interference between these contributions is the reason for this instability. Therefore, the fit results obtained for these individual fit fraction should not be be taken seriously. Only the total 2^- fit fraction is measurable. In spite of this problem, the masses and widths of these states are well reproduced. This problem also exists to a lesser extent in the 1^+ partial wave. Even though the average fit fractions for $\mathrm{NR}_{\phi K}$, K_1 and K_1' do not agree within the statistical errors of the simulations with the generated values, the deviations are within the assigned systematic errors. The latter must already probe related instability, thus we do not assign additional systematic contribution. Most of masses and widths of the resonances are well reproduced. A few inconsistencies are well within the assigned systematic errors. The RMS values over pseudo-experiments are either in agreement or smaller than the fit errors reported on the real data sample.

The pseudo-experiments can also be used to calibrate various goodness-of-fit measures summarized in Table 16. The value of the $-2\ln\mathcal{L}$ in the data is $(2.0 \pm 0.3)\sigma$ worse than the average value over the pseudo-experiments assuming that its value follows the Gaussian distribution. Since using the likelihood value itself as a goodness-of-fit measure can sometimes lead to a self-fulfilling test, it is also important to look at χ^2 tests. The χ^2 variables are expected to follow the χ^2 distribution with ndf value somewhere in between $\mathrm{N_{bin}} - 1$ and $\mathrm{N_{bin}} - 1 - n_{\mathrm{par}}$ (where $\mathrm{N_{bin}}$ is the number of bins used and n_{par} is the number

of free parameters in the fit) depending how well the data bins used in the χ^2 definition probe the full 6D space of the fitted data. Since the average value in the χ^2 distribution is equal to ndf, the average χ^2 values over the pseudo-experiments determine effective number of degrees of freedom $\mathrm{ndf}^{\mathrm{eff}}$, which we also turn into ${n_{\mathrm{par}}}^{\mathrm{eff}} \equiv \mathrm{N_{bin}} - 1 - \mathrm{ndf}^{\mathrm{eff}}$. The latter should be compared to the actual number of free parameters in the fit, $n_{\mathrm{par}} = 98$. We see that the χ^2_{6D} test using the adaptive binning in 6D described in Sec. 8.11, probes all fit dimensions well since ${n_{\mathrm{par}}}^{\mathrm{eff}}$ comes close to n_{par}. Applying the χ^2 PDF with $\mathrm{ndf} = \mathrm{ndf}^{\mathrm{eff}}$ rounded to the nearest integer gives the χ^2_{6D} value obtained in the data, χ^2_{data}, a probability of $P_{\chi^2} = 2.3\%$[21], which is the same as probability for a $N_\sigma = 2.0\sigma$ deviation in the Gaussian distribution.[22] Thus the likelihood value and the χ^2_{6D} test give similar results. While the 2.3% probability likely indicates some deficiency of our amplitude model, it cannot be ruled out as a statistical fluctuation. In any case, this kind of fit quality is fairly reasonable for fitting the data in their 6D correlations.

The χ^2_{2D} using adaptive binning on the Dalitz plane has also a large ${n_{\mathrm{par}}}^{\mathrm{eff}}$, and gives $P_{\chi^2} = 17\%$ and $N_\sigma = 1.0\sigma$. Therefore, the data are described on the Dalitz plane better than in all dimensions.

The 1D χ^2 variables obtained with the fixed bins for the three mass projections have very low ${n_{\mathrm{par}}}^{\mathrm{eff}}$, which is not surprising. The calibrated P_{χ^2} probabilities are high for $m_{J/\psi\,\phi}$ and $m_{J/\psi K}$, 22% and 39% respectively, and marginal for $m_{\phi K}$, 0.6% ($N_\sigma = 2.5\sigma$). Substantially better fits to $m_{\phi K}$ can be obtained by allowing narrow (< 100 MeV) ϕK^+ states in the model, which would have to be exotic. Since none of them appears to be significant (see Sec. 8 and Table 6) we don't consider this to be a plausible choice. The fit qualities with the default model to the $m_{\phi K}$ distribution become high when further background suppression cuts are applied, $p_{1\mathrm{D}} = 16\%$ for $p_{\mathrm{T}}(K) > 500$ MeV (Fig. 60) and

[21] $P_{\chi^2} = TMath :: Prob(\chi^2_{\mathrm{data}}, \mathrm{ndf}^{\mathrm{eff}})$.

[22] Using double-sided probability: $N_\sigma = \sqrt{2}\,TMath :: ErfcInverse(2\,P_{\chi^2})$ for $P_{\chi^2} < 50\%$, and $N_\sigma = \sqrt{2}\,TMath :: ErfcInverse(2\,(1 - P_{\chi^2}))$ for $P_{\chi^2} > 50\%$.

$p_{1D} = 37\%$ for $DLL_{sig/bkg} < 0.0$ (Fig. 61) vs. $p_{1D} = 2\%$ for the default selection (Fig. 45).[23] Therefore, the most likely explanation for the low P_{χ^2} on $m_{\phi K}$ distribution for the default fit is statistical fluctuation.

8.14 Statistical simulations for significances of selected fit components.

As discussed previously, the significance of a fit components can be estimated from the value of $\Delta(-2\ln\mathcal{L})$ between the default fit and the fit in which a given component is excluded. For components which have a fixed shape, if the component is not present in the data (null hypothesis), the $\Delta(-2\ln\mathcal{L})$ follows the χ^2 probability distribution with ndf $= \Delta n_{\rm par}$, where $\Delta n_{\rm par}$ is the number of free parameters in that component (Wilks theorem). This theorem can be used to translate the $\Delta(-2\ln\mathcal{L})$ value in the data to a probability (p-value) under the null hypothesis. If very small, then the hypothesis can be rejected which is usually described as the significance of the fit component. Since we fit masses and width of the resonances, the look-elsewhere effect is expected to increase the probability for larger $\Delta(-2\ln\mathcal{L})$ values, thus the Wilks theorem sets an upper limit on significance of its contribution. Statistical simulations of pseudo-experiments (see above 8.13) under the null hypothesis can be used to estimate the modified PDF of the $\Delta(-2\ln\mathcal{L})$ distribution. In previous amplitude analyses such distributions were well approximated by a χ^2 probability distribution with effective ndf value (ndf$^{\rm eff}$) [49] which was close to $2\Delta n_{\rm par}$. We have assumed such behavior when estimating significances of fit components in the other sections. Every amplitude analysis may be very different in effective ndf, primarily due to the different structure of free parameters affecting the angular distributions, and because of the different mass ranges where non-existent fit

[23] Since pseudo-experiments were not simulated for the reduced data samples, we use $p_{1D} \equiv P_{\chi^2}(n^{\rm eff}_{\rm par} = 0)$ for this comparison.

Table 15: Fit validation on the default amplitude model.

Quantity	Generated value	Mean over toy exp.	fit error on the data	RMS over toy exp.
1^+ X total FF %	16.0	15.8 ± 0.4	2.8	2.5 ± 0.4
$X(4140)$ M_0 MeV	4146.5	4145.8 ± 0.7	4.5	4.0 ± 0.7
Γ_0 MeV	82.8	78.8 ± 3.7	20.7	22.5 ± 3.7
FF %	13.0	12.6 ± 0.4	3.2	2.5 ± 0.4
$X(4274)$ M_0 MeV	4273.3	4275.0 ± 1.0	8.3	6.4 ± 1.0
Γ_0 MeV	56.2	56.6 ± 1.6	10.9	9.6 ± 1.6
FF %	7.1	7.7 ± 0.3	2.5	2.0 ± 0.3
0^+ X total FF %	27.6	27.4 ± 0.7	5.1	4.2 ± 0.7
$\mathrm{NR}_{J/\psi\phi}$ FF %	46.2	44.3 ± 1.2	10.7	7.7 ± 1.2
$X(4500)$ M_0 MeV	4506.1	4507.7 ± 1.6	11.1	9.8 ± 1.6
Γ_0 MeV	91.9	97.3 ± 3.3	21.2	20.4 ± 3.3
FF %	6.6	7.5 ± 0.3	2.4	1.9 ± 0.3
$X(4700)$ M_0 MeV	4704.2	4704.5 ± 1.5	10.1	9.5 ± 1.5
Γ_0 MeV	119.7	119.4 ± 4.3	30.7	26.7 ± 4.3
FF %	12.4	12.2 ± 0.5	4.9	3.2 ± 0.5
1^+ total FF %	41.7	39.3 ± 0.6	8.1	3.4 ± 0.6
$NRKst$ FF %	15.9	19.1 ± 1.2	13.1	7.6 ± 1.2
K_1 M_0 MeV	1793.3	1799.3 ± 9.1	59.0	56.0 ± 9.1
Γ_0 MeV	364.7	365.3 ± 17.6	157.0	108.5 ± 17.6
FF %	11.7	19.3 ± 2.2	10.3	13.8 ± 2.2
$K_1^{'}$ M_0 MeV	1967.9	1974.2 ± 7.2	65.0	44.2 ± 7.2
Γ_0 MeV	396	358.6 ± 17.4	170.3	107.4 ± 17.4
FF %	23.4	27.4 ± 2.8	20.4	17.5 ± 2.8
2^- total FF %	10.8	11.6 ± 0.3	2.8	1.6 ± 0.3
$K_2(1770)$ M_0 MeV	1777.2	1781.8 ± 4.0	34.9	24.8 ± 4.0
Γ_0 MeV	217.5	209.8 ± 15.6	116.3	96.5 ± 15.6
FF %	14.2	52.2 ± 12.8	11.0	78.9 ± 12.8
$K_2(1820)$ M_0 MeV	1853.4	1856.6 ± 4.9	26.6	30.4 ± 4.9
Γ_0 MeV	167	169.8 ± 10.3	58.1	63.2 ± 10.3
FF %	11.8	48.2 ± 12.0	11.2	74.2 ± 12.0
1^- $K^*(1680)$ M_0 MeV	1721.6	1732.9 ± 3.4	19.9	20.7 ± 3.4
Γ_0 MeV	353.7	388.6 ± 13.8	74.7	84.8 ± 13.8
FF %	6.7	7.4 ± 0.3	1.9	1.8 ± 0.3
2^+ $K_2^*(1980)$ M_0 MeV	2072.5	2039.1 ± 11.8	94.2	72.7 ± 11.8
Γ_0 MeV	677.7	574.0 ± 35.7	310.6	219.8 ± 35.7
FF %	2.9	3.0 ± 0.1	0.8	0.6 ± 0.1
0^- $K(1830)$ M_0 MeV	1873.9	1867.1 ± 5.0	43.2	30.7 ± 5.0
Γ_0 MeV	167.5	169.4 ± 11.1	90.4	68.3 ± 11.1
FF %	2.6	2.9 ± 0.2	1.1	1.2 ± 0.2

Table 16: Various goodness-of-fit measures for the default fit. See the text for the explanation of various variables. Actual number of free parameters in the fit is $n_{\rm par} = 98$. The errors given in the third and fourth columns are statistical due to the finite number of generated toy experiments.

Test quantity		Mean (RMS) toy experiments		Data	χ^2 probability	Equivalent standard dev.
$-2\ln\mathcal{L}$	—	$-1408.5\,(89.0)\pm 14$	—	-1226.8		2.0σ
	$\mathrm{N_{bin}}$	$\mathrm{ndf^{eff}}$	${n_{\rm par}}^{\rm eff}$	$\chi^2_{\rm data}$	P_{χ^2}	N_σ
χ^2_{6D}	501	$404.7\,(26.1)\pm 4.9$	95.3 ± 4.9	462.9	2.3%	2.0σ
χ^2_{2D}	496	$411.3\,(24.6)\pm 4.0$	83.7 ± 4.0	438.7	17 %	1.0σ
$\chi^2_{1D}\ m_{J/\psi\phi}$	68	$63.0\,(13.5)\pm 2.2$	4.0 ± 2.2	71.5	22 %	0.8σ
$\chi^2_{1D}\ m_{\phi K}$	23	$19.2\,(\ 5.0)\pm 0.8$	2.8 ± 0.8	37.9	0.6%	2.5σ
$\chi^2_{1D}\ m_{J/\psi K}$	24	$20.3\,(\ 6.7)\pm 1.1$	2.7 ± 1.1	21.1	39 %	0.3σ

components can find local fluctuations in data and optimize to them. In this subsection, we present the results of the statistical simulation of the $\Delta(-2\ln\mathcal{L})$ distributions for several resonances present in the default amplitude model. If the $\Delta(-2\ln\mathcal{L})$ distribution follows the χ^2 distribution, then the mean $\Delta(-2\ln\mathcal{L})$ value is equal to $\mathrm{ndf^{eff}}$. A better estimate of $\mathrm{ndf^{eff}}$ can be obtained by fitting the χ^2 PDF to the $\Delta(-2\ln\mathcal{L})$ distribution. Such fits are illustrated for the X resonances in Fig. 58. The results obtained with these simulations are shown in Table 17. The effective $\mathrm{ndf^{eff}}$ values vary from $1.2\Delta n_{\rm par} - 1.7\Delta n_{\rm par}$. One of the smallest $\mathrm{ndf^{eff}}/\Delta n_{\rm par}$ ratios is obtained for the simulations of the $X(4140)$ component, which is perhaps not surprising since this contribution is confined to the relatively narrow threshold region. Once it reaches the $X(4274)$ region, it loses its identity and such fits are not accepted. Conservatively, we use $\mathrm{ndf^{eff}} = 2.0\Delta n_{\rm par}$ for all contributions when the mass and width of a resonance are free parameters.

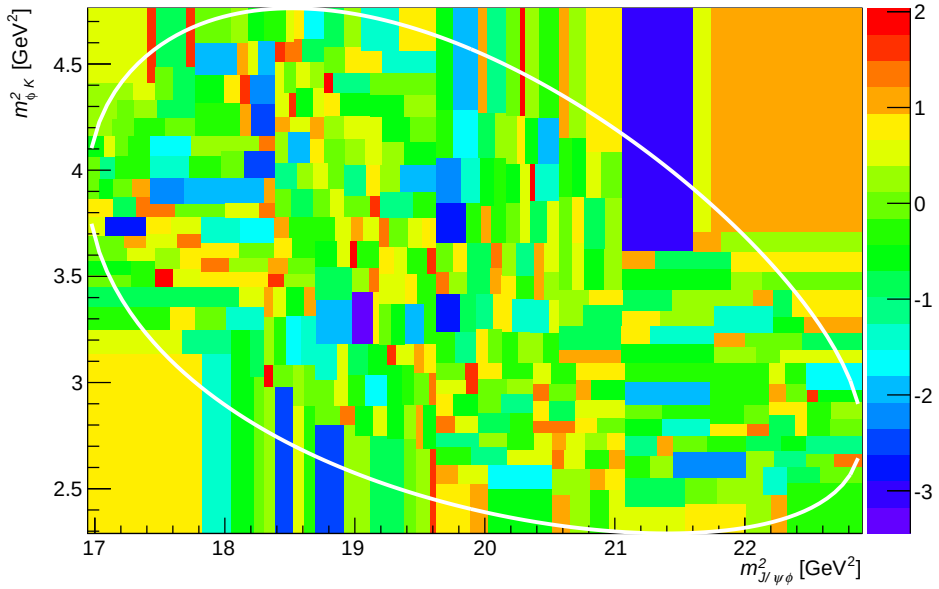

Figure 51: Pulls of the default fit displayed for the adaptive binning on the Dalitz plane.

Table 17: The results for mean, rms values of $\Delta(-2\ln\mathcal{L})$ distributions between fits without and with the listed resonance for pseudo-experiments generated without that resonance present in the amplitude model. Results for ndf$^{\text{eff}}$ when fitting the χ^2 PDF to the $\Delta(-2\ln\mathcal{L})$ distributions are also given.

resonance	Δn_{par}	Number of exp.	mean	rms	stat.error	fitted ndf$^{\text{eff}}$	ndf$^{\text{eff}}/\Delta n_{\text{par}}$
$X(4140)$	8	40	9.9	10.4	1.6	9.9 ± 0.7	1.24 ± 0.08
$X(4274)$	8	40	13.2	14.1	2.2	13.0 ± 0.8	1.62 ± 0.10
$X(4500)$	6	40	9.7	9.9	1.6	10.2 ± 0.7	1.70 ± 0.11
$X(4700)$	6	40	9.3	10.6	1.7	10.0 ± 0.6	1.67 ± 0.10
$K^{'}(1^+)$	10	40	13.1	14.4	2.3	11.7 ± 0.7	1.17 ± 0.10
$K^*(1^-)$	8	40	10.2	10.8	1.7	9.3 ± 0.6	1.16 ± 0.08

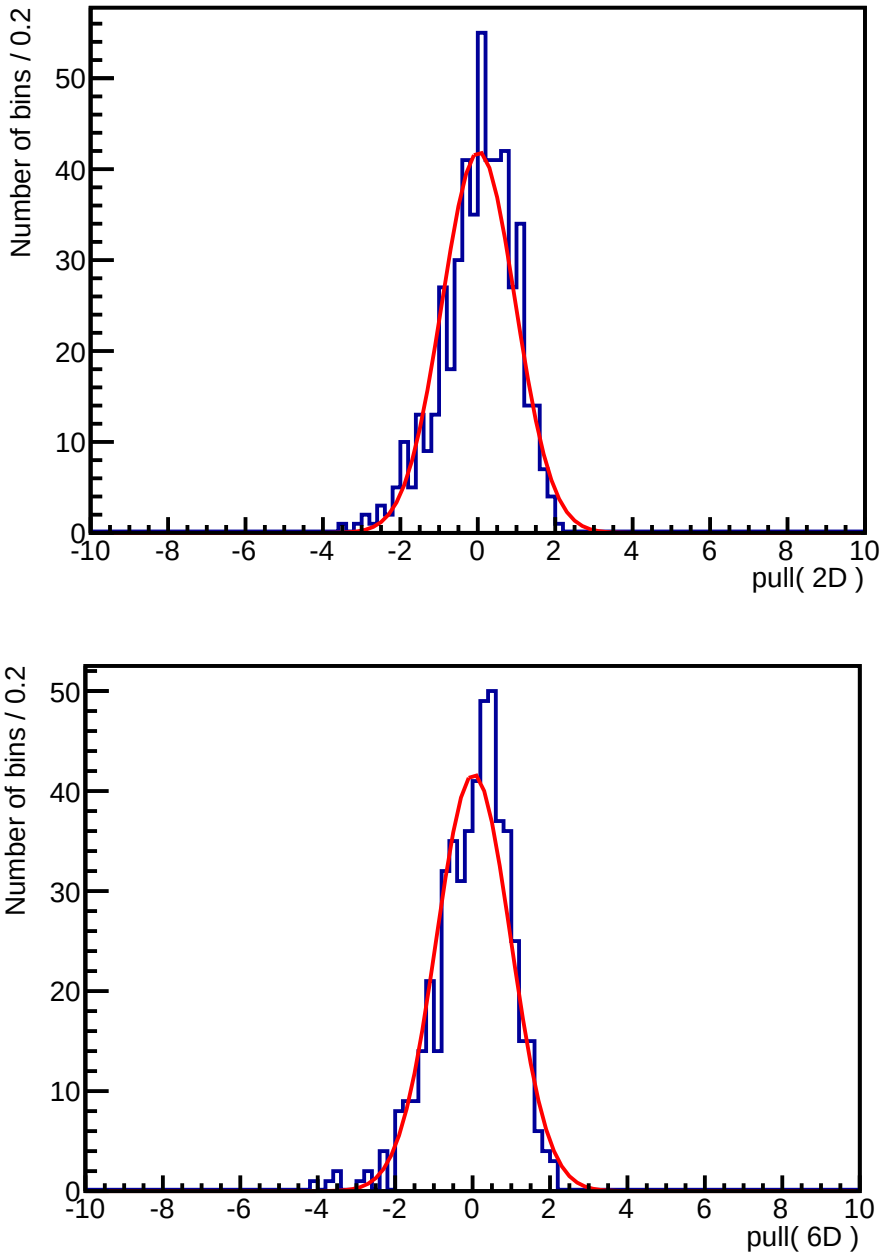

Figure 52: Distribution of pulls for the default fit model for the two dimensional (top) and six dimensional (bottom) adaptive binning.

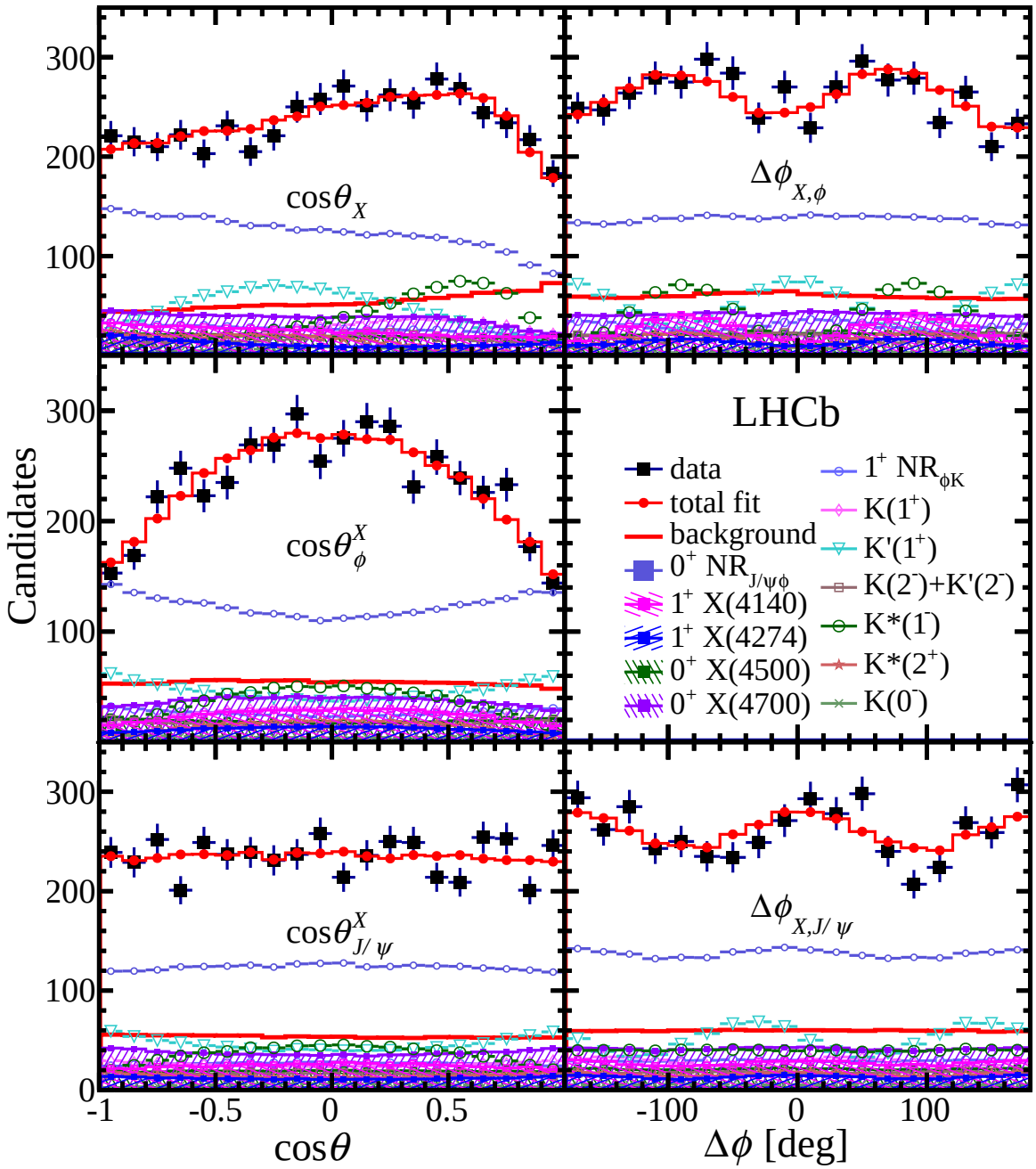

Figure 53: Distributions of all X angles with the default model. See the legend in Fig. 45 for a description of all shown components.

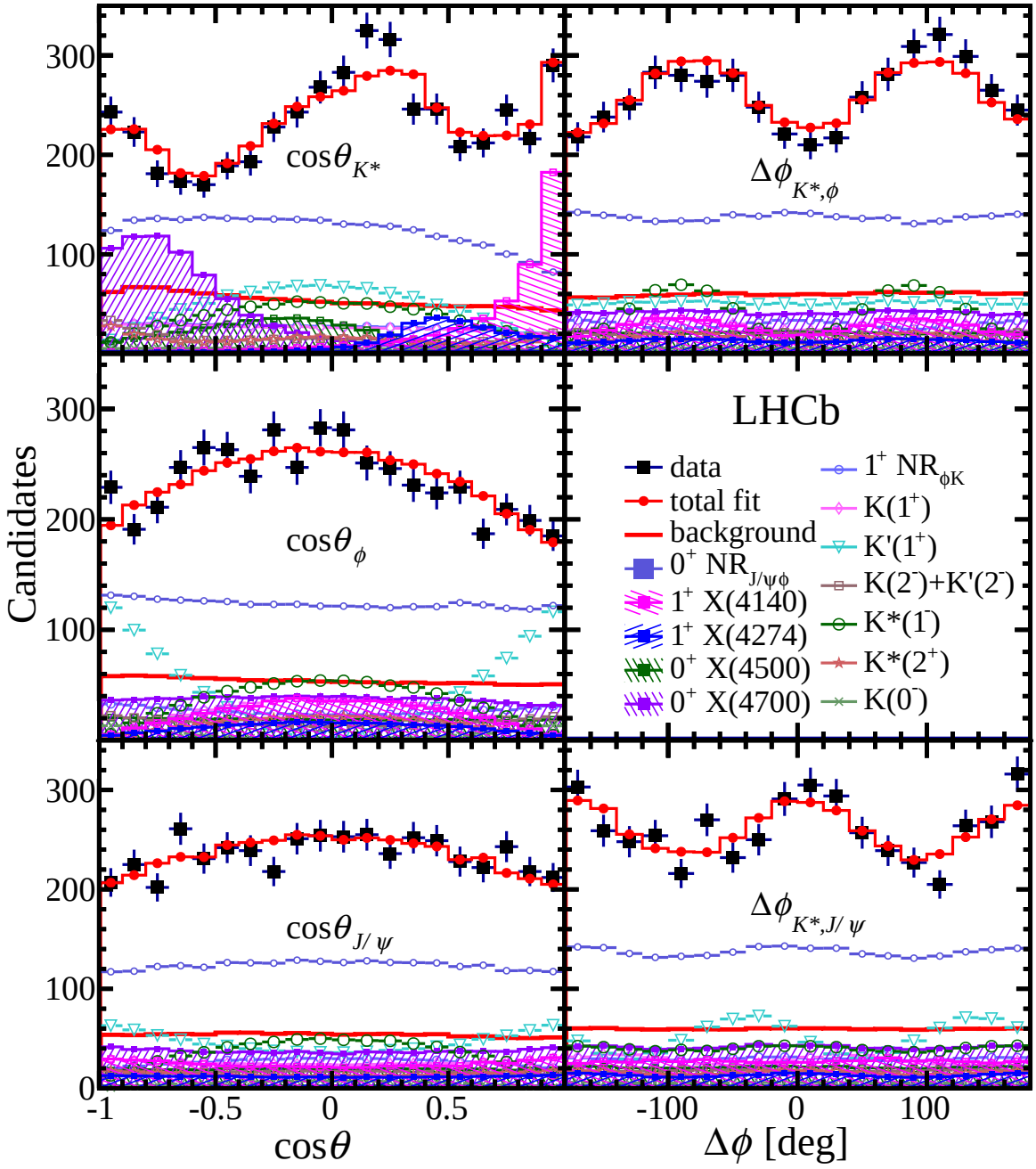

Figure 54: Distributions of all K^* angles with the default model. See the legend in Fig. 45 for a description of all shown components.

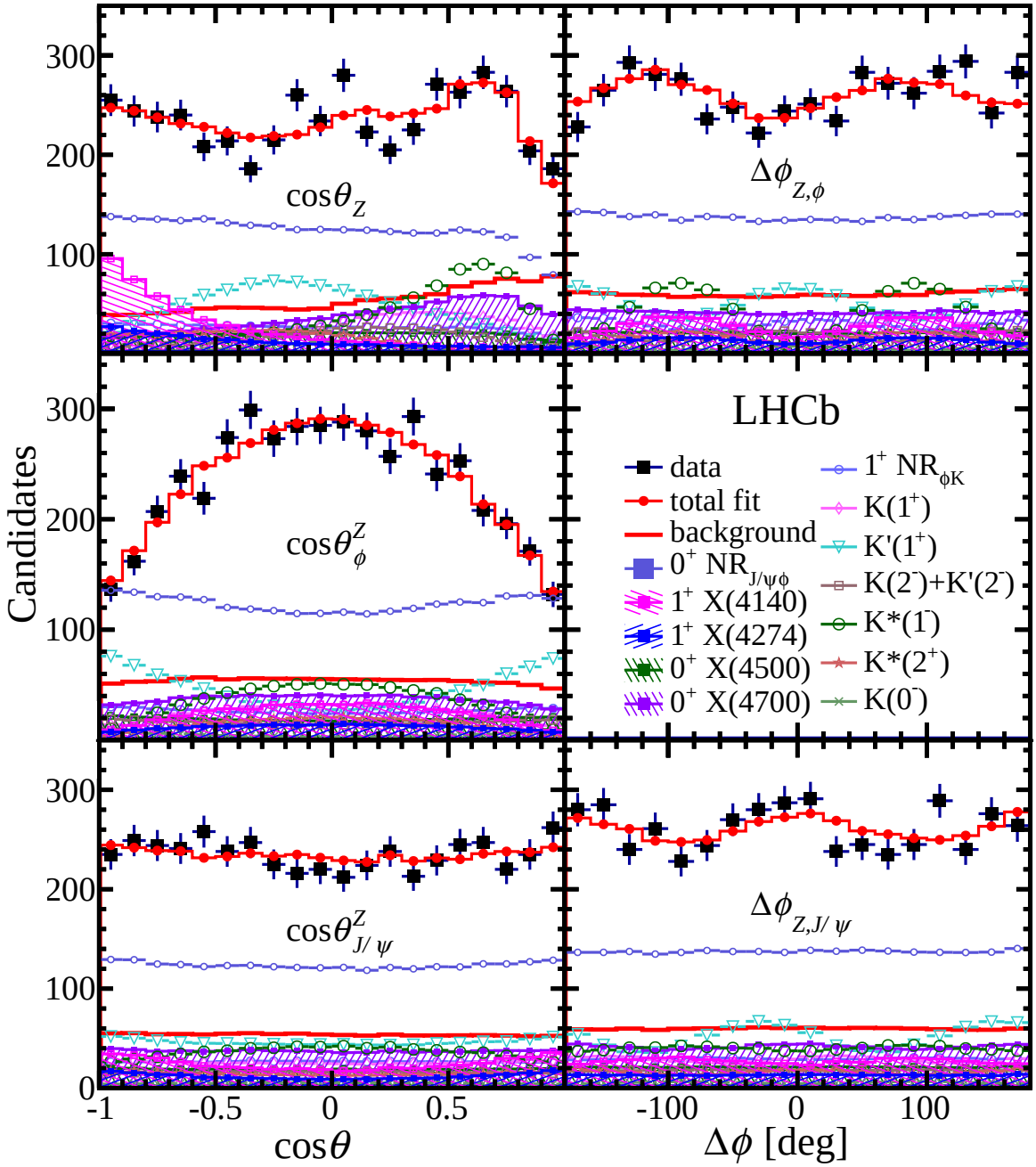

Figure 55: Distributions of all Z angles with the default model. See the legend in Fig. 45 for a description of all shown components.

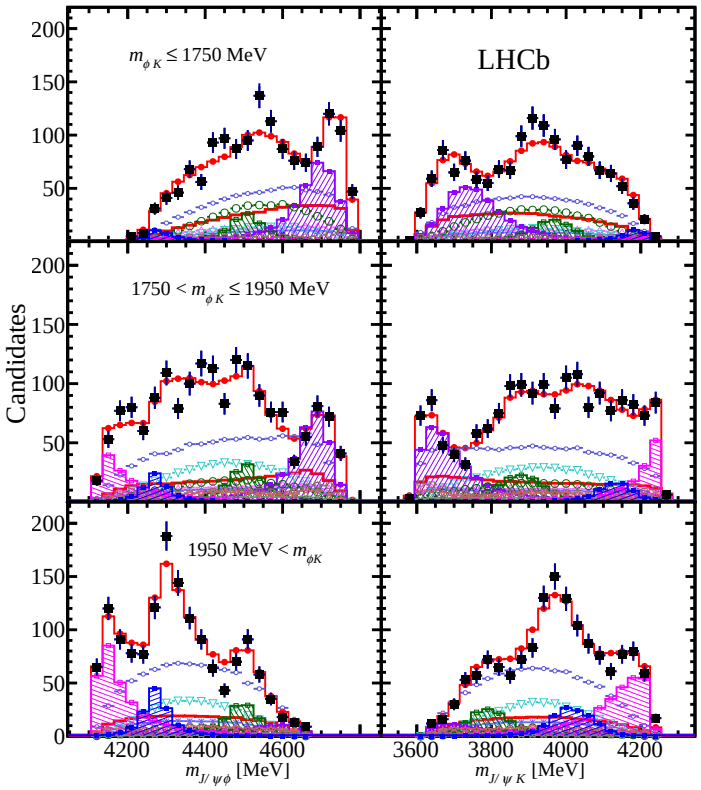

Figure 56: Distribution of (left) $m_{J/\psi\phi}$ and (right) $m_{J/\psi K}$ in three slices of $m_{\phi K}$: $< 1750\,\text{MeV}$, $1750 - 1950\,\text{MeV}$, and $> 1950\,\text{MeV}$ from top to bottom, together with the projections of the default amplitude model. See the legend in Fig. 45 for a description of all shown components.

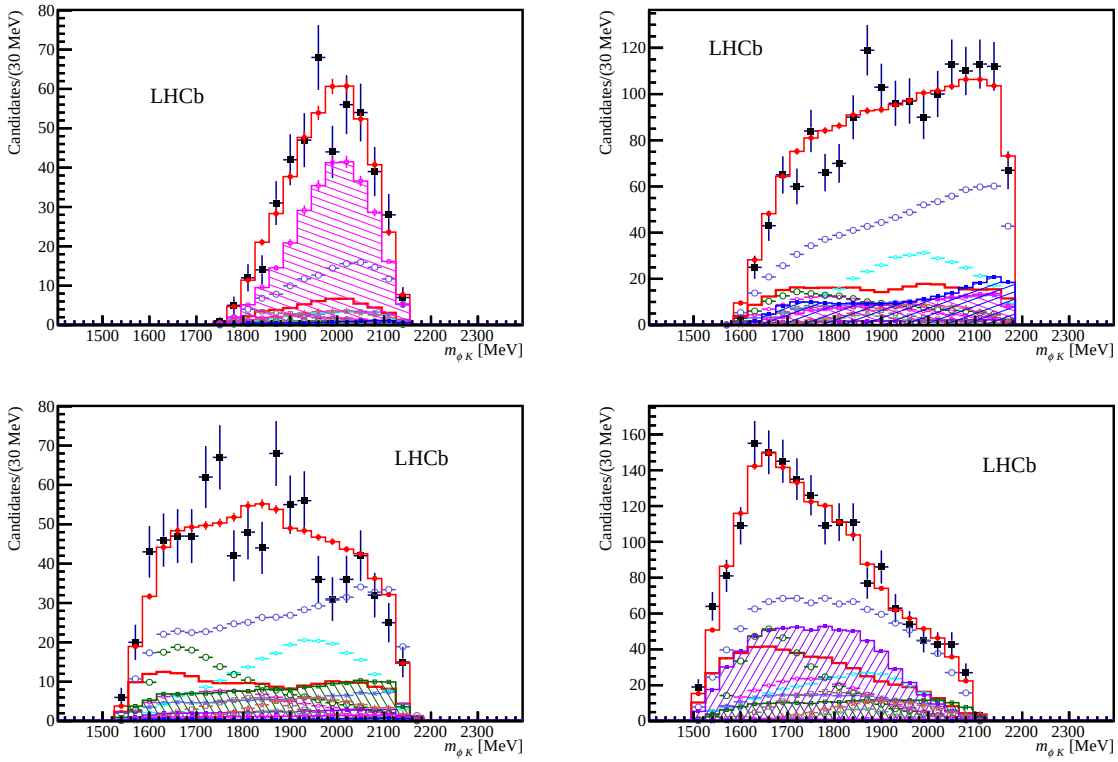

Figure 57: Distribution of m(ϕK) in four slices of m($J/\psi\,\phi$); [0,4200 MeV], (4200,4400 MeV], (4400,4500 MeV) and (4500 MeV, inf) from the top to bottom. See the legend in Fig. 45 for a description of all shown components.

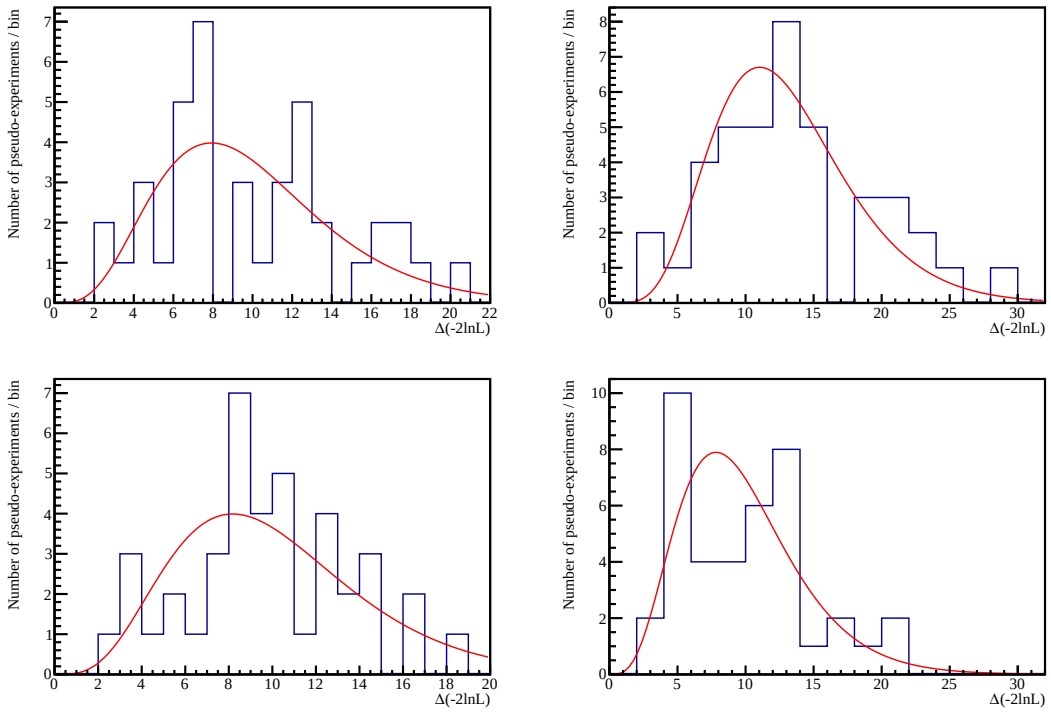

Figure 58: Distribution of $\Delta(-2\ln\mathcal{L})$ between the fits with and without given fit component in the fit, when generated from the amplitude model fit to the data without that component ("null hypothesis"). Fits of the χ^2 PDF are superimposed. The plots are for the following components: $X(4140)$ (top left), $X(4274)$ (top right), $X(4500)$ (bottom left) and $X(4700)$ (bottom right).

9 Systematic errors

In this section we explore systematic uncertainties on masses, widths and fit fractions. The changes in these parameters under systematic variations are shown for $X \to J/\psi\,\phi$ contributions in Table 18 and for $K^{*+} \to \phi K^+$ contributions in Tables 19 and 20. For the total systematic errors, we sum up positive and negative deviations in quadrature separately. We have included statistical errors for comparison.

The energy release in $B^+ \to J/\psi\,\phi K^+$ decay is small ($\sim 13\%$ on M_B), thus the phase-space is very limited, not offering much range for non-resonant interactions to change. In the default model the non-resonant terms are represented by constant amplitudes. We have investigated making them decrease exponentially with mass-squared: $\exp(-|\alpha|\,(m^2 - m^2_{\rm min}))$. The improvement in fit quality is completely negligible: $\Delta(-2\ln\mathcal{L}) = -0.5$ for $\Delta n_{\rm par} = 2$, as the fitted mass slope parameters are consistent with zero: $\alpha_X = (7.1 \pm 7.0) \times 10^{-8}$ MeV $^{-2}$ and $\alpha_{K^*} = (0.0 \pm 1.5) \times 10^{-9}$ MeV $^{-2}$. We have included any change in the values of the fitted parameters in the systematic uncertainty.

Like in similar amplitude analyses, the largest systematic uncertainty is due to the K^{*+} model composition. To explore it, we allow one extra resonance in each partial wave. The 1^+ wave is an exception. Since the second 1^+ resonance included in the default model is already borderline significant, instead of adding another one, we remove the second one. The effects of these model variations are presented in Tables 21-23. The total errors from these variations are transferred to the summary Tables 18-20. In addition, we also include among the systematics the fit variation in which the $X(4140)$ is represented by $D_s^+ D_s^{*-}$ cusp amplitude replacing the Breit-Wigner representation, as discussed later in Sec. 11.

The other source of systematic uncertainty is due to L_B and L_{K^*} (or L_X) dependence of the Breit-Wigner amplitude in the numerator of Eq. 34 via Blatt-Weisskopf factors. Helicity states correspond to the mixtures of allowed L values, but we assume the lowest L values in Eq. 34 in the default fit. We increase L_B values by 1 for all the components as

shown in Tables 24-26. L_{K^*} or L_X values can change only in units of 2 because parity is conserved in strong decays. We performed such variation for states in which the higher value is allowed, except for the X states, since the fit results indicate that the $L_X = 2$ amplitudes are insignificant. These variations are also shown in Tables 24-26, and the total contribution from them is also shown in the summary Tables 18-20.

There is also L_{K^*} dependence in the formula for the total width of the resonance given by Eq. 36. This formula is only an approximation, valid in the case when the total width is dominated by the decay mode being analyzed. A better formula would include a sum over all partial widths. In fact, all K^{*+} states are expected to have sizable widths to the other decay modes, $K\pi$, $K\rho$, $K^*(892)\pi$ etc. Since ratios of these partial widths to the ϕK partial width are unknown, it is not possible to implement such a formulation. However, as a systematic check we have performed a fit in which instead of assuming ϕK^+ partial width mass dependence for the total width, we switch all K^{*+} total width formulae to the lightest possible decay mode allowed, which is $K\pi$ for natural spin-parity resonances and $K\omega$ for the others, which also changes L_{K^*} value. The observed changes in the fit values are shown in Tab. 18-20, tagged as Γ_{tot} entries.

The Blatt-Weisskopf factors contain d parameter for the effective hadron size, which we set to 3.0 GeV^{-1} in the default fit. In systematic variation we change its value between 1.5 and 5.0 GeV^{-1}.

The default ϕ mass selection window is ± 15 MeV. We remove candidates in which more than one K^+K^- pair falls within this window, which removes 3.2% of the events. After these cuts non-ϕ fraction of the selected $B^+ \to J/\psi K^+K^-K^+$ events is 2.1% as estimated in Sec. 3. In our amplitude models, we neglect this S-wave component. To evaluate systematics of this approximation we narrow down the ϕ mass selection window to ± 10 and ± 7 MeV, which reduces the signal yield by up to 13%, while decreasing the $S-$wave fraction by a factor of 2. The observed deviations in the fit values include

statistical fluctuations due to the decreased data sample, but we nevertheless include them in the total systematic error.

A good check on uncertainty in the background parameterization is to use only left, or only right sideband of the B^+ peak in the $J/\psi\,\phi K^+$ mass distribution (in the fit default we add them together).

In order to address systematics associated with the determination of the background fraction (β) we varied how the fit to B-mass distribution was performed, as discussed in Sec. 3. We increased the order of the background polynomial function by one, we changed the signal shape from a symmetric double-sided Crystal Ball function to a simple Gaussian, and finally we varied both. All three variations are given in the tables below, however only the largest deviation (when both are varied) is actually included in the total systematics.

To address efficiency systematic we perform two variations. We remove weights given to MC events (w^{MC} discussed in Sec. 4) used in the PDF integrals when fitting the data. The fit results are remarkably stable. As additional cross-checks we tighten the cut on $DLL_{\rm sig/bkg}$ (Sec. 3) from < 5 to < 0. This reduces the signal statistics by 30% and reduces the background fraction by 33%. We also tighten $p_{\rm T}$ cut off in kaon selection (which applies to all three kaons) from 250 to 500 MeV, we lose 20% of signal but also reduce the backgrounds fraction β by 54% (compare Fig. 59 with Fig. 20). The fit results for the X resonances remain very stable. The fit displays for this variation are shown in Fig. 60. A similar effect is observed when tightening kaon ID cut from $\mathrm{PID}_K > 0$ to > 5, which reduces the signal by 16% and background by 56%. The changes of the fit parameters from these cross-checks are shown at the bottom of the tables with the systematic variation, since we do not include them in the systematic errors as many of them are likely statistical in nature. The deviations are within, or not far from, the assigned systematic errors.[24] The fit displays for this cross-check are shown in Fig. 61.

[24]No results for K_1' are given since with such reduced statistics, there is no evidence for the second 1^+ K_1 state, which we have removed from the fit.

To check that the default fit results do not correspond to a local likelihood maximum, we have performed a fit with the same fit components but fitting helicity couplings[25] directly instead of using their decomposition into LS couplings. This provides for a different starting point and a different approach path towards the likelihood maximum. The same maximum was found in terms of the likelihood value, masses, widths, and fit fractions. Large number of fit variations included among the systematic exercises discussed above also probes potential fit ambiguities. Furthermore, we have performed 10 additional fits with the default approach, but initialized at different starting points for the fit parameters, throwing them randomly around the default fit results in the $\pm 3\sigma$ range. All fits converged to the same likelihood maximum. Randomization of the starting points in even larger range ($\pm 10\sigma$) does produce many fits which converge to different local likelihood maxima; none better than the default fit among 10 tried. It is not surprising that the global maximum cannot be always found by random initialization in too wide a range given a large number of components in the model, all with free masses and widths. When initialized too far from the data structures which they are supposed to describe, they pick up on local fluctuations.

[25]For strong decays parity conservation imposes constraints on helicity couplings, thus not all are independent parameters.

Table 18: Summary of the systematic errors on the parameters of the $X \to J/\psi\,\phi$ states. All numbers for masses and widths are in MeV and fit fractions in %.

sys	1^+	$X(4140)$			$X(4274)$			0^+	$X(4500)$			$X(4700)$			$\mathrm{NR}_{J/\psi\,\phi}$
var	FF	M_0	Γ_0	FF	M_0	Γ_0	FF	FF	M_0	Γ_0	FF	M_0	Γ_0	FF	FF
NR exp	+0.4	-0.2	-0.1	+0.4	-0.2	+0.6	+0.8	-1.7	+6.3	+0.3	+0.2	+7.1	-15.7	-1.7	-9.1
K^*	+2.0	+3.6	+17.1	+2.2	+11.2	+7.9	+1.4	+1.8	+9.3	+13.8	+2.0	+7.5	+38.6	+6.7	+8.0
Model	-1.7	-2.6	-11.7	-1.9	-2.5	-8.5	-1.5	-11.0	-8.6	-16.6	-1.7	-18.9	-13.5	-4.8	-16.6
L var.	+3.2	+2.2	+7.3	+2.1	+10.6	+1.4	+1.0	+0.3	+1.3	+10.8	+1.7	+9.0	+12.4	+1.5	+1.2
	+0.0	-1.2	-6.2	-0.5	-0.8	-4.6	-1.2	-4.7	-9.6	-11.2	-1.6	-6.8	-24.9	-0.8	-8.5
Γ_{tot}	-0.6	+0.2	+1.5	-0.4	+3.2	+0.2	-0.3	+0.1	+0.8	-0.1	-0.3	+0.9	-5.8	-0.9	-1.1
d=1.5	-0.9	+1.1	+5.3	-0.5	+2.2	+0.8	-0.4	+0.5	+1.7	+3.2	+0.1	-0.1	+1.7	+0.0	+1.1
d=5.0	+1.1	-0.2	-2.0	+0.6	+0.2	-0.8	+0.3	-0.5	-1.0	-3.1	-0.1	-1.2	-3.2	-0.7	-2.5
Lside.	+0.1	-0.4	-2.0	+0.1	+0.4	-0.8	+0.1	-0.5	-2.4	-2.6	-0.2	-1.5	-3.1	-0.7	-1.2
Rside.	-0.3	+0.3	+2.6	-0.2	-0.6	+1.0	+0.0	+0.5	+3.7	+3.4	+0.4	+1.2	+7.0	+0.8	+1.6
ϕwin 7	+2.5	+1.1	+4.7	+2.4	-1.6	+1.4	+1.8	+4.2	-4.3	+7.1	+1.2	-9.3	+5.8	+0.7	+4.7
No w^{MC}	+1.6	+0.0	+0.0	+0.1	+0.0	+0.0	+1.4	+1.7	+0.0	+0.2	+0.2	+0.1	+0.0	+1.2	+2.7
β bkg.	+0.0	+0.0	+0.2	+0.0	-0.1	+0.0	+0.0	+0.1	+0.1	+0.5	+0.0	-0.1	+0.1	+0.0	+0.0
β sig.	+0.7	-0.5	-3.0	+0.6	+1.1	-0.6	+0.5	-1.0	-2.5	-7.1	-0.3	-1.0	-5.2	-0.8	-0.8
β both	+1.2	-0.6	-3.6	+1.2	+1.7	-0.7	+0.9	-2.5	-4.6	-11.1	-0.5	-3.9	-6.1	-1.4	-1.4
$X(4140)Cusp$	+2.2			+0.9	+6.4	-5.4	-1.4	-1.2	+0.0	+1.2	+0.2	+1.9	-2.5	0.5	-1.6
Total	+5.9	+4.6	+20.7	+4.7	+17.2	+8.4	+3.5	+6.5	+12.0	+20.8	+3.2	+13.9	+42.0	+7.2	+11.0
Sys	-2.1	-2.8	-13.5	-2.0	-3.6	-11.1	-2.4	-6.7	-14.5	-20.4	-2.3	-24.1	-33.3	-5.3	-21.0
stat.	2.8	4.5	20.7	3.2	8.3	10.9	2.5	5.1	11.1	21.2	2.4	10.1	30.7	4.9	10.7
DLL<0	+0.9	+7.3	+34.6	+3.5	-10.9	+14.1	+3.8	+0.9	+12.1	+2.6	+0.0	+12.8	+20.9	+5.7	+7.5
${p_{\mathrm{T}}}^K$>500	-1.3	+1.6	+1.7	-2.7	+7.8	+12.2	+0.2	-9.6	-10.9	-18.6	-3.2	-4.7	-12.7	-6.6	-17.1
$Z(2^-)$	-2.2	+0.2	+4.5	-2.2	+3.0	-2.8	-1.8	+3.3	+0.2	-10.0	-1.3	-7.2	+15.6	-3.7	-0.8

Table 19: Summary of the systematic errors on the parameters of the $K^{*+} \to \phi K^+$ states with $J^P = 2^-$ and 1^+. All numbers for masses and widths are in MeV and fit fractions in %.

sys	2^-	$K_2(1770)$			$K_2(1820)$			1^+	K_1			K_1'			$\mathrm{NR}_{\phi K}$
var	FF	M_0	Γ_0	FF	M_0	Γ_0	FF	FF	M_0	Γ_0	FF	M_0	Γ_0	FF	FF
NR exp	+0.5	-4.8	-13.5	+0.4	-0.6	+8.6	+1.8	-2.2	-5.9	-3.7	+0.7	-21.4	-45.4	+0.8	+0.3
K^*	+1.2	+118.1	+194.8	+4.0	+16.2	+53.8	+4.4	+3.9	+150.8	+122.4	+15.6	+49.0	+159.5	+28.5	+34.4
Model	-4.1	-22.3	-71.0	-8.6	-14.9	-38.5	-5.5	-7.5	-79.2	-196.2	-6.1	-53.8	-143.2	-27.2	-5.1
Lvar.	+0.7	+8.6	+54.1	+3.7	+5.5	+14.0	+3.5	+0.8	+22.3	+20.4	+3.4	+47.5	+37.7	+4.8	+5.0
	-1.5	-63.3	-127.9	-9.3	-31.2	-59.5	-8.6	-2.2	-48.6	-70.3	-0.9	-159.9	-72.5	-8.7	-2.2
Γ_{tot}	-0.2	+0.8	+38.7	-1.6	-1.9	-12.6	-2.4	+0.6	-29.5	+17.2	+0.9	-0.1	+7.1	-2.3	+2.2
d=1.5	+0.1	+18.2	+67.2	-0.6	+2.7	+6.0	-1.5	+0.7	-17.4	-5.6	-1.0	+8.2	+13.9	-2.1	+1.7
d=5.0	+0.2	-7.2	-25.8	-0.1	-1.0	-0.5	+1.3	-1.5	+12.2	-6.9	+0.5	-8.4	-42.8	-1.0	-1.5
Lside.	+0.1	-4.2	-9.5	-0.2	-1.1	+2.0	+0.9	-1.0	+0.9	+0.2	+1.1	-8.7	-30.2	+0.9	+0.3
Rside.	-0.1	+3.2	+5.0	-0.4	+3.8	+0.1	-1.2	+1.2	-1.3	+12.5	-0.4	+11.6	+36.5	-1.5	-0.1
No w^{MC}	-0.8	-0.2	+0.4	-1.1	+0.0	-0.5	-1.5	-0.8	+1.9	+1.2	+0.1	+0.6	+1.8	-0.7	+0.7
ϕwin 7	-1.0	-25.0	-27.2	-2.6	-1.1	+41.2	-1.4	-2.7	-11.3	-36.5	+0.0	-15.2	-23.1	+6.0	-1.9
β poly.	+0.0	+0.3	+2.3	-0.1	+0.5	+0.7	+0.0	+0.1	-1.1	+1.3	+0.1	+0.1	+0.4	+0.1	+0.2
β sig.	+0.2	-4.8	-18.2	+0.3	-4.2	-7.6	+0.5	-1.5	+23.1	+7.9	+1.7	-7.0	-19.5	+2.2	-1.1
β both	+0.2	-8.1	-35.4	+1.7	-9.3	-6.7	+2.6	-2.7	+28.0	-8.2	+4.0	-23.4	-63.0	+4.8	-0.8
$X(4140)Cusp$	+0.0	+24.6	+42.2	+5.4	-0.8	+10.8	+3.8	+1.8	+4.5	+5.5	+4.4	-12.0	+40.6	+8.4	-0.3
Total	+1.5	+122.3	+220.7	+7.7	+17.7	+82.0	+7.2	+4.7	+153.0	+138.0	+16.7	+69.7	+173.5	+31.3	+34.5
sys.	-4.6	-76.5	-154.3	-13.3	-34.7	-72.0	-10.9	-9.2	-100.5	-214.8	-6.3	-172.3	-177.9	-28.8	-6.4
stat.	2.8	34.9	116.3	11.0	26.6	58.1	11.2	8.1	59.0	157.0	10.3	65.0	170.3	20.4	13.1
DLL<0	-2.2	-25.0	-79.1	-8.8	+33.0	-105.4	-6.8	+7.1	+110.9	-56.2	+6.6				+12.4
${p_\mathrm{T}}^K$>500	-2.7	-0.4	+4.9	-3.7	-10.1	-67.0	-5.7	+6.4	+95.2	-238.7	-3.7	-87.7	+33.6	-3.8	+4.7
$Z(2^-)$	-0.5	-20.3	-16.5	-5.3	+16.2	+27.8	-4.5	+2.1	+9.0	+38.8	-1.1	+67.6	-75.2	-10.9	+2.3

Table 20: Summary of the systematic errors on the parameters of the $K^{*+} \to \phi K^+$ states with $J^P = 0^-$, 1^- and 2^+. All numbers for masses and widths are in MeV and fit fractions in %.

systematic	1^- $K(1680)$			0^- $K(1830)$			2^+ $K_2^*(1980)$		
variation	M_0	Γ_0	FF	M_0	Γ_0	FF	M_0	Γ_0	FF
NR exp	+3.3	+11.5	+0.2	-22.9	+36.3	+0.4	-13.7	-65.1	+0.0
K^*	+19.9	+31.4	+2.6	+54.8	+236.9	+1.7	+214.3	+805.2	+1.6
Model	-33.1	-141.0	-2.7	-90.2	-96.3	-1.7	-66.9	-223.8	-0.6
Lvar	+14.2	+59.3	+1.8	+12.8	+51.6	+0.7	+52.0	+172.3	+0.3
	-17.7	-44.7	-0.2	-44.4	-31.1	-0.2	-19.1	-107.4	-0.3
Γ_{tot}	-101.5	-93.1	+0.2	-2.8	-6.2	-0.1	-167.6	-230.0	+0.3
d=1.5	+21.1	+121.7	+0.0	+12.1	+2.5	-0.1	+102.2	+806.2	+0.0
d=5.0	-4.9	-21.0	+0.0	-10.3	+6.3	+0.2	-72.0	-242.5	+0.0
Left side.	+2.7	+7.7	+0.0	-12.6	20.1	+0.2	-17.9	-28.8	+0.2
Right side.	-3.0	+7.7	+0.0	+10.0	-23.5	-0.2	+19.2	+24.7	-0.2
Φ win. 7	+0.5	-28.9	-1.8	-33.6	+94.5	+0.9	-97.0	-258.9	+0.2
No w^{MC}	+0.2	-0.4	+0.1	+1.0	-2.4	-0.4	-0.4	-3.1	-0.2
β poly.	+0.2	+1.5	+0.0	+0.2	+1.1	+0.0	-0.5	-3.8	+0.0
β sig.	+0.5	-4.2	+0.0	-10.5	+9.9	+0.2	-7.7	+8.4	+0.2
β both	+2.2	-4.1	+0.1	-43.0	+32.2	+0.5	-18.5	+1.1	+0.4
$X(4140)Cusp$	+4.5	+5.5	-1.2	+7.8	+11.4	+0.1	+26.5	+6.1	-0.2
Total	+32.9	+139.8	+3.2	+59.0	+280.2	+2.3	+245.2	+1152.7	+1.7
sys.	-108.4	-180.7	-3.9	-114.8	-104.1	-1.8	-239.7	-559.0	-0.7
stat.	19.9	74.7	1.9	43.2	90.4	1.1	94.2	310.6	0.8
DLL<0	+1.1	+7.4	-0.6	+69.6	-150.9	-2.1	+287.3	-157.2	-0.6
${p_{\rm T}}^K$>500	-15.6	-47.1	-0.2	-161.9	-2.4	-0.2	-10.1	-102.2	-0.1
$Z(2^-)$	-10.3	-15.2	-1.1	+25.9	-67.5	-0.2	-21.3	+38.1	-0.7

Table 21: Summary of the systematic errors on the parameters of the $X \to J/\psi\,\phi$ states when the K^* model is modified. All numbers for masses and widths are in MeV and fit fractions in %.

sys	1^+	$X(4140)$			$X(4274)$			0^+	$X(4500)$			$X(4700)$			$\mathrm{NR}_{J/\psi\,\phi}$
var	FF	M_0	Γ_0	FF	M_0	Γ_0	FF	FF	M_0	Γ_0	FF	M_0	Γ_0	FF	FF
$K_3^*(1780)(3^-)$	-0.8	-1.3	-6.8	-0.7	+3.0	-2.6	+0.0	-1.5	-4.3	-2.7	+0.1	-2.8	+10.2	+1.4	+0.5
$K_4^*(2045)(4^+)$	+0.1	-0.9	-1.9	+0.2	-0.4	+1.2	+0.1	+0.0	+0.5	+0.3	+0.1	+1.5	-0.6	+0.1	-0.6
$K^{*'}(1^-)$	+1.0	-1.1	-3.1	+0.5	+7.0	+0.2	+0.6	-0.2	+1.3	+2.5	+1.6	+0.3	+23.2	+6.2	+6.5
$K'(0^-)$	-0.4	-0.2	-1.1	-0.4	+1.6	+0.8	+0.3	-3.0	-4.5	-5.0	-0.9	-6.4	-3.8	-2.2	-3.0
$K'''(2^-)$	+0.8	+3.0	+15.2	+2.0	-2.5	+5.0	+0.8	-0.8	+5.5	+4.9	+0.5	+5.6	+2.3	+2.2	-0.8
$K^{*'}(2^+)$	+0.1	-1.4	-6.4	-0.5	+2.6	-3.4	-0.5	-2.0	-5.9	-10.2	-1.1	-3.7	-7.4	-2.1	-5.2
$K^*(3^+)$	+1.4	+0.7	+2.4	+0.1	+2.4	-3.8	-0.3	+0.1	-0.9	-4.2	+0.1	-7.8	-0.8	-3.3	-4.3
no $K'(1^+)$	+0.7	+1.8	+7.4	+0.7	+0.4	+5.5	+1.0	-1.1	+0.3	+5.8	-0.7	+4.7	-10.6	+0.5	+0.8
$K^*(1410)$	-1.5	+0.2	+0.3	-1.6	+1.9	+2.3	-0.1	+1.8	+7.3	+11.3	+1.1	-8.6	+28.8	-0.1	+4.6
no $K'(2^-)$	+0.8	-0.9	-5.9	+0.2	+7.0	-6.3	-1.4	-10.2	+0.2	-11.0	-0.5	-12.6	+3.5	-1.7	-14.6
Total	+2.0	+3.6	+17.1	+2.2	+11.2	+7.9	+1.4	+1.8	+9.3	+13.8	+2.0	+7.5	+38.6	+6.7	+8.0
Sys	-1.7	-2.6	-11.7	-1.9	-2.5	-8.5	-1.5	-11.0	-8.6	-16.6	-1.7	-18.9	-13.5	-4.8	-16.6

Table 22: Summary of the systematic errors, due to variation of the K^* model, on the parameters of the $K^{*+} \to \phi K^+$ states with $J^P = 2^-$ and 1^+. All numbers for masses and widths are in MeV and fit fractions in %.

sys	2^-	$K_2(1770)$			$K_2(1820)$			1^+	K_1			K_1'			$\mathrm{NR}_{\phi K}$
var	FF	M_0	Γ_0	FF	M_0	Γ_0	FF	FF	M_0	Γ_0	FF	M_0	Γ_0	FF	FF
$K_3^*(1780)(3^-)$	-0.4	-11.0	-27.4	-1.0	-6.5	+0.2	-0.3	-2.8	-7.8	+1.6	+1.1	-17.0	-64.5	-1.1	+1.0
$K_4^*(2045)(4^+)$	+0.3	+7.6	+26.0	+0.2	+0.2	-5.7	+0.2	-0.1	+13.1	+32.6	+0.6	-9.9	-6.5	+0.4	-0.1
$K^{*'}(1^-)$	+0.2	-4.2	-56.0	+3.4	+2.1	+35.1	+3.9	-1.8	+98.5	+95.7		-42.8	+123.7		-4.2
$K'(0^-)$	-0.2	-9.1	-27.6	+0.5	-7.6	+1.6	+1.3	-0.2	-27.2	-82.1	-3.7	-7.3	-77.4	-5.9	+3.5
$K'''(2^-)$	+0.9	+22.0	+59.8	-2.0	+10.5	-18.8	-3.2	+1.3	+44.0	+68.8	+14.4	-9.1	+100.7	+28.5	+27.1
$K^{*'}(2^+)$	-0.5	-16.6	-19.6	-2.8	-2.8	+14.7	-2.1	-2.7	-18.9	+5.2	+0.6	-18.3	-57.8	-3.1	-0.3
$K^*(3^+)$	-0.2	+13.8	+83.8	-2.6	-10.7	-13.7	-3.8	-6.0	-9.2	-24.0	+0.4	-14.3	-58.4	-4.3	-2.5
no $K'(1^+)$	+0.3	+25.9	+37.3	+1.0	+0.1	-30.1	-1.1	+2.2	+104.6	-14.9	+5.9				+8.9
$K^*(1410)$	+0.6	+3.9	-2.7	+1.8	+12.1	+38.0	+1.6	-1.4	-3.2	-23.2	-3.8	+41.4	-31.0	-10.0	-1.4
no $K'(2^-)$	-4.0	+111.9	+159.0	-7.4				+3.0	-70.9	-174.4	-3.1	+26.2	-51.0	-5.3	+18.8
Total	+1.2	+118.1	+194.8	+4.0	+16.2	+53.8	+4.4	+3.9	+150.8	+122.4	+15.6	+49.0	+159.5	+28.5	+34.4
Sys	-4.1	-22.3	-71.0	-8.6	-14.9	-38.5	-5.5	-7.5	-79.2	-196.2	-6.1	-53.8	-143.2	-27.2	-5.1

Table 23: Summary of the systematic errors, after variation of the K^* model, on the parameters of the $K^{*+} \to \phi K^+$ states with $J^P = 0^-$, 1^- and 2^+. All numbers for masses and widths are in MeV and fit fractions in %.

systematic	1^- $K(1680)$			0^- $K(1830)$			2^+ $K_2^*(1980)$		
variation	M_0	Γ_0	FF	M_0	Γ_0	FF	M_0	Γ_0	FF
$K_3^*(1780)(3^-)$	+0.0	+20.5	+1.2	-33.3	+29.2	+0.9	-31.6	-8.7	+0.9
$K_4^*(2045)(4^+)$	+2.4	+9.5	-0.4	+6.2	-8.3	-0.2	-10.8	-48.6	-0.1
$K^{*'}(1^-)$	-29.2	-137.5	-2.0	-13.8	+8.3	+0.4	+34.0	-48.1	-0.4
$K'(0^-)$	+2.4	-1.5	-0.2	+50.3	+217.7		-27.9	+6.2	+0.3
$K'''(2^-)$	+7.8	+2.4	-0.2	+8.7	+2.4	-0.3	+38.5	+72.9	-0.3
$K^{*'}(2^+)$	-4.1	-7.0	+0.2	-25.9	+41.0	+1.1	-39.4	-212.9	+1.3
$K^*(3^+)$	-9.7	-29.6	+0.1	-31.7	+47.5	+0.7	-32.1	+45.2	+0.0
no $K'(1^+)$	-11.6	-5.9	-0.6	+12.0	-1.4	-1.7	+199.9	757.3	-0.2
$K^*(1410)$	+10.7	+2.4	-1.7	+14.7	-95.9	+0.0	+21.3	+103.5	+0.2
no $K'(2^-)$	+14.5	+21.6	-3.1	-71.9	+62.0	+0.4	+53.4	238.2	-0.1
Total	+19.9	+31.4	+2.6	+54.8	+236.9	+1.7	+214.3	+805.2	+1.6
Sys	-33.1	-141.0	-2.7	-90.2	-96.3	-1.7	-66.9	-223.8	-0.6

Table 24: Summary of the systematic errors on the parameters of the $X \to J/\psi\,\phi$ states when the value of L used in each decay (where applicable) is changed. All numbers for masses and widths are in MeV and fit fractions in %.

sys	1^+	$X(4140)$			$X(4274)$			0^+	$X(4500)$			$X(4700)$			$\mathrm{NR}_{J/\psi\,\phi}$
var	FF	M_0	Γ_0	FF	M_0	Γ_0	FF	FF	M_0	Γ_0	FF	M_0	Γ_0	FF	FF
K_1 L_{K^*}+2	+0.6	+0.7	+2.8	+0.7	+9.7	+0.8	+0.7	-1.5	-0.2	-1.4	-0.1	+0.2	-1.5	+0.0	-1.9
K_1 L_B+1	+0.0	+0.0	-0.2	+0.2	-0.2	+0.1	+0.3	-0.5	-0.7	+0.1	+0.1	-1.2	+0.6	-0.1	-0.1
$K(1680)$ L_B+1	+0.6	+0.3	+1.3	+0.4	+0.6	+0.7	+0.6	-0.3	+0.3	+0.3	+0.1	-0.2	+0.8	+0.2	+0.2
$K(1770)$ L_{K^*}+2	+0.1	-1.0	-5.6	-0.3	+1.2	-3.6	-1.1	-2.0	-1.3	-10.7	-1.2	+6.1	-13.1	-0.7	-5.4
$K(1770)$ L_B+1	+0.1	-0.1	-0.1	-0.2	+0.4	-0.3	+0.0	+0.1	+0.0	+1.2	+0.0	-0.9	+2.1	+0.0	+0.3
$K_2(1820)$ L_{K^*}+2	+0.4	+0.1	+1.8	+0.5	+0.3	+0.3	+0.3	-2.0	-1.3	+9.6	+1.7	-6.4	+12.0	+1.5	+1.0
$K_2(1820)$ L_B+1	+0.0	+0.1	+0.5	+0.2	-0.1	+0.1	+0.1	-0.2	-1.2	-3.0	-0.3	+0.4	-2.9	-0.3	-0.5
$K(1830)$ L_B+1	+0.2	+0.0	-0.2	+0.3	+0.2	+0.1	+0.2	-0.9	-1.3	+0.3	+0.1	-1.6	+1.1	+0.0	-0.5
K_1' L_{K^*}+2	+1.0	+2.0	+6.1	+1.9	+3.3	+0.9	-0.1	+4.0	-9.2	+4.4	-1.0	+6.5	-20.9	+0.0	-6.2
K_1' L_B+1	+0.0	+0.2	+1.9	+0.1	-0.8	+0.0	+0.1	+0.3	+1.2	+0.8	+0.0	+1.4	+0.2	+0.2	+0.6
$K_2^*(1980)$ L_B+1	+0.2	-0.6	-2.7	-0.3	+2.4	-2.9	-0.4	-0.1	+0.4	+1.5	+0.1	-0.9	+1.6	+0.2	+0.3
Total	+3.2	+2.2	+7.3	+2.1	+10.6	+1.4	+1.0	+0.3	+1.3	+10.8	+1.7	+9.0	+12.4	+1.5	+1.2
sys.	+0.0	-1.2	-6.2	-0.5	-0.8	-4.6	-1.2	-4.7	-9.6	-11.2	-1.6	-6.8	-24.9	-0.8	-8.5

Table 25: Summary of the systematic errors, due to variation in the L-value used in decays, on the parameters of the $K^{*+} \to \phi K^+$ states with $J^P = 2^-$ and 1^+. All numbers for masses and widths are in MeV and fit fractions in %.

sys	2^-	$K_2(1770)$			$K_2(1820)$			1^+	K_1			K_1'			$\mathrm{NR}_{\phi K}$
var	FF	M_0	Γ_0	FF	M_0	Γ_0	FF	FF	M_0	Γ_0	FF	M_0	Γ_0	FF	FF
K_1 L_{K^*}+2	-0.4	-4.7	-20.9	-2.0	+1.6	-4.3	-0.6	-0.3	-43.6	-28.7	+2.3	+35.1	-63.0	-7.5	-1.9
K_1 L_B+1	+0.0	-3.4	-15.0	+0.1	-0.5	+2.7	+0.6	-0.4	-6.0	-14.9	-0.3	+0.1	-17.4	-0.5	+2.1
$K(1680)$ L_B+1	-0.1	-0.5	-5.2	+0.3	-0.8	+0.4	+0.3	-0.3	+8.1	-0.3	+0.5	+2.8	-12.2	-0.9	+0.5
$K_2(1770)$ L_{K^*}+2	-1.3	-62.1	-124.0	-7.5	-4.9	-33.2	-6.2	+0.3	-19.1	-41.5	+0.3	+12.2	-10.4	-3.7	+4.5
$K_2(1770)$ L_B+1	+0.3	+7.6	+20.4	-0.9	+4.4	-0.4	-0.6	-0.2	+4.4	+15.6	+0.2	-4.8	-2.3	+0.0	-0.6
$K_2(1820)$ L_{K^*}+2	+0.6	-10.5	-15.1	-3.7	-24.8	-38.4	-3.8	-1.7	-3.1	+4.3	+2.5	-10.2	-10.3	+4.8	+0.6
$K_2(1820)$ L_B+1	+0.0	+3.8	+6.5	+3.4	-0.9	+13.0	+3.0	+0.0	-1.3	-12.0	-0.4	-1.8	-10.6	-0.5	-0.2
$K(1830)$ L_B+1	+0.1	-1.2	-4.5	+0.6	-1.9	+2.6	+0.8	-1.0	-5.5	-11.3	-0.3	-3.4	-18.1	-0.6	-0.2
K_1' L_{K^*}+2	-0.5	-2.0	+48.8	-3.1	-17.9	-30.1	-4.3	+0.1	+20.3	-42.5	0.0	-159.5	+8.6	+0.0	+0.0
K_1' L_B+1	+0.0	+1.4	+9.3	-1.3	+2.8	-6.4	-1.3	+0.7	-3.8	+12.4	-0.6	+29.4	+36.8	-1.9	-0.9
$K_2^*(1980)$ L_B+1	+0.1	+0.8	-6.3	+1.4	-3.1	+3.5	+1.4	-0.6	-1.6	-9.8	-0.4	+1.2	-13.4	-0.8	-0.1
Total	+0.7	+8.6	+54.1	+3.7	+5.5	+14.0	+3.5	+0.8	+22.3	+20.4	+3.4	+47.5	+37.7	+4.8	+5.0
sys.	-1.5	-63.3	-127.9	-9.3	-31.2	-59.5	-8.6	-2.2	-48.6	-70.3	-0.9	-159.9	-72.5	-8.7	-2.2

Table 26: Summary of the systematic errors, after variation of the L-value used in the decays, on the parameters of the $K^{*+} \to \phi K^+$ states with $J^P = 0^-$, 1^- and 2^+. All numbers for masses and widths are in MeV and fit fractions in %.

systematic	1^- $K(1680)$			0^- $K(1830)$			2^+ $K_2^*(1980)$		
variation	M_0	Γ_0	FF	M_0	Γ_0	FF	M_0	Γ_0	FF
K_1 L_{K^*}+2	-2.8	-13.2	+0.0	-15.6	+17.4	+0.3	-2.3	+27.0	+0.2
K_1 L_B+1	+1.6	+3.1	+0.0	-8.6	+8.3	+0.1	-2.3	+1.1	+0.1
$K(1680)$ L_B+1	+13.5	+54.9	-0.1	-1.5	+1.5	+0.0	+0.1	-3.1	+0.0
$K_2(1770)$ L_{K^*}+2	+0.5	+21.6	+1.4	-7.3	+11.5	+0.3	+16.5	+99.6	+0.0
$K_2(1770)$ L_B+1	+0.0	-1.4	-0.2	+2.8	-4.4	-0.1	-10.9	-29.8	+0.0
$K_2(1820)$ L_{K^*}+2	+4.0	+3.2	+0.1	-39.9	+43.1	+0.4	-12.6	-55.0	+0.0
$K_2(1820)$ L_B+1	-0.5	+0.3	+0.0	-0.4	+0.8	+0.1	+4.4	+15.8	+0.1
$K(1830)$ L_B+1	+1.1	+3.0	+0.1	-2.0	+17.3	+0.3	-8.7	-13.6	+0.1
K_1' L_{K^*}+2	-17.4	-42.6	+1.1	+9.8	-27.7	-0.2	+45.2	+135.4	-0.3
K_1' L_B+1	-1.5	-2.6	-0.1	+7.7	-13.4	-0.1	+8.3	+21.2	-0.1
$K_2^*(1980)$ L_B+1	-0.4	+1.8	+0.1	-2.0	+1.3	+0.1	+17.3	-86.2	-0.1
Total	+14.2	+59.3	+1.8	+12.8	+51.6	+0.7	+52.0	+172.3	+0.3
sys.	-17.7	-44.7	-0.2	-44.4	-31.1	-0.2	-19.1	-107.4	-0.3

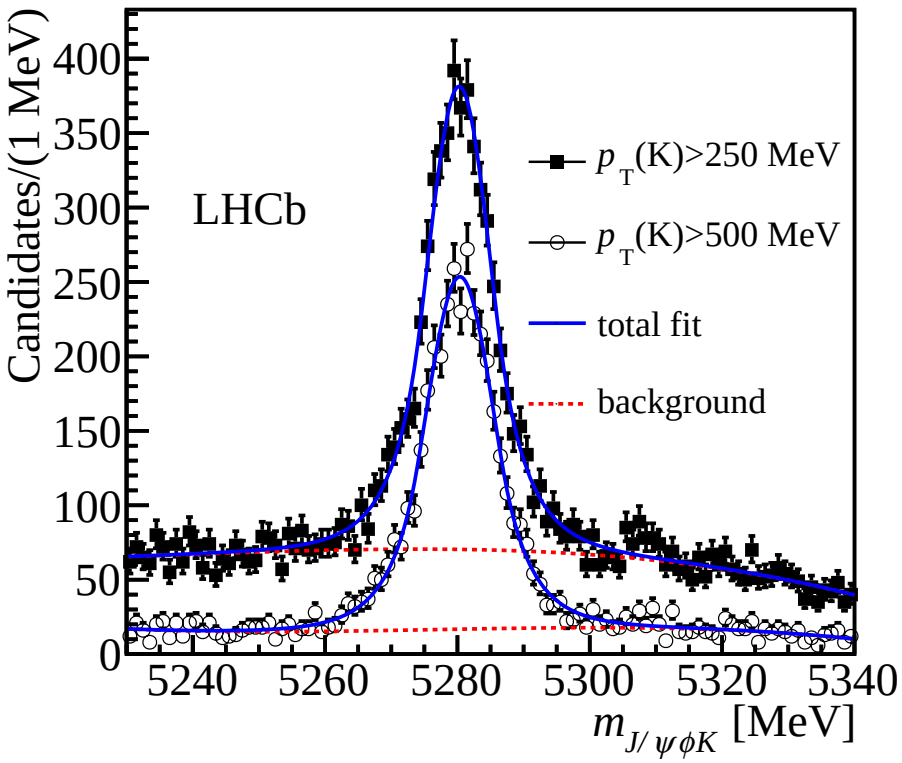

Figure 59: Mass of $B^+ \to J/\psi\,\phi K^+$ candidates in the data with the $p_{\rm T}(K) > 250\,{\rm MeV}$ (default) and $p_{\rm T}(K) > 500\,{\rm MeV}$ selection requirements.

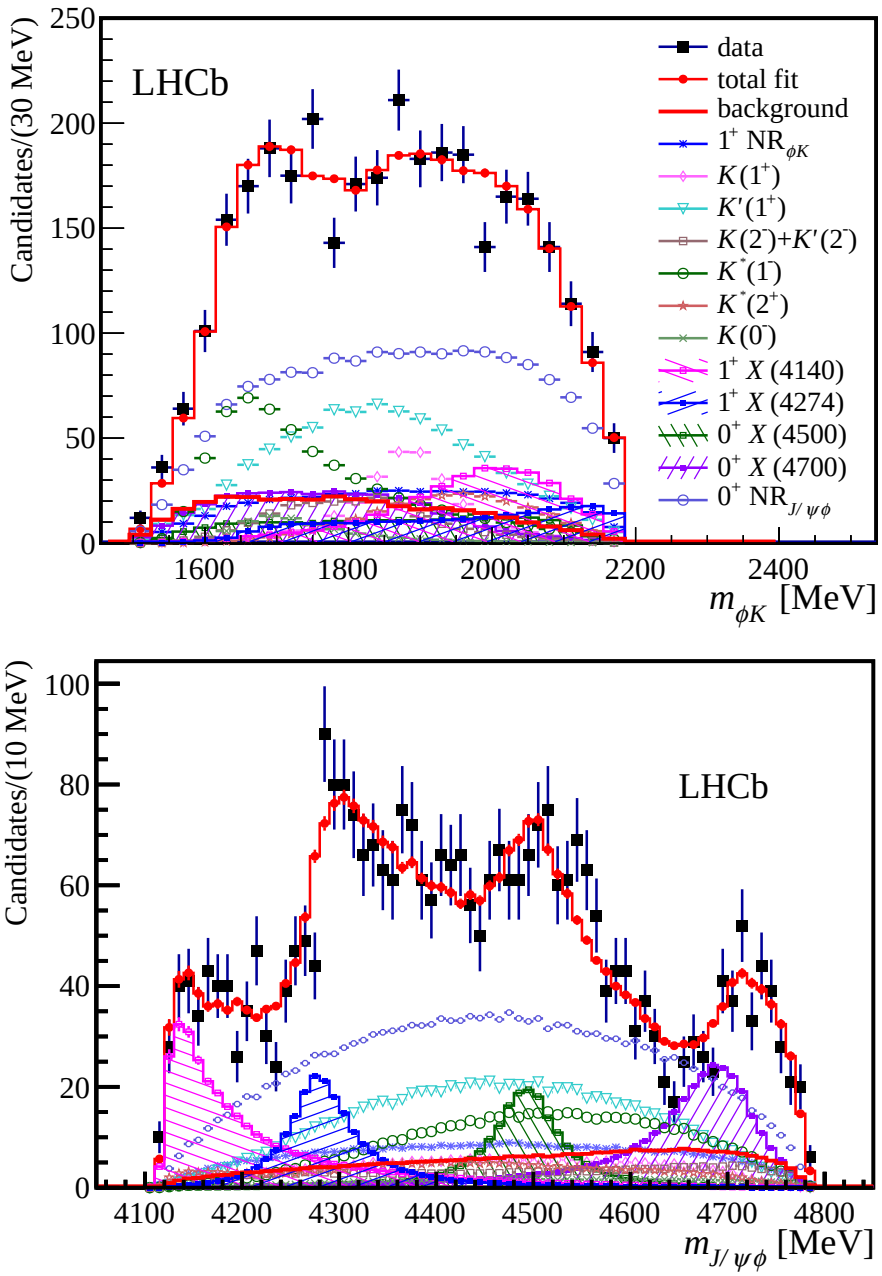

Figure 60: The distribution of $m_{\phi K}$ (top) and $m_{J/\psi\phi}$ (bottom) for the data and the fit of the default model with the tighter cut of $p_{\rm T}(K) > 500$. See the legend in the top for the description. Compare to Figs. 45-46 obtained with the default cuts.

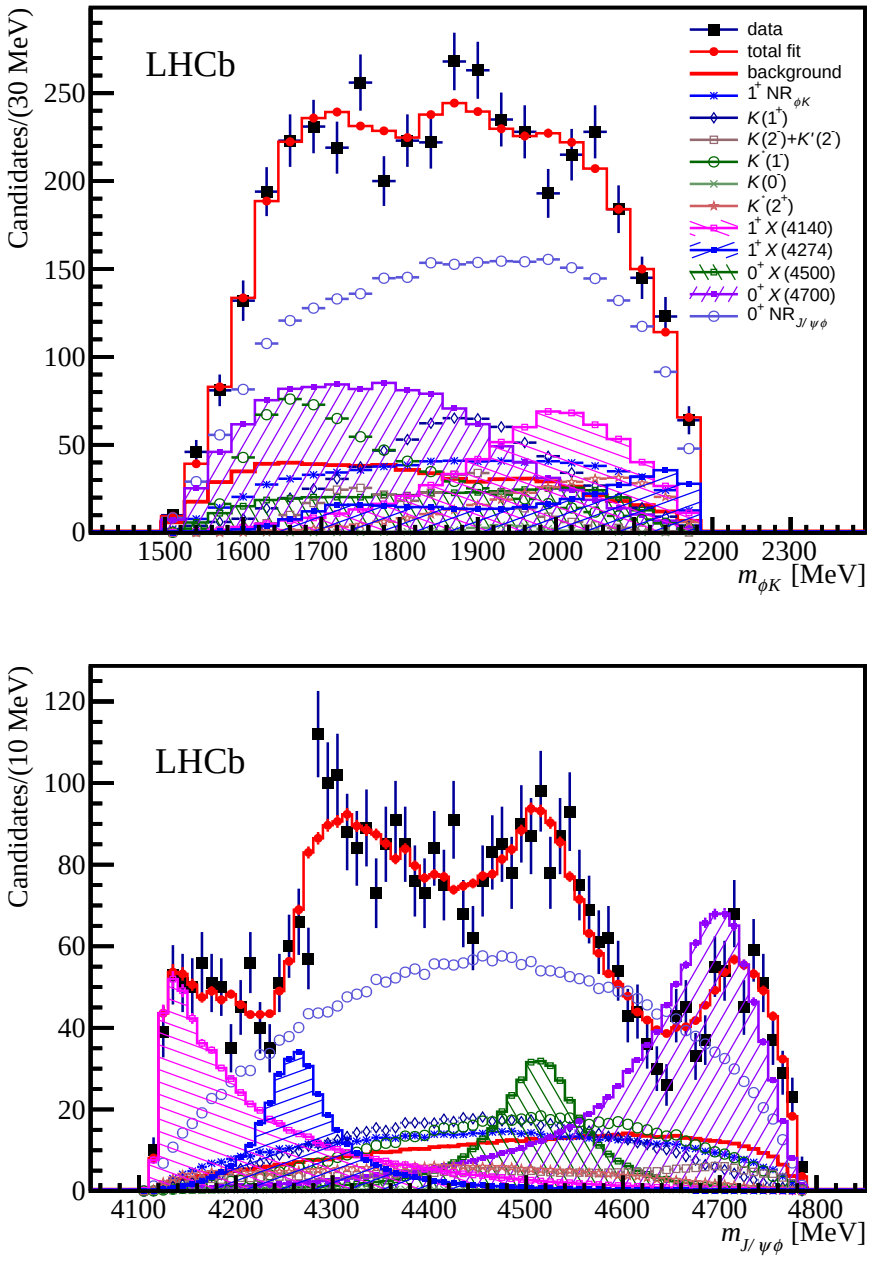

Figure 61: The distribution of $m_{\phi K}$ (top) and $m_{J/\psi\phi}$ (bottom) for the data and the fit of the default model with the tighter cut of $DLL_{\rm sig/bkg} < 0$. See the legend in the top for the description. Compare to Figs. 45-46 obtained with the default cuts.

To probe a sensitivity of the significance of the X states to systematic effects, we have investigated fit variations which have produced the largest changes in values of the parameters describing these states. The results of this study are shown in Table 27. No dramatic changes are observed.

Table 27: Significance of the X states for various systematic variations evaluated assuming $\chi^2(\text{ndf} = 2\Delta n_{\text{par}})$ distribution for $\Delta(-2\ln\mathcal{L})$. The lowest value for each state is highlighted.

sys. variation	$X(4140)$	$X(4274)$	$X(4500)$	$X(4700)$
default	9.0	6.8	6.7	6.1
K_1' L_{K^*}+2	11.2	6.8	6.7	8.0
$K_2(1770)$ L_{K^*}+2	9.2	**6.0**	6.4	5.7
$K_3^*(1780)(3^-)$	**8.4**	6.9	**6.1**	**5.6**
NR exp	9.6	6.9	7.3	6.7
$K^{*'}(1^-)$	8.6	6.2	7.3	6.9
$K^{'''}(2^-)$	9.7	6.5	6.2	6.0

10 Spin analysis

To determine the quantum numbers of each X state, fits are done under alternative spin and parity hypotheses. The likelihood-ratio test is used to quantify the rejection of these hypotheses. Since different spin assignments are represented by different functions in the angular part of the fit PDF, they represent separate hypotheses. For two models representing separate hypotheses, assuming a χ^2 distribution with one degree of freedom (ndf = 1) for $\Delta(-2\ln\mathcal{L})$ under the disfavored J^P hypothesis gives a lower limit on the significance of its rejection, *i.e.* p–value [51]. Statistical simulations can be employed and usually lead to a higher rejection level, since the data give positive $\Delta(-2\ln\mathcal{L})$ values[26] while $\Delta(-2\ln\mathcal{L})$ distribution under the disfavored hypothesis tends to peak at large negative values (see *e.g.* Ref. [52]) unlike the $\chi^2(\text{ndf} = 1)$ distribution which cannot extend below zero. Since our fits are very CPU intensive we rely on the lower significance limit given by the χ^2 method, in which the significance of the rejection can be simply calculated as $\sqrt{\Delta(-2\ln\mathcal{L})}$.

The results for the default fit approach are shown in Table 28. The spin of $X(4140)$ state is determined to be 1^+ with 7.6σ significance. The spin of $X(4274)$ state is established to be also 1^+ at 6.4σ level. The spins of $X(4500)$ and of $X(4700)$ states are established to be 0^+ at 5.2σ and 4.9σ level, respectively.

Given the limitations on available CPU resources[27], it is an impossible task to perform as many systematic variations as we did for the mass and width determinations in Sec. 9, for every J^P hypothesis and four exotic candidates. Therefore, we have investigated one (or two) alternative J^P assignment for each state with the smallest separation from the favored quantum numbers in the default fit model and we pick the systematic variations which had the biggest effect on parameters of these states. This study is summarized in

[26] $\Delta(-2\ln\mathcal{L}) \equiv (-2\ln\mathcal{L})_{\text{disfavored J}^\text{P}} - (-2\ln\mathcal{L})_{\text{favored J}^\text{P}} > 0$.

[27] Each fit requires about 2 days of exclusive use of a 12-core computer. Multi-core computing resources are not easily available.

Table 28: Significance of J^P preference for the X states in the default model. The lowest value for each state is highlighted.

J^P/Component	$X(4140)$	$X(4274)$	$X(4500)$	$X(4700)$
0^+	10.3σ	7.8σ	preferred	preferred
0^-	12.5σ	7.0σ	8.1σ	8.2σ
1^+	preferred	preferred	$\mathbf{5.2}\sigma$	$\mathbf{4.9}\sigma$
1^-	10.4σ	$\mathbf{6.4}\sigma$	6.5σ	8.3σ
2^+	$\mathbf{7.6}\sigma$	7.2σ	5.6σ	6.8σ
2^-	9.6σ	6.4σ	6.5σ	6.3σ

Table 29. Accepting the lowest rejection figure found, the significance of 1^+ determination for $X(4140)$ ($X(4274)$) is 5.7σ (5.8σ) and of 0^+ determination for $X(4500)$ ($X(4700)$) is 4.0σ (4.5σ).

Table 29: Effect of systematic variations on the significance of the J^P determination for the four X states. The lowest significance found for each state is highlighted.

systematic variation	1^+ $X(4140)$	1^+ $X(4274)$		0^+ $X(4500)$		0^+ $X(4700)$
alternative J^P	2^+	1^-	2^-	1^+	2^+	1^+
default	7.6	6.4	6.4	5.2	5.6	4.9
K_1' L_K^*+2	12.2	6.2	7.4	5.4	6.5	5.1
$K_2(1770)$ L_K^*+2	**5.7**	6.0	**5.8**	5.2	4.9	4.5
$K_3^*(1780)$ (3^-)	6.2	6.6	6.3	4.9	5.1	**4.5**
NR exp	7.5	6.5	6.1	8.9	5.8	4.7
$K^{*\prime}(1^-)$	6.8	6.1	**5.8**	5.8	6.2	4.7
$K^{\prime\prime\prime}(2^-)$	6.9	6.7	6.2	**4.0**	6.6	4.8

11 Coupled channel threshold effects from pairs of D_s excitations

The quark content of $D_s^{(*)+}D_s^{(*)-}$ pairs, where $D_s^{(*)+}$ denotes D_s^+ excitations (D_s^+, D_s^{*+}, $D_{s0}^*(2317)^+$, $D_{s1}(2460)^+$, $D_{s1}(2536)^+$, $D_{s2}^*(2573)^+$), is the same as of $J/\psi\,\phi$. Virtual $D_s^{(*)+}D_s^{(*)-}$ pairs can be produced in $B^+ \to K^+[D_s^{(*)+}D_s^{(*)-}]$ decays and rearrange their quark content to materialize as a $J/\psi\,\phi$ final state. Many $D_s^{(*)+}D_s^{(*)-}$ thresholds fall in kinematically allowed $m_{J/\psi\,\phi}$ range.

Attractive forces between the D_s^* mesons can give a rise to a molecular bound state. Because molecular binding energies are unlikely to be large, masses of such states are expected not too far below the production threshold for the unbound meson pairs. For example, deutron has binding energy of 2 MeV, while even in heavy nuclei they stay below 9 MeV per nucleon. Molecular forces drop quickly to zero beyond rather small interaction ranges, thus only the ground state is expected to be bound. That implies no angular momentum between mesons ($L_{D_sD_s} = 0$). Therefore quantum numbers of the molecular state are those which can be obtained from addition of spins of the constituent mesons, and its parity is simply a product of the constituent parities.

Molecular forces are often described with pion exchange. The $D_s^{(*)}$ mesons have no isospin, thus coupling via pion exchange would be isospin violating. This did not stop several authors from suggesting that the $X(4140)$ state is a 0^{++} or 2^{++} $D_s^{*+}D_s^{*-}$ molecule with ~ 83 MeV binding (this threshold is at 4266 MeV) [53–57]. Some authors used η and ϕ exchange model [53, 56], while others used QCD sum rules [54, 55, 57]. However, Wang *et al.* used QCD sum rules and found such system not to form a bound state [58]. The 1^{++} quantum numbers are not allowed for such molecule [53], since $C = (-1)^{L+S}$ must be satisfied for identical D_s excitations in the $D_s\bar{D}_s$ pair ($C = C_{J/\psi}C_\phi = (-1)(-1) = +1$). Therefore, for an S-wave molecule ($L = 0$), $J = S$ must be even. It was also suggested

that the $X(4274)$ structure is a 0^{-+} $D_s^+ D_{s0}^-$ molecule with $\sim$ 12 MeV binding energy (this threshold is at 4286 MeV) [59, 60], which is a more plausible value.

Our default parameterization which assumes Breit-Wigner amplitudes for $J/\psi\,\phi$ mass peaks is appropriate for molecular bound states. Our 1^{++} assignment to the $X(4140)$ rules out its explanation as $D_s^{*+} D_s^{*-}$ molecule. Also our assignment of 1^{++} to $X(4274)$ does not match its molecular explanation as 0^{-+} $D_s^+ D_{s0}^-$ state. We have assigned 0^{++} to the presumed $X(4500)$ and $X(4700)$ resonances. The $D_{s0}^+ D_{s0}^-$ threshold is at 4635 MeV, which falls in the depression between these two peaks. We were unable to construct a model with only one 0^{++} resonances destructively interfering with the $\mathrm{NR}_{J/\psi\,\phi}$; with a free mass the state always ran away to one side or the other. With the fixed mass, the likelihood is significantly worse ($+77 = 8.8^2$). The $X(4500)$ is ~ 129 MeV below the threshold which seems too large to make it a molecular candidate.

Even if there is no bound state, opening of a threshold for production of unbound $D_s^{(*)+} D_s^{(*)-}$ pairs may produce a peaking structure called a cusp in the $J/\psi\,\phi$ mass distribution near the threshold mass value, as explicitly predicted for this channel by Swanson [61]. Couplings to cusps are expected to be large only for $L_{DsDs} = 0$, thus effective quantum numbers are the same as for molecular bound states made out of the same components.

The Breit-Wigner amplitude for an ideal bound state, which is not distorted by overlapping with a cusp, creates a circular trajectory in the complex plane (so called Argand diagram, with x-axis being the real component), with counter-clockwise motion with mass. The imaginary part of the amplitude peaks smoothly at the pole mass, while the real part crosses zero at this point passing from the positive to the negative values. Both obviously go to zero far from the pole mass. The magnitude peaks at the pole. The complex phase starts at zero, undergoes rapid change where the magnitude peaks, crossing 90^o at the pole and then flattens out to 180^o far above the pole mass. With the present data statistics replacing Breit-Wigner amplitudes with model independent amplitudes

binned in mass in attempt to obtain Argand diagrams does not lead to useful results. In this section we investigate the possibility that some of the observed $J/\psi\,\phi$ structures can be interpreted as cusps, which differ from Breit-Wigners in a more subtle way.

A cusp amplitude is also zero far away from the threshold (see Fig. 62 and its explanation below). There is no imaginary part below the threshold. The real part is positive and peaks sharply towards the threshold. It starts dropping abruptly above the threshold, crosses to negative side before it tends to zero way above the threshold. The imaginary part is positive and rises from zero above the threshold, peaks, and then decreases to zero. This gives a trajectory on the Argand diagram which is also counter-clockwise with mass, but it is not circular (Fig. 63). The exact shape of the trajectory is model dependent.

We employ a relatively simple model of cusps by Swanson [62] (this is an improved model over his initial work in Ref. [61]). A virtual loop with two mesons A and B inside (Fig.1 left in Ref. [62]) contributes in non-relativistic near-threshold approximation the following amplitude:[28]

$$\Pi(m) = \int \frac{d^3q}{(2\pi)^3} \frac{q^{2l}\, e^{-2q^2/\beta_{AB}^2}}{m - M_A - M_B - \frac{q^2}{2\,\mu_{AB}} + i\,\epsilon}, \tag{45}$$

where m is $J/\psi\,\phi$ mass, μ_{AB} is the reduced mass of the pair ($= M_A\,M_B/(M_A + M_B)$), ϵ is a very small number ($\epsilon \to 0$), l is the angular momentum between A and B. The lowest l value is expected to dominate. The denominator of the integrand in Eq. (45) is related to virtual-D_s propagators. The numerator contains an exponential form-factor, taking into account that hadrons are not point-like objects, which has a free parameter β_{AB} which should be at a typical hadronic scale of order of $\Lambda_{\rm QCD}$ (can be AB dependent). The formula contains purely "kinematical" terms and does not implement any dynamics between the virtual Ds pairs.

[28]The formulae are not given explicitly in Ref. [62]. We have obtained them directly from the author.

The above integral (Eq. (45)) can be conveniently expressed as:

$$\Pi(m) = -\frac{\mu_{AB}\,\beta_{AB}}{\sqrt{2}\pi^2}\,I(Z) \tag{46}$$

$$Z = \frac{4\mu_{AB}}{\beta_{AB}^2}(M_A + M_B - m) \tag{47}$$

$$I(Z) = \int_0^\infty dx\,\frac{x^{2+2l}\,e^{-x^2}}{x^2 + Z - i\,\epsilon}, \tag{48}$$

where $-Z$ is the scaled mass deviation from the AB threshold. For $l = 0$, the integral above evaluates to:

$$I(Z) = \frac{1}{2}\,\sqrt{\pi}[1 - \sqrt{\pi\,Z}\,e^Z\,\mathrm{erfc}(\sqrt{Z})]. \tag{49}$$

For masses below the AB threshold $Z > 0$ and $I(Z)$ (thus $\Pi(Z)$) has no imaginary part. For masses above the threshold $Z < 0$, $\sqrt{Z}$ is complex, which leads both to the real and imaginary parts having non-zero magnitude. The real and imaginary parts of $-I(Z)$ in a function of $-Z$, which are proportional to the real and imaginary parts of $\Pi(m)$ in a function of $m - m_A - m_B$ are shown in Fig. 62, while the corresponding Argand diagram is shown in Fig. 63.

The function $\Pi(m)$ replaces the $BW(m|M_0, \Gamma_0)$ in Eq. (35), however the Blatt-Weisskopf functions in Eq. (34) still apply.[29]

All possible $D_s^{(*)+}D_s^{(*)-}$ cusps with shapes predicted using the Swanson's model are shown in Fig. 64. It is clear that the $D_s^+D_s^{*-}$ cusp, which peaks below the $J/\psi\,\phi$ kinematic threshold, is a good candidate to explain the 1^+ $X(4140)$ structure. It is also enticing to try the $D_s^+D_{s0}^{*-}$ cusp as an explanation for the $X(4274)$ structure, since it peaks at the right mass, even though this cusp is expected with 0^- quantum numbers which don't agree with 1^+ obtained in our analysis. The $D_s^{*+}D_{s1}(2536)^{*-}$ cusp peaks near the $X(4500)$ structure, again with mismatch of its 1^- quantum numbers with 0^+ from our Breit-Wigner based

[29]This was done on advice from E. Swanson.

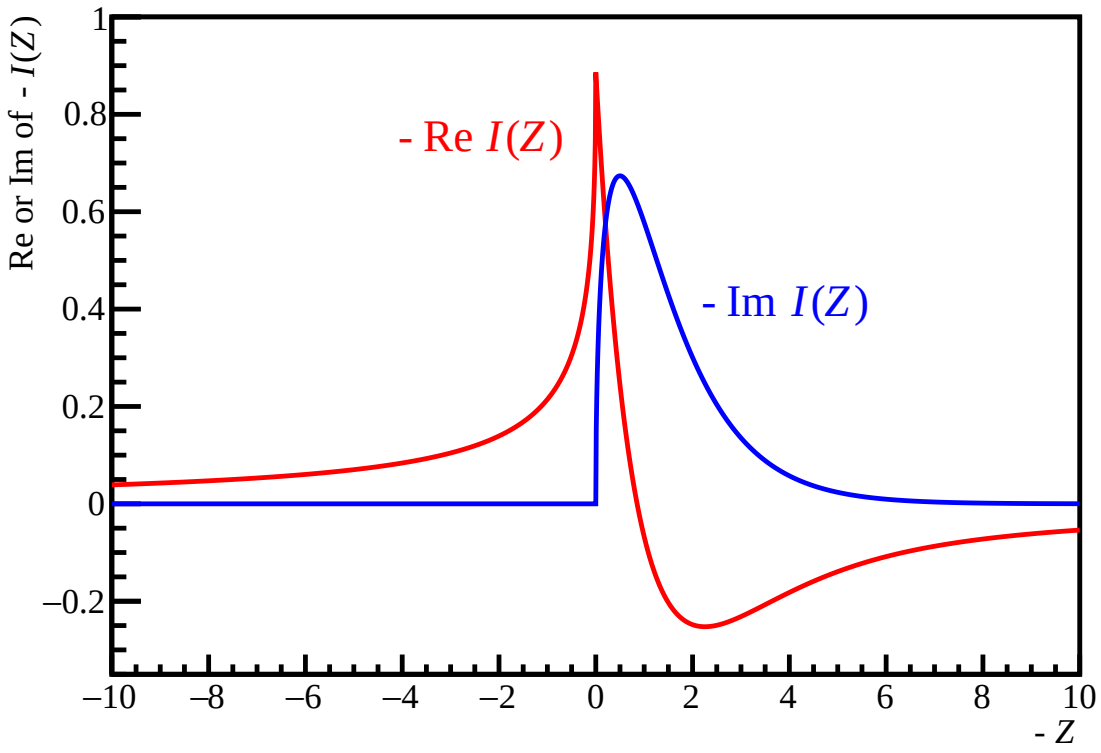

Figure 62: Dependence of the real and imaginary parts of the cusp amplitude on the mass in the Swanson's model. See the text for a more precise explanation what is plotted.

analysis. Similarly the $D_s^{*+}D_{s2}^{*-}$ 1^-, 2^- and 3^- cusps peak near the $X(4700)$ structure but do not match 0^+ from our default analysis. There is an abundance of cusps at the high mass region which perhaps can interfere and complicate the analysis.

In the initial exploration we have used the $D_s^+D_s^{*-}$ 1^+ cusp for $X(4140)$ and the $D_s^+D_{s0}^{*-}$ 0^- cusp for $X(4274)$, while leaving the high mass X structure as that used in the default approach ($\mathrm{NR}_{J/\psi\phi}$ plus two 0^+ Breit-Wigner amplitudes). We also did not allow B_{LS} cusp amplitudes with L larger than the minimal value ("Lmin" constraint). The fit results are compared to our default fit in Table 30. The mass projections are shown in Figs 65, 66 and 67. The $\Delta(-2\ln\mathcal{L})$ value is worse by $43.7 = 6.6^2$ but with 10 fewer parameters. To check that this is not due to the Lmin constraint, we also performed the fit in which we allowed

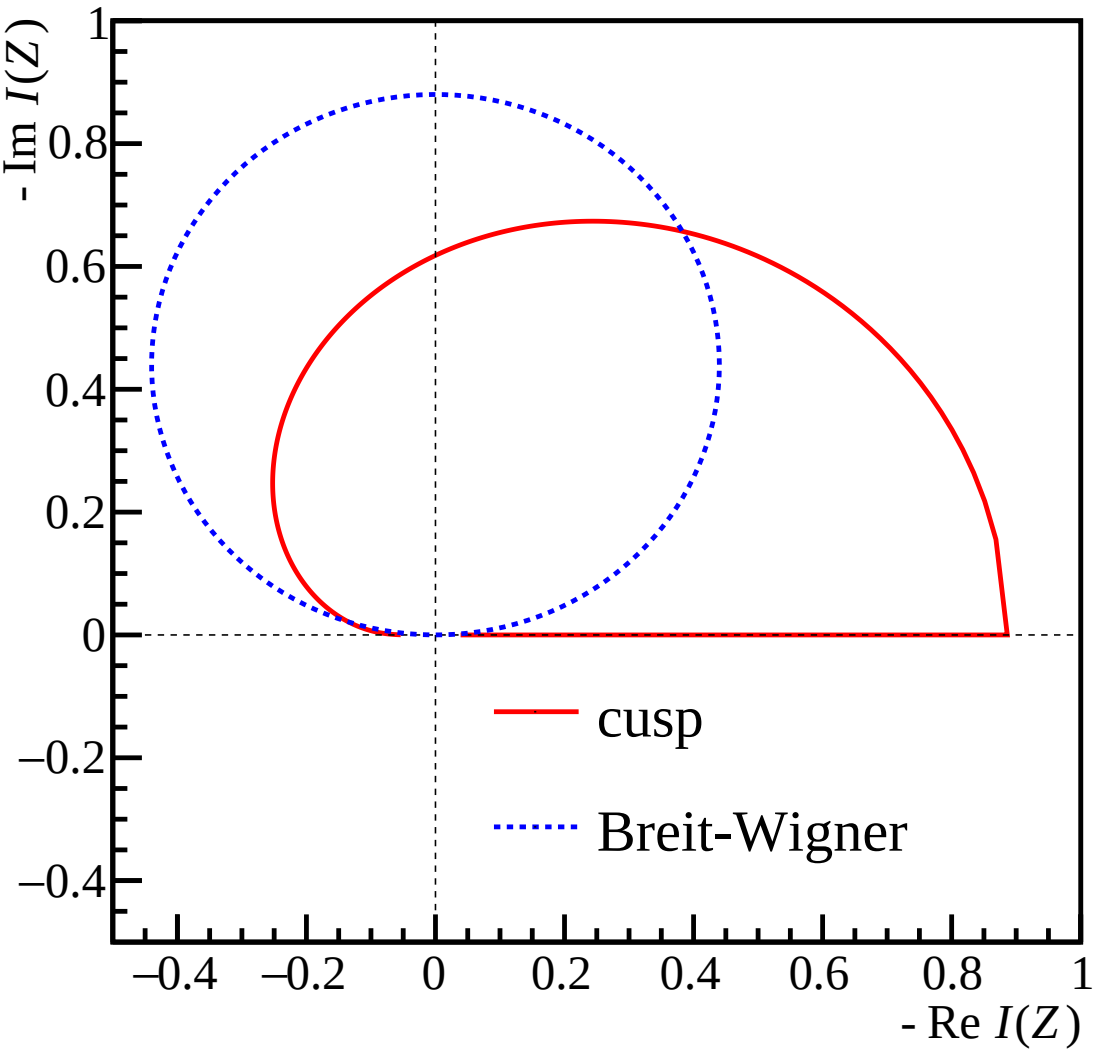

Figure 63: The Argand diagram of the the cusp amplitude in the Swanson's model. Motion with the mass is counter-clockwise. See the text for a more precise explanation what is plotted.

all B_{LS} cusp amplitudes. Now the likelihood is $34.3 = 5.9^2$ worse than the default fit for only 4 fewer fit parameters. The higher-L B_{LS} amplitudes are only 1.9σ significant. The default fit is also preferred by χ^2_{6D}, χ^2_{2D} and 1D fit qualities in mass projections, but by the smaller margins than from the fit likelihood values. Even though cusps with l different from zero are not expected to be prominent we have tried $l = 1$ option for the $D_s^+ D_{s0}^-$ cusp

to make its effective quantum numbers 1^+. This did not improve the fit qualities much. Therefore, we have also tried a fit in which $X(4274)$ is a 1^+ resonance, but the $X(4140)$ is represented by the $D_s^+ D_s^{*-}$ 1^+ cusp. The mass projections are shown in Figs 68, 69 and 70. This fit has the likelihood and χ^2_{6D} which are better than the default fit by an insignificant amount (1.6^2 and 1.8^2, respectively). The χ^2_{2D} on the Dalitz plane and fit qualities of 1D mass projections are about equal, as well. In these fits, the results for the K^* states and for $X(4500)$ and $X(4700)$ parameters stay very close to the default fit results, especially for the fit with one cusp only. The values of β obtained in the fits are close to a value of 300 MeV, with which Swanson was successful in describing the other near-threshold exotic meson candidates [62]. Since the default resonant model of $X(4140)$ has a much larger number of free parameters (8) than the cusp representation (3), we have also performed a fit with a modified default model in which we allowed only S-wave decays for $X(4140)$ like in the cusp model. This is justified since the combined significance of all D-wave couplings is only 0.9σ. This brings the number of free $X(4140)$ parameters down to 4, thus only 1 more than in the cusp representation. This is perhaps a more fair comparison between these models. The cusp model is preferred by $\Delta(-2\ln\mathcal{L})_{\rm data} = 3.0^2$. Simulations of pseudoexperiments from the Breit-Wigner amplitude model, and then fit with the Breit-Wigner and cusp models gives an average $\Delta(-2\ln\mathcal{L})$ of -9.7 ± 1.0 with RMS of 6.8 ± 1.0 for the same sign convention. Thus, the data are inconsistent with the Breit-Wigner model at $(2.8 \pm 0.4)\sigma$ level. This estimate, based on the simulations, is in agreement with the value obtained using the asymptotic theorem for separate hypotheses: $\sqrt{\Delta(-2\ln\mathcal{L})} = 3.0\sigma$. While this may not be enough to rule out the resonant hypothesis for $X(4140)$, these results strongly suggest that molecular forces in $D_s^+ D_s^{*-}$ coupled channel may be responsible for its creation, and that this structure is not necessarily related to a bound state. The $D_s^+ D_s^{*-}$ cusp is only 36 MeV below the kinematic limit for $J/\psi\,\phi$ decay. This coincidence of the thresholds provides for very favorable conditions for rescattering of

$D_s^+ D_s^{*-}$ into $J/\psi\,\phi$, since the hadrons in both of these final states are nearly at rest in their center-of-mass frame. This mechanism provides a natural explanation for the peaking of the observed rate very near the kinematic boundary.

We have included the fit in which $X(4140)$ is represented as a cusp among the systematic variations used to determine parameters or the other components.

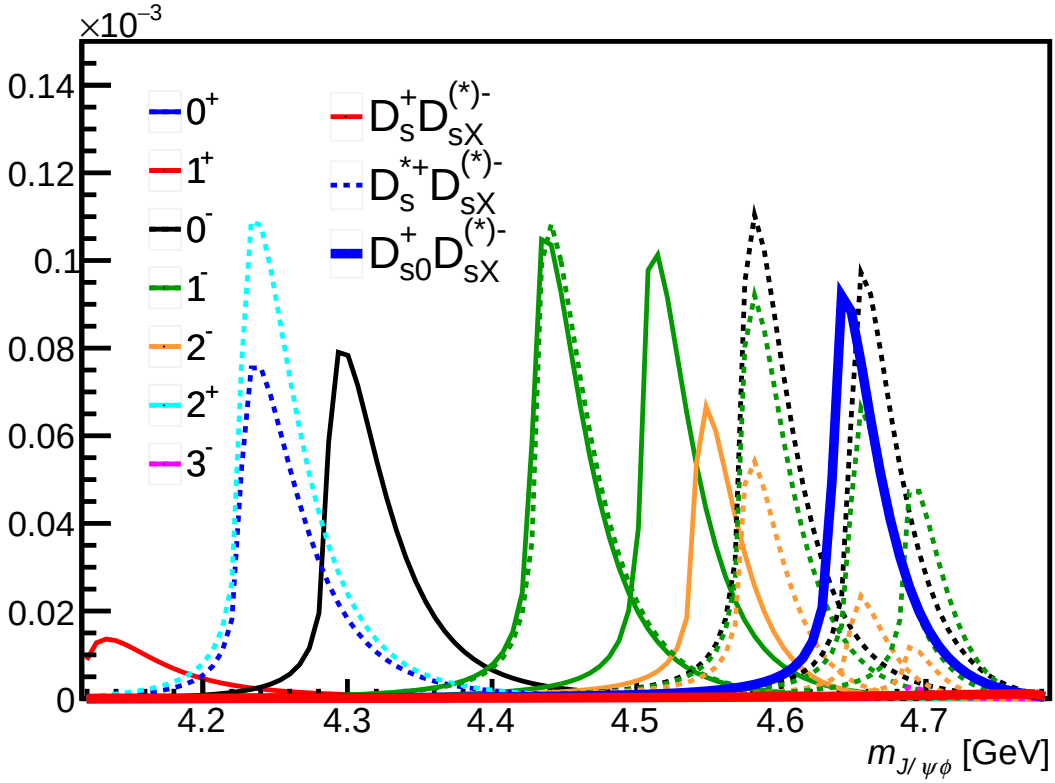

Figure 64: The shapes of $X = D_s^{(*)+} D_s^{(*)-}$ cusps predicted with Swanson's model using $\beta = 0.3$ GeV [62] and $l = 0$. Relative intensities of various cusps reflect the phase-space factors only assuming the minimal L_B and L_X values.

We have also tried a fit with no X Breit-Wigners but all possible cusps (Fig. 64) included in the fit (with the minimum L and S couplings). With 110 free parameters compared to the fit with only $X(4140)$ replaced by a cusp and the other three X peaks represented by Breit-Wigners (93 parameters) the $\Delta(-2\ln\mathcal{L})$ value is $66.1 = 8.1^2$ worse, favoring the 1 cusp plus 3 Breit-Wigners model (this fit is shown in Figs. 71-72).

Table 30: The results of fitting $X(4140)$ and $X(4274)$ structures as $D_s^+ D_s^{*-}$ 1^+ and $D_s^+ D_{s0}^-$ J_2^P (given below) cusps, respectively. Lmin (all L) means that the cusps were implemented allowing only the lowest (all) L in the corresponding B_{LS} couplings. The last column is for the fit in which only $X(4140)$ is represented as cusp. The change of likelihood or χ^2 (in brackets) values are given in form of number of standard deviations squared. Masses and widths are in MeV. Fit fractions are in percent.

Quantity	Default	Lmin,$J_2^P = 0^-$	all L,$J_2^P = 0^-$	Lmin,$J_2^P = 1^+$	Lmin
$n_{\rm par}$	98	88	92	88	93
$\Delta(-2\ln\mathcal{L})$	0.0	$+43.7 = 6.6^2$	$+34.3 = 5.9^2$	$+18.4 = 4.4^2$	$-2.6 = 1.6^2$
$(\Delta)\chi^2_{6D}$	462.88 (0.0)	478.54 ($+4.0^2$)	475.40 ($+3.5^2$)	474.80 ($+3.5^2$)	459.62 (-1.8^2)
$(\Delta)\chi^2_{2D}$	438.73 (0.0)	443.66 ($+1.1^2$)	440.3 ($+1.2^2$)	461.11 ($+4.7^2$)	438.84 ($+0.3^2$)
$p_{1D}(J/\psi\,\phi)$	33.1%	2.1%	2.8%	0.7%	35.5%
$p_{1D}(\phi K)$	1.9%	0.9%	2.1%	0.5%	1.6%
$p_{1D}(J/\psi\,K)$	57.6%	15.6%	17.4%	16.8%	49.7%
state					
$K(1^+)M_0$	1793 ± 59	1863 ± 41	1914 ± 62	1784 ± 16	1795 ± 37
Γ_0	365 ± 157	537 ± 100	607 ± 88	412 ± 57	421 ± 102
$K'(1^+)M_0$	1968 ± 65	1964 ± 31	1970 ± 21	1993 ± 50	1956 ± 35
Γ_0	396 ± 170	411 ± 77	420 ± 53	497 ± 151	437 ± 84
K_1 1^+ tot F.F.	41.7	40.5	40.2	44.6	43.5
$K(2^-)$ M_0	1777 ± 35	1766 ± 27	1752 ± 17	1823 ± 32	1802 ± 31
$K_2(1770)?$ Γ_0	217 ± 116	211 ± 68	131 ± 25	396 ± 119	260 ± 80
$K'(2^-)$ M_0	1853 ± 27	1844 ± 12	1875 ± 27	1831 ± 13	1853 ± 19
$K_2(1820)?$ Γ_0	167 ± 58	140 ± 33	205 ± 72	141 ± 28	178 ± 40
K_2 2^- tot F.F.	10.9	12.5	11.9	11.0	10.8
$K^*(1^-)$ M_0	1722 ± 20	1750 ± 20	1748 ± 19	1731 ± 14	1726 ± 19
$K^*(1680)?$ Γ_0	354 ± 75	422 ± 77	432 ± 77	388 ± 53	359 ± 69
F.F.	6.7	8.3	10.1	6.8	5.5
$K^*(2^+)M_0$	2073 ± 94	2045 ± 46	2046 ± 39	2105 ± 50	2099 ± 71
$K^*(1980)?$ Γ_0	678 ± 311	521 ± 151	536 ± 12	745 ± 174	684 ± 236
F.F.	2.9	2.8	2.7	3.2	2.7
$K(0^-)$ M_0	1874 ± 43	1870 ± 34	1875 ± 27	1879 ± 29	1882 ± 27
Γ_0	168 ± 90	218 ± 81	205 ± 72	186 ± 74	179 ± 75
F.F.	2.6	2.8	2.9	2.6	2.7
$X(4140)$ M_0	4146.5 ± 4.5				
Γ_0 (β)	82.8 ± 20.7	(247 ± 19)	(250 ± 12)	(244 ± 20)	(297 ± 20)
F.F.	13.0	12.1	10.0	10.6	13.9
$X(4274)M_0$	4273.3 ± 8.3				4279.7 ± 6.4
Γ_0 (β)	56.2 ± 10.9	(275 ± 40)	(255 ± 29)	(303 ± 21)	50.8 ± 11.3
F.F.	7.1	2.0	2.0	2.1	5.7
$X(4500)M_0$	4506.1 ± 11.1	4498.7 ± 7.5	4501.9 ± 6.2	4501.7 ± 6.1	4506.1 ± 9.4
Γ_0	91.9 ± 21.1	71.4 ± 14.6	79.2 ± 12.0	88.4 ± 14.8	93.1 ± 18.8
F.F.	6.6	4.8	4.6	5.7	6.8
$X(4700)M_0$	4704.2 ± 10.1	4709.7 ± 6.5	4711.0 ± 5.0	4709.6 ± 4.9	4706.1 ± 7.9
Γ_0	119.7 ± 30.7	96.7 ± 19.4	95.2 ± 14.7	109.8 ± 12.2	117.2 ± 25.2
F.F.	12.4	10.9	10.7	12.3	12.9
X 0^+ tot F.F.	27.6	21.6	21.5	24.5	26.4

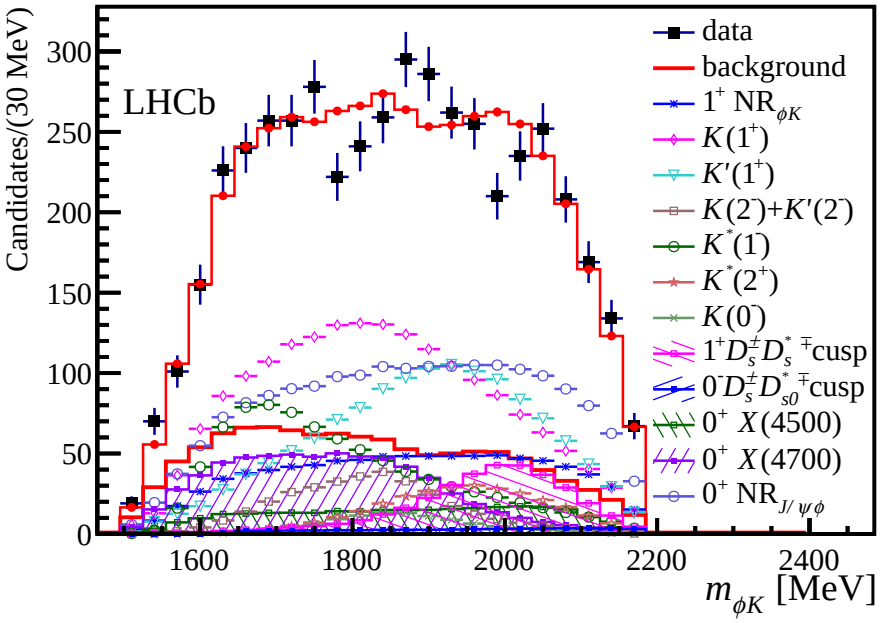

Figure 65: The invariant mass of ϕK with the data in black and the total fit in red when $X(4140)$ and $X(4274)$ are represented with $D_s^+ D_s^{*-}$ 1^+ and $D_s^+ D_{s0}^-$ 0^- cusps, respectively. Lmin approximation. The p_{1D} is 0.9%.

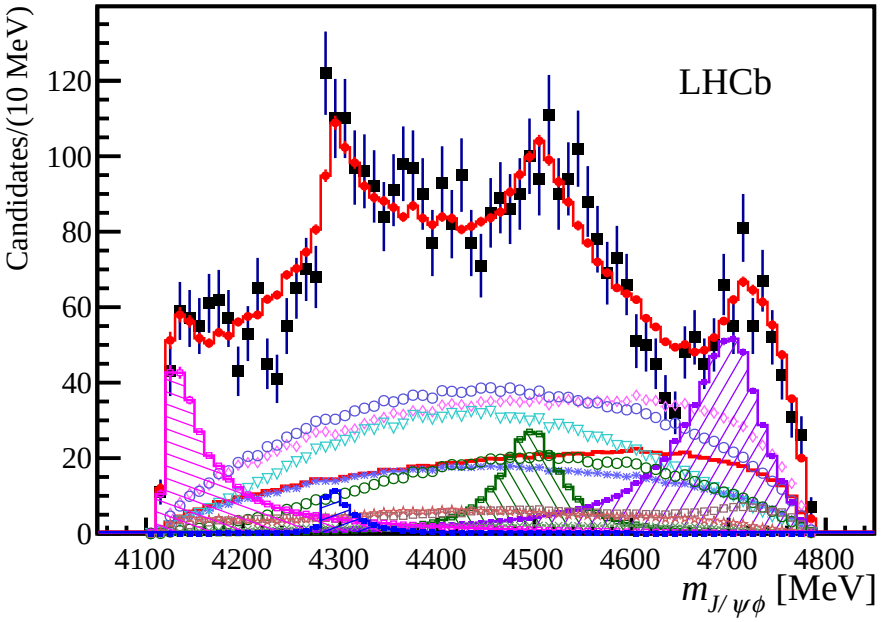

Figure 66: The invariant mass of $J/\psi\,\phi$ with the data in black and the total fit in red when $X(4140)$ and $X(4274)$ are represented with $D_s^+ D_s^{*-}$ 1^+ and $D_s^+ D_{s0}^-$ 0^- cusps, respectively. Lmin approximation. The p_{1D} is 2.1%.

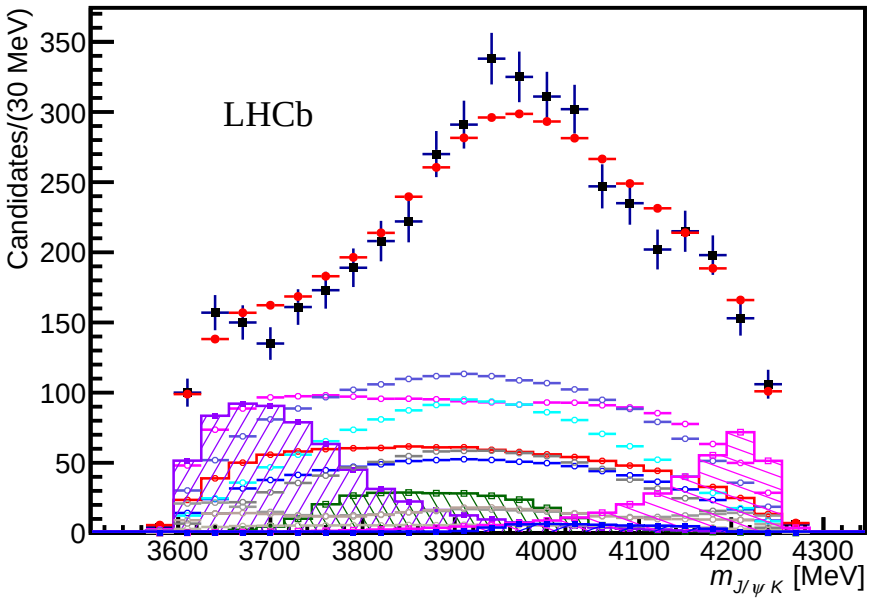

Figure 67: The invariant mass of $J/\psi K^+$ with the data in black and the total fit in red when $X(4140)$ and $X(4274)$ are represented with $D_s^+ D_s^{*-}$ 1^+ and $D_s^+ D_{s0}^-$ 0^- cusps, respectively. Lmin approximation. The p_{1D} is 15.6%.

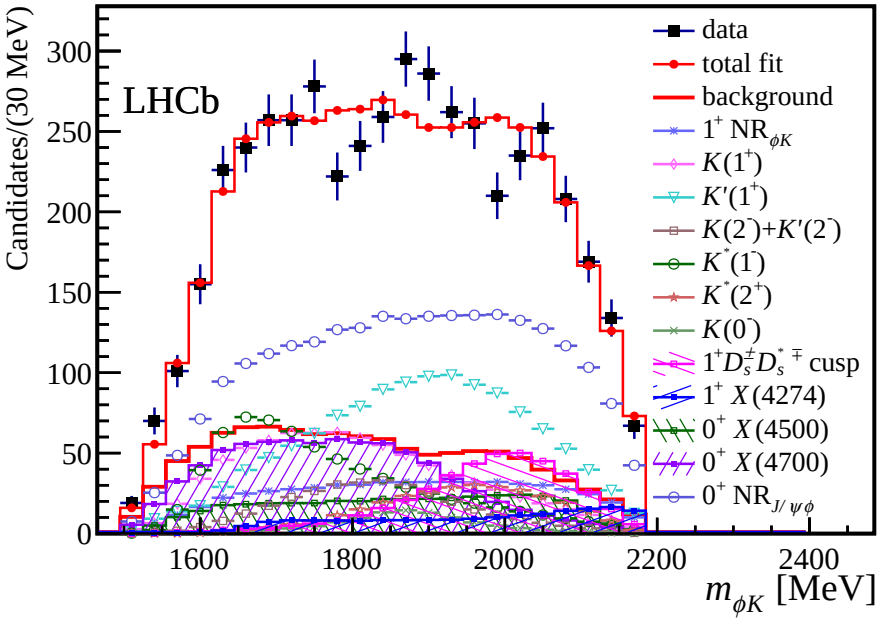

Figure 68: The invariant mass of ϕK with the data in black and the total fit in red when $X(4140)$ is represented with $D_s^+ D_s^{*-}$ 1^+ cusp. Lmin approximation. The p_{1D} is 1.6%.

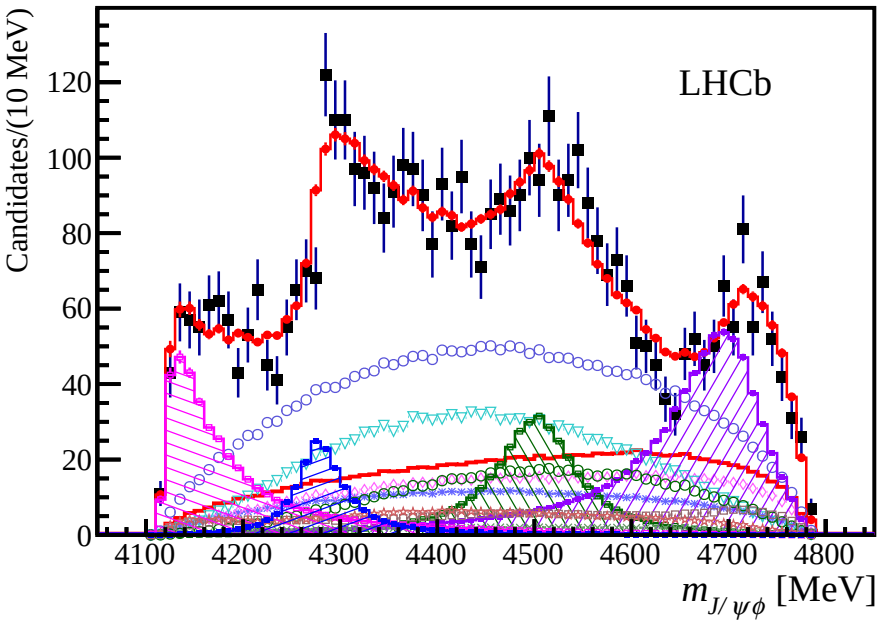

Figure 69: The invariant mass of $J/\psi\,\phi$ with the data in black and the total fit in red when $X(4140)$ is represented with $D_s^+ D_s^{*-}$ 1^+ cusp. Lmin approximation. The p_{1D} is 35.5%.

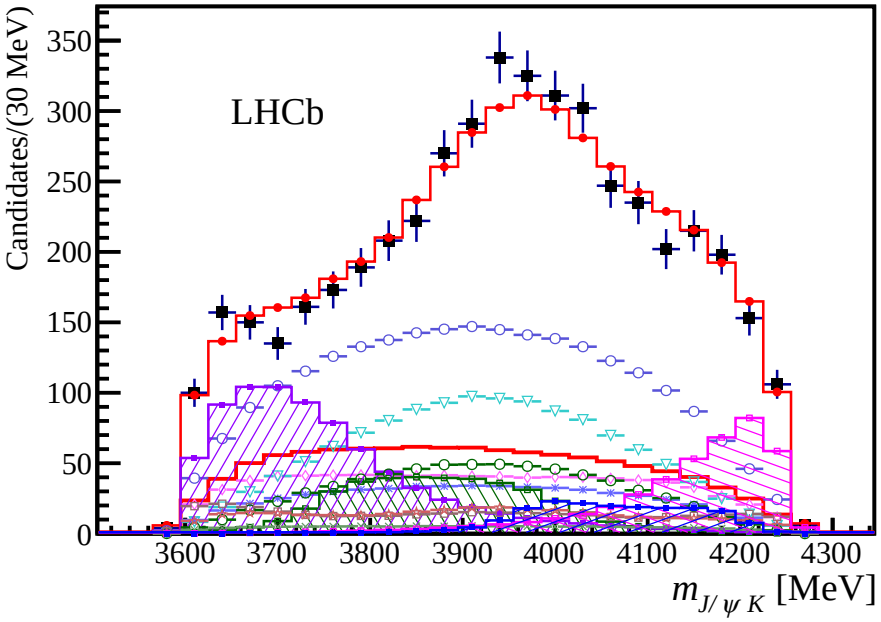

Figure 70: The invariant mass of $J/\psi K^+$ with the data in black and the total fit in red when $X(4140)$ is represented with $D_s^+ D_s^{*-}$ 1^+ cusp. Lmin approximation. The p_{1D} is 49.7%.

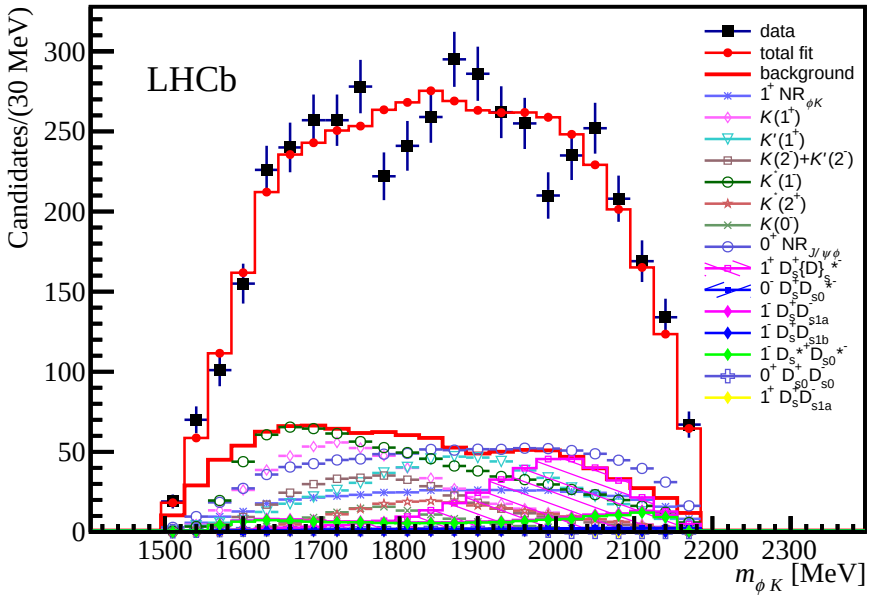

Figure 71: The invariant mass of ϕK with the data in black and the total fit in red when all predicted cusps are included. The p_{1D} is 1.9%. Many cusps with invisible contributions are not labeled.

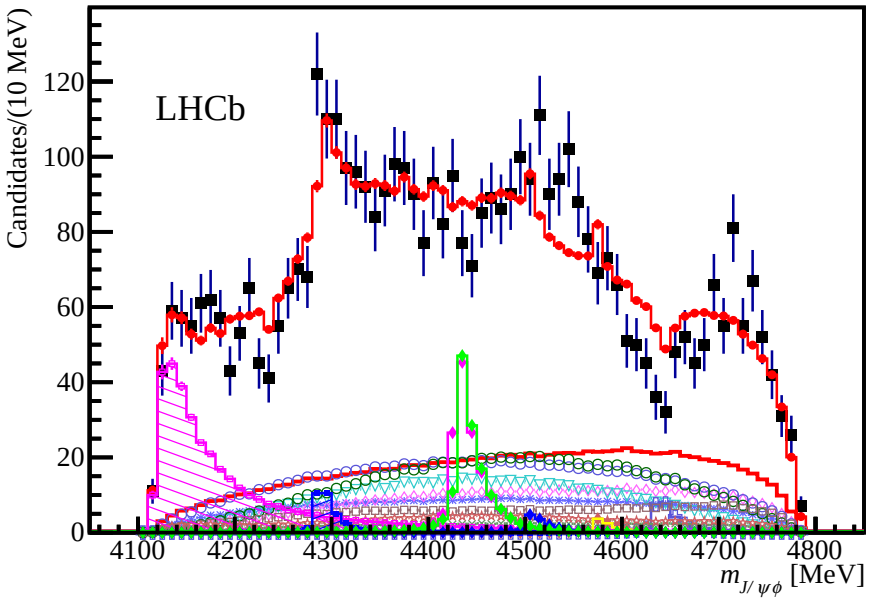

Figure 72: The invariant mass of $J/\psi\,\phi$ with the data in black and the total fit in red when all predicted cusps are included. The p_{1D} is 0.02%. The two large cusp contributions at ~ 4430 MeV are 1^- cusps from $D_s^+ D_{s1}(2460)^-$ and $D_s^{*+} D_{s0}^{*-}$ which are very close in mass, and cancel each other via negative interference. Leaving only one of them in the fit leads to a very small F.F. and almost no change in fit quality.

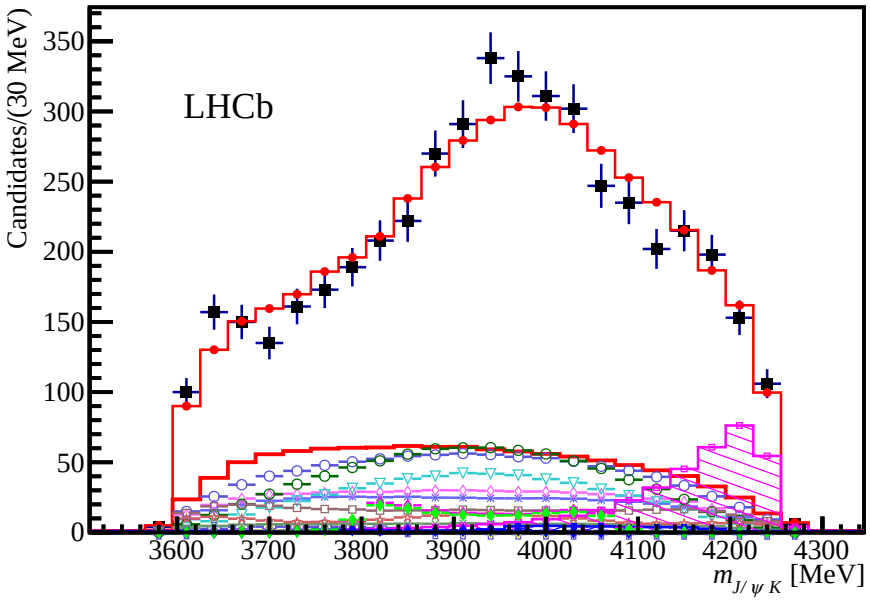

Figure 73: The invariant mass of $J/\psi\,K^+$ with the data in black and the total fit in red when all predicted cusps are included. The p_{1D} is 9.6%.

12 Summary of experimental results

The amplitude analysis of 4.3k $B^+ \to J/\psi\,\phi K^+$ signal events performed using all six degrees of freedom of their decay kinematics and 3 fb^{-1} of pp collision data collected at $\sqrt{s} = 7 - 8$ TeV with the LHCb detector provides good sensitivity to resonant structures and their quantum numbers in both the ϕK^+ and $J/\psi\,\phi$ systems.

Even though no peaking structures are observed in the ϕK^+ mass distribution, correlations in decay angles reveal a rich spectrum of K^{*+} resonances. In addition to the angular information contained in the K^{*+} and the subsequent ϕ decay, the J/ψ decay also helps probe these resonances, as the helicity states of the K^{*+} and J/ψ coming from the decay of spinless B^+ must be equal. Unlike the earlier scattering experiments investigating $K^* \to \phi K$ decays, we have a good sensitivity to states with both natural and unnatural J^P combinations.

The dominant 1^+ partial wave, $(42 \pm 8\,^{+5}_{-9})\%$ fit fraction, has a substantial non-resonant component, $(16 \pm 13\,^{+35}_{-\ 6})\%$, and at least one resonance 7.6σ significant. There is also 2σ evidence that this structure can be better described with two resonances at $1793 \pm 59\,^{+153}_{-\ 101}$ MeV and $1968 \pm 65\,^{+\ 70}_{-172}$ MeV with large widths $365 \pm 157\,^{+138}_{-215}$ MeV and $396 \pm 170\,^{+174}_{-178}$ ($(12 \pm 10\,^{+17}_{-\ 6})\%$ and $(23 \pm 20\,^{+31}_{-29})\%$ F.F.). The observed structure fits the expectations for the two $2P_1$ excitations of the kaon.

Also prominent is the 2^- partial wave, $(10.8 \pm 2.8\,^{+1.5}_{-4.6})\%$ fit fraction. It contains at least one resonance at 5.0σ significance. This structure is also better described with two resonances at 3.0σ significance. Their masses, $1777 \pm 35\,^{+122}_{-\ 77}$ MeV and $1853 \pm 27\,^{+\ 18}_{-\ 35}$ MeV, and widths, $217 \pm 116\,^{+221}_{-154}$ MeV and $167 \pm 58\,^{+\ 82}_{-\ 72}$ MeV, are in good agreement with the well established $K_2(1770)$ and $K_2(1820)$ states, which in turn matches the predictions for the two $1D_2$ kaon excitations.

The 1^- partial wave, $(6.7 \pm 1.9\,^{+3.2}_{-3.9})\%$ F.F., has a strong 8.5σ evidence for a resonant state with the mass $1722 \pm 20\,^{+\ 33}_{-108}$ MeV and width $354 \pm 75\,^{+140}_{-181}$ MeV which match very

well with the $K^*(1680)$ state, which was already well established in other decay modes, and matches the expectations for the 1^3D_1 kaon excitation. This represents the first observation of its decay to ϕK.

The 2^+ partial wave has a smaller intensity, $(2.9 \pm 0.8\,^{+1.7}_{-0.7})\%$ F.F., but provides a significant 5.4σ evidence for a broad, $678 \pm 311\,^{+1153}_{-\ 559}$ MeV in width, structure at $2073 \pm 94\,^{+245}_{-240}$ MeV. With the very large errors, it is consistent with the $K_2^*(1980)$ state observed previously in other decay modes and matching expectations for the 2^3P_2 state.

Last but not least, we confirm the $K(1830)$ state (3^1S_0 candidate) at 3.5σ significance, $(2.6 \pm 1.1\,^{+2.3}_{-1.8})\%$ F.F., earlier observed in the ϕK decay by the K^-p scattering experiment. We determine its mass and width with properly evaluated errors for the first time: $1874 \pm 43\,^{+\ 59}_{-115}$ MeV and $168 \pm 90\,^{+280}_{-104}$ MeV.

Overall, our $K^{*+} \to \phi K^+$ results show excellent consistency with the states observed earlier in other experiments, often in other decay modes, and fit the mass spectrum predicted for the kaon excitations by Godfrey-Isgur model. Most of the K^{*+} structures we observe were previously observed or hinted by the previous $Kp \to \phi K(p \text{ or } n)$ experiments, which were sometimes inconsistent with each other. Proper statistical analysis of the $K^* \to \phi K$ states has been performed for the first time.

While many statistical and systematic errors on the parameters of the K^{*+} resonances are large, the plausible composition of the ϕK^+ model extracted from our data without experimental or theoretical constraints, gives us confidence in our amplitude model which also requires several $J/\psi\,\phi$ components, as the K^{*+} states alone cannot reproduce the several sharp mass structures observed in the $J/\psi\,\phi$ mass distribution. In this work, we have attempted to describe such contributions as resonances and obtain a good statistical and systematic sensitivity to parameters of these presumed states including their quantum numbers. We have also investigated a possibility for these structure to be cusps related to many opening thresholds for production of pairs of various excitations of the D_s meson.

The parameterization of cusps is adopted from Swanson's model [62].

The $X(4140)$ state, first reported as a narrow near-threshold peak is observed as a broad $\Gamma = 83 \pm 21\,^{+20.7}_{-13.5}$ MeV resonance with a mass of $4146.5 \pm 4.5\,^{+4.6}_{-2.8}$ MeV, a fit fraction of $(13.0 \pm 3.2\,^{+4.7}_{-2.0})\%$ and significance of 7.6σ including systematic effects. Observation of this broad structure is not at odds with the upper limit on production of the narrow 15.3 MeV state at the similar mass, which was previously set based on 0.37 fb^{-1} subset of our data. The $X(4140)$ mass measurement is consistent with the previous determinations by the CDF, CMS, and D0 collaborations. The width measurement is significantly larger than the average over the previous experiment, which used naive mass fits, but agrees within errors with the width determined by the CMS experiment. The quantum numbers of the $X(4140)$ state are established for the first time to be $J^{PC} = 1^{++}$ with significance of 5.7σ. However, this structure can be even better described as 1^+ $D_s^+ D_s^{*-}$ cusp. Possibility of such cusp in this channel was explicitly pointed out by Swanson [61]. With its mass threshold nearly coinciding with the $J/\psi\,\phi$ mass threshold, this provides a natural explanation for peaking of the rate very near to the kinematic boundary.

We confirm existence of the $X(4274)$ structure, first observed by CDF. We observe it with a statistical significance of 6.0σ, at a mass of $4273.3 \pm 8.3\,^{+17.2}_{-\ 3.6}$ MeV and with a width of $56.2 \pm 10.9\,^{+8.4}_{-\ 11.1}$ MeV and a fit fraction of $(7.1 \pm 2.5\,^{+3.5}_{-2.4})\%$. Due to the interference effects with the other contributions, the data peaks above the pole mass. This could explain why the naive mass fits which we performed with a small subset of our present data sample showed inconsistency with the state proposed by CDF. These results are now superseded by this analysis. Such effects underline the importance of a proper amplitude analysis and are also likely to account for 3.2σ discrepancy in the mass of the second state as determined by CDF and CMS via the naive mass fits. Different experimental acceptances can also pick different interference patterns and lead to disagreements in the position of a state. We establish the quantum numbers of the $X(4274)$ structure to also

be 1^{++} with 5.5σ significance. The combined F.F. of these two 1^{++} contributions together is $(16.0 \pm 2.8\,^{+5.9}_{-2.1})\%$. The resonance interpretation of $X(4274)$ is favored by our model over the 0^- $D_s^+ D_{s0}^{*-}$ cusp. However, the latter peaks in the right mass region and provides fits which are not unreasonable.

The high $J/\psi\phi$ mass region also shows strong evidence for significant structure, best described in our resonant model by two $J^{PC} = 0^{++}$ resonances at $4506 \pm 11\,^{+12}_{-15}$ MeV and $4704 \pm 10\,^{+14}_{-24}$ MeV, with widths of $92 \pm 21\,^{+21}_{-20}$ MeV and $120 \pm 31\,^{+42}_{-33}$ MeV, fit fractions $(6.6 \pm 2.4\,^{+3.5}_{-4.0})\%$ and $(12.4 \pm 4.9\,^{+9.2}_{-8.5})\%$, and significance of 6.1σ and 5.6σ, respectively, interfering with an also significant, 6.4σ, non-resonant contribution. Its fit fraction is large, $(46.2 \pm 10.7\,^{+11.0}_{-21.0})\%$, and it interferes destructively with the two resonant contributions to produce a combined fit fraction of the 0^{++} $J/\psi\,\phi$ wave of $(27.6 \pm 5.1\,^{+6.5}_{-6.7})\%$. The significance of the quantum number determinations for these mass peaks is 4.0σ and 4.5σ, respectively. The high $J/\psi\phi$ mass region could not be explored by the CDF, CMS and D0 because of the large backgrounds in these experiments which lacked kaon identification devices. Belle and BaBar did not have sufficient signal statistics to probe this region in a meaningful way.

None of the observed $J/\psi\,\phi$ structures match the evidence of a state at 4351 MeV observed in $\gamma\gamma$ collisions by the Belle collaboration.

Since cusps [61–66] and other rescattering mechanisms, like triangular anomalies [67], may be present in this channel, the results based on our resonant model for the $J/\psi\,\phi$ structures should be taken with caution. More data and a survey of various coupled-channel models are needed to provide a more in depth study of their nature.

13 Theoretical implications

Our results have a large impact on the possible theoretical interpretations of the $J/\psi\,\phi$ mass structures observed in $B^+ \to J/\psi\,\phi K^+$ decays, which we discuss in this section.

13.1 Molecular interpretations

While we confirm the existence of the near threshold structure, previously named $X(4140)$ (or $Y(4140)$), our results contradict the claim for this structure to be narrow that drove many initial interpretations. Our determination of its effective quantum numbers to be $J^{PC} = 1^{++}$ directly rules out many previous hypotheses concerned with this $J/\psi\,\phi$ mass peak, while a few survive as discussed below.

Perhaps the largest camp are those who believe $X(4140)$ is a hadronic molecule, with a focus on molecules of D_s meson excitations. R. Albuquerque et al [68] used QCD sum rules to predict the mass spectrum of a $D_s^{*\pm}D_s^{*\mp}$ current with $J^{PC} = 0^{++}$. They arrived at mass predictions very much consistent with the observations. In 2015 an additional study was performed [69]; by assuming a 0^{++} molecular state, they attempted to predict the width and arrived at 0.34 ± 0.11 MeV which is far too narrow to explain the widths measured by any of the previous analyses and even more so the width measured in this analysis. The wrong quantum numbers definitely rule this model out.

Zhi-Gang Wang [70] also used QCD sum rules and assumed 0^{++} molecular $D_s^{*\pm}D_s^{*\mp}$ state to predict a mass of 4430 MeV. While noting that it is not consistent with the observed mass of $X(4140)$, they mention that other possibilities, such as hybrid charmonium states, are not excluded. The hybrid state description would have $J^{PC} = 1^{-+}$ which is ruled out by our results as well.

Xiang Liu and Shi-Lin Zhu [71] opened up the possibility that $X(4140)$ was the molecular partner of $Y(3930)$ and could possibly have $J^{PC} = 0^{++}$ or 2^{++}, both of which

we now know are wrong.

Similarly, Tanja Branz et al [72] calculated the width of a $D_s^{*\pm}D_s^{*\mp}$ molecule with either $J^{PC} = 0^{++}$ or 2^{++} and obtained 3.26±0.21 Mev or 4.41±0.16 MeV, respectively, far below the width observed in this analysis, and predicting the wrong quantum numbers.

It should be noted that in 2009 Gui-Jun Ding [56] presented a wide swath of molecular models with different quantum numbers to search for the states with the highest binding energy. He mentions that the experimentally determined $J^{PC} = 1^{++}$ is possible for $D_s^{*\pm}D_s^{*\mp}$ in the one boson exchange potential but is less attractive for a bound state than the similar 0^{-+} state due to a higher centrifugal barrier. However, he was not aware that such quantum numbers are forbidden for $D_s^{*\pm}D_s^{*\mp}$ molecule by the symmetry arguments as explained in Ref. [71].

The only molecular models which can accommodate 1^{++} quantum numbers for the $X(4140)$ structure are those invoking molecular forces between $D_s^{\pm}D_s^{*\mp}$ meson pairs. However, the sum of their masses is below the $J/\psi\,\phi$ mass threshold, thus such interactions cannot create a molecular bound state with a resonant pole mass consistent with the $X(4140)$ mass determined by fitting Breit-Wigner amplitude to $B^+ \to J/\psi\,\phi K^+$ data. In 2014 Eric Swanson [61] suggested that a tail of $D_s^{\pm}D_s^{*\mp}$ cusp can be responsible for $X(4140)$. His parameterization of the cusp amplitude fits our data better than the Breit-Wigner formula. While the $D_s^{\pm}D_{s0}^{*\mp}$ cusp peaks at the right mass to explain the $X(4274)$ structure in our data, it cannot account for its 1^{++} quantum numbers. The high $J/\psi\,\phi$ mass structures seen in our data also do not find explanation in his model. More complicated rescattering effects between virtual $D_s^{(*)\pm}D_s^{(*)\mp}$ meson pairs than a simple kinematic cusp should be explored.

Recently, also Marek Karliner and Jonathan Rosner mentioned the possibility of a broad enhancement near the $J/\psi\,\phi$ mass threshold due to $D_s^{\pm}D_s^{*\mp}$ interactions [73]. However, none of the other bound structures of $D_s^{(*)\pm}D_s^{(*)\mp}$ molecules predicted by Karliner-Rosner

matches our results for the higher $J/\psi\,\phi$ mass structures seen in our data.

13.2 Tetraquark interpretations

There have been many models presented that assume $X(4140)$ is a tetraquark candidate.

In 2009, right before CDF presented 3.8σ evidence for $X(4140)$, N.V. Drenska et al [74] calculated the mass spectrum of $[cs][\overline{cs}]$ tetraquarks using the diquark approach. They predicted some states decaying to $J/\psi\,\phi$, none of them near $X(4140)$. They did, however, tentatively assign $J^{PC} = 0^{-+}$ to $X(4274)$, which we can now reject based on our analysis.

In 2015 Zhi-Gang Wand and Ye-Fan Tian [75] used QCD sum rules to predict the quantum numbers of $X(4140)$. They favored assigning $J^{PC} = 2^{++}$ to $X(4140)$ but disfavored assigning either $J^{PC} = 0^{++}$ or $J^{PC} = 2^{++}$ to $X(4274)$. The J^{PC} prediction of $X(4140)$ turn out to be incorrect based one this analysis but it is indeed true that $X(4274)$ is not 0^{++} nor is it 2^{++}. They did not study 1^{++} states.

F. Stancu asked the question "Can Y(4140) be a $c\bar{c}s\bar{s}$ tetra quark" [76] in 2010. He utilized a model proposed by Hogaasen et al. [77] and explored it for many quantum numbers. He concluded that $J^{PC} = 1^{++}$ is the best candidate for $X(4140)$ in the tetraquark interpretation, and would be an analog of tetraquark interpretation of $X(3872)$, which is also a $J^{PC} = 1^{++}$ state as determined later by LHCb [78] (Bin Gui, Ph.D., Syracuse University 2014). The D0 claim for prompt $p\bar{p}$ production of $X(4140)$ at Tevatron [10] can also be invoked as evidence for tightly bound structure of $X(4140)$, since prompt production of molecular states is suppressed by their large spatial dimensions. Stancu also predicted a second 1^{++} tetraquark state at the mass 83 MeV higher than the mass of the $X(4274)$ 1^{++} state observed in our analysis. However, his mass predictions were very crude, as evidenced by his overestimation of the $X(4140)$ mass by 49 MeV. The 0^{++} tetraquark states predicted by Stancu are too low in mass to explain the 0^{++} $J/\psi\,\phi$ components needed in our amplitude model in $4500 - 4700$ MeV range.

13.3 The future

Many theoretical models have been ruled out by our results. A few models have limited success describing certain features of our data, but none can reproduce all observed $J/\psi\,\phi$ structures. It is possible that more than one dynamical effect shape them. More theoretical and experimental effort will be required in the future to clarify their nature.

Appendices

A Display of moments of helicity angles

Often times interesting insight into orbital-momentum structures in the data and fits is provided by calculating the moments of the $\cos\theta_{K^*}$, $\cos\theta_X$, and $\cos\theta_Z$ distributions and plotting them as a function of the mass associated with each decay chain (*e.g.* $m_{\phi K}$ for the K^* decay chain). This method can reveal the origin, in terms of orbital-momentum, of structures in the mass distribution. By analyzing each moment in turn we may obtain hints as to the quantum numbers of the various structures in the moment. It turns out that due to the interference between and widths of the states involved there is a noticeable lack of structure(s) in almost all moments. Thus we show them here to illustrate the quality of the amplitude fit. The unnormalized moment of l^{th} degree is defined as:

$$< P_l^U >= \sum_{i=1}^{N_{\rm data}} \frac{1}{\epsilon_i} P_l(\cos\theta_{K^*}) \tag{50}$$

for K^* decay chain; where ϵ_i is the efficiency for event i and $P_l(x)$ is a Legendre polynomial of order l. Moments for the other helicty angles can be similarly determined from the above equation.

We use the parameterized efficiency to calculate ϵ_i as described in Sec. 5. We calculate moments for both the data, and the phase-space MC re-weighted by the square of the matrix element obtained from the fit. The latter represent displays of the fitted amplitude model. Because the distribution of moments is based on efficiency corrected data, we also show the efficiency corrected data distributions for $m_{\phi K}$, $m_{J/\psi\,\phi}$, and $m_{J/\psi\,K}$ ("0^{th} moments") in Figure 74 below.

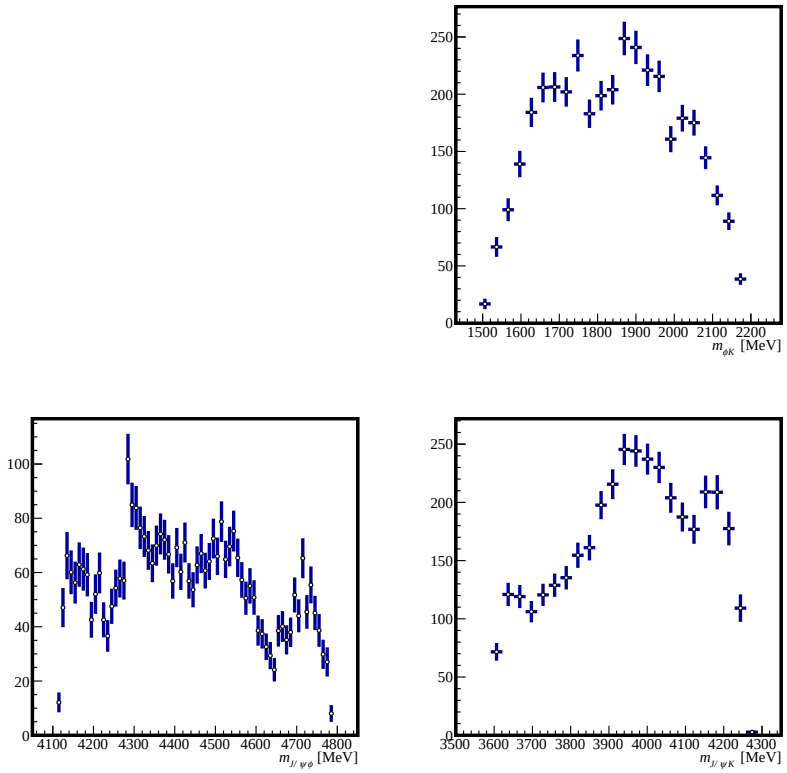

Figure 74: The three efficiency corrected mass distributions of $m_{\phi K}$ (top right), $m_{J/\psi\phi}$ (bottom left), and $m_{J/\psi K}$ (bottom right). The data are black points, while the default amplitude fit is represented by the red points.

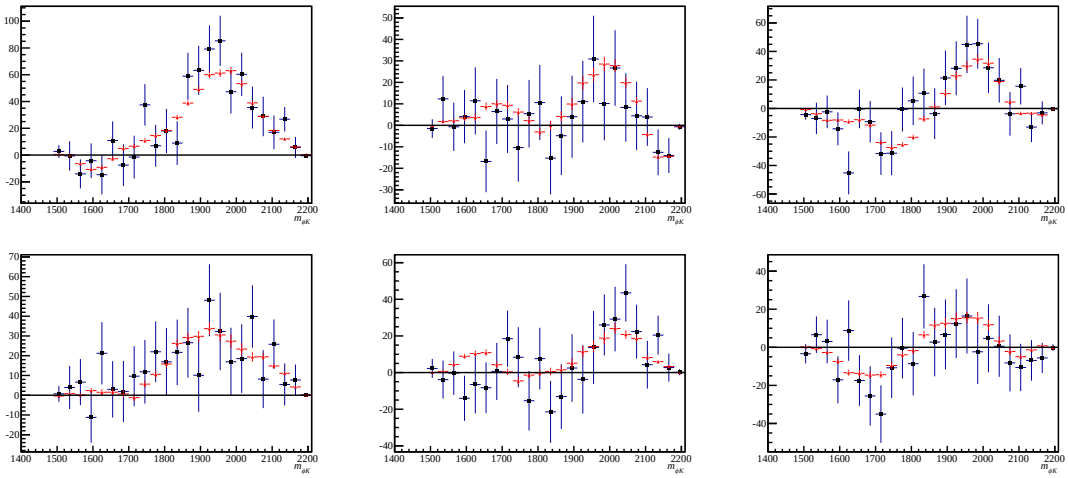

Figure 75: The first six Legendre moments of the K^* decay chain starting with the first in the upper left and proceeding left to right and row by row. The data are black points, while the default amplitude fit is represented by the red points.

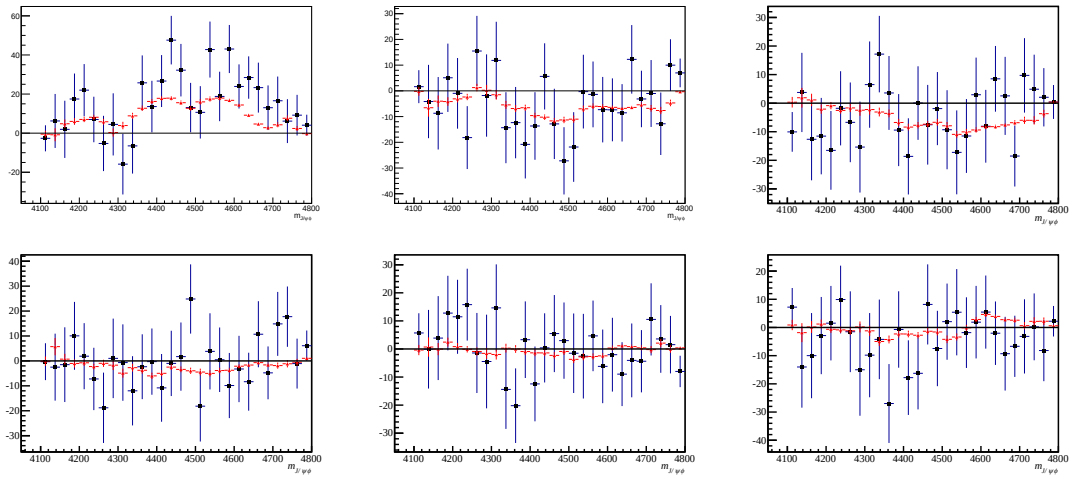

Figure 76: The first six Legendre moments of the X decay chain starting with the first in the upper left and proceeding left to right and row by row. The data are black points, while the default amplitude fit is represented by the red points.

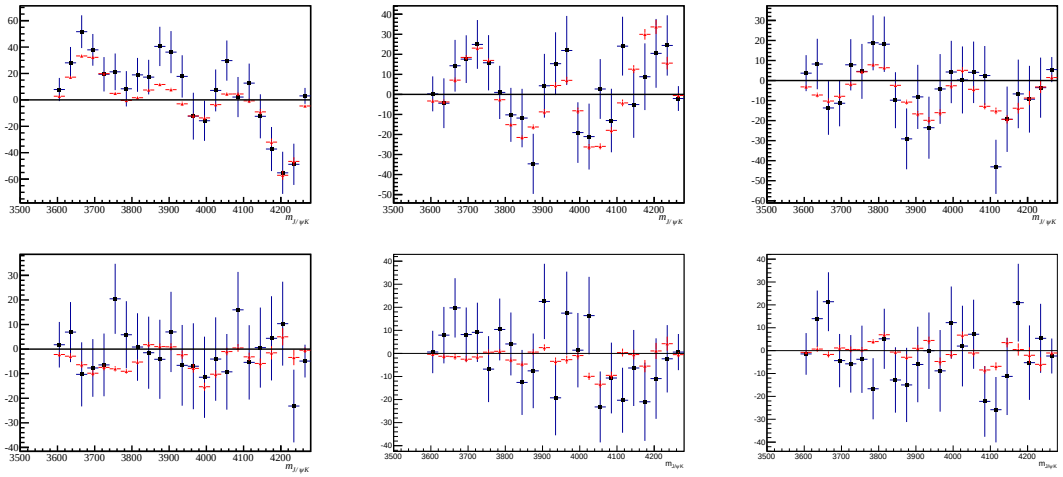

Figure 77: The first six Legendre moments of the Z decay chain starting with the first in the upper left and proceeding left to right and row by row The data are black points, while the default amplitude fit is represented by the red points.

B Amplitudes obtained in the default fit

Numerical values of the fit parameters in the default fit are given in Table 31 and continued in Table 32. Polarization parameters of K^{*+} and of ϕ for various K^* contributions determined from the LS couplings listed here are given in C.2.

Table 31: Amplitude model based on the default fit to the data. "BLS" all have the meaning of the complex ratio of $B_{LS}/B_{L_{min},S_{min}}$). The coupling convention is set by the overall amplitude of$NR_{J/\psi\phi}$. This table is continued on the next page 32

Resonance	J^P	M_0 MeV	Γ_0 MeV	Overall Amplitude	$B_{L,S}$ couplings	
$NR_{\phi K}$	1^+	$--$	$--$	$(-0.066\pm0.084, -0.059\pm0.133)$	$B_{0,0}^{B\to J/\psi K^*}$	$(1,0)$
					$B_{1,1}^{B\to J/\psi K^*}$	$(+1.923\pm1.948, +1.537\pm3.450)$
					$B_{2,2}^{B\to J/\psi K^*}$	$(-0.274\pm7.349, -4.620\pm4.469)$
					$B_{0,1}^{K^*\to\phi K}$	$(1,0)$
					$B_{2,1}^{K^*\to\phi K}$	$(+0.396\pm0.491, -1.369\pm0.618)$
K_1	1^+	1793.3 ± 59.0	364.7 ± 157.0	$(-2.624\pm4.259, -3.200\pm4.136)$	$B_{0,0}^{B\to J/\psi K^*}$	$(1,0)$
					$B_{1,1}^{B\to J/\psi K^*}$	$(-0.471\pm1.632, +2.394\pm2.346)$
					$B_{2,2}^{B\to J/\psi K^*}$	$(+2.782\pm3.285, +1.173\pm2.196)$
					$B_{0,1}^{K^*\to\phi K}$	$(1,0)$
					$B_{2,1}^{K^*\to\phi K}$	$(+0.947\pm0.922, +0.008\pm1.026)$
K_1'	1^+	1967.9 ± 65.0	396.0 ± 170.3	$(+4.704\pm4.001, -6.878\pm3.052)$	$B_{0,0}^{B\to J/\psi K^*}$	$(1,0)$
					$B_{1,1}^{B\to J/\psi K^*}$	$(+0.617\pm0.380, +0.905\pm0.299)$
					$B_{2,2}^{B\to J/\psi K^*}$	$(+0.428\pm0.352, -0.277\pm0.423)$
					$B_{0,1}^{K^*\to\phi K}$	$(1,0)$
					$B_{2,1}^{K^*\to\phi K}$	$(-2.048\pm1.620, -0.306\pm1.119)$
$K(1680)$	1^-	1721.6 ± 19.9	353.7 ± 74.7	$(-5.979\pm1.911, +2.475\pm2.140)$	$B_{0,0}^{B\to J/\psi K^*}$	$(1,0)$
					$B_{1,1}^{B\to J/\psi K^*}$	$(-0.446\pm0.424, +0.613\pm0.367)$
					$B_{2,2}^{B\to J/\psi K^*}$	$(-3.956\pm1.169, +1.553\pm1.266)$
					$B_{1,1}^{K^*\to\phi K}$	$(1,0)$
$K_2(1770)$	2^-	1777.2 ± 34.9	217.5 ± 116.3	$(+4.192\pm3.679, -0.076\pm3.127)$	$B_{1,1}^{B\to J/\psi K^*}$	$(1,0)$
					$B_{2,2}^{B\to J/\psi K^*}$	$(+0.911\pm0.555, -0.207\pm0.588)$
					$B_{3,3}^{B\to J/\psi K^*}$	$(-0.978\pm0.951, -1.931\pm0.833)$
					$B_{1,1}^{K^*\to\phi K}$	$(1,0)$
					$B_{3,1}^{K^*\to\phi K}$	$(+1.501\pm1.303, -1.243\pm1.143)$

Table 32: Amplitude model based on the default fit to the data

Resonance	J^P	M_0 MeV	Γ_0 MeV	Overall Amplitude	$B_{L,S}$ couplings	
$K_2(1820)$	2^-	1853.4±26.6	167.0±58.1	(−5.008±3.445, +1.811±4.473)	$B_{1,1}^{B\to J/\psi K^*}$	$(1,0)$
					$B_{2,2}^{B\to J/\psi K^*}$	(−0.720±0.865, +0.097±1.189)
					$B_{3,3}^{B\to J/\psi K^*}$	(+0.414±1.584, −3.288±1.630)
					$B_{1,1}^{K^*\to\phi K}$	$(1,0)$
					$B_{3,1}^{K^*\to\phi K}$	(+0.495±0.351, +0.108±0.403)
$K(1830)$	0^-	1873.9±43.2	167.5±90.4	(−5.138±1.385, +0.007±2.501)	$B_{1,1}^{B\to J/\psi K^*}$	$(1,0)$
					$B_{1,1}^{K^*\to\phi K}$	$(1,0)$
$K_2^*(1980)$	2^+	2072.6±94.2	677.7±310.6	(+0.815±2.952, +8.272±3.441)	$B_{1,1}^{B\to J/\psi K^*}$	$(1,0)$
					$B_{2,2}^{B\to J/\psi K^*}$	(−0.669±1.091, −2.892±1.212)
					$B_{3,3}^{B\to J/\psi K^*}$	(−0.505±0.709, +1.033±0.556)
					$B_{2,1}^{K^*\to\phi K}$	$(1,0)$
$X(4140)$	1^+	4146.5±4.5	82.8±20.7	(−30.060±5.981, +17.076±7.884)	$B_{0,1}^{X\to J/\psi\phi}$	$(1,0)$
					$B_{2,1}^{X\to J/\psi\phi}$	(−0.022±0.055, +0.033±0.152)
					$B_{2,2}^{X\to J/\psi\phi}$	(−0.160±0.068, −0.115±0.121)
$X(4274)$	1^+	4273.3±8.3	56.2±10.9	(+1.552±4.768, +13.348±2.177)	$B_{0,1}^{X\to J/\psi\phi}$	$(1,0)$
					$B_{2,1}^{X\to J/\psi\phi}$	(−0.143±0.118, −0.208±0.136)
					$B_{2,2}^{X\to J/\psi\phi}$	(−0.005±0.096, −0.006±0.119)
$NR_{J/\psi\phi}$	0^+	−−	−−	$(1,0)$	$B_{0,0}^{X\to J/\psi\phi}$	$(1,0)$
					$B_{2,2}^{X\to J/\psi\phi}$	(−0.080±0.106, −0.215±0.120)
$X(4500)$	0^+	4506.1±11.2	91.9±21.2	(−8.959±1.430, +0.755±2.402)	$B_{0,0}^{X\to J/\psi\phi}$	$(1,0)$
					$B_{2,2}^{X\to J/\psi\phi}$	(−0.088±0.107, +0.033±0.130)
$X(4700)$	0^+	4704.2±10.1	119.7±30.7	(−11.406±2.097, +9.755±3.223)	$B_{0,0}^{X\to J/\psi\phi}$	$(1,0)$
					$B_{2,2}^{X\to J/\psi\phi}$	(+0.128±0.125, −0.403±0.179)

C Additional K^* studies

C.1 $J/\psi\,\phi$ reflection of helicity amplitudes of ϕK

To get a sense of what features of $m_{J/\psi\,\phi}$ might be explainable by ϕK resonances, we plotted each combination of helicity couplings ($A_{\lambda_{J/\psi}}$ and A_{λ_ϕ}) projected onto the $J/\psi\,\phi$ mass spectrum. To accomplish this, plots were produced in which each combination of $A^{B^+\to J/\psi\,K^{*+}}_{\lambda_{J/\psi}}$ and $A^{K^{*+}\to\phi K^+}_{\lambda_\phi}$ are set to (1,0) while all other amplitudes are set to (0,0). This was done for each combination of amplitudes in each set of quantum numbers of K^{*+} states that were found in the default fit. Masses and widths of the resonances were set to their default fit values, which agree well with the known K^* states and are not far from the Godfrey-Isgur theoretical expectations. The distributions shown here are affected by the selection efficiency.

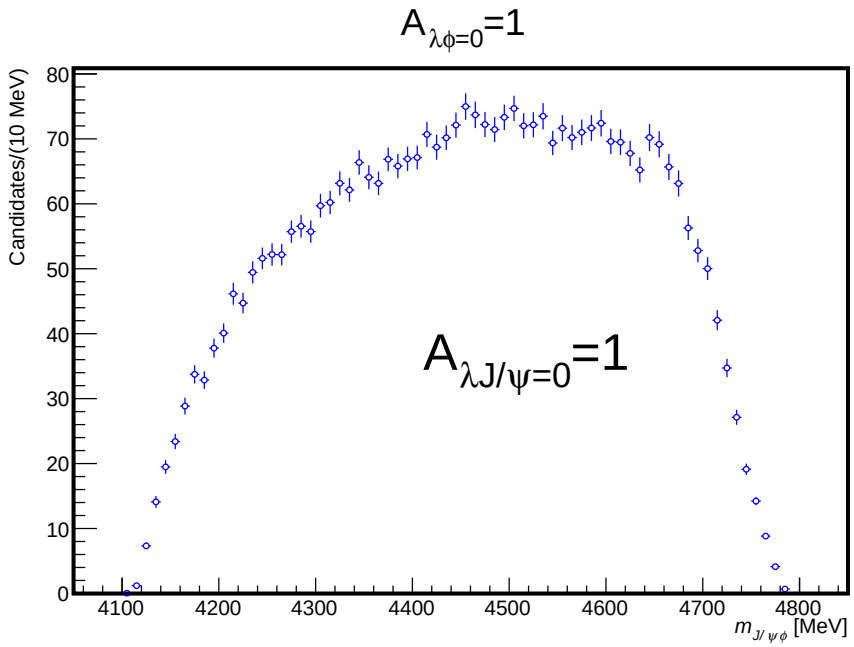

Figure 78: The projection of the single set of $J^P = 0^-$ helicity amplitudes on to $m_{J/\psi\,\phi}$ for a K^* with a mass of 1874 MeV and a width of 168 MeV.

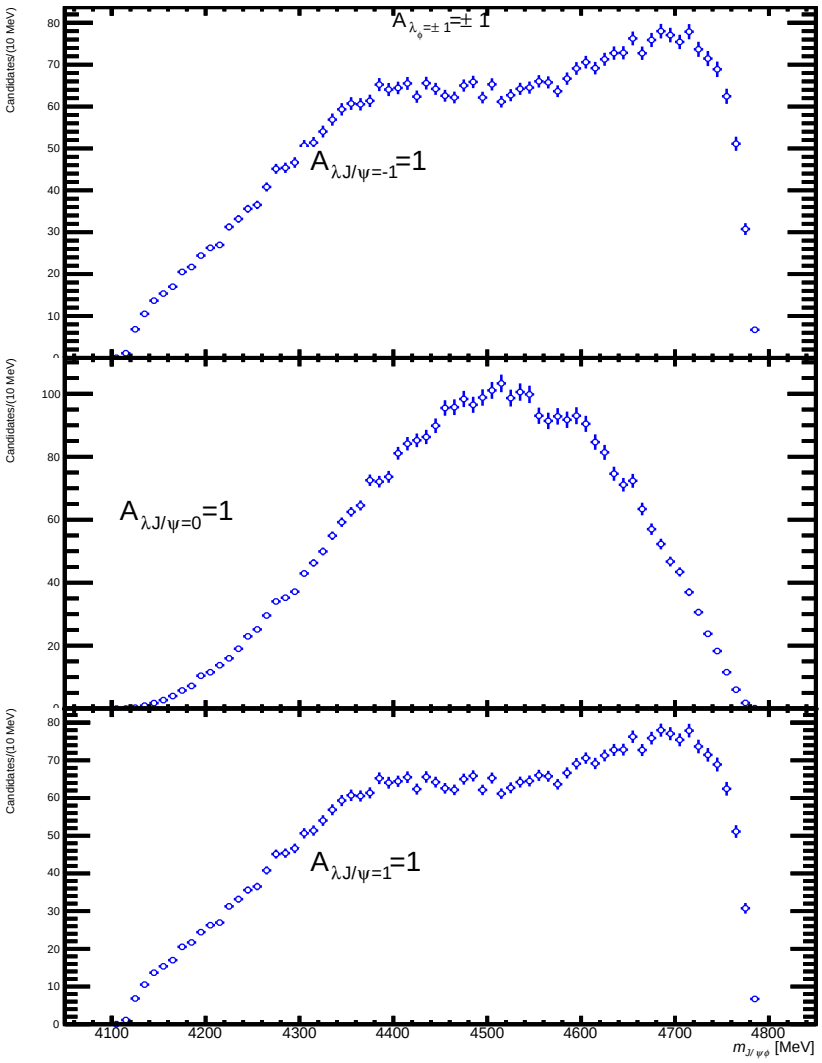

Figure 79: The projection of the 3 possible sets of $J^P = 1^-$ helicity amplitudes on to $m_{J/\psi\,\phi}$ for a K^* with a mass of 1722 MeV and a width of 354 MeV.

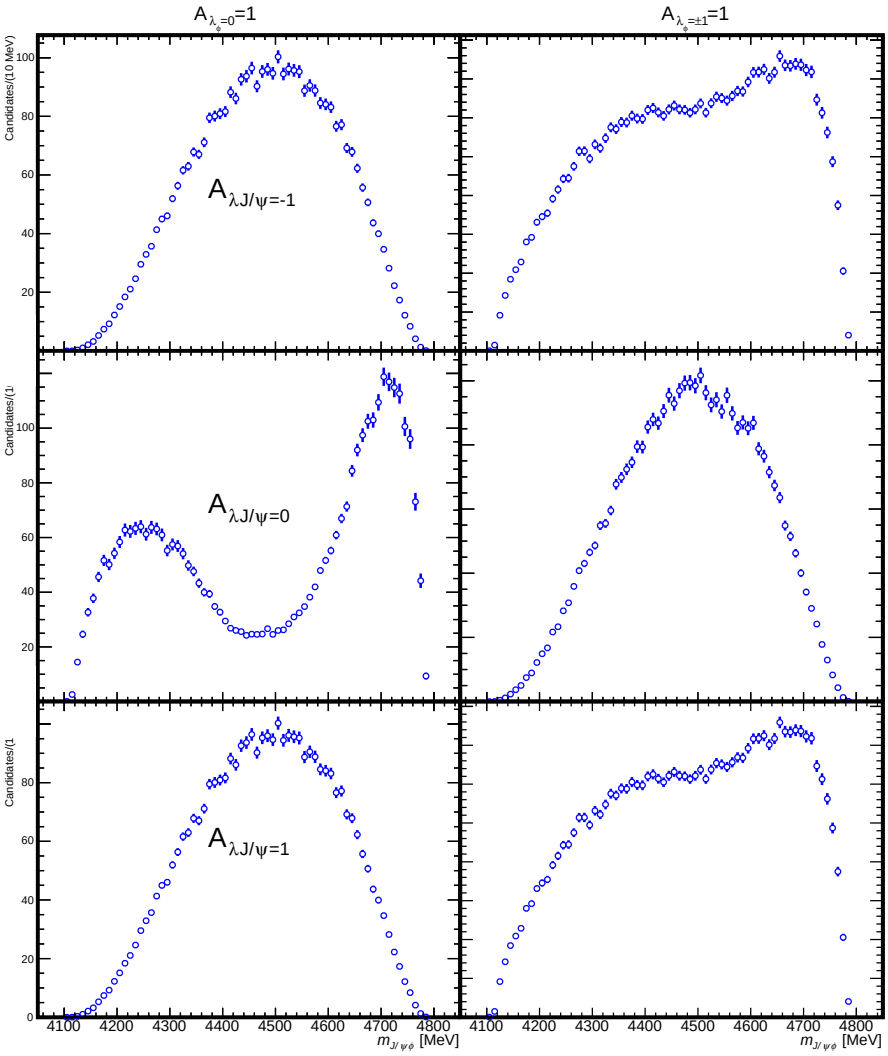

Figure 80: The projection of the 6 possible sets of $J^P = 1^+$ helicity amplitudes on to $m_{J/\psi\,\phi}$ for a K^* with a mass of 1793 MeV and a width of 365 MeV.

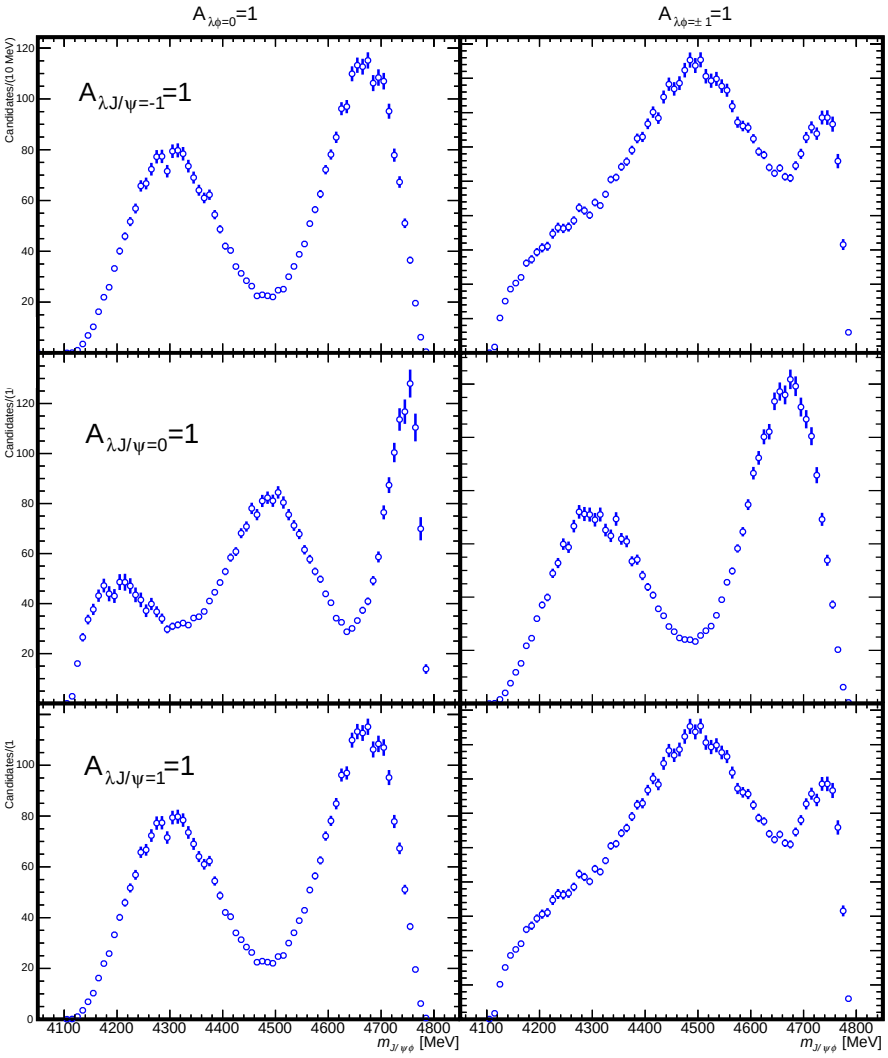

Figure 81: The projection of the 6 possible sets of $J^P = 2^-$ helicity amplitudes on to $m_{J/\psi\,\phi}$ for a K^* with a mass of 1777 MeV and a width of 217 MeV.

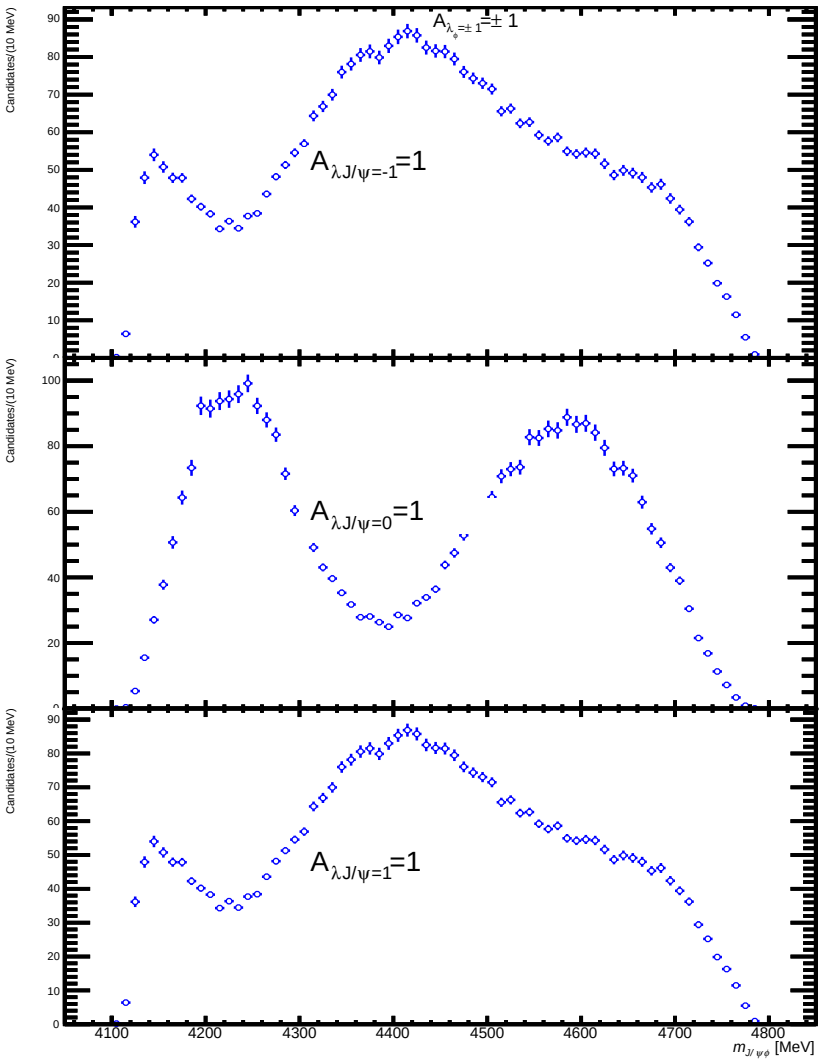

Figure 82: The projection of the 3 possible sets of $J^P = 2^+$ helicity amplitudes on to $m_{J/\psi\,\phi}$ for a K^* with a mass of 2073 MeV and a width of 678 MeV.

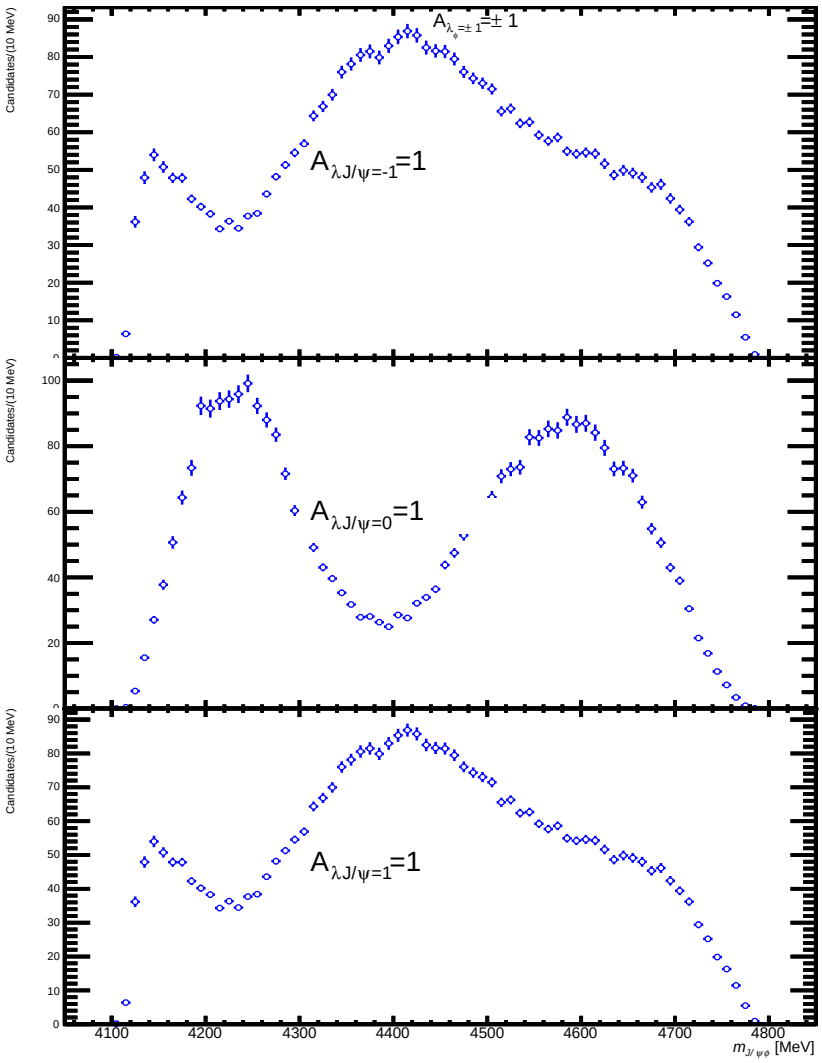

Figure 83: The projection of the 3 possible sets of $J^P = 2^+$ helicity amplitudes on to $m_{J/\psi\,\phi}$ for a K^* with a mass of 2073 MeV and a width of 678 MeV.

C.2 Polarizations of K^* states

Given the advances made in K^* spectroscopy from this analysis it is of some interest to calculate the polarizations of K^{*+} in $B^+ \to J/\psi K^{*+}$ decay and of ϕ in $K^{*+} \to \phi K^+$ decay. The longitudinal polarization (f_L) is defined as:

$$f_L \equiv \frac{|A_0|^2}{|A_{-1}|^2 + |A_0|^2 + |A_{+1}|^2} \tag{51}$$

where A are helicity couplings in either B^+ ($A_{\lambda_{J/\psi}}^{B^+ \to J/\psi K^{*+}}$, $\lambda_{K^*} = \lambda_{J/\psi}$) or K^{*+} decays ($A_{\lambda_\phi}^{K^* \to \phi K^+}$). The transverse polarizations are calculated similarly:

$$\begin{aligned} A_\perp &\equiv \frac{A_{+1} - A_{-1}}{\sqrt{2}} \\ f_\perp &\equiv \frac{|A_\perp|^2}{|A_{-1}|^2 + |A_0|^2 + |A_{+1}|^2} \end{aligned} \tag{52}$$

It is important to note that for the case of strong decays, as in the decay of K^*, the various amplitudes are related by parity constraints, which implies $f_\perp$ equal to 0 or 1. Depending on J^P f_L may also be sometimes forced to 0 or 1. While these values are not very interesting the are included in the table below for completeness.

Table 33: Longitudinal and perpendicular polarizations are given for each K^* state in the default model. The errors are statistical only.

State	J^P	B decay		K^* decay	
		f_L	$f_\perp$	f_L	$f_\perp$
$NR_{\phi K}$	1^+	0.522±0.289	0.213±0.159	0.434±0.185	0
K_1	1^+	0.236±0.214	0.371±0.165	0.020±0.138	0
$K_1^{'}$	1^+	0.042±0.084	0.488±0.099	0.969±0.091	0
$K(1680)$	1^-	0.820±0.043	0.029±0.030	0	1
$K_2(1770)$	2^-	0.636±0.114	0.133±0.128	0.252±0.209	0
$K_2(1820)$	2^-	0.526±0.144	0.042±0.077	0.055±0.117	0
$K(1830)$	0^-	1	0	1	0
$K_2^*(1980)$	2^+	0.152±0.061	0.791±0.078	0	1

In $X \to J/\psi\,\phi$ decays the helicity couplings depend on both J/ψ and ϕ helicities, f_L and $f_\perp$ definitions do not apply.

D Studies of possible $J/\psi K$ contributions

We have investigated adding exotic $Z^+ \to J/\psi K^+$ components to the default amplitude model.

For $J^P = 2^+$ and 0^- the fits make the width of such contributions very small ($4 - 5$ MeV), with very small fit fractions ($0.5 - 0.6\%$). Additionally, there are no noticeable improvements in the description of the various mass distributions and with insignificant changes in the fit likelihood: 1.2σ and 2.5σ, respectively (using ndf $= 2n_{\rm par}$).

For fits with an additional $J^P = 1^+$ or 2^- Z^+ state, the widths ($47 - 51$ MeV), the fit fractions ($1.9 - 2.5\%$) and significances (2.5σ and 3.1σ, respectively) are larger, and there is a slight improvement in the quality of the fit. The mass of hypothetical Z^+ states is near the broad peak seen in the distribution of $m_{J/\psi K}$. The parameters of the other fit components remain within the assigned systematic errors (see Tables 18-20 in Sec. 9). The fit projections for the better of these two fits ($J^P = 2^-$, $M_Z = 3937 \pm 7$ MeV, $\Gamma_Z = 51 \pm 25$ MeV) are shown in Fig. 84 and have the following fit qualities: $\chi^2_{\rm 1D}/({\rm N_{bin}} - 1) = 67.0/67$, $p_{\rm 1D} = 48\%$ for $m_{J/\psi\phi}$, $\chi^2_{\rm 1D}/({\rm N_{bin}} - 1) = 32.5/22$, $p_{\rm 1D} = 7\%$ for $m_{\phi K}$ and $\chi^2_{\rm 1D}/({\rm N_{bin}} - 1) = 17.4/23$, $p_{\rm 1D} = 79\%$ for $m_{J/\psi K}$. Even though there are some improvements to the fit, we do not include such a contribution in the default model, since 3.1σ is marginal for an exotic hadron component (the smallest significance among the accepted X components is 6.1σ).

For a Z^+ state with $J^P = 1^-$ the fit fails to converge, but ends with the Z^+ mass (~ 4220 MeV) very close to the upper kinematic limit of $J/\psi K$ and obtains an unreasonably large width (~ 500 MeV). While its fit fraction becomes large ($\sim 10\%$), the mass projections(85 show no improvement: $\chi^2_{\rm 1D}/({\rm N_{bin}} - 1) = 77.7/67$, $p_{\rm 1D} = 17\%$ for $m_{J/\psi\phi}$, $\chi^2_{\rm 1D}/({\rm N_{bin}} - 1) = 36.5/22$, $p_{\rm 1D} = 3\%$ for $m_{\phi K}$ and $\chi^2_{\rm 1D}/({\rm N_{bin}} - 1) = 23.2/23$, $p_{\rm 1D} = 45\%$ for $m_{J/\psi K}$. There is also no improvement in the multidimensional fit qualities. Therefore, we dismiss such an amplitude contribution from the model.

Just as $B^+ \to K^+(D_s^{(*)+}D_s^{(*)-})$ cusps can generate peaks in $J/\psi\,\phi$ mass distribution (see Sec. 11), $B^+ \to \phi(\bar{D}^{(*)0}D_s^{(*)+})$ cusps can generate peaks in $J/\psi\,K^+$ mass distribution. Their expected positions are shown in Fig. 86. We have tried all such possible cusp contributions added one-by-one to the amplitude model which already has $X(4140)$ represented as a cusp. They are all insignificant ($< 1.2\sigma$).

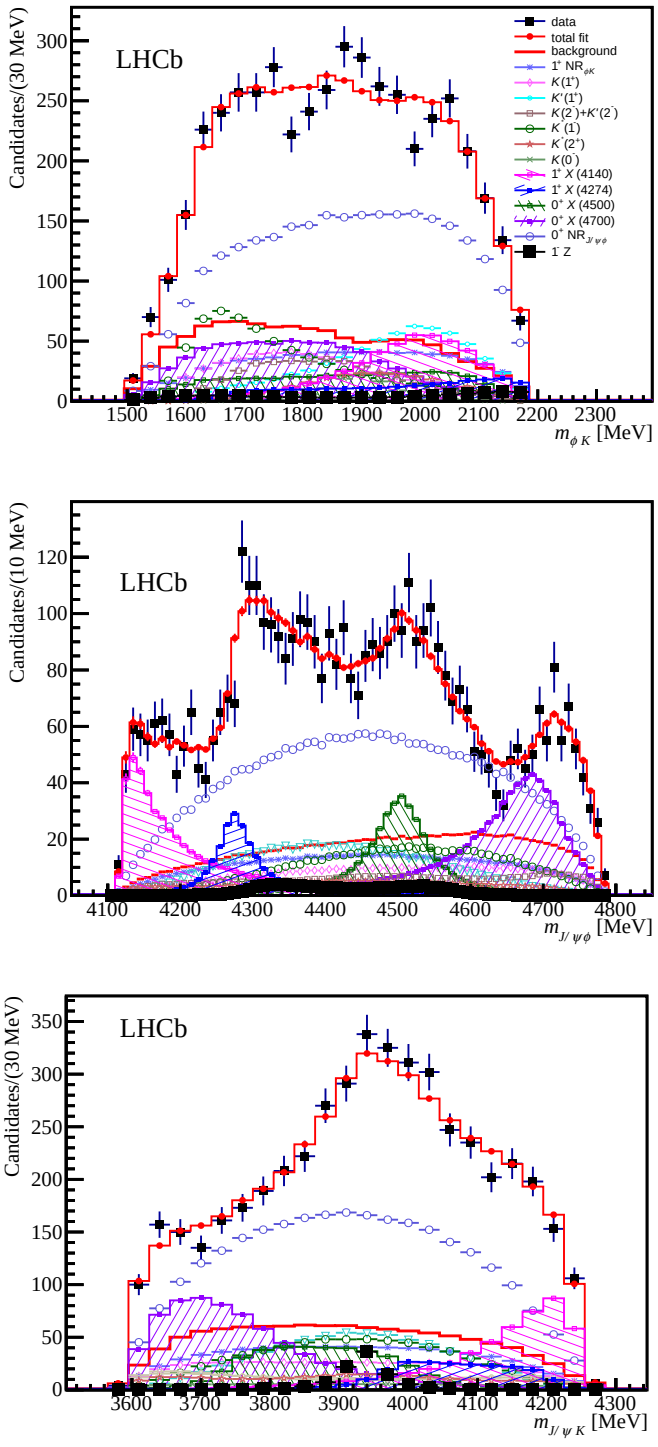

Figure 84: The three mass projections when a $Z^+ \to J/\psi K^+$ 2^- is added to the default model.

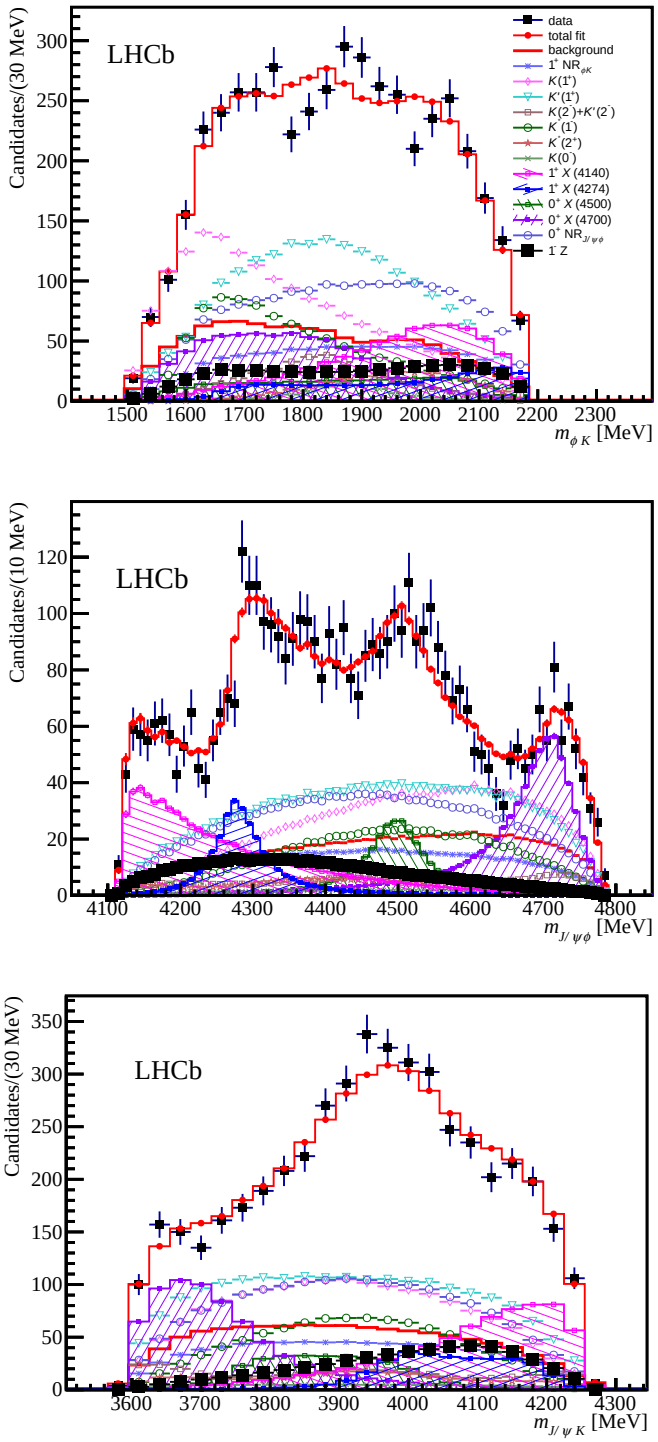

Figure 85: The three mass projections when a $Z^+ \to J/\psi K^+$ 1^- state is added to the default model.

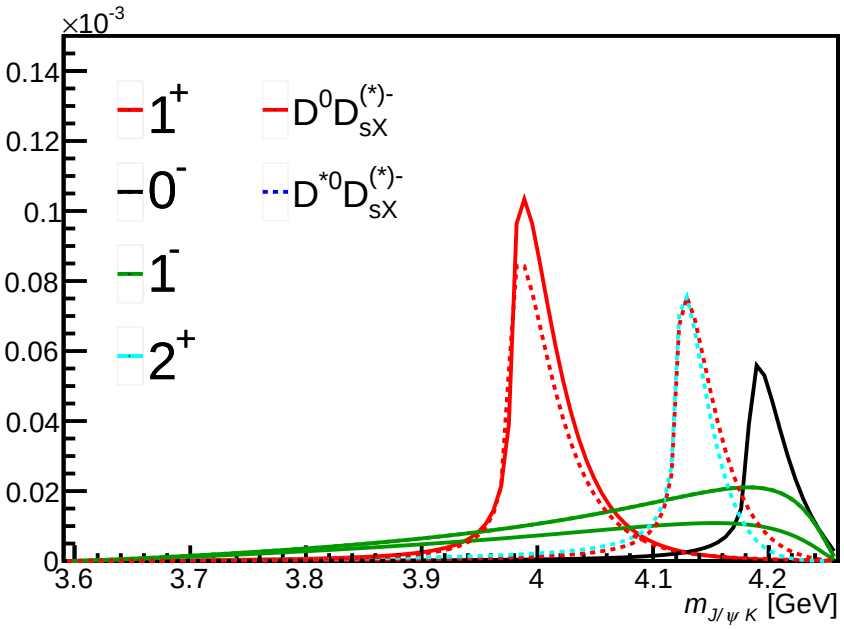

Figure 86: The possible $D^0 D_s$ cusps that can contribute to the $J/\psi K$ spectrum.

E $B^+ \to J/\psi K^+K^-K^+$ signal without ϕ selection.

The invariant mass distribution for $B^+ \to J/\psi K^+K^-K^+$ candidates, without any requirements on masses of the K^+K^- combinations, is shown in Fig. 87. The B^+ signal yield is about 46% higher than with the nominal selection which requires one $\phi \to K^+K^-$ candidate. The background subtracted distribution of $K^+K^-K^+$ mass shows no peaking structures (Fig. 88). The upper sideband of the ϕ peak in the K^+K^- mass also does not show any significant peaking structures in the corresponding $J/\psi K^+K^-$ (Fig. 89) or $J/\psi K^+$ (where K^+ is the "bachelor" kaon; Fig. 90) mass distributions.

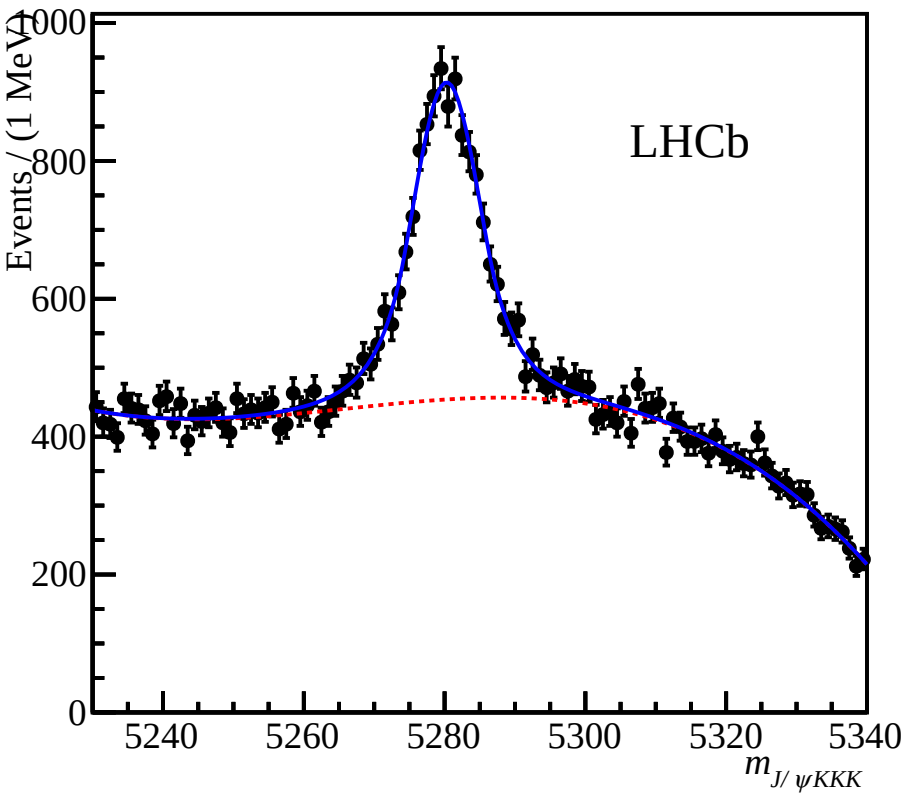

Figure 87: The invariant mass of $J/\psi K^+K^-K^+$ candidates with no selection for ϕ made. The signal yield is 6248 ± 439 as compared to the nominal 4289 ± 151 with ϕ selection (Fig. 20).

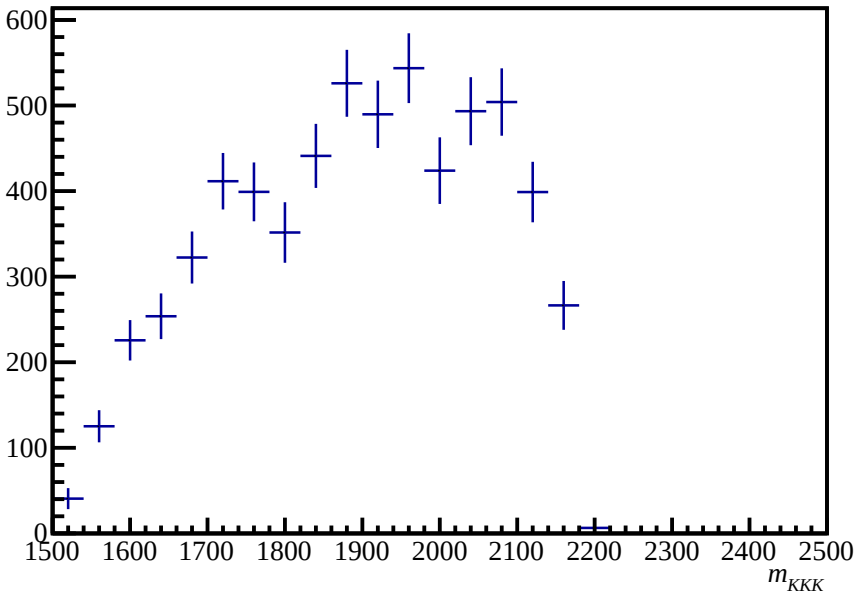

Figure 88: The invariant mass of $K^+K^-K^+$ for $B^+ \to J/\psi K^+K^-K^+$ events (no ϕ selection imposed). The background has been subtracted using sWeights based on the fit shown in Fig. 87.

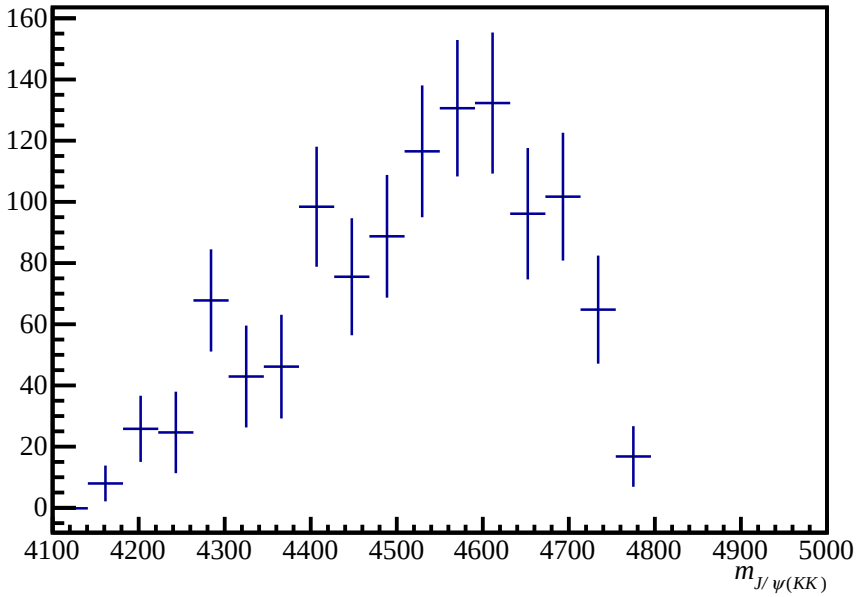

Figure 89: The invariant mass of $J/\psi K^+K^-$ where the kaon pair satisfies $1040\,\text{MeV} < m_{K^+K^-} < 1100\,\text{MeV}$. The background has been subtracted using sWeights.

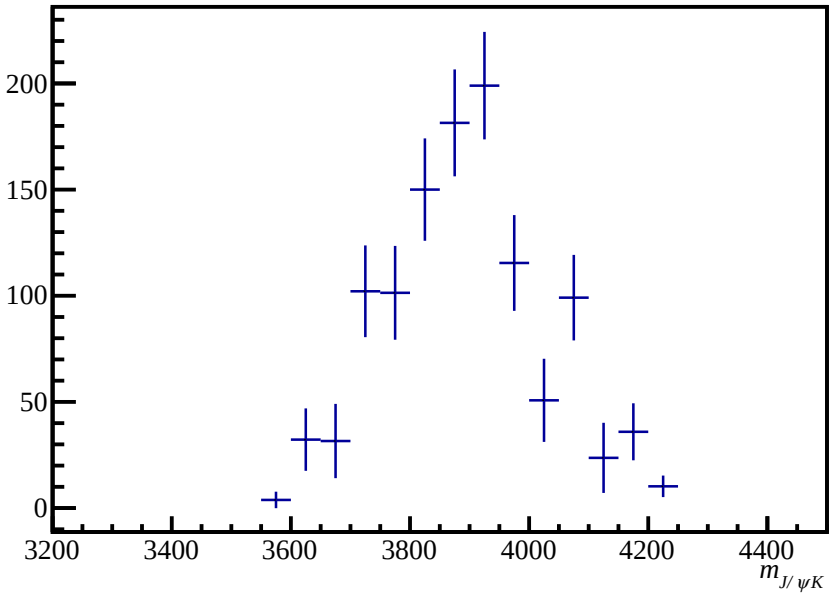

Figure 90: The invariant mass of $J/\psi K^+$ where the other kaon pair satisfies $1040\,\text{MeV} < m_{K^+K^-} < 1100\,\text{MeV}$. The background has been subtracted using sWeights.

References

[1] CDF collaboration, T. Aaltonen *et al.*, *Evidence for a narrow near-threshold structure in the $J/\psi\phi$ mass spectrum in $B^+ \to J/\psi\phi K^+$ decays*, Phys. Rev. Lett. **102** (2009) 242002, arXiv:0903.2229.

[2] CDF collaboration, T. Aaltonen *et al.*, *Observation of the $Y(4140)$ structure in the $J/\psi\,\phi$ mass spectrum in $B^\pm \to J/\psi\,\phi K$ decays*, arXiv:1101.6058.

[3] LHCb collaboration, *Search for $X(4140)$ in $B^+ \to J/\psi\phi K^+$*, LHCb-CONF-2011-045.

[4] LHCb collaboration, R. Aaij *et al.*, *Search for the $X(4140)$ state in $B^+ \to J/\psi\phi K^+$ decays*, Phys. Rev. **D85** (2012) 091103(R), arXiv:1202.5087.

[5] CMS, S. Chatrchyan *et al.*, *Observation of a peaking structure in the $J/\psi\phi$ mass spectrum from $B^\pm \to J/\psi\phi K^\pm$ decays*, Phys. Lett. **B734** (2014) 261, arXiv:1309.6920.

[6] D0, V. M. Abazov *et al.*, *Search for the $X(4140)$ state in $B^+ \to J/\psi\,\phi K^+$ decays with the D0 detector*, Phys. Rev. **D89** (2014), no. 1 012004, arXiv:1309.6580.

[7] J. Brodzicka, *Heavy flavour spectroscopy*, , Prepared for 24th International Symposium on Lepton-Photon Interactions at High Energy (LP09), Hamburg, Germany, 17-22 Aug 2009.

[8] BaBar, J. P. Lees *et al.*, *Study of $B^{\pm,0} \to J/\psi K^+K^-K^{\pm,0}$ and search for $B^0 \to J/\psi\phi$ at BABAR*, Phys. Rev. **D91** (2015), no. 1 012003, arXiv:1407.7244.

[9] Belle collaboration, C. P. Shen *et al.*, *Evidence for a new resonance and search for the $Y(4140)$ in the $\gamma\gamma \to \phi J/\psi$ process*, Phys. Rev. Lett. **104** (2010) 112004, arXiv:0912.2383.

[10] D0, V. M. Abazov *et al.*, *Inclusive Production of the $X(4140)$ State in $p\overline{p}$ Collisions at D0*, Phys. Rev. Lett. **115** (2015), no. 23 232001, arXiv:1508.07846.

[11] Belle collaboration, S. K. Choi *et al.*, *Observation of a resonance-like structure in the $\pi^{\pm}\psi'$ mass distribution in exclusive $B \to K\pi^{\pm}\psi'$ decays*, Phys. Rev. Lett. **100** (2008) 142001, arXiv:0708.1790.

[12] Belle collaboration, K. Chilikin *et al.*, *Experimental constraints on the spin and parity of the $Z(4430)^+$*, Phys. Rev. **D88** (2013) 074026, arXiv:1306.4894.

[13] Belle collaboration, R. Mizuk *et al.*, *Dalitz analysis of $B \to K\pi^+\psi'$ decays and the $Z(4430)^+$*, Phys. Rev. **D80** (2009) 031104, arXiv:0905.2869.

[14] LHCb collaboration, R. Aaij *et al.*, *Observation of the resonant character of the $Z(4430)^-$ state*, Phys. Rev. Lett. **112** (2014) 222002, arXiv:1404.1903.

[15] L. Evans and P. Bryant, *LHC Machine*, JINST **3** (2008) S08001.

[16] LHCb Collaboration, S. Amato *et al.*, *LHCb technical proposal*, .

[17] LHCb Collaboration, F. C. D. Metlica, *The LHCb detector and triggers*, Nucl. Phys. Proc. Suppl. **167** (2007) 173.

[18] LHCb Collaboration, *LHCb VELO TDR: Vertex locator. Technical design report*, .

[19] P. A. Cerenkov, *Visible luminescence of pure fluids induced by gamma rays*, Dokl. Akad. Nauk Ser. Fiz. **2** (1934) 451.

[20] LHCb RICH Collaboration, N. Brook *et al.*, *LHCb RICH1 Engineering Design Review Report*, Tech. Rep. LHCb-2004-121. CERN-LHCb-2004-121, CERN, Geneva, Oct, 2005.

[21] M. Adinolfi *et al.*, *LHCb RICH 2 engineering design review report*, Tech. Rep. LHCb-2002-009, CERN, Geneva, Mar, 2002. revised version number 1 submitted on 2002-05-21 14:24:22.

[22] LHCb Collaboration, R. Forty, *RICH pattern recognition for LHCb*, Nucl. Instrum. Meth. **A433** (1999) 257.

[23] M. Benayoun and C. Jones, *RICH reconstruction and particle identification using ring fit methods: Application to the RICH2 detector*, .

[24] LHC-B Collaboration, *LHCb magnet: Technical design report*, .

[25] M. Tobin, *Performancs of the LHCb Silicon Tracker in pp collisions at the LHC, in Nuclear Science Symposium Conference Record (NSS/MIC)*, 1010 IEEE, pp. 935-938.

[26] A.-N. et al. *LHCb reoptimized detector design and performance: Technical Design Report*, Technical Design Report LHCb, CERN, Geneva, 2012.

[27] *LHCb: Outer tracker technical design report*, .

[28] T. Ferbel, *Experimental Techniques in High Energy Physics*, 1st ed., Addison-Wesley, Menlo Park, CA, 1987.

[29] LHCb Collaboration, P. R. Barbosa-Marinho *et al.*, *LHCb muon system: Technical Design Report*, Technical Design Report LHCb, CERN, Geneva, 2001.

[30] A. A. J. et al. *Performancs of the LHCb muon system*, tech. rep., CERN, Geneva, 2012.

[31] B.-M. et al. *LHCb muon system: second addendum to the Technical Design Report*, CERN, Geneva, 2005.

[32] LHCb, *LHCb trigger system technical design report*, .

[33] LHCb, H. Ruiz, *The LHCb trigger: Algorithms and performance*, Nucl. Instrum. Meth. **A623** (2010) 525.

[34] E. Aslanides *et al.*, *The Level-0 muon trigger for the LHCb experiment*, Nucl. Instrum. Meth. **A579** (2007) 989, arXiv:0705.0310.

[35] V. V. Gligorov, *A single track HLT1 trigger*, .

[36] R. Aaij and J. Albrecht, *Muon triggers in the High Level Trigger of LHCb*, .

[37] LHCb collaboration, R. Aaij *et al.*, *Observation of the resonant character of the $Z(4430)^-$ state*, Phys. Rev. Lett. **112** (2014) 222002, arXiv:1404.1903.

[38] S. Godfrey and N. Isgur, *Mesons in a relativized quark model with chromodynamics*, Phys. Rev. **D32** (1985) 189.

[39] Particle Data Group, K. A. Olive *et al.*, *Review of Particle Physics*, Chin. Phys. **C38** (2014) 090001.

[40] R. Kokoski and N. Isgur, *Meson Decays by Flux Tube Breaking*, Phys. Rev. **D35** (1987) 907.

[41] Bari-Birmingham-CERN-Milan-Paris-Pavia, T. Armstrong *et al.*, *A Partial Wave Analysis of the $K^-\phi$ System Produced in the Reaction $K^-p \to K^+K^-K^-p$ at 18.5-GeV/c*, Nucl. Phys. **B221** (1983) 1.

[42] Particle Data Group, K. A. Olive *et al.*, *Review of particle physics*, Chin. Phys. **C38** (2014) 090001.

[43] D. Aston *et al.*, *Evidence for two J(P) = 2- strange meson states in the K(2)(1770) region*, Phys. Lett. **B308** (1993) 186.

[44] D. Frame *et al.*, *A Spin Parity Analysis of the ϕK^+ System Produced in the Reaction $K^+p \to \phi K^+p$, $\phi \to K^+K^-$ at 13-GeV/c*, Nucl. Phys. **B276** (1986) 667.

[45] ACCMOR, C. Daum *et al.*, *Diffractive Production of Strange Mesons at 63-GeV*, Nucl. Phys. **B187** (1981) 1.

[46] D. Aston *et al.*, *The Strange Meson Resonances Observed in the Reaction $K^- p \to \bar{K} 0 \pi^+ \pi^- n$ at 11-GeV/c*, Nucl. Phys. **B292** (1987) 693.

[47] F. P. Bird, *CHERENKOV RING IMAGING AND SPECTROSCOPY OF CHARGED KSTAR CHARGED KSTAR INTERACTIONS AT 11-GeV/c*, PhD thesis, SLAC, 1988.

[48] Y.-j. Kwon, *Strange meson spectroscopy in K omega and K phi at 11-GeV/c and Cherenkov ring imaging at SLD*, PhD thesis, SLAC, 1993.

[49] (LHCb Collaboration), R. e. a. Aaij, *Observation of the resonant character of the $z(4430)^-$ state*, Phys. Rev. Lett. **112** (2014) 222002.

[50] Belle, K. Chilikin *et al.*, *Observation of a new charged charmoniumlike state in $\bar{B}^0 \to J/\psi K^- \pi^+$ decays*, Phys. Rev. **D90** (2014), no. 11 112009, arXiv:1408.6457.

[51] F. James, *Statistical methods in experimental physics*, World Scientific Publishing, 2006.

[52] LHCb, R. Aaij *et al.*, *Quantum numbers of the $X(3872)$ state and orbital angular momentum in its $\rho^0 J\psi$ decay*, Phys. Rev. **D92** (2015), no. 1 011102, arXiv:1504.06339.

[53] X. Liu and S.-L. Zhu, *$Y(4143)$ is probably a molecular partner of $Y(3930)$*, Phys. Rev. **D80** (2009) 017502, arXiv:0903.2529.

[54] T. Branz, T. Gutsche, and V. E. Lyubovitskij, *Hadronic molecule structure of the $Y(3940)$ and $Y(4140)$*, Phys. Rev. **D80** (2009) 054019, arXiv:0903.5424.

[55] R. M. Albuquerque, M. E. Bracco, and M. Nielsen, *A QCD sum rule calculation for the $Y(4140)$ narrow structure*, Phys. Lett. **B678** (2009) 186, arXiv:0903.5540.

[56] G.-J. Ding, *Possible molecular states of $D_s^* \bar{D}_s^*$ system and $Y(4140)$*, Eur. Phys. J. **C64** (2009) 297, arXiv:0904.1782.

[57] J.-R. Zhang and M.-Q. Huang, *$(Q\bar{s})^{(*)}(\bar{Q}s)^{(*)}$ molecular states from QCD sum rules: a view on $Y(4140)$*, J. Phys. **G37** (2010) 025005, arXiv:0905.4178.

[58] Z.-G. Wang, Z.-C. Liu, and X.-H. Zhang, *Analysis of the $Y(4140)$ and related molecular states with QCD sum rules*, Eur. Phys. J. **C64** (2009) 373, arXiv:0907.1467.

[59] J. He and X. Liu, *The line shape of the open-charm radiative and pionic decays of $Y(4274)$ as a molecular charmonium*, arXiv:1102.1127.

[60] S. I. Finazzo, M. Nielsen, and X. Liu, *QCD sum rule calculation for the charmonium-like structures in the $J/\psi\phi$ and $J/\psi\omega$ invariant mass spectra*, Phys. Lett. **B701** (2011) 101, arXiv:1102.2347.

[61] E. S. Swanson, *Z_b and Z_c Exotic States as Coupled Channel Cusps*, Phys. Rev. **D91** (2015), no. 3 034009, arXiv:1409.3291.

[62] E. S. Swanson, *Cusps and Exotic Charmonia*, arXiv:1504.07952.

[63] D. V. Bugg, *How Resonances can synchronise with Thresholds*, J. Phys. **G35** (2008) 075005, arXiv:0802.0934.

[64] D. V. Bugg, *An Explanation of Belle states $Z_b(10610)$ and $Z_b(10650)$*, Europhys. Lett. **96** (2011) 11002, arXiv:1105.5492.

[65] D.-Y. Chen, X. Liu, and T. Matsuki, *Reproducing the $Z_c(3900)$ structure through the initial-single-pion-emission mechanism*, Phys. Rev. **D88** (2013), no. 3 036008, arXiv:1304.5845.

[66] X.-H. Liu and G. Li, *Exploring the threshold behavior and implications on the nature of Y(4260) and Zc(3900)*, Phys. Rev. **D88** (2013) 014013, arXiv:1306.1384.

[67] A. P. Szczepaniak, *Triangle Singularities and XYZ Quarkonium Peaks*, Phys. Lett. **B747** (2015) 410, arXiv:1501.01691.

[68] R. M. Albuquerque, M. E. Bracco, and M. Nielsen, *A {QCD} sum rule calculation for the narrow structure*, Physics Letters B **678** (2009), no. 2 186 .

[69] R. M. Albuquerque and R. D. Matheus, *The decay channel of the y(4140) molecular state*, Nuclear and Particle Physics Proceedings **258259** (2015) 148 , 17th International Conference in Quantum Chromodynamics (QCD 14)The {XVII} International Conference on Quantum Chromodynamics.

[70] Wang, Zhi-Gang, *Analysis of the y(4140) with qcd sum rules*, Eur. Phys. J. C **63** (2009), no. 1 115.

[71] X. Liu and S.-L. Zhu, $y(4143)$ *is probably a molecular partner of* $y(3930)$, Phys. Rev. D **80** (2009) 017502.

[72] T. Branz, T. Gutsche, and V. E. Lyubovitskij, *Possible Hadronic Molecule Structure of the Y(3940) and Y(4140)*, AIP Conf. Proc. **1257** (2010) 432, arXiv:1001.3959.

[73] M. Karliner and J. L. Rosner, *Exotic resonances due to η exchange*, arXiv:1601.00565.

[74] N. V. Drenska, R. Faccini, and A. D. Polosa, *Exotic hadrons with hidden charm and strangeness*, Phys. Rev. D **79** (2009) 077502.

[75] Z.-g. Wang and Y.-f. Tian, *Tetraquark state candidates: Y(4140), Y(4274) and X(4350)*, Int. J. Mod. Phys. **A30** (2015) 1550004, arXiv:1502.04619.

[76] F. Stancu, *Can* $Y(4140)$ *be a* $c\bar{c}s\bar{s}$ *tetraquark ?*, J. Phys. **G37** (2010) 075017, arXiv:0906.2485.

[77] H. Hogaasen, J. M. Richard, and P. Sorba, *A Chromomagnetic mechanism for the X(3872) resonance*, Phys. Rev. **D73** (2006) 054013, arXiv:hep-ph/0511039.

[78] LHCb collaboration, R. Aaij *et al.*, *Determination of the $X(3872)$ meson quantum numbers*, Phys. Rev. Lett. **110** (2013) 222001, arXiv:1302.6269.

14 Vita

Thomas Britton

Degrees:

Ph.D. Physics, Syracuse University, 2016

Concentration: High Energy Physics-Experimental

Dissertation: Amplitude Analysis of $B \to J/\psi\,\phi K$

B.A, Physics/Mathematics, Coe College, 2009

Majors: Physics, Mathematics

Minor: Computer Science

Experience:

Research Assistant, 2011-2015

Syracuse University LHCb group

Head Teaching Assistant (PHY 212), 2009-2011

Syracuse University

Summer Undergraduate Research Fellow 2007

National Institute of Standards and Technology

Topic: Self-Assembling Mono-layers

Presentations:

LHCb Workshop on Multi-body decays of B and D mesons – Rio de Janeiro, July 29, 2015

"X(3872) and other neutral exotic meson candidates"

HADRON Conference – Newport News, VA Sept 12-17th, 2015

LHCb Results on Exotic Meson Spectroscopy

APS Meeting – Salt Lake City, UT April 16-19th 2016

Latest results on tera- and penta-quark candidates from LHCb

Publications:

On the author list of LHCb since 2009 (299 papers as of Feb. 2016)

In progress: Amplitude analysis of $B \to J/\psi\,\phi K$ (PRL+PRD)

Awards and Honors:

University of Iowa 24-hour mathematical modeling competition: 1st place 2007

MCM Meritorious winner 2009